The Messenger

VLT Science Products Produced by Pipelines: A Status Report

Using the Data Flow System, ESO is producing calibrated science data products for all VLT and VLTI instruments. For many users, these products can be used directly for scientific analysis without further processing. In the end, the scientific usefulness of these products depends strongly on the needs of the individual investigators.

David R. Silva and Michèle Peron (ESO)

ONE OF THE GOALS for the VLT Data Flow System (Quinn 1996) is to provide calibrated data products ready for science analysis for the instrument modes used most heavily during service observing. Achieving this goal depends on a complex interaction between the science goals of the astronomer, the operational model of the observatory, and the implementation of **instrument calibration pipelines**. The VLT Science Policy document establishes the following guidelines for instrument calibration and data products:

ESO will execute and maintain a calibration plan for all VLT/VLTI instruments. The calibration data resulting from this plan shall be made available to the ESO community. ESO will also use these data to monitor the long-term evolution of instruments and to produce data products. These data products will result from pipeline processing using the VLT/VLTI Data Flow System. Data products will consist of data with the instrumental signature removed as well as data calibrated into physical units. The accuracy of the instrumentation and physical unit calibration will be monitored and maintained by ESO.

In order to allow the ESO community to reproduce and modify the output of instrument calibration pipelines, ESO will make the pipeline reduction recipes and code available to the ESO community for all supported instrument modes. Over time, the number of supported modes for each instrument will be increased to ensure that the most actively used modes have calibrated data products available.

The accuracy of ESO pipelines should be such to satisfy a major fraction of the scientific needs of the users and ESO will attempt to increase their accuracy over time following the guidance of its community and in-house scientists.
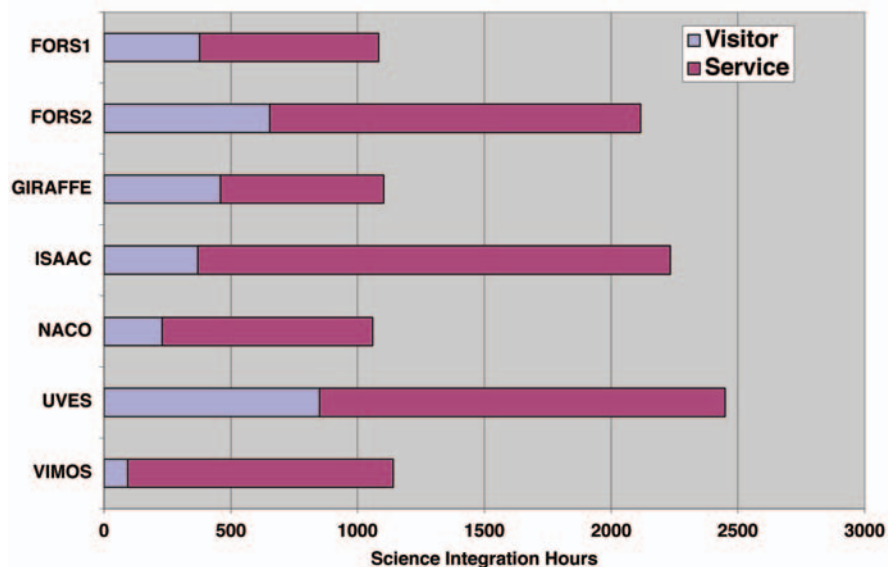

Figure 1: Science integration hours per VLT instrument, Period 70 – 73. The FORS1, FORS2, ISAAC, and UVES instruments were operational during this entire two-year period. VIMOS and GIRAFFE operations did not start until February 2003. Exact dates are 2002 October 1 to 2004 September 30. Guaranteed Time Observations (GTO) data have been excluded.

In this article, the current status of VLT/VLTI science products delivered by instrument calibration pipelines is presented with an emphasis towards science readiness, i.e. whether the currently delivered science products can be used for science analysis without further processing. For the most heavily used instrument modes over the last two years, we believe the answer is "yes", depending on the science objective and the required calibration precision. In the end, however, the usefulness and quality of any given science data product is in the eye of the beholder, i.e. it strongly depends on the technical needs and science objectives of the end-user astronomer or data analysis team. We hope this article will not only provide information to the ESO user community but also elicit feedback to help us improve our service.

In the following article, VLT is used as a metaphor for all science instruments operated on Cerro Paranal. Messenger articles by Comerón et al. (2003) and Mathys (2004) provide recent overviews of the VLT service observing operational model. Discussion of instrument calibration pipelines and science products for La Silla instruments are outside the scope of this article.

INSTRUMENT CALIBRATION PIPELINES
Operational fundamentals
All VLT science observations are executed using Observation Blocks (OBs) that are in turn composed of observation templates. Automatic instrument calibration pipelines have been implemented for the most heavily used instrument modes. These pipelines produce master calibration products used to monitor instantaneous and long-term instrument performance. Using the master calibration products, the pipelines also process raw

science data into science products. Data are processed on a template-by-template basis. Data from different templates (or different OBs) are not processed together. In general, only so-called standard instrument configurations are supported.

The *automatic* production of science products using instrument calibration pipelines requires an electro-mechanically stable instrument (including detector), the acquisition of sufficient calibration data, and the implementation of proper software algorithms, where proper is defined as an algorithm that does not degrade scientific usefulness. How is ESO doing in these areas?

• **Stability:** at present, most of our instruments are stable (FORS1, FORS2, UVES, GIRAFFE), some are semi-stable (ISAAC, NACO) and one is (mechanically) unstable (VIMOS). Despite various mechanical problems, high quality VIMOS science products are often produced in automatic mode if sufficient night-time calibrations are available.

• **Calibration data:** calibration plans exist for all instruments and calibration data are obtained on a regular basis. These data are used to monitor instrument health and process science data. The target photometric calibration accuracy is 5–10% in magnitude for imaging and in the relative flux calibration for spectroscopy. The achieved photometric accuracy is often much better in both cases. Nevertheless, the achieved accuracy may not be sufficient for all science programmes.

• **Proper algorithms:** for imaging, essentially no problems exist today. For spectroscopy, the situation is more complex. While UVES pipeline results are universally proclaimed as science-ready for most users, this is not necessarily true for other instruments.

Instrument usage for science observa-

tions during the last two years is summarized in Figure 1. During this interval, more science data was produced in Service Mode than in Visitor Mode for all instruments. This information is broken down by instrument mode in Figure 2. Modes without pipeline support are indicated by vertical stripes. The vast majority of science data obtained during this period came from instrument modes with pipeline support. The most glaring exception is FORS2-MXU. Unfortunately, it was necessary in the last two years to shift pipeline development resources originally scheduled for FORS2-MXU to VIMOS.

Recipe development and availability

At the core of each instrument calibration pipeline are a set of instrument-specific software data processing engines known as **pipeline recipes**. For FORS1, FORS2, VIMOS, GIRAFFE, and MIDI, the instrument consortia that built and commissioned those instruments developed the original pipeline recipes. Since their delivery, these recipes have been maintained by ESO and modified to meet ESO operational goals. Recipes for the other currently operational instruments (VIMOS-IFU, ISAAC, UVES, and NACO) were developed within ESO where they are still actively maintained and extended as needed.

Recipes are released to the community as soon as possible after instrument operations begin, but not before their performance has been verified using data from the as-built, as-operated instrument in all standard configurations. In the past, this verification process has taken as long as a year but has recently accelerated. Recipe upgrades are released as needed. For information about how to download available recipes, see http://www.eso.org/pipelines/.

All released pipeline recipes come with technical documentation – some good and some not so good. More useful for astronomers are the science reduction discussions maintained for each of the VLT instruments on the ESO QC Web pages (http://www.eso.org/qc). But astronomer-oriented cookbooks are really needed, preferably written by experienced astronomers familiar with the pipeline recipes. Such a guidebook exists for ISAAC. ESO is trying to find ways to facilitate the creation of such cookbooks for other instruments, but unfortunately no direct resources for this activity exist right now.

Recent pipeline recipes (VIMOS, GIRAFFE) were built partially or in whole using the Common Pipeline Library (CPL) developed by ESO. All future recipes will be based on CPL (http://www.eso.org/cpl). This has two benefits for end-user astronomers. First, all CPL-based recipes will have common Unix shell behavior, creating a more unified and stable user interface. Such behavior allows rapid development of user-specific processing scripts using the Unix shell or such common scripting languages as Perl or Python. The tools *dfits* and *fitsort* (see http://archive.eso.org/saft) can be used to extract and organize FITS header information within such scripts. Second, CPL-based recipes can be executed within the **Gasgano** data organization and management tool developed by ESO (available from http://www.eso.org/gasgano/). Gasgano provides a user-friendly Java-based environment for data organization and processing within a single graphical user interface.

At ESO, the pipeline recipes are embedded in an infrastructure that automatically classifies raw data frames, associates them with appropriate master calibration products, and then executes the appropriate

Figure 2: Science integration time per VLT instrument mode, Period 70 – 73. Modes with active instrument calibration pipelines are shown with solid colors, while modes without pipelines are indicated by vertical stripes. Exact dates are 2002 October 1 to 2004 September 30. Guaranteed Time Observations (GTO) data have been excluded.
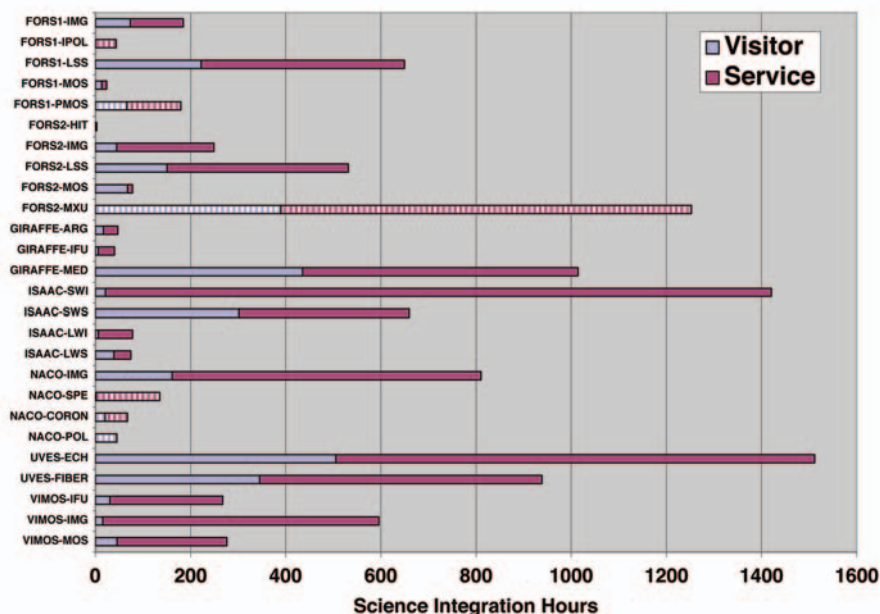
pipeline procedure. This infrastructure is tuned to the ESO operational environment and cannot be easily exported to external sites. As our pipeline infrastructure evolves this situation may change, and ESO will explore ways of providing more automatic data organization tools to the community.

SCIENCE PRODUCTS

Creation of science products
For instrument modes with pipeline support (see Figure 2), science products can be produced automatically on Paranal, if appropriate calibration data are available. Immediately after an OB template is completed, the Paranal-based pipelines attempt to create science products using pre-loaded calibration data. These pre-loaded data are not necessarily the best possible and are typically updated only at 1 – 3 month intervals. On a best effort basis, Paranal Science Operations can sometimes pre-load more appropriate calibration data for specific programmes. If appropriate calibration data are not available (e.g. mask-specific flats for multi-object spectroscopy reductions obtained in morning after science observations or non-standard instrument configuration used), no science products are created. If created, science products are made available to visiting astronomers at the appropriate off-line workstation. Visitors also have the option of using the off-line workstations to process (or re-process) their science data.

In Garching, all Service Mode science data are processed (or re-processed) using the same pipeline recipes, although sometimes with different control parameters (e.g. average vs. median combination, block-average vs. optimal spectral extraction). Furthermore, the best available and most appropriate calibration data are used, even if they were obtained after the science observation. Service Mode science products are delivered in due time to the principal investigator. At this time, Visitor Mode data are not re-processed and delivered due to staffing limitations, but such a service may be provided in the future. In general, the quality of the science products produced in Garching are higher than the products produced on Paranal because better calibration data are used and the pipelines are more closely monitored by ESO staff for output quality.

Science data product quality: what is it?
The VLT Science Policy guidelines indicate that pipelines should remove the instrument signature and calibrate the data into physical units to an accuracy that is satisfactory for a major fraction of users. What is the current general situation?

For **imaging**, the current goal is to produce photometrically flat images with astrometrically accurate World Coordinate System (WCS) coefficients and a nightly

Table 1: Summary of Science Product Status By Instrument Mode

Instrument	Mode	Science Ready?	Product Remarks
FORS1/2	IMG	Yes	No jitter combination
FORS1/2	LSS	Maybe	Polynomial correction for distortion and dispersion too low (?), no correction for slit response or sensitivity, not all grisms supported. Spectrophotometric standards observed but not applied by pipeline.
FORS1/2	MOS	Maybe	Same comment as FORS/LSS.
FORS1	PMOS/IPOL	No	Not supported yet
FORS2	MXU	No	Not supported yet
FORS2	HIT	No	Not supported yet
GIRAFFE	All	Maybe	Science pipeline still under development. Products produced with flat-field correction or optimal extraction. Not all setups supported.
ISAAC	SWI/LWI	Yes	For data before April 2003, image stacks should be reprocessed with the latest recipe.
ISAAC	SWS/LWS	Maybe	Polynomial correction for distortion and dispersion too low (?), no correction for slit response or sensitivity. Telluric standards can be used to determine sensitivity function.
ISAAC	SW-POL	No	Not supported yet
NACO	IMG	Yes	
NACO	Other	No	No pipeline support
MIDI	HIGH_SENS	Yes	Dispersed modes not yet supported. See Ballester et al. (2004)
UVES	ECH	Yes	
UVES	SLICER	Yes	
UVES	FIBRE	Yes	Fibre-to-fibre correction but no sensitivity correction. No automatic background correction, since no dedicated sky monitoring fibre.
VIMOS	IMG	Yes	No jitter combination.
VIMOS	MOS	Maybe	Flat-field not applied, pending further investigation of internal reflections and fringing. No sensitivity correction. Dispersion correction quality variable due to problems related to mask insertion and mechanical flexure. If present, more than one object extracted per slit.
VIMOS	IFU	Maybe	See VIMOS-MOS comments as well as Izzo et al. (2004)

zeropoint with 5 – 10% accuracy if a standard filter was used. Zeropoint accuracy is limited by the number of standard field observations per night (typically, 2). Nightly reports from the Paranal Astronomical Site Monitor (available from http://archive.eso.org/asm/ambient-server) can be used to constrain whether or not the night was photometric. Color terms and extinction coefficients are measured several times a year but not in all filters. Values are published on the ESO Quality Control Web pages (http://www.eso.org/qc). If a non-standard filter is used or higher photometric transformation accuracy is required, the user must obtain additional calibration observations. However, ESO leaves the responsibility for building object catalogs in the hands of the user. So, strictly speaking, the objects on delivered images

have not been calibrated into physical flux units – roaming over an image with a WCS aware image browser will show the celestial coordinates of each object but not their magnitudes. But ESO provides the information necessary to convert instrumental flux measurements into physical units once (project specific) object identification and extraction is complete.

In the most general sense, the current goal for **spectroscopy** is to produce background corrected one or two-dimensional spectra with linear scales in the spatial and dispersion direction and their true relative continuum shapes. WCS coefficients should be set to relevant wavelength units (e.g. Ångstroms or microns) in the dispersion direction and arc seconds in the spatial direction. In the future, the spatial WCS

coordinates may be updated to support true celestial coordinates. The flux units are relative counts. If users require a conversion to absolute flux units (e.g. ergs s^{-1} cm^{-2} $Å^{-1}$), they must request additional observations of flux standards with appropriate slit sizes and at appropriate time intervals. For all instruments that produce two-dimensional spectra, ESO provides the processed 2D spectra and an extracted 1D spectrum for the brightest object in each slit. If spectra are extracted, signal-to-noise should be optimized. Of course, details of spectral extraction (or even deciding what to extract) are usually science-driven, so many users may choose to re-extract their objects.

Nevertheless, the usefulness of any given science product for a specific programme may be limited by the quality of the available calibration data and the choice of parameters used when running the recipes (e.g. type of spectral extraction, order of polynomial used for spatial correction). By design, these automatic pipelines process science type of similar type in a similar way in all cases. In the end, astronomers need to decide for themselves and for every project if the science products produced by ESO are right for them or if they need to reprocess their raw data.

Specific goals

Over time, the following goals for science product creation have emerged:

● **All instrument modes:** as appropriate for the specific instrument and detector, corrections for bias, dark, small scale pixel-to-pixel sensitivity variations and large scale illumination variations are applied. WCS coefficients are updated appropriately for instrument mode and situation. Instrument specific quality control parameters are provided.

● **Imaging (IMG):** all frames acquired through the same filter within a single OB template are combined. If the image group is a jitter stack, they are co-aligned and co-added using average with some form of outlier rejection; a byproduct weight map is produced. For mosaic imagers (WFI, OmegaCam), the entire field-of-view is placed on a common astrometric grid; this requires geometric rectification of images from the individual detectors. For imaging polarimetry, images are grouped by relevant optical element, and processed; but Stokes parameters are not computed. *Final product*: single corrected image. *Instruments*: FORS1/FORS2 IMG, ISAAC SWI/LWI, NACO, VIMOS IMG, WFI, OmegaCam.

● **Spectroscopy (general):** corrections are applied for optical distortion, wavelength dispersion, slit response function (only long-slit spectroscopy), fibre response function (fibre-fed instruments only), spectral cross-talk (for densely packed spectra, e.g. IFUs), and relative sensitivity (flux). No

Figure 3: Example FORS MOS Science Product. From FORS1 MOS using 150I grism at λ_{cen} = 7100 Å. Notice alignment of skylines. Courtesy of R. Mignani.
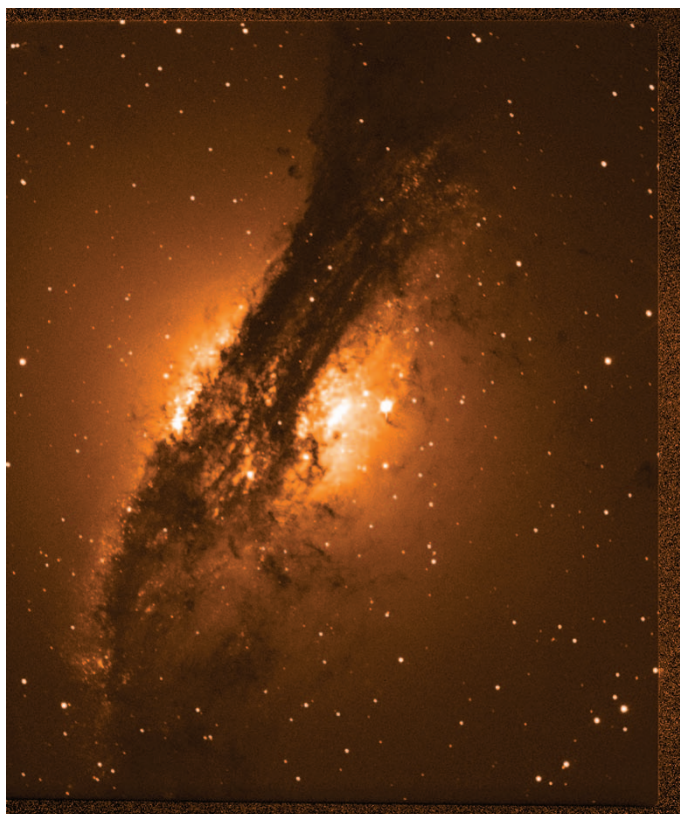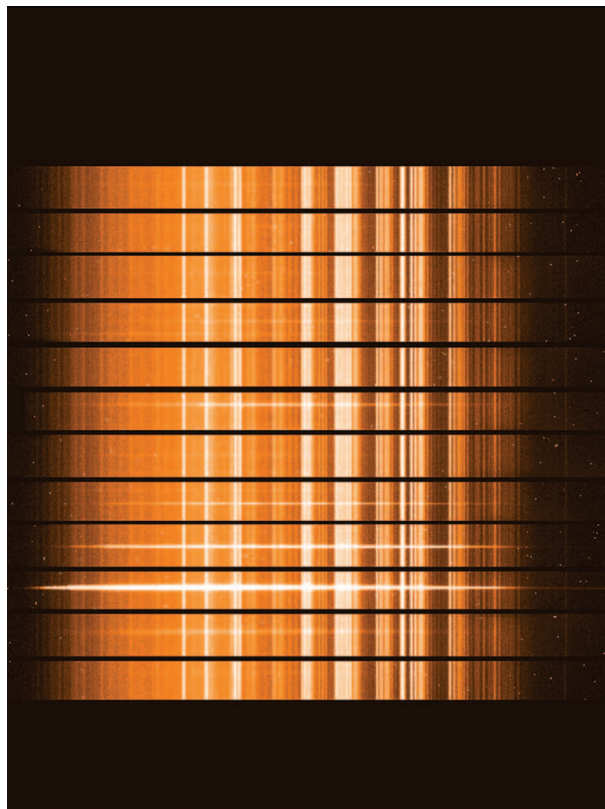

Figure 4: Example VIMOS IMG Science Product. *B*-band image of the center of Cen A (NGC 5128) – quadrant 3 only. Courtesy of P. Sartoretti.

corrections are made for fringing, atmospheric differential refraction, telluric absorption, or airmass. For instrument modes with slits, the background is subtracted; the derived background spectrum used for correction is provided to the user. The brightest object (or objects in some cases) within each slit are extracted into 1D spectra.

● **Long-slit spectra (LSS) and echelle (ECH):** *Final product:* two-dimensional (2D) frame with linear spatial and dispersion scales, extracted 1D spectrum of brightest

Figure 5: Example GIRAFFE IFU Science Product. Left panel: reduced science spectra from 15 GIRAFFE IFU units. Right panel: reconstructed images for each IFU unit. For VIMOS IFU example, see Izzo et al. (2004). Courtesy of R. Hanuschik.
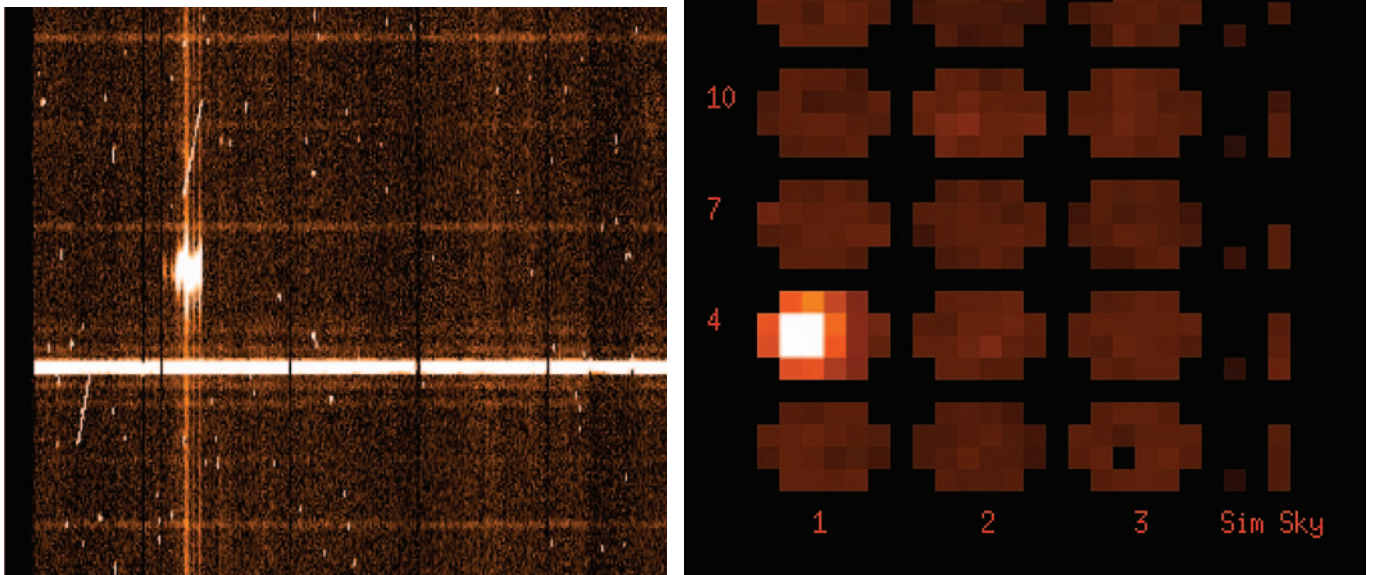
object, and various related spectra depending on instrument (e.g. background spectrum). *Instruments:* FORS1, FORS2, ISAAC SW/LW, UVES (2D spectra by request only).

• **Multi-object spectra (MOS) with slits:** *Final product:* corrected two-dimensional slit images with linear spatial and dispersion scales, aligned in wavelength space, and stacked into one plane of a FITS image. Also: 1D spectra for brightest objects in slits with various supporting spectra as appropriate for instrument (e.g. background spectra). *Instruments:* FORS1/FORS2 MOS, FORS2 MXU, VIMOS MOS.

• **Multi-object spectra (MOS) with fibres:** *Final product:* extracted, flux-corrected one-dimensional spectra with linear dispersion scales, aligned in wavelength space, and stacked into one plane of a FITS image. Various supporting spectra (e.g. error vector). *Instruments:* GIRAFFE MEDUSA, UVES FIBRE.

• **Integral-field spectroscopy (IFU):** *Final product:* same as fibre MOS plus reconstructed (broad-band) image corrected for fibre efficiencies. *Instruments:* VIMOS IFU, GIRAFFE ARGUS, GIRAFFE IFU, SINFONI.

At this time, none of our pipelines make specific corrections for fringing, an optical phenomena caused by interference between incident light and internal reflections between the thin layers in a detector. Internal discussions about this complex topic continue but are beyond the scope of the current article. Likewise, no corrections for telluric absorption lines in spectral regions beyond 7000 Å are made, although spectra of tel-

luric absorption standard stars are obtained as part of the standard ISAAC and NACO calibration plans and delivered to users.

The goal of **VLT interferometry** is to deliver calibrated visibilities. For further details, see Ballester et al. (2004).

Status

Science products created by pipelines during the first years of Paranal operations had variable usefulness for science analysis. Within ESO, higher priority was given initially to producing quick-look data products necessary to confirm field acquisition and quality control parameters to monitor instrument health, rather than science-ready data products. The number one priority for ESO was (and remains) to assure that the raw science data stream is fundamentally sound and produced in a controlled manner. Nevertheless, the quality of pipeline-produced science products has steadily improved and today is quite good in many cases.

Table 1 summarizes current pipeline product status. In the *Remarks* column, deviations from the goals listed above are described. For a brief summary with more details, see Pipeline Status Web page (http://www.eso.org/qc/pipeline-status.html). For complete details, see the instrument-specific sections of the Quality Control Group Web site (http://www.eso.org/qc/). *In particular, readers are urged to read the Known Problems information provided for each instrument.*

A few example science products are shown in Figures 3 – 5. Examples for all supported instrument modes can be found on the QC Group Web pages.

Future Development

Although the current pipeline recipes receive maintenance as time permits, implementation of instrument calibration pipelines for new instruments using CPL-based recipes remains the highest priority. Thanks to early and fruitful collaboration with the instrument development teams during commissioning and science verification, the SINFONI and VISIR pipelines are close to completion and should be operational at the start of Period 75. Next will come OmegaCam, Hawk-I and CRIRES, followed by the various VLT 2nd generation instruments. As soon as possible, FORS1, FORS2 (including MXU), ISAAC, NACO and UVES pipelines will be re-implemented, using CPL-based modules written for other instruments. Realistically, it may take more than two years to complete this conversion work, given higher priority projects.

In parallel, ESO is investigating ways of providing science products produced from data with expired proprietary periods to the community. Possibilities include ingesting existing Service Mode science products kept on off-line archival media or re-created science products produced by re-processing raw science data with improved pipeline recipes. A pilot project involving UVES data is active. In the future, ESO will also ingest into the Science Archive Facility science products produced by ESO for Service Mode users immediately after their creation and then make them available to the community after the proprietary period is completed. If resources permit, it may also be possible to start created products from Visitor Mode data on a regular basis. Finally, as

Table 2: On-line Resources Related to Science Products

Resource	URL	Remarks
ESO Quality Control Group	http://www.eso.org/qc/	Instrument-specific information about quality control, data processing, and science products
Gasgano	http://www.eso.org/gasgano	Java-based tool for file organization and recipe execution
Common Pipeline Library (CPL)	http://www.eso.org/cpl	ISO-C libraries to build pipeline recipes
Pipeline recipes	http://www.eso.org/pipelines	Released recipes and documentation
Pipeline status	http://www.eso.org/qc/pipeline-status.html	Brief overview of pipeline status, updated before every ESO Period
Site Monitor	http://archive.eso.org/asm/ambient-server	Daily meteorological data for Paranal and La Silla
Standalone FITS Tools	http://archive.eso.org/saft/	Tools for working with FITS files

appropriate, on-the-fly recalibration systems will be activated for appropriate instruments modes. Many of these efforts will fall under the responsibility of the Virtual Observatory Systems department created recently within the Data Management and Operations Division.

ACKNOWLEDGMENTS

REFERENCES

Ballester, P. et al. 2004, Messenger, 116, 4
Comerón, F. et al. 2003, Messenger, 113, 32
Izzo,C. et al. 2004, Messenger,117, 33
Mathys, G. 2004, Messenger, 116, 8
Quinn, P.J. 1996, Messenger, 84, 30

H. Heyer (ESO)

Signature in Copenhagen of the agreement for the construction of the *X-shooter*, a second generation VLT instrument scheduled to go into operation in 2008. From left to right, sitting: Jens Hjorth (Astronomy Professor, Copenhagen University Observatory), Henning Jørgensen (Astronomy Professor, Copenhagen University and Danish ESO Council Member), Jørgen Olsen (Vice-Chancellor, Copenhagen University), Catherine Cesarsky (Director General of ESO), Per Kjærgaard Rasmussen (P.I. for the *X-shooter*, Copenhagen University Observatory); standing: Nils O. Andersen (Director of the Niels Bohr Institute for Astronomy, Physics and Geophysics), Sandro D'Odorico (*X-shooter* P.I. at ESO) and Jens Viggo Clausen (Director of Copenhagen Observatory). (see Page 71)

The FLAMES-UVES Pipeline

In this paper we describe features associated with the data reduction of UVES when operated in Fibre Mode, the required calibrations, the data processing steps and the quality checks performed by the pipeline. We also summarise some results.

Andrea Modigliani[1], Giacomo Mulas[2], Ignazio Porceddu[2], Burkhard Wolff[1], Francesco Damiani[3], Klaus Banse[1]

[1]European Southern Observatory, Germany
[2]INAF - Osservatorio Astronomico di Cagliari, Italy
[3]INAF - Osservatorio Astronomico di Palermo, Italy

FLAMES, the Fibre Large Array Multi-Element Spectrograph, is the multi-object, intermediate and high resolution spectrograph mounted at the Nasmyth A platform of UT2 of the Very Large Telescope (VLT, see Pasquini et al. 2003, or www.eso.org/instruments/flames). Among its components is the link to the UVES Red Arm fed by eight fibres with a nominal resolution power of R=47,000. The UVES red arm also has a fibre link, the *SimCal* fibre, to a calibration unit.

To solve the specific problems associated with the FLAMES-UVES data reduction, a new data reduction software (DRS) has been developed in a collaborative effort between ESO and the Ital-FLAMES consortium. The software is offered to the user community (www.eso.org/projects/dfs/dfs-shared/web/vlt/vlt-instrument-pipelines.html) as part of a MIDAS context and extends the UVES pipeline functionalities (Ballester et al. 2000).

Pipelines are crucial in supporting operations of the VLT instruments. They are used mainly in three modes: 1) Paranal Science Operations (PSO) uses them as a quick-look and quality control tool to monitor the instrument status almost in real-time and to detect if a calibration or an observation needs to be repeated. PSO monitors the Quality Control (QC) parameters which are logged by the online environment. 2) The Data Flow Operation's department (DFO) in Garching provides permanent and in-depth knowledge of the instrument status. QC parameters are extracted from the data, stored in a database and made available via the Web (www.eso.org/qc) to PSO and the user community. From this information it is possible to control, predict, and often improve the performance of the instruments (QC articles can be found under www.eso.org/qc). Additionally, DFO creates calibration products to reduce Service Mode science observations. 3) Users may use a pipeline to interactively reduce data at their home institutes. To achieve such demanding goals, a pipeline must be robust, reliable and able to work in an unattended, fast and flexible way.

Required calibrations

Several calibrations are necessary to reduce FLAMES-UVES science data. Some of them are common to UVES data obtained in Slit Mode such as biases, necessary to evaluate the read-out of the detector at zero integration time, as well as darks to estimate the detector read-out arising from the isotropic thermal background emission from the instrument.

As the UVES instrument setup may have a drift of up to a few pixels, a set of Slit Flat Fields in echelle mode is taken to correct PSFs for varying pixel-to-pixel efficiency. To be able to evaluate inter-order background and to cover the entire fibre Y span, three sets of three slit Flat Fields each, taken at three different Y positions, are used.

Other calibrations are specific to the fibre mode. A format check frame is obtained by illuminating the *SimCal* fibre with a ThAr lamp. A single fibre flat field is taken by exposing the *SimCal* fibre with a continuum source. These two frames are used to bootstrap the wavelength calibration and the order and fibre trace definition, respectively.

A frame obtained while illuminating all the fibres with a ThAr lamp is taken to find a wavelength calibration solution and a frame taken when illuminating all fibres with a continuum source (all-flat) is needed to compute different fibre throughputs.

A set composed of two exposures illuminating odd-numbered (odd-flat) and even-numbered (even-flat) fibres respectively is also taken to have a set of uncontaminated fibre flat fields for accurate cross dispersion Point Spread Functions (PSFs) evaluation. These are used to assess and correct the non-negligible contamination of adjacent fibres during the extraction of each fibre spectrum.

The user may request all-flat frames at night to get very accurate flat-field corrected science frames. These are obtained by illuminating the fibres with the light reflected by a Nasmyth screen. If particularly accurate wavelength calibrations are required, observations are done in *SimCal* mode, with seven fibres allocated to objects and sky and the SimCal fibre fed by a ThAr lamp.

Data reduction steps

For the FLAMES-UVES data reduction (Mulas et. al. 2002.) the following steps are required:

1. A master bias and a master dark are created and subtracted from the other raw frames.

2. The location of the *SimCal* fibre and a selected list of ThAr lines are determined with the help of a physical model of the instrument on the format check frame. A guess-line table and a guess-order table are generated.

3. Using the single fibre flat field frame a more precise guess-order table is created. Such a table is used to bootstrap the fibre-order tracing and the frame itself to extract the ThAr spectra carried from the *SimCal* fibre in science observations taken in *SimCal*-Mode.

4. From each set of slit Flat Fields a Master Slit Flat field is derived to lower the noise level.

5. The order-fibre definition is made on the odd and even fibre flat field spectra and is refined on the all fibre flat field spectra starting from the guess-order table determined previously. This generates a raw order-fibre table which will be refined to correct for fibre shifts.

6. The slit flat fields positions and extensions are measured in order to define the minimal set which fully covers the maximum Y span. The slit flat field frames are then equalised in flux and cleaned.

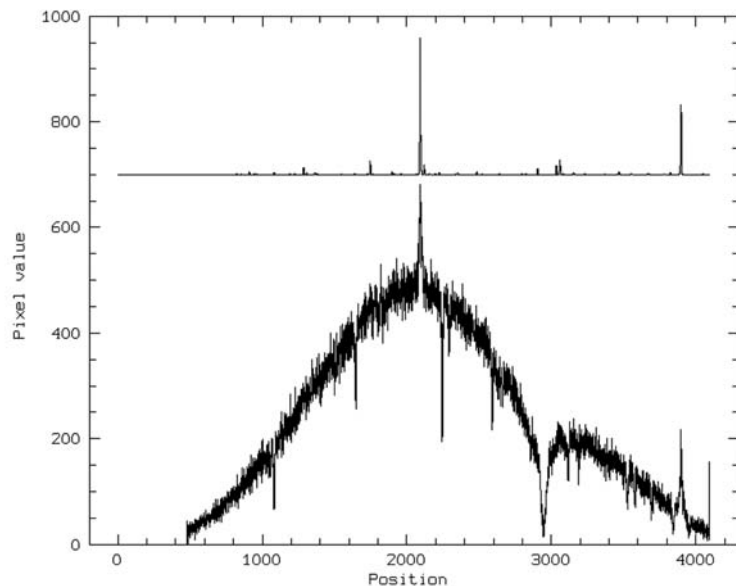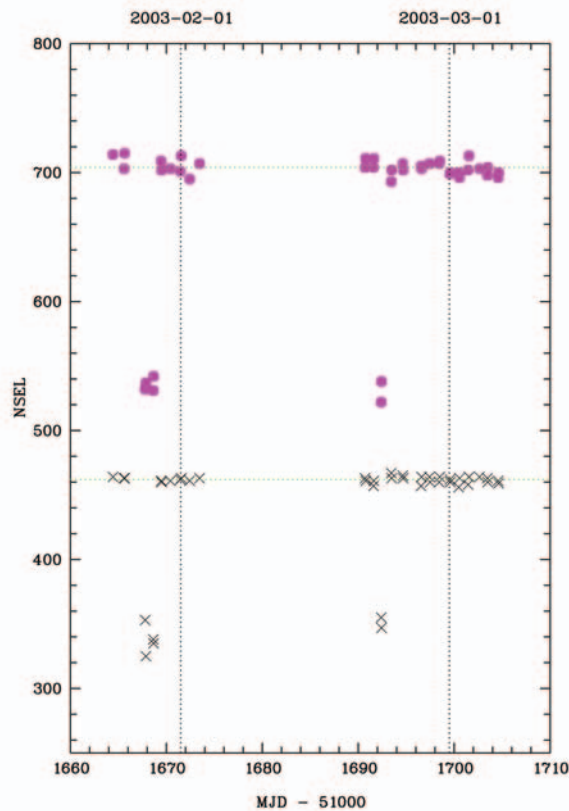7. As the extraction is very sensitive to

Figure 1: (Left:) Trending of the number of selected lines in format check frames with 580 nm central wavelength recorded during the science verification phase and the first FLAMES Service Mode period. Results for the lower CCD are plotted as filled circles, for the upper CCD as crosses. The green horizontal lines indicate reference values. (Right:) The lower part of the plot shows H_β observed on the fibre next to the one fed by a ThAr lamp (rescaled by a factor 1000, shifted, at the top). The spectral contamination coming from the adjacent fibre is of the order of 0.001.

mismatches in the assumed fibre positions, fibre shifts are determined and corrected during data reduction.

8. Odd and even Flat Fields are background subtracted, divided by the slit Flat Fields to get their PSFs and normalised to simplify fibre shifting.

9. The all-fibre Flat Field is (standard or optimally) extracted, the resulting spectra are stored as relative normalisation factors for the subsequent reduced science spectra so that the fibre positions and transmittances in science frames can be measured later on.

10. During wavelength calibration each fibre ThAr spectrum is extracted and ThAr lines are detected above the background. They are then located and identified using a previous guess-solution and a line table is generated containing independent solutions for all fibres.

11. The science frame is extracted. A correlation function between the science frame and a synthetic frame composed of Gaussian shaped fibres is computed as a function of the cross dispersion shifts of the simulated fibres. Its maximum yields to the measured shift of the fibres on the science frame with respect to their positions on the all fibre flat field frame.

12. The single fibre PSFs are shifted accordingly, and re-multiplied by the slitFF frames. In this way one mimics calibrations taken simultaneously with the science frame. Standard or optimal extraction is performed.

13. Using standard extraction, the adjacent fibres' contribution to the flux centred over one fibre is obtained using an integration over the same interval of the fibre PSFs. The solution of the resulting linear system gives the disentangled spectra.

14. Using optimal extraction the whole fibre pattern is fitted by a linear combination of all fibre PSFs. The solution of the resulting linear system gives the disentangled spectra. Next, a kappa-sigma clipping is performed to identify and reject bad-pixels. Thus, the system solution has to be iterated until convergence is achieved. Optimal extraction provides a computationally more expensive but more accurate solution than standard extraction.

The results of the extraction are the deconvolved spectra in pixel-order space (both raw and throughput normalised) along with their variances and bad pixel masks. The right panel of Figure 1 shows that the residual contamination from adjacent fibres is only of ≈ 0.001 after data reduction. Finally, the extracted spectra are wavelength calibrated and merged.

QUALITY CHECKS

One of the main tasks for a pipeline is to produce Quality Control (QC) parameters, which are logged both in the FITS header of the pipeline products and by the online environment in ASCII files. The FLAMES-UVES pipeline generates QC parameters for each reduction step (see Wolff et al. 2004).

During master bias generation the read-out-noise of the master and of one raw frame are measured to verify the overall CCD stability. The pipeline also determines the average value of the master and any residual slope along X and Y to spot potential global and local problems on the CCD. During master slit flat field generation the number of frames co-added is recorded.

The spectral format instrument stability is monitored on format check frames. Using a reference format check frame and cross-correlating the guess-table solutions obtained on the actual and reference frame, it is possible to measure shifts of the spectral format. As an example, left panel of Fig. 1 shows the number of selected lines in format check frames during science verification and the first FLAMES Service Mode period. On two occasions, there have been shifts of the spectral format in cross-dispersion direction of up to ten pixels. Such shifts made a proper data reduction using daytime calibration impossible. But they could be detected easily using format check results because the number of selected lines decreased dramatically. During the single-fibre order tracing step the pipeline checks that the single fibre
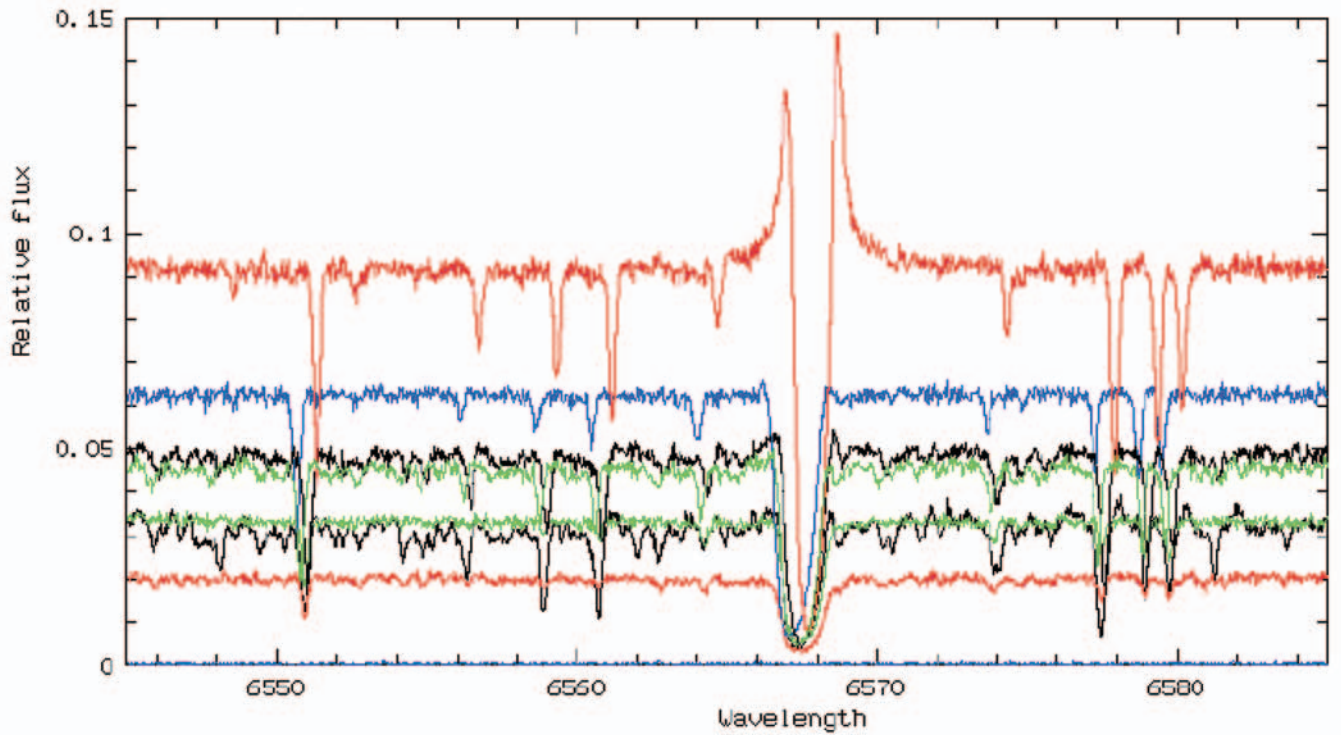
Figure 2: The upper plot shows the reduced spectra of seven giants in ω Cen taken in March 2003 with the UVES fibre around the Hα line. The plot on the left shows the Diffuse Interstellar Band spectrum which appears to be shifted with respect to the "nominal" position.

input frames are well and uniformly illuminated. The order-fibre traces detection step checks that all fibres are traced for each detected order. This is necessary to generate proper wavelength calibration solutions to calibrate the extracted science data. It measures cross order shifts between the all fibre flat field and the odd and even fibre flat fields.

The wavelength calibration step measures the spectral power and the residual difference between the line wavelength values from a reference table and the corresponding values obtained from each fibre solution. Good residuals are characterised by an RMS around 0.0004 nm. Typical values of the resolving power are around 48,000. The intensity of a list of ThAr lines is measured in order to monitor the ThAr lamp health. Science data reduction monitors the Y shifts

between the science frame and the odd-even frames.

RESULTS

We give here only a few examples of results obtained reducing FLAMES-UVES data. In the top panel of Fig. 2 we show an example of the merged spectra obtained for seven giants of the ω Cen globular cluster.

The bottom plot in Fig. 2 shows the Diffuse Interstellar Band (DIB) known to be present at about 661.4 nm. The shown spectrum was taken toward ω Cen during the FLAMES GTO run by the INAF - Cagliari Astronomical Observatory FLAMES team. The DIB is shifted with respect to the "nominal" position, although not according to the ω Cen radial velocity.

In conclusion, the FLAMES-UVES pipeline has been demonstrated to be a very useful tool to reduce FLAMES-UVES cali-

brations and science observations since first commissioning, during Science Verifications (Primas, 2003) and then to support operations for more than 20 months. Additionally, although this is just an "extra", FLAMES-UVES pipeline reduced data may be used by users to do science.

REFERENCES
Ballester P. et al. 2000, ESO Messenger 101, 31
Mulas et al. 2002, "Automatic Data reduction in support of the FLAMES-UVES VLT facility", SPIE 4844, 310
Pasquini L. et al. 2003, ESO Messenger 111, 1
Primas F. 2003, ESO Messenger 112, 3
Wolff et al. 2004, "Quality control for UVES-fibre at the VLT-Kueyen Telescope", SPIE, 5493, 574

Observing During Bright Time: Tips and Tricks

In this paper we present and discuss the effects of scattered moonlight on optical observations, the current status of the moonlit night sky modelling and the implications this has on the Service Mode observations and the maximisation of scientific outcome.

Ferdinando Patat

User Support Dept. - ESO, DMD

EVEN THOUGH it is certainly one of the most fascinating celestial objects, the moon is indeed a disturbing companion when one is to push ground-based telescopes and instruments to their limits, since it causes a significant increase in the sky brightness, at least in the UV and optical domains (see Fig. 1 for a real example). This is why such observations are usually carried out during dark time, when the sky brightness reaches its minimum values. In general, the effect of an enhanced night sky emission translates into an increased background photon shot noise, which in turn, degrades the signal-to-noise one can reach in the science exposures. For example, in the most extreme case of full moon, the night sky in the *B*-band is typically four magnitudes brighter than during dark time. For any given exposure time, this causes the signal-to-noise ratio of background dominated images to decrease by more than a factor of six with respect to the same exposure obtained in dark time. Of course, not all astronomical observations need dark conditions and, depending on the apparent luminosity of the targets, they can be successfully carried out with a moderate contribution by the moon. In some extreme cases, like high-resolution spectroscopy of bright stars, the observations can be safely performed even with full moon.

In an era when Service Mode appears to be the most efficient way of operating large telescopes, it is clear that having a tool for setting the moon constraints in an optimal way would increase the chances that a given programme is effectively executed. For these reasons, the quantitative study of the moon impact on astronomical observations is an important task, which most large ground-based observatories are starting to pursue.

In this paper we will present the effects of moonlight, the basic ingredients that contribute to the physical problem, the current status of modelling and we will finally discuss the future perspectives.

Figure 1: Image taken by the ESO Mini All-Sky Cloud Observation Tool (MASCOT) on 19-09-2004, when the moon was at 16 degrees above the horizon and the fractional lunar illumination (FLI) was 0.2. The greyscale is logarithmic and the bright circular structure visible in the upper right corner of the image is a reflection within the camera optics.

A Spectrum of the Moonlit Night Sky

An example of the moon effects on the night sky is shown in Fig. 2, where we have plotted a low-resolution spectrum taken with FORS1 on the first of September 2004. On that night, the moon was almost full and, at the time of the observation, it was shining at an elevation of about 55 degrees above the horizon and at an angular distance of 30 degrees from the direction pointed by UT2-Kueyen, at an elevation of 65 degrees. For comparison we have also plotted a night sky spectrum obtained at Paranal in dark time (see Patat 2003). Several interesting aspects emerge from this comparison. First of all, the moonlit sky spectrum is dominated by a rather blue continuum, which peaks at about 450 nm, right at the centre of the *B* passband. In the specific example shown in Fig. 2, the night sky is about 25 times (i.e. 3.5 magnitudes) brighter than in dark time in this wavelength range. For *V, R* and *I* this difference reduces to 2.9, 2.4 and 1.3 magnitudes respectively. The synthetic (*B–V*) colour of the moonlit night sky turns out to be about 0.4, while (*B–V*)=1.0 is the typical value one measures during dark time (see for example Patat 2003).

Another interesting feature is the appearance of absorption lines, especially in the bluer part of the spectrum. One can in fact easily identify the hydrogen Balmer lines (H_α, H_β, H_γ and so on), the so-called *G*- band (430 nm), Mg I (517, 518 nm) and the prominent H&K CaII lines (393, 397 nm) at the red edge of the Balmer jump. Of course, all these spectral features and the stellar continuum are an imprint of the solar spectrum, which is reflected by the moon and scattered into the line of sight by Earth's atmosphere. To illustrate this effect, in Fig. 2 we have overplotted the model spectrum for the sun (Kurucz, 1993). What one can immediately notice is that the moonlit night sky spectrum is definitely bluer than the solar spectrum, for which it is in fact (*B–V*)=0.65, and the difference is particularly marked at wavelengths shorter than 400 nm. Finally, as one goes into the red, the contribution by the solar continuum becomes less and less relevant and, at wavelengths longer than 900 nm, the emission bands produced by the atmospheric OH are
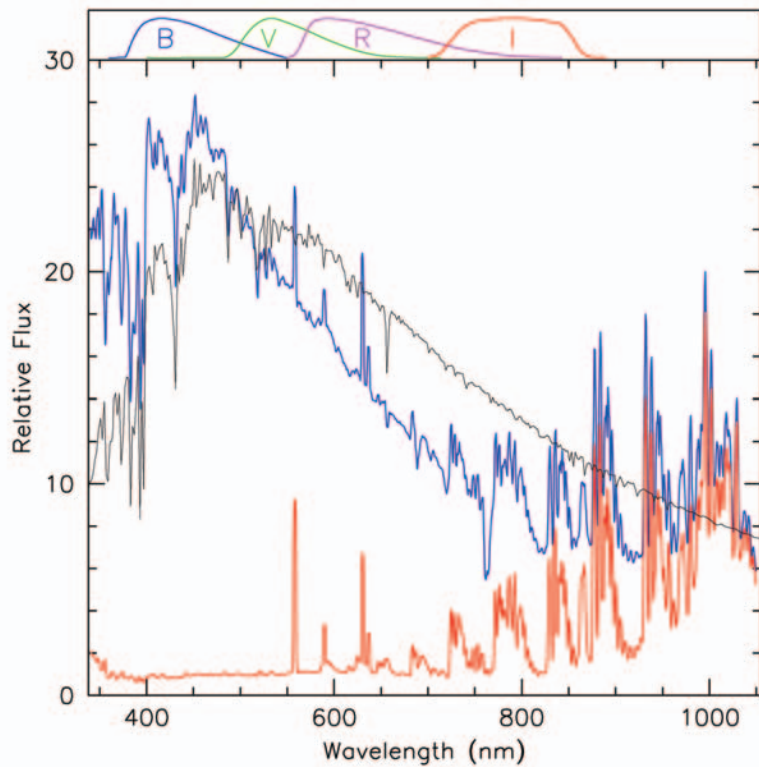
Figure 2: Comparison between the night sky spectrum during dark time (red line, Patat 2003) and bright time (blue line). The latter was obtained with FORS1 on September 1, 2004 using the low dispersion grism 150I and no order sorter filter. Due to the very blue continuum, the spectral region at wavelengths redder than 650 nm is probably contaminated by the grism second order. Both spectra have been normalized to the continuum of the first one at 500 nm. For comparison, the model spectrum of a solar-type star is also plotted (black line). For presentation, this has been normalized to the moonlit night sky spectrum at 500 nm. The upper plot shows the standard *BVRI* Johnson-Cousins passbands.
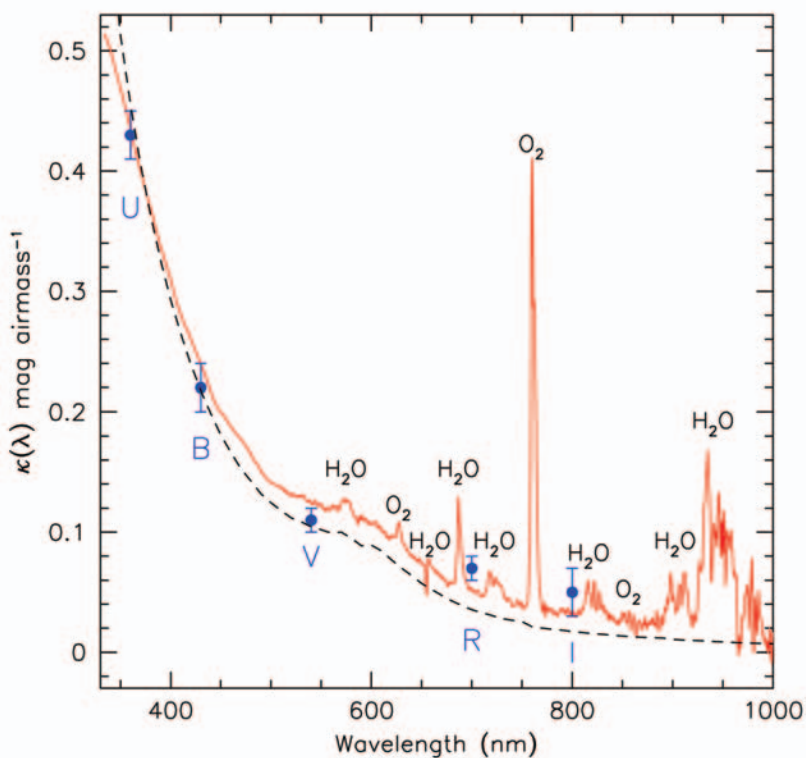

Figure 3: Atmospheric extinction at Paranal estimated from FORS1 observations of the spectrophotometric standard star EG274 (red line). For comparison, the *UBVRI* broadband measurements (filled circles, Patat 2003) and a standard atmosphere model including Air molecules, Ozone and Aerosols (dashed line, Hayes & Latham 1975) are also plotted.

the prominent source of night sky radiation. At even longer wavelengths, in the near-IR, they then completely dominate the night sky emission, even in the presence of full moon. The wavelength dependence on the moonlit night sky spectrum is in fact dictated by two different ingredients: the input source spectrum, that we have just seen, and the physical characteristics of the Earth's atmosphere, which is the topic of the next section.

ATMOSPHERIC EXTINCTION

The physical processes that take place in the scattering of moonlight are exactly the same that are at work during daytime, when the sun illuminates the atmosphere. The amount of radiation reflected at a given wavelength and in a given direction depends on the physical properties of the scattering elements. In the case of Earth's atmosphere, these are mainly identified as molecules of air, water and Ozone (O_3) and, to a smaller extent, the so-called aerosols, which include dust, salt particles and water droplets. These are of course responsible also for the atmospheric extinction, which is just another manifestation of the same phenomenon. In fact, on the one hand the scattering brings the incoming photons out of the line of sight, while on the other it averts photons originally arriving out of the line of sight into the observer's direction.

Therefore, in order to understand the diffusion of moonlight at a given astronomical site, one first needs to study the atmospheric extinction as a function of wavelength. This can be easily done taking spectra of bright stars at different airmasses. An example for the case of Paranal is shown in Fig. 3, where we have plotted the extinction coefficient $\kappa(\lambda)$ computed from FORS1 archival data. At wavelengths bluer than 500 nm the extinction shows a very steep increase, which is due to the well-known λ^{-4} Rayleigh scattering by the Air molecules and which is the responsible for the blue colour of the daytime sky. At longer wavelengths (500-650 nm), the extinction is dominated by the scattering produced by aerosols, which shows a much flatter behaviour (λ^{-a}, with a=0.5–0.9). Finally, water vapour is the dominant source of absorption for $\lambda > 700$ nm, accompanied also by some O_2 bands between 650 and 1000 nm. These features strongly change with time and site and for this reason are pretty difficult to model (see for example Hayes & Latham 1975). Given the wavelength dependency of the $\kappa(\lambda)$ function, and as in the case of the daylight, the moonlit night sky is bluer than the input light source. Therefore, the effect of moonlight is stronger in the blue, both because of the input source spectrum and the higher scattering efficiency. Below 475 nm, the increase in the extinction coefficient is compensated by the decrease of the solar flux (see Fig. 2) and this causes the observed spectrum to remain rather flat. Finally, due to the increased thickness of the atmosphere, the amount of scattered light is expected to be in general higher at higher airmasses, causing the sky to become brighter towards the horizon. This
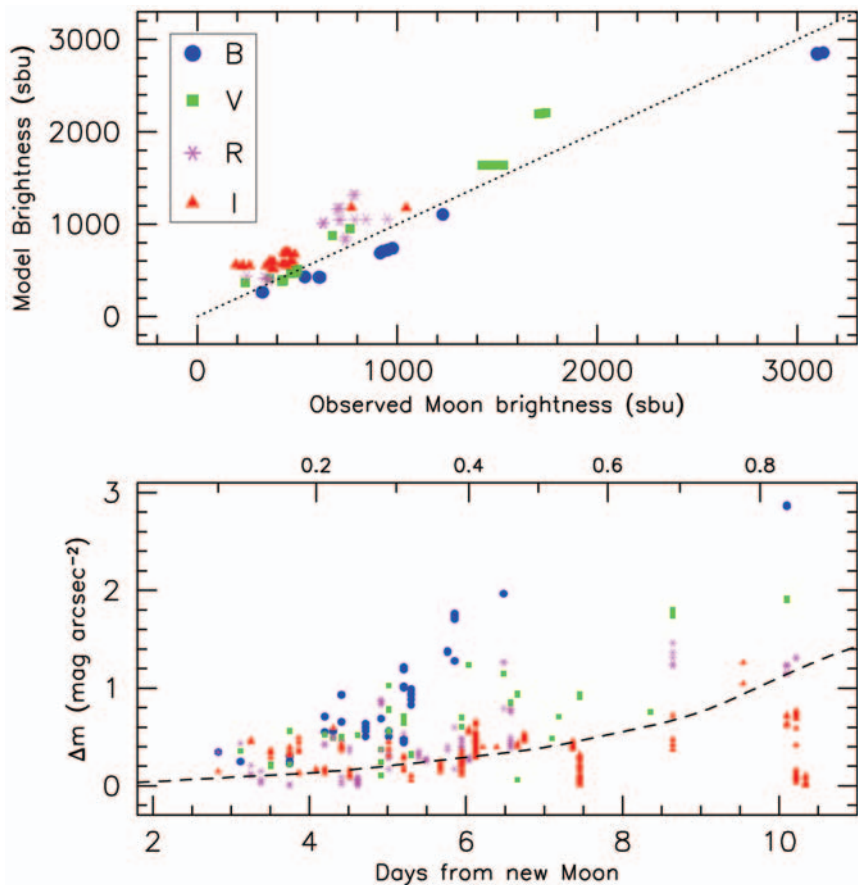
Figure 4: Lower panel: observed sky brightness as a function of moon age for *B, V, R* and *I* (Patat 2003). The solid curve traces the data published by Walker (1987) for the *V* passband, while the upper scale shows the fractional lunar illumination. Upper panel: comparison between observed and predicted moon contribution (Krisciunas & Schaefer 1991). Surface brightness is expressed in surface brightness units (1 sbu = 10^{-8} W m^{-2} μm^{-1} sr^{-1}).

is in fact clearly visible in the image presented in Fig. 1.

MOONLIGHT MODELLING

Of course, when one is to predict the sky brightness enhancement produced by the presence of the moon at a given position in the sky, besides the atmospheric extinction, several other parameters have to be taken into account. First of all, one would have to know the moon's albedo as a function of wavelength, in order to correctly compute the input spectrum at the top of the atmosphere. Then, since the scattering efficiency is generally a function of wavelength and scattering angle, one would have to characterize these functions for the different molecules and particulates present in the atmosphere. For example, Air molecules produce a Rayleigh scattering, while aerosols (which are responsible of phenomena like the aureole) rather produce a Mie scattering (see for example the classical textbook by v. d. Hulst 1957).

An approximate approach, which to our knowledge is the only one available in the literature, is that proposed by Krisciunas & Schaefer (1991, hereafter KS) for the *V* passband and its generalization to the whole UBVRI photometric system (Schaefer 1998). In the KS treatment, the expected sky brightness depends in the extinction coeffi-

cient κ(λ), the apparent magnitude of the moon (which is usually parameterised with the Fractional Lunar Illumination, or FLI), its zenith distance, the angular separation between the moon and the target and the zenith distance of the target itself. Another fundamental ingredient is the function that describes the dependence of scattering efficiency from the scattering angle, which practically coincides with the moon-target angular separation. The KS model includes both Rayleigh and Mie scattering expressions for this function and it has been calibrated using daytime sky brightness measurements. It is important to notice that this function shows a minimum at 90 degrees, which is therefore the angular distance at which the contribution is expected to reach its minimum. As we will see below, this distance is actually decreased by the effects of airmass. The model accuracy in the *V* passband was tested by the authors, who reported root mean square deviations as large as 23% in a brightness range that spans over 20 times the typical value observed during dark time. These can be attributed to the model approximations but also to fluctuations in the atmospheric conditions (aerosols, thin cirrus clouds).

Even though FORS1 is typically a dark time instrument, some data are obtained when the moon contribution to the sky

brightness is conspicuous and this gave us the possibility of directly measuring its effect and comparing it with the KS model in the other passbands (see Patat 2003). To estimate the fraction of sky brightness generated by scattered moonlight, one simply needs to subtract the dark time estimates to the observed fluxes for each passband. The results of this operation are presented in the lower panel of Fig. 4. As expected, the largest deviations are seen in *B*, where the sky brightness can increase by about 3 magnitudes at 10 days after new moon, while in I, at roughly the same moon age, this deviation just reaches about 1.2 magnitudes. It is interesting to note that most exposure time calculators for modern instruments make use of the function published by Walker (1987) to compute the expected sky brightness as a function of moon age. As already noticed by Krisciunas (1990), this gives rather optimistic estimates, real data being most of the time noticeably brighter. This is clearly visible in Fig. 4, where we have overplotted Walker's function for the *V* passband on our data: already at six days past new moon the observed *V* data (green squares) show maximum deviations of the order of one magnitude. These results are fully compatible with those presented by Krisciunas (1990). Clearly, a one-parameter description (i.e. moon phase) is not enough to predict with sufficient accuracy the sky brightness. In this respect, the KS model is much more promising, since it takes into account all relevant astronomical circumstances, some of which, admittedly, are known only when the time the target is going to be observed is known. This limits the applicability to a "nowcast" by the observer rather than a forecast by the user, an important issue which we will come back to at the end of the paper.

In the upper panel of Fig. 4 we have compared our results with the KS model predictions, including *B, V, R* and *I* data. We emphasise that we have used average values for the extinction coefficients and dark time sky brightness of Paranal and this certainly has some impact on the computed values. The unaccounted presence of thin cirrus clouds can also cause significant deviations. On the other hand, this is the typical configuration under which the procedure would be implemented in an exposure time calculator, and hence it gives a realistic evaluation of the model practical accuracy. Figure 4 shows that, even if maximum deviations as large as 0.4 magnitude are present, the model gives a reasonable reproduction of the data in the brightness range covered by our observations. This is actually less than half the one encompassed by the *V*-band data used by KS, which reach about 8300 sbu. For comparison, the typical dark time sky brightness in *V* is about 370 sbu (Patat 2003). Another feature that can be noticed is that the model predicts the moonlit sky to be redder than

Figure 5: Example isophotal *alt-az* map for the expected moonlight contribution. The dashed white lines trace the loci at constant angular distance from the moon, while the two dotted red lines indicate the extreme apparent lunar paths during a full Saros cycle.
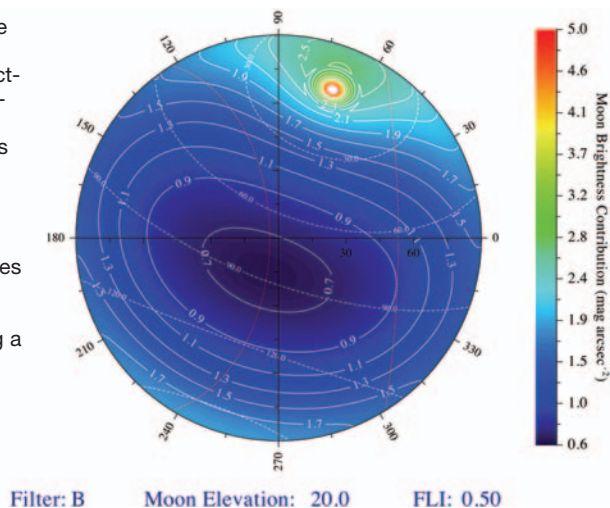
observed, since the *B* data points are systematically brighter than the model, while for *R* and *I* the opposite is true.

Due to the large number of input parameters involved in the KS model, the overall effects of moonlight are better understood with the use of isophotal maps, one example of which is presented in Fig. 5. The calculations were done in the *B* passband, using the broadband extinction coefficients measured on Paranal (Patat 2003), for FLI=0.5 (half moon) and moon elevation 20 degrees. The *alt-az* map shows the isophotal contours (solid white lines), the moon-target angular separation (dashed white lines) and the region spanned by the moon's apparent paths during the 18 years Saros cycle computed for Paranal (dotted red curves). As one can see the minimum surface brightness (0.6 mag arcsec^{-2}) is attained at about 80 degrees from the moon, on the great circle passing through zenith and the moon itself. Actually, computing several models for different moon positions and different passbands, it is easy to verify that while the minimum lies always on that great circle, its angular distance from the moon is 90 degrees when the moon is close to the horizon (see for example Fig. 1), while it tends to decrease for higher moon elevations, reaching about 60 degrees when the moon is at zenith. The opposite happens to the minimum surface brightness, which steadily grows with moon elevation, reaching its maximum when the moon culminates. Of course, the exact value of minimum surface brightness and the isophotal shape depends on the passband; in the case of the example reported in Fig. 5, the minimum surface brightness enhancement is 0.4 mag arcsec^{-2}, reached when the moon rises or sets, while this value grows to about 1.3 mag arcsec^{-2} when the moon is at zenith. Finally, to evaluate the effects produced by scattered light when the moon is below the horizon, we have included the moon twilight, following the prescriptions given by Schaefer (1998). According to the model, the *B* sky brightness enhancement is

smaller than 0.1 mag arcsec^{-2} on the whole sky when the full moon is more than five degrees below the horizon. This reduces to one degree when FLI=0.5.

The main conclusion is that there are regions of the sky where the moon contamination can be minimized, and this has important consequences in the optimisation of Service Mode observations of programmes that can be executed in grey or bright time.

Towards a New Perspective

As far as moon illumination is concerned, astronomical programmes are generally classified as suitable for dark or bright time. In the case of ESO, the programmes are actually grouped into three classes, according to the user required FLI: dark (FLI<0.4), grey (0.4<FLI<0.7) and bright (FLI>0.7). Taking into account that the time when FLI<0.4 and the moon is below the horizon is also considered as dark time, grey and bright fractions account for 11% and 32% of the total observing time respectively. Therefore, there is a substantial amount of time in which the moon contribution is significant and that, for the same reason, is normally used for IR observations, which are essentially not affected by the moon presence. In fact, the considerations we have been developing here are relevant to optical instruments only.

At present, ESO requests Service Mode users to specify the maximum acceptable FLI and the minimum acceptable angular distance to the moon at the time of defining their observation blocks. While these two parameters alone do not suffice to accurately predict the sky brightness at the target position as we have discussed, they do provide a simple set of constraints whose fulfilment can be predicted in advance and still allow the user to have a fair amount of control on the sky brightness conditions under which the observations will be executed. Furthermore, they do not severely constrain the short-term scheduling flexibility that is

essential to the efficiency of Service Mode observing. However, experience has shown that users often tend to request a moon-target separation larger than needed. This, besides reducing the observability window, does not necessarily guarantee that the sky background is minimized. In fact, as we have seen in the previous section, under certain circumstances a separation of 70 degrees is better than one of 120 degrees.

In the long run, it may be possible to directly incorporate the sky brightness at the target position as a constraint. This will require a well calibrated model for the scattered moonlight allowing the night time operations astronomers to estimate in an accurate and straightforward manner the expected sky brightness. To this end, it will be necessary to develop and test more sophisticated models and to obtain extensive datasets sampling the parameter space well. As far as the models are concerned, Krisciunas & Schaefer proposed a series of improvements on their own model in order to increase its predictive power, already in their original work. As a matter of fact, extensions and refinements of the KS model are currently in progress (K. Nordsieck, private communication). Regarding the experimental side, besides the *V* data published by Krisciunas & Schaefer and the first *BVRI* data set presented by Patat (2003), which were collected only as a by-product of the night sky survey, to our knowledge no other systematic observing campaigns have been carried out. Collecting a large database containing measurements of sky brightness obtained through multiple filters and sampling as wide a parameter space as possible is a considerable effort, which may perhaps be best undertaken by coordinating dedicated small-sized telescopes. Nevertheless, the outcome of such a project, resulting in an improved ability to predict the actual observing conditions, can be regarded as a necessary step in maximizing the efficiency of the precious observing time at current and future large telescopes.

References

Hayes, D.S. & Latham, D. W., 1975, ApJ, 197, 593
Krisciunas, K., 1990, PASP, 102, 1052
Krisciunas, K. & Schaefer, B. E., 1991, PASP 103, 1033
Kurucz, R.L., 1993, Kurucz CD-ROM No. 13
Patat, F., 2003, A&A, 400, 1183
Schaefer, B. E., 1998, Sky & Telescope, May 1998, p.57
v. d. Hulst, H.C., 1957, Light Scattering by Small Particles, John Wiley & Sons, New York
Walker, A., 1987, N.O.A.O. Newsletter, No. 10, 16

Filter: B   Moon Elevation: 20.0   FLI: 0.50

THE SKY DISTRIBUTION OF VLT OBSERVATIONS

THE SKY IS NOT ALL THE SAME. OBSERVERS HAVE FAVORITE REGIONS WHERE MOST TELESCOPE TIME IS SPENT WHILE OTHERS ARE APPARENTLY IGNORED. TO QUANTIFY THIS PREDILECTION WE CONSTRUCTED AN ALL-SKY DISTRIBUTION OF VLT POINTINGS AND FOUND THE EXISTENCE OF A WELL DEFINED UNPOPULAR REGION, A ~20° BAND ABOVE AND BELOW THE GALACTIC PLANE, WHERE THE VLT RARELY SPENDS ANY TIME.

JOÃO ALVES AND MARCO LOMBARDI

VISAS, ESO

It comes as no surprise that observers have favorite target regions in the sky. A simple classification of observers as extragalactic, galactic, or solar system observers implies immediately a clear division of regions of interest. Even within each of these classes of observers one can expect preferences towards well known targets, or targets involving multi-observatory international projects. This can be clearly seen in Figure 1 where we present an all-sky map of VLT pointings for Service Mode runs during 2 years (Periods 68 to 71), in an Equatorial Aitoff equal-area projection. Greyscale intensity in this map is proportional to observing time and does not represent sky coverage, which is much less than at first suggested in this representation. As expected, the distribution is far from uniform. There are several interesting features in this map worth a more thorough analysis but perhaps the most striking of all is the well defined unpopular region, roughly characterized as a ~20° band above and below the Galactic plane, where the VLT rarely spends any time. A possible reason for this "void" is that extragalactic observers do not venture too close to the Galaxy (interstellar dust extinction fear comes to mind), while galactic observers prefer to stay close to the galactic plane (note in Figure 1 the string of observations along the Galactic plane, especially towards the inner Galaxy). We present in Figure 2 the same data as in Figure 1 but binned into Right Ascension bins of 2h (about a month per bin; October~0h bin, April~12h bin).

OPPORTUNITY

For the telescope scheduler, favorite sky regions mean higher demand for observation time at certain parts of the year, i.e., increased competition for specific Right Ascensions. For example, there is only a limited number of photometric dark nights in April (a particularly popular month) which is on average 10 times less than the total requested by observers. A direct consequence of this is that only the top OPC ranked programs can make it to the telescopes during April's dark time. On the other hand, the opposite is true for January and August. The time request for targets in

these months is very low, allowing almost all programs applying for time at these RAs, and considered at least useful by the OPC, to be scheduled.

While an accurate knowledge of the distribution of favorite sky regions helps the observatory in optimizing short and long term scheduling of observations and engineering activities, this optimization can only go so far when the demand for time is as nonuniform as in Figure 2. As a consequence, a genuine scheduling opportunity exists for observers ready to find targets in the less visited areas of the sky. Observers: check your catalogs and you might be in for a treat.
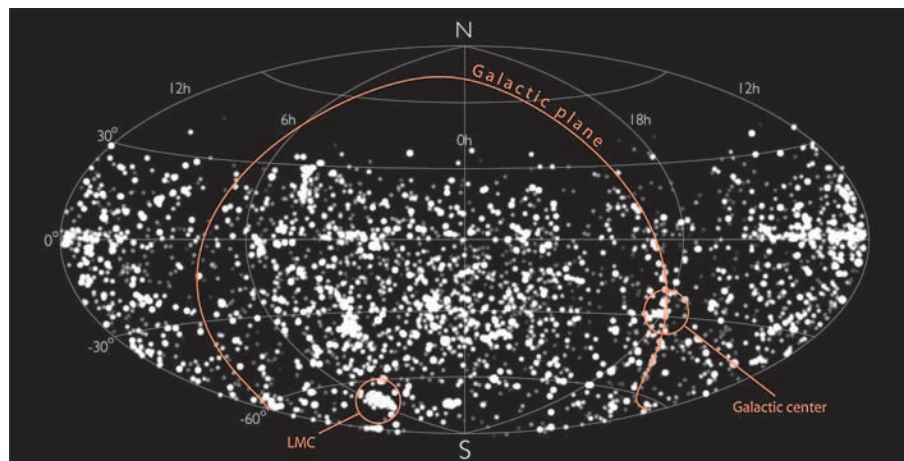

Figure 1: All-sky map of VLT pointings for Service Mode runs during 2 years (Periods 68 to 71) in an Equatorial Aitoff equal-area projection. Greyscale intensity is proportional to observing time. Sky coverage is much less than suggested in this representation. The Galactic plane and several popular targets are indicated. Note the unpopular voids above and below the Galactic plane.
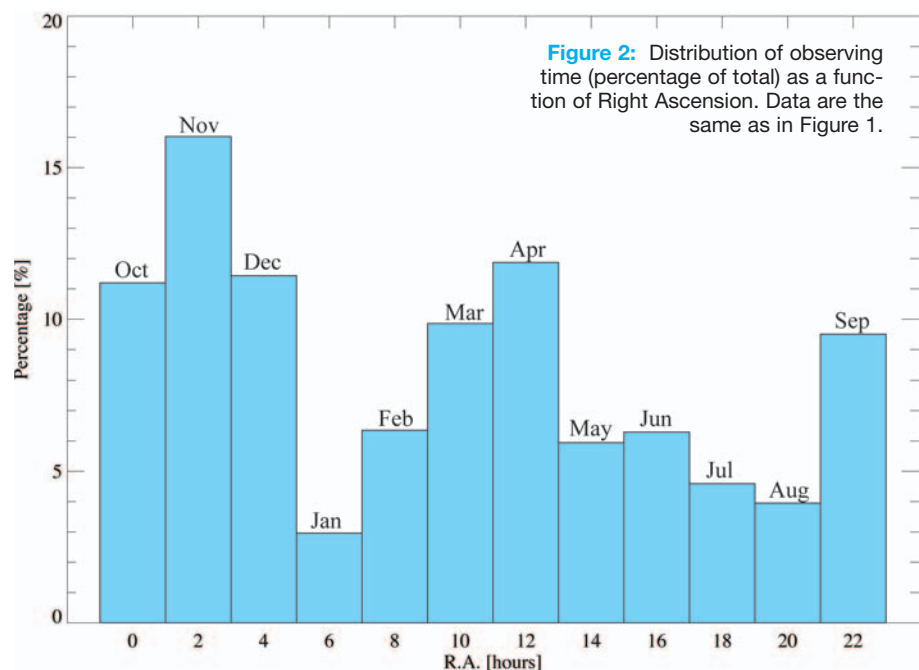

Figure 2: Distribution of observing time (percentage of total) as a function of Right Ascension. Data are the same as in Figure 1.

A PROGRESS REPORT ON ALMA

TOM WILSON, CARLOS DE BREUCK AND MARTIN ZWAAN

EUROPEAN SOUTHERN OBSERVATORY

The last article about ALMA in the *Messenger* was by the Director General, in the June 2003 issue. In the present article we give an update of activities since that time. An important event was the Community Day meeting in Garching on 24 September, which is summarized on page 68 of this issue.

The actual construction of the ALMA facilities in Chile has now begun. To give an impression of what the ALMA sites currently look like, we present here some pictures taken by J. Eschwey, J. Mella and C. De Breuck (ESO). A first priority is the construction of the access road from the Chilean highway 23 to the Operations Support Facility (OSF). A sign introducing ALMA has been set up (see Fig. 1). Because of ongoing construction activity and medical risks of high altitude, all visits must have prior approval from the ALMA project office (Tel: +56-55-448-409/410/416).

At the future site of the OSF at an altitude of 2900m, there is now a camp for construction workers (Fig. 2). Some optical astronomers may recognize the containers, which are indeed the ones that previously were used at Paranal. Currently, approximately 50 people work at the OSF. In the future, the OSF will be the main site from where ALMA will be operated. Figure 3 shows a proposed design for the future OSF building, which will also house laboratories and a large assembly hall where antenna integration and major repairs can be done.

One of the major activities in 2004 has been the construction of a full width road (Fig. 4) connecting the OSF to the 5000m high Llano de Chajnantor, where the ALMA telescopes will be located. This road is 12 metres wide because it will be used for the transport of the antennas from the OSF to the ALMA site. The road passes through an area between 3500 and 3800m altitude, dominated by huge cacti (Echinopsis Atacamensis), which can reach heights of up to 9m (Fig. 5). To protect the local fauna and sites of archaeological importance, the blasting work for road construction is being coordinated with local authorities and consultants.

The actual site of the telescopes is called the Array Operations Site (AOS). Figure 6 shows a sketch of the planned building of which construction begins in 2005. Among other items, the AOS will house the ALMA correlator. The number of personnel at the

Figure 1: The sign introducing ALMA at the access road to the ALMA Operations Support Facility (OSF) and Array Operations Site (AOS).

Figure 2: A camp for construction workers at the OSF site at an altitude of 2900m.
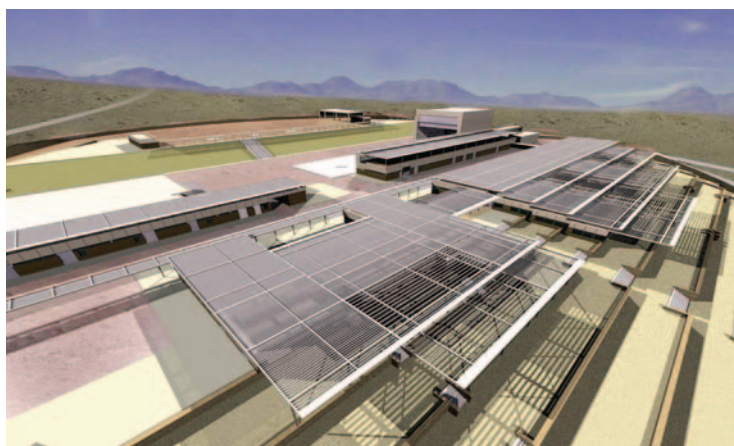

Figure 3: Birds eye view over the proposed design for the future OSF building. The large telescope assembly hall can be seen in the back.
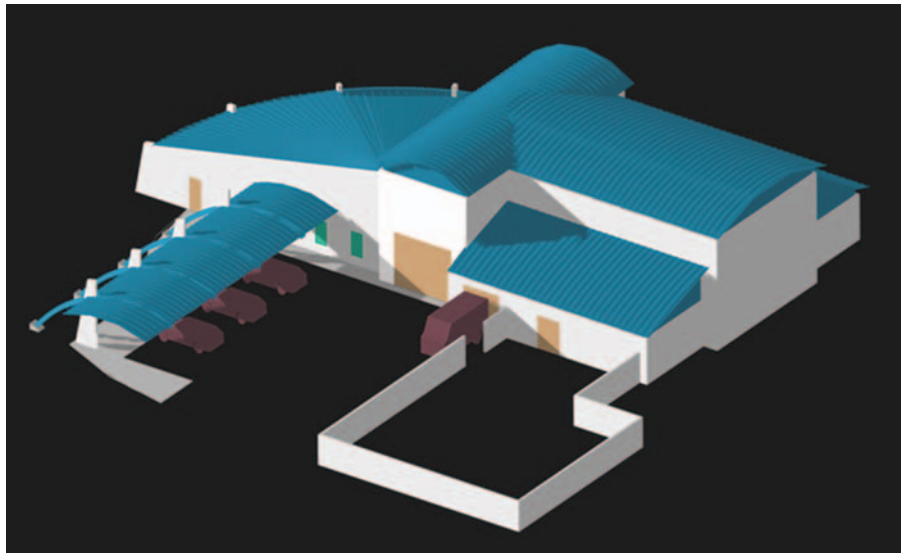
Figure 4: Construction of the 12-m wide road connecting the OSF to Llano de Chajnantor, the telescope site at 5000 m.

Figure 5: An Echinopsis Atacamensis can reach a height of 9 m.

Figure 6: Sketch of the planned building at the Array Operations Site.

AOS will be kept to a minimum to reduce the risks of working at high altitude.

The ALMA astronomers in Chile will be working in a turno system, much like the La Silla and Paranal observatories. While not at the OSF, they will be at the Santiago Central Office.

ALMA work is also progressing in Europe. At the Rutherford-Appleton Laboratory, UK, the first pre-production cryostat is now complete. It is shown in Fig. 7 where one can clearly distinguish the ten openings for the complete set of ALMA receiver bands. The four openings shown with black mounting rings will be used for the first receiver bands in the baseline plan. A description of two of these bands is given in the article by G. H. Tan and others on page 18 of this issue.

For further information we refer the reader to the newly set up quarterly European ALMA newsletter, which is available electronically from http://www.eso.org/projects/alma/newsletter/. Information on how to subscribe to email announcements of this newsletter is given on this web page.
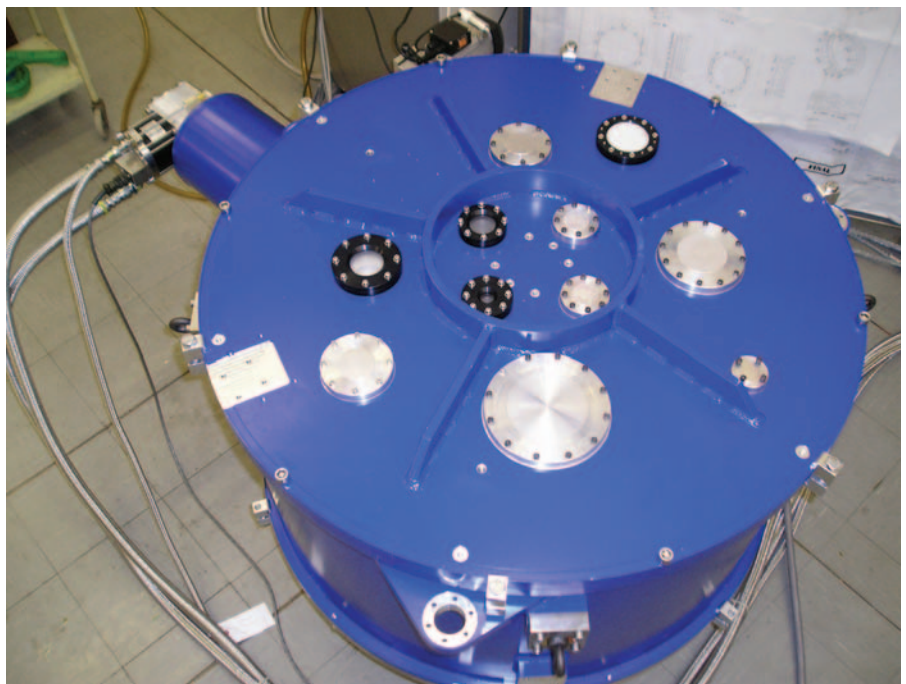
Figure 7: View from the top of the first pre-production cryostat at RAL, UK. It shows 10 openings for the complete set of ALMA receiver bands. The four openings shown with black mounting rings will be used for the first receiver bands in the baseline plan.

THE EUROPEAN RECEIVERS FOR ALMA

TO A LARGE EXTENT THE SCIENTIFIC CAPABILITIES OF THE ATACAMA LARGE MILLIMETER ARRAY (ALMA) WILL DEPEND ON THE RECEIVERS MOUNTED ON EACH OF THE 64 ANTENNAS. IN THE LAST YEAR, SUBSTANTIAL PROGRESS HAS BEEN MADE IN THE DESIGN OF THESE RECEIVERS AND CURRENTLY A TRANSITION TOWARDS PRODUCTION IS UNDERWAY. TWO OUT OF THE FOUR INITIAL BASELINE FREQUENCY BANDS FUNDED UNDER THE BILATERAL PROJECT BETWEEN EUROPE AND NORTH AMERICA ARE A EUROPEAN RESPONSIBILITY. THIS EUROPEAN CONTRIBUTION WILL BE FOR THE SHORTEST WAVELENGTH ALMA BANDS DESIGNATED 7 AND 9, COVERING THE FREQUENCY RANGES 275 GHZ TO 373 GHZ AND 602 GHZ TO 720 GHZ.

G.H. TAN[1],
B.D. JACKSON[2,4],
B. LAZAREFF[3],
J. ADEMA[2,5],
A.M. BARYSHEV[2,5],
R. HESPER[2,5],
T.M. KLAPWIJK[6],
M. KROUG[6],
S. MAHIEU[3],
D. MAIER[3],
K. SCHUSTER[3],
K. WIELINGA[7],
T. ZIJLSTRA[6]

[1]EUROPEAN SOUTHERN OBSERVATORY
[2]NETHERLANDS RESEARCH SCHOOL FOR ASTRONOMY (NOVA), LEIDEN, THE NETHERLANDS
[3]INSTITUT DE RADIO ASTRONOMIE MILLIMÉTRIQUE (IRAM), GRENOBLE, FRANCE
[4]SRON NATIONAL INSTITUTE FOR SPACE RESEARCH, GRONINGEN, THE NETHERLANDS
[5]KAPTEYN INSTITUTE, UNIVERSITY OF GRONINGEN, THE NETHERLANDS
[6]KAVLI INSTITUTE OF NANOSCIENCE, DELFT UNIVERSITY OF TECHNOLOGY, THE NETHERLANDS
[7]MECON ENGINEERING BV, DOETINCHEM, THE NETHERLANDS

The Atacama Large Millimeter Array (ALMA) is an international astronomy facility. ALMA is an equal partnership between Europe and North America, in cooperation with the Republic of Chile, and is funded in North America by the U.S. National Science Foundation (NSF) in cooperation with the National Research Council of Canada (NRC), and in Europe by the European Southern Observatory (ESO) and Spain. ALMA construction and operations are led on behalf of North America by the National Radio Astronomy Observatory (NRAO), which is managed by Associated Universities, Inc. (AUI), and on behalf of Europe by ESO.

ALMA will be a single instrument composed of 64 high-precision antennas located in the II Region of Chile, in the District of San Pedro de Atacama, at the Chajnantor altiplano, 5,000 metres above sea level. ALMA's primary function will be to observe and image with unprecedented clarity the enigmatic cold regions of the Universe, which are optically dark, yet shine brightly in the millimetre portion of the electromagnetic spectrum.

ALMA will initially be equipped with four out of the total of ten possible frequency bands. The two highest baseline frequency bands, making ALMA a true sub-millimeter instrument, are a European responsibility. These sub-millimeter receiver bands make full use of the high altitude location of the ALMA instrument where the disturbing influence of the atmosphere is minimal. The exceptional receiver performance at Bands 7 and 9 in terms of sensitivity are a prime justification for locating the ALMA instrument at this high altitude.

The ALMA Band 7 receiver cartridge, covering the frequency range 275 GHz to 373 GHz, is developed and produced by Institut de Radio Astronomie Millimétrique (IRAM) in France, while the Band 9 receiver cartridge, covering the frequency range 620 GHz to 702 GHz, is developed and produced by a Dutch consortium led by the Nederlandse Onderzoeksschool voor Astronomie (NOVA).

ALMA RECEIVER SUB-SYSTEM

The ALMA receivers are located at the interface to the antenna secondary focal plane, inside the receiver cabin at each antenna. ALMA will observe over the frequency

Table 1: ALMA frequency bands and associated noise performance.

ALMA Band	Frequency Range	Receiver noise temperature		Receiver technology
		T_{Rx} over 80% of the RF band	T_{Rx} at any RF frequency	
1	31.3 – 45 GHz	17 K	28 K	HEMT
2	67 – 90 GHz	30 K	50 K	HEMT
3	84 – 116 GHz	37 K	62 K	SIS
4	125 – 169 GHz	51 K	85 K	SIS
5	163 – 211 GHz	65 K	108 K	SIS
6	211 – 275 GHz	83 K	138 K	SIS
7	275 – 373 GHz*	147 K	221 K	SIS
8	385 – 500 GHz	98 K	147 K	SIS
9	602 – 720 GHz	175 K	263 K	SIS
10	787 – 950 GHz	230 K	345 K	SIS

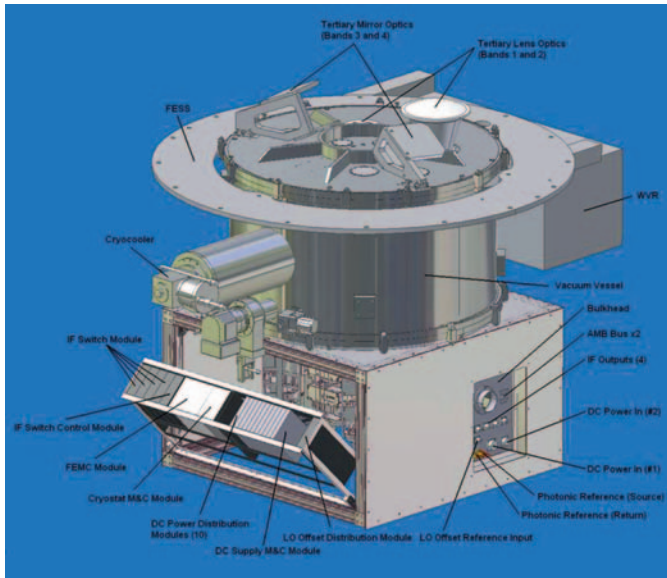* - between 370 – 373 GHz T_{rx} is less then 300 K

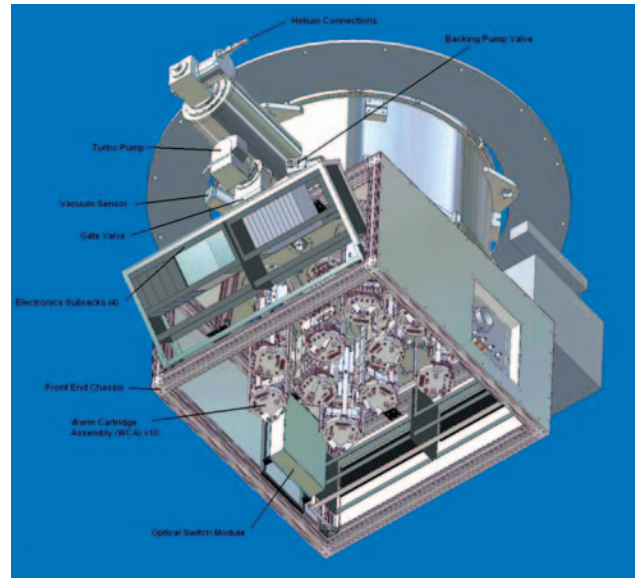**Figure 1:** Top side view of the ALMA front end assembly.

Figure 2: Bottom side view of the ALMA front end assembly.

region from approximately 30 GHz to 950 GHz. For technical reasons this frequency coverage has been split into 10 bands that are shown in Table 1. There will be two identical receiver channels for each band, observing the full polarization state of the received radiation, in order to maximize the system's sensitivity, and to allow polarization-sensitive observations to be performed.

ALMA will observe in only one band at any given time. In the baseline construction project, only the four frequency ranges of highest scientific priority, designated Bands 3, 6, 7, and 9, will be implemented.

At the extremely high frequencies of ALMA, current technology provides direct amplification of the received radiation only in the lowest two bands, where a few radio astronomy groups have developed state of the art HEMT amplifiers. The remainder of the front-ends will use SIS (superconductor-insulator-superconductor) junctions, either Niobium or Niobium-Titanium-Nitrogen based, to mix the received signal to an intermediate frequency (IF) in the range of 4 to 12 GHz, where it can be readily amplified. A great challenge for ALMA is to obtain good control of the processes needed to reach good performance that will also be reliable and suitable for series fabrication.

The complete front end unit will have a diameter of 1 m, be about 1-m high and have a mass of about 750 kg. Figures 1 and 2 show respectively top and bottom side views of the front end assembly. The cryostat will be cooled down to 4 Kelvin by a closed-cycle cryo-cooler driven by a compressor. The individual frequency bands will be made in the form of cartridges that will be inserted in a large common cryostat. The cartridge concept allows for great flexibility in operation of the array. Another advantage of the cartridge layout with well-defined

interfaces is the fact that different cartridges can be developed and built by different groups among the ALMA participants without the risk of incompatibility between them.

Because interferometric observations at (sub-)millimetre wavelengths are extremely sensitive to changes in the amount of water vapour in the earth's atmosphere, causing a variation in electrical path length, every antenna will be equipped with a water vapour radiometer (WVR), which is essentially a separate, dedicated receiver tuned to the frequency of a water vapour absorption line at about 183 GHz. The WVR will be an uncooled receiver and will take atmospheric data continuously, while the astronomical observations at other frequencies are underway. The WVR will enable these observations to be corrected for the influence of water vapour in the lines of sight between each antenna and the observed source.

PROGRAMMATIC OVERVIEW

The early project development, including the design and development Phase 1, is summarized in a previous *Messenger* article (Kurz et al., 2002).

The 10-year construction phase of the project (Phase 2) began in 2002 with approval by the ESO Council on behalf of its 10 member states, and the National Science Board in the U.S. The ESO/NSF Bilateral Agreement was signed in February 2003. Spain participates in Phase 2 of ALMA through an ESO-Spain Agreement signed in January 2003. The total estimated cost for Phase 2 of the bilateral project is 552.5 million (year 2000 US$), to be shared equally between Europe and North America.

After approval of ALMA Phase 2 by the ESO Council, a Call for Tender for development and prototyping, including the Band 7

and 9 cartridges, was issued by ESO in August 2002. At the request of the Joint ALMA Office the original development proposals were amended to include a pre-production run of 8 units. The aim of this approach was to gain more experience with series production early on in the project and expedite the transition from development to series production. Contracts with both IRAM and NOVA for the development and a pre-production series were placed covering a contract period running from the start of 2003 until early 2006.

Spread out over the first half of 2004 individual Preliminary Design Reviews were held for all four ALMA cartridges, including Bands 7 and 9. Currently both groups are working towards the production and delivery of the pre-production cartridges. Delivery of the first pre-production units is imminent and scheduled for early 2005, well in time to be integrated with the rest of the front end assembly at the ALMA front end integration centres.

Critical Design Reviews (CDR) for both cartridge bands are planned shortly after the delivery of these first pre-production units. The CDR will formally conclude the design phase of these cartridges and release the production design. Delivery of the remaining seven pre-production units of the Band 7 and 9 cartridges is distributed over 2005 and early 2006.

Starting in 2005, preparations will also be made by ESO leading to contracts for series production. This series production contract covers the delivery of the remaining 56 units to equip all 64 ALMA antennas with these unique receiver cartridges.

ALMA BAND 7 CARTRIDGE
Band 7 of ALMA covers the signal frequency (RF) range 275 GHz to 373 GHz. Briefly
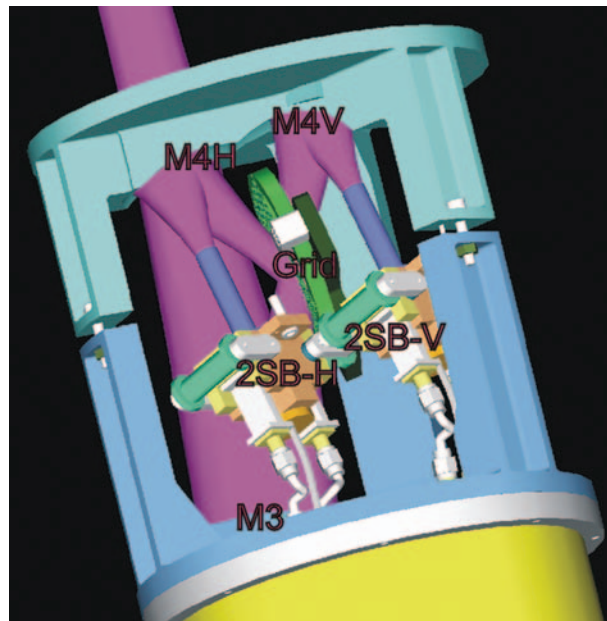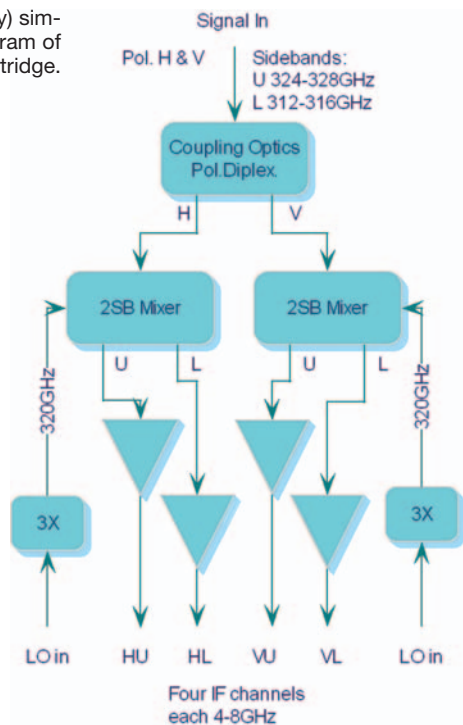
stated, the role of the Band 7 cartridge is to accept the cosmic signal that has been collected by the antenna and concentrated at its Cassegrain focus, transpose that signal to a lower frequency range (intermediate frequency, IF), and, after suitable amplification, deliver the IF to the rest of the signal processing chain.

A short tour of the block diagram (Fig. 3). *Optics*: The optics of the cartridge couples the f/D=8 beam supplied by the telescope to the two mixers. The optics comprises a first offset elliptical mirror M3, then a wire grid that separates the two linear polarizations (the grid acts as a near-perfect mirror when the E-field is parallel to the conducting wires, and is virtually transparent to the orthogonal polarization). Each of the two orthogonally polarized beams is refocused by twin elliptical mirrors M4H and M4V onto the apertures of the horns of the two mixers (see also Fig. 4 and Fig. 5).

Long wavelength optics: For millimetre and sub-millimetre systems, where λ is typically three orders of magnitude larger than in the optical domain, while the systems themselves are of comparable dimensions, ray optics is not a valid starting point for design. In fact, the mirrors of the Band 7 cartridge are always in the close vicinity of the beam's focal point. Instead Gaussian beam optics (originally developed in the 60's for laser beams) is the basic design tool.

Sideband separating (2SB) mixers: Their function is to convert a slice of the RF band to a fixed IF band: 4 – 8 GHz. This is done by making the RF signal beat with the local oscillator (LO) in a non-linear element: the SIS junction, a sandwich of an insulating layer of Aluminium oxide only a few molec-

ular layers thick between two layers of superconducting Niobium. Such a device combines the two desirable properties of having a non-linear I-V characteristic on a scale of order one mV, well matched to the energy of the incoming photons, and of performing the down conversion with very low noise. The SIS junction operates at a temperature of 4K. The SIS junctions for the Band 7 mixers, together with superconducting impedance matching circuits, are fabricated by IRAM's SIS Group (see Fig. 6). For an "ordinary" (DSB) mixer, operating at an LO frequency of, say, 320 GHz, there are two RF frequencies that produce the same beat frequency, say 6 GHz, in the IF band, one in the upper side band, at 326 GHz, and the other in the lower side band, at 314 GHz. A sideband-separating mixer provides two separate IF outputs, each one carrying the conversion product from just one of the two RF side bands. This is accomplished by splitting the input signal, with appropriate phase shifts, before feeding two identical DSB mixers, and recombining their IF signals with again appropriate phase shifts. This is detailed in Fig. 7 and its caption.

IF amplification: Four low-noise amplifiers (one for each combination of polarization and sideband) amplify the outputs of the 2SB mixers by approximately 35 dB. These amplifiers are supplied within the ALMA project by Centro Astronomico de Yebes in Spain. Outside the vacuum enclosure, the IF signal is further amplified by another 35 dB by room-temperature amplifiers.

LO system: The local oscillator signal is tuneable in the range 283 – 365GHz. This is obtained from a microwave oscillator operating in the range from 15,7 GHz to 20,3 GHz, followed by a chain of solid-state fre-

quency multipliers and amplifiers; the final stage, a tripler, is located within the cryogenic enclosure and operates at 80K. The LO system is supplied within the ALMA project by the National Radio Astronomy Observatory in the U.S.

All the cryogenically cooled components are mounted in/on and cooled by a cylindrical structure (the so-called blank cartridge), supplied within the ALMA project by our colleagues of Rutherford Appleton Laboratory in the UK.

Several design challenges had to be met in the design and prototyping of the Band 7 cartridge. The first one is common to all SIS mixers: due to the capacitance of the S-I-S sandwich (typically 80fF), the junction's impedance is highly reactive, while it must be matched to the real source impedance over the RF band; Band 7 has the largest relative bandwidth (f_{max}/f_{min} = 1.356) of all ALMA bands implemented with SIS mixers. Another major challenge is the actual fabrication of the junctions. The junction area must be within 10% of its nominal value of 1 μm^2, corresponding to linear tolerances of 0.05 μm. This is made possible by electron beam lithography. As already stated, the thickness of the insulating layer of the junction is only a few molecular layers, and is especially critical because of the exponential dependence of the junction's resistance on its thickness. The pair of DSB mixers that enter the fabrication of the sideband separating (2SB) mixers must be well matched in amplitude and phase to maintain the properties of the 2SB scheme. The optical assembly must be aligned with the telescope optics, without any adjustment, requiring tight fabrication tolerances; this has led to the fabrication of the optical assembly (see

Figure 5: Photo of the cold optics assembly, with the two 2SB mixers.

Figure 6: A SEM picture of the Band 7 SIS junction with RF tuning circuits.

Fig. 4, 5) by machining from just three metal blocks, with suitable heat treatment for stabilization.

Results achieved with one of the 2SB mixers produced so far are shown on Fig. 8. Similar results are obtained when the mixer is integrated in the cartridge. As can be seen, the noise specifications that were set at the outset of the project several years ago (and had never been realized at that time) are met or exceeded.

ALMA BAND 9 CARTRIDGE

The ALMA Band 9 cartridges are state-of-the-art heterodyne receivers that cover the 602 GHz to 720 GHz atmospheric window with a unique combination of high sensitivity and a broad instantaneous bandwidth (8 GHz per side-band of this double side-band receiver). The Band 9 receivers are the highest-frequency receivers in the baseline plan of the joint European – North American ALMA project. As such, the observatory's maximum spatial resolution will be obtained with these receivers (as the maximum spatial resolution scales with the ratio of the telescope separation to the operating wavelength). Furthermore, when combined with lower-frequency observations, the higher temperature scales that high-frequency molecular line observations probe will be important to allow the observatory to probe warm, dense gas close to protostars and galactic nuclei. Similarly, continuum observations are needed over a wide frequency range in order to fully characterize the emission of dust, especially for nearby sources, whose emission spectra peak in the 60–200 µm range.

CRITICAL COMPONENTS IN THE BAND 9 CARTRIDGE

In order to achieve the desired combination of high sensitivity, full 602 GHz to 720 GHz frequency coverage, and a broad instantaneous bandwidth, state-of-the-art technologies are needed in three areas: the mixers
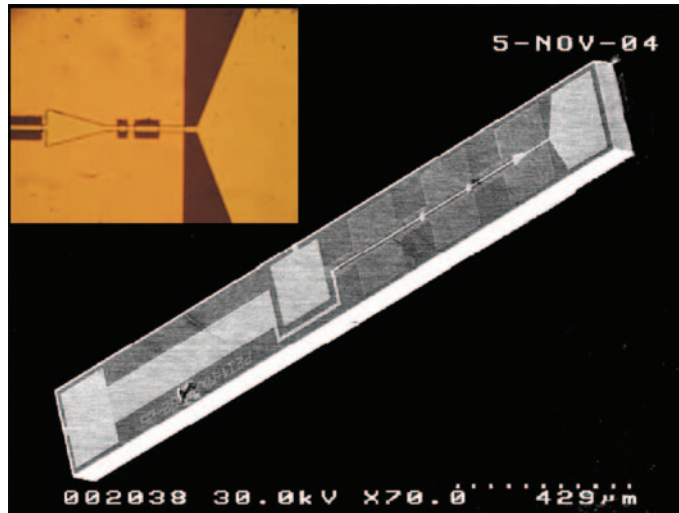
which form the "eyes" of the receiver, the local oscillator that "pumps" the mixers at the operating frequency, and the cryogenic "intermediate frequency" (IF) amplifier chains that are needed to amplify the mixer's weak output signal before it leaves the cryostat.

The superconductor-insulator-superconductor (SIS) mixers used in the ALMA Band 9 cartridge (the "eyes" of the system) are the product of a 15-year collaboration between the National Institute for Space Research (in Dutch: Stichting Ruimteonderzoek in Nederland (SRON)) and the SIS junction group at Delft University of Technology (formerly at the University of Groningen). In particular, the Band 9 mixers are descendents of the design of 600-700 GHz mixers that were developed by SRON and the University of Groningen for use at the James Clerk Maxwell Telescope, in Hawaii (Baryshev et al., 2001). More recently, advances in mixer design and SIS junction fabrication have yielded substantial improvements in mixer performance, such that the ALMA project's sensitivity require-

ment (T_{rx} = 175 K across 80% of the band) can now be met, as is seen in Figure 9. Figure 10 includes pictures of the Band 9 mixer, including its two critical mechanical components – a corrugated horn antenna (from Radiometer Physics GmbH, in Germany) and a waveguide device mount (produced by a local company using high-precision machining techniques). Note that
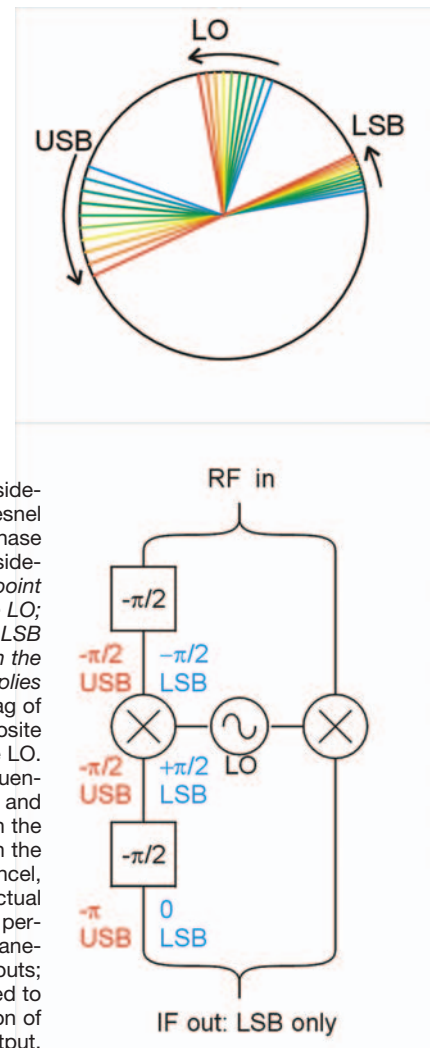

Figure 7: A pictorial explanation of the sideband separation mechanism. Top: a Fresnel diagram illustrating the frequency and phase relationships between the two signal sidebands and the LO frequency. *The key point is that the LSB is lagging behind the LO; therefore, a phase lag applied to the LSB increases the phase difference between the LO and the LSB, while the converse applies to the USB.* Bottom: The same phase lag of π/2 applied to the RF results in opposite phase offsets after mixing with the LO. Another phase lag, applied at the IF frequency, results in zero net phase for the LSB, and in a phase lag of π for the USB. When the left-hand signal path is combined with the right-hand path, the USB signals cancel, while the LSB signals add up. In the actual mixer, two different summations are performed at the output, providing simultaneously the USB and LSB on separate outputs; the diagram shown has been simplified to focus the explanation on the production of the LSB output.
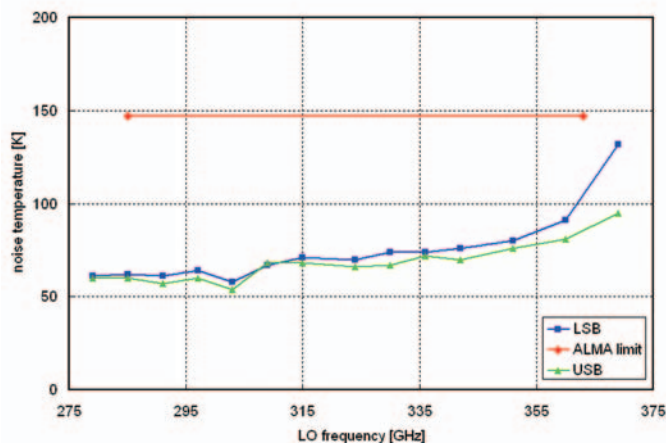
Figure 8: Results achieved with one of the first 2SB mixer assemblies produced. Note: the horizontal scale applies to the LO frequency; therefore, the RF signal range extends an extra 8 GHz on either side. The red line is the ALMA specification for receiver noise.
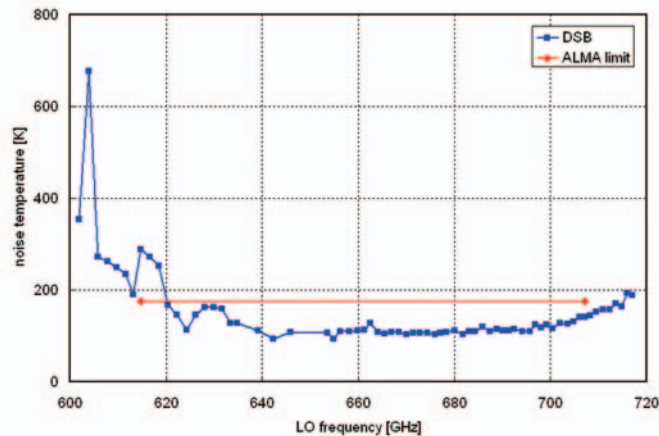
Figure 9: 600 GHz – 720 GHz SIS mixer noise performance.

the relatively short wavelength of 650 GHz radiation (~ 0,5 mm) results in these components having critical dimensions of ~100 µm, which requires machining tolerances of ~ 5 µm.

The local oscillators and IF amplifiers in the Band 9 cartridge are being developed and produced by partners in the ALMA project. In particular, the local oscillator (LO) chains are being developed at the National Radio Astronomy Observatory (NRAO), based upon state-of-the-art millimetre-wave power amplifiers from NRAO and solid-state frequency multipliers (from Virginia Diodes, Inc., in the United States). The low-noise 4 – 12 GHz cryogenic amplifiers that are being used in the Band 9 cartridge are being developed by the Centro Astronomico de Yebes, in Spain (Lopez-Fernandez et al. 2001).

On top of the need for these unique development items, the development of the Band 9 cartridge has been further complicated by the ALMA project's unique need to produce, operate, and maintain 64 state-of-the-art cartridges for each frequency band. This has required eliminating moving parts (such as the mechanical tuners that have traditionally been used in solid-state local oscillator chains and SIS mixers) to improve the system's reliability, and simplifying the manufacturing and assembly of the cartridge to as great an extent as possible (including taking advantage of commercial manufacturing capabilities where possible).

4K OPTICS ASSEMBLY DESIGN AND DEVELOPMENT

A key element of this "design for manufacturing" has been in the design of the cooled (down to 4 Kelvin) optical assembly that will combine the astronomical signal from the telescope with the local oscillator signals (two) and focus the combined beam into the cartridge's two mixers. Beyond the "usual" requirements for low optical coupling losses

and high image quality, the design of this system has been further complicated by the limited volume available (the cartridge is only 17 cm in diameter), and the need to manufacture and assemble 64 of these assemblies at the rate of one per month, or faster. This has pushed the development of a design in which no alignment is needed (or possible). Instead, high-precision CNC machining is used to machine four of the system's five mirrors into a single metal block (in a single machining step, to ensure that they are correctly aligned with respect to each other). The fifth mirror is then machined into a second part and the absolute accuracy of a well-controlled CNC machine is used to ensure that the two mirror blocks can be assembled with sufficient accuracy that the desired optical alignment and imaging quality is achieved by machining tolerances alone. This "alignment-by-machining-accuracy" philosophy is also applied to the mounting of two LO-combining beam splitters and a polarization-splitting grid in the space between the two mirror blocks.

Preliminary verification of this design principle was provided by manufacturing and testing a two-mirror prototype of the 4 K mirror assembly (Baryshev et al., 2004), while recent measurements of the first full 4K optical assembly have provided further design verification. Figure 11 shows a picture of the first 4 K optical assembly. In addition to the two mirror blocks, the polarization-splitting grid and the LO combining beam splitters can also be seen, together with absorbing beam-dumps that are used to absorb stray light in the system.

CARTRIDGE DESIGN AND DEVELOPMENT OVERVIEW

The assembly of the first complete Band 9 cartridge has started, and Figure 12 shows pictures of the integrated 4K opto-mechanical structure mounted on a prototype of the cartridge body.

Figure 12 shows a cut-out view of the cryogenic portion of the cartridge design (with the fibre-glass cylinders that separate the cartridge's four temperature stages removed from the left-hand image to allow the internal components to be seen). The warm local oscillator (a high-power millimetre-wave source) and the cartridge's bias electronics will be mounted in a structure that bolts to the outside of the 300 K stage of this assembly (this structure is not seen in this figure). Inside the cartridge, waveguides run from the 300 K plate to the 90 K temperature level to feed the high-power millimetre-wave LO signal (at 100 – 120 GHz) to a cryogenic frequency multiplier on the 90 K stage that produces the 614 – 708 GHz LO power that is needed to pump the SIS mixers. The local oscillator power produced by the multiplier is coupled via an optical beam to the optics assembly on the cartridge's 4 K stage. Within this optical assembly, the LO beam is optically combined with the signal beam from the telescope and the combination is then focussed into the SIS mixer's horn-antenna. The 4 – 12 GHz IF output from the mixer passes through a 4 – 12 GHz isolator (from Passive Microwave Technologies) before being amplified in a low-noise amplifier that is mounted on the bottom side of the 4K stage. The IF signal is then coupled out of the cartridge and further amplified in room-temperature amplifiers that are located in the mechanical assembly that also contains the warm LO components and bias electronics.

The assembly of the first complete Band 9 cartridge has started with the integration of the 4 K opto-mechanical structure on a prototype of the cartridge body to allow a first cool down of the optics assembly. Further integration of the cartridge is now proceeding, including the other temperature levels and the inter-stage wiring harness is now proceeding. In parallel with this cartridge manufacturing and assembly effort, the
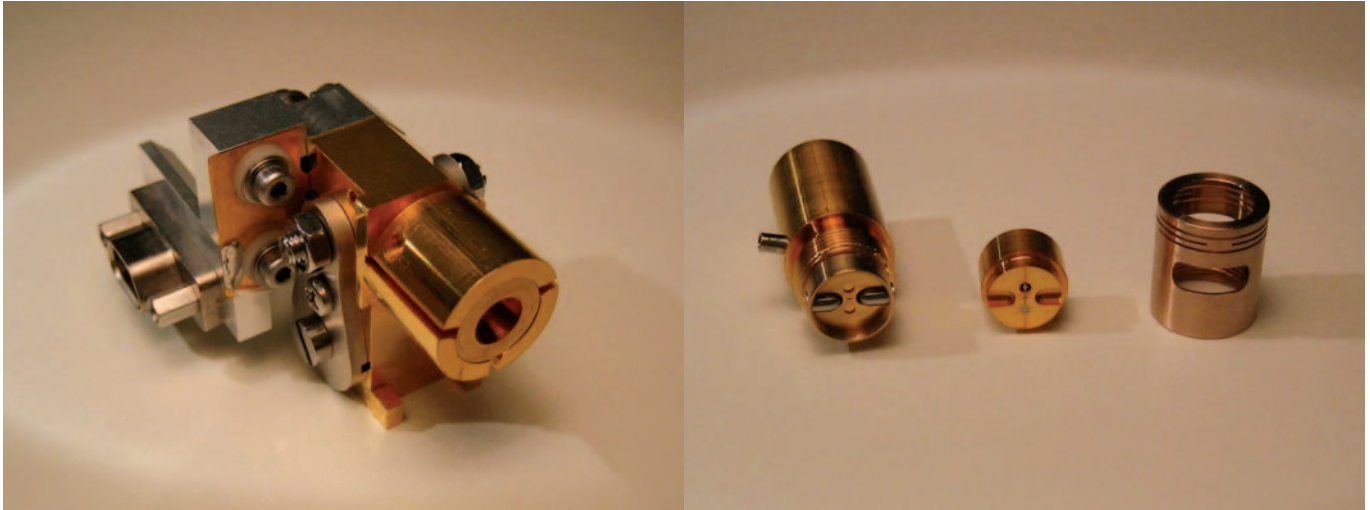
Figure 10: The ALMA Band 9 mixer: (left) an assembled mixer, (right) the two critical components of the mixer – the corrugated horn and the waveguide device mount in which the SIS mixer chip is mounted.
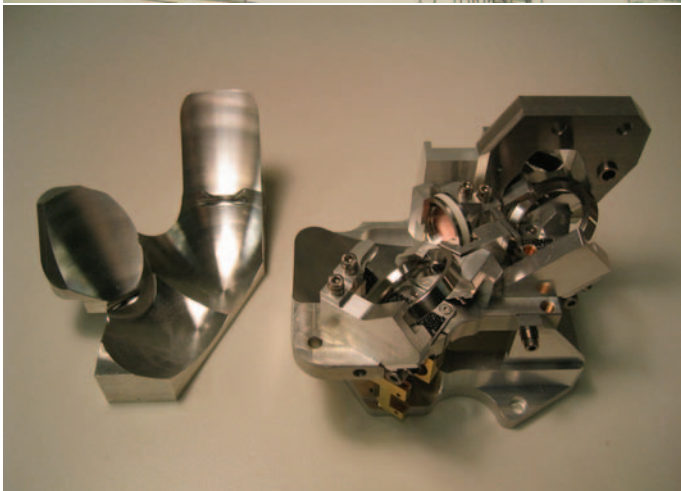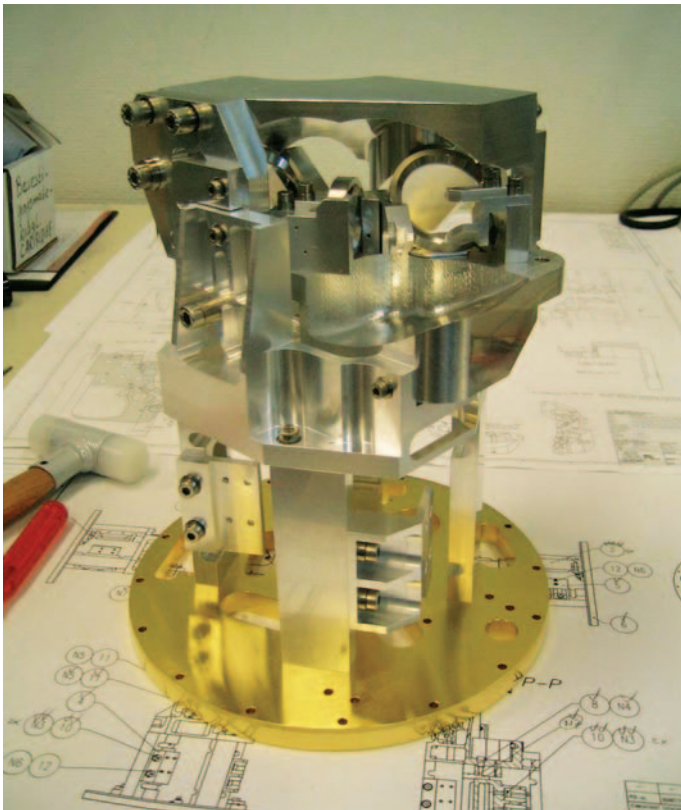

Figure 12: 3-D drawing of the mechanical design of the Band 9 cartridge.

development of test equipment is proceeding, with testing of the first cartridge expected to start this fall.

REFERENCES

A. M. Baryshev, H. van de Stadt, H. Schaeffer, R. Hesper, T. Zijlstra, M. Zuiddam, W. Wild, and L. de Jong, "Development of a 0.6 THz SIS receiver for ALMA," in *Proc. 12th Int. Symp. on Space THz Technology*, I. Mehdi, Ed. San Diego, CA: CIT, 2001, pp. 581-590.

A. Baryshev, R. Hesper, K. Wielinga, G. Gerlofsma, and M. Carter, "Design and verification of ALMA Band 9 receiver optics," to appear in *Proc. of the 15th Int. Symp. on Space THz Technology*, Northampton, Massachusetts, USA, April 27-29, 2004.

R. Kurz et al., 2002, ESO Messenger 107, 7

I. Lopez-Fernandez, J. D. Gallego Puyol, A. B. Cancio, and F. Colomer, "New trends in cryogenic HEMT amplifiers for radio astronomy," presented at the Int. Science and Technology Meeting on the Square Kilometer Array, Berkeley, CA, July 9-13, 2001.

Figure 11: (top) The Band 9 4K optics assembly, (bottom) a disassembled view of the optics assembly in which the machined mirrors can be seen, as can the grids, beam splitters, and absorbing beam dumps.
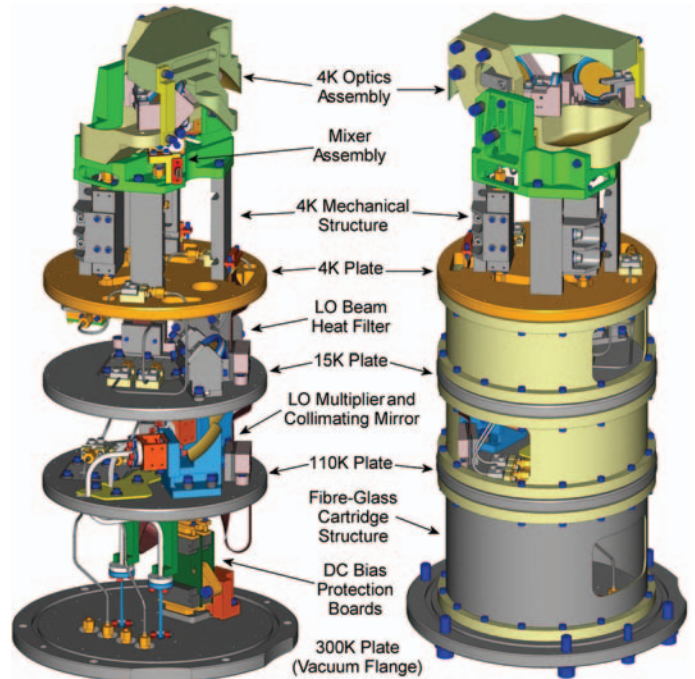
Tan G.H. et al., *The European Receivers for ALMA*

Observing Distant Type Ia Supernovae with the ESO VLT

The discovery of the accelerating universe through observations of distant Type Ia supernovae (SNe Ia) was one of the most exciting scientific discoveries of the past decade. The acceleration is apparently driven by a mysterious "dark" energy which overcomes the gravitational pull of matter. One of the best ways of constraining the nature of the dark energy is to build a larger, better-observed sample of distant SNe Ia over a wide range of redshifts. The Supernova Cosmology Project (SCP) has been using ESO and other telescopes to do just that and, in this article, we give an overview of the data we have collected thus far and we present some preliminary results.

Chris Lidman (ESO)
for The Supernova Cosmology Project[1]

Towards the end of the 1990's, two international collaborations independently used the apparent brightness of distant[2] Type Ia supernovae (SNe Ia) to discover that the rate of the Universe's expansion, contrary to what was then the common wisdom, is currently accelerating, and to infer that a mysterious form of energy – now called the dark energy – dominates the Universe (Riess et al. 1998; Perlmutter et al. 1999; for reviews, see Leibundgut 2001 and Perlmutter and Schmidt 2003). Since this discovery, measurements of the Cosmic Microwave Background (CMB) anisotropy, statistical analysis of galaxy redshift surveys, and measurements of the number density of massive galaxy clusters have shown that the Universe is flat and that matter, including dark matter, makes up about a quarter of the critical energy density. When these results are combined with the results from distant SNe Ia (Fig. 1), we infer that about 75% of Universe is made up of dark energy.

This is a remarkable result, and an extraordinary number of diverse theories have been proposed to explain the nature of the dark energy and the reason why it now dominates our Universe. For both matter and dark energy, the equation of state[3] relates the pressure to the energy density via

$$p = w(z)\,\rho,$$

where p is the pressure, ρ is the energy density, z is the redshift and $w(z)$ is the equation of state parameter. For non-relativistic matter, w is zero; for photons, it is 1/3; and for dark energy, it is negative. Candidates for dark energy include Einstein's cosmological constant, in which w is exactly –1, quintessence, in which it is variable and greater than –1, and other more exotic theories, such as

"phantom energy" theories, in which it is less than –1. Recent results, which combine high-quality HST data of distant SNe Ia (Knop et al. 2003, Riess et al. 2004) with the data from galaxy redshift surveys and the CMB, show that it is close to –1. Is w equal to –1 and is it a constant? The answer to this question will fundamentally change the way we see our Universe.

As a tool to measure cosmological distances, SNe Ia are unique. Their peak luminosities are very uniform, which means that an accurate measure of the distance can be obtained from the apparent brightness, and they are also intrinsically very bright, so they can be observed over enormous distances. In terms of redshift, SNe Ia with redshifts as high $z\sim1.5$ are now observed. This corresponds to a time when the Universe was about one-third of its current age[4].

Although the Universe is now accelerating, this was not always the case. Up until about 5 billion years ago, the Universe was matter dominated and decelerating. The change between deceleration and acceleration occurred around $z=0.5$. By observing SNe Ia over a wide range of redshifts, one can get a picture of the expansion history of the Universe from just a few billion years after the big bang to today, and this includes the epochs of deceleration and acceleration.

In 2000 and following a successful pilot program that discovered a SN Ia at $z=1.2$ (Aldering 1998), the SCP embarked on a program to discover and follow a large number of SNe Ia over a wide range of redshifts.

We use these data to extend observations of SNe Ia to redshifts greater than one, to measure the expansion history of the Universe from deceleration to acceleration, to constrain the dark energy equation of state, and to assess the importance of SN Ia evolution and extinction from dust. This program has made extensive use of ESO facilities and included spectroscopic confirmation and follow-up imaging with FORS1 and FORS2 and infra-red (IR) J-band imaging with ISAAC.

In this article we give an overview of how SNe Ia are discovered, we discuss the follow-up observations that we have done with the ESO VLT and we present some preliminary results. These results will appear in a series of papers, which, at the time of writing, have either been submitted or are in preparation (Lidman et al. 2004; Nobili et al. in preparation; Garavini et al. in preparation).

Search and Discovery

Starting in 2000 and ending in 2002, the SCP performed 8 separate high-redshift supernova searches involving the CFHT12k camera on CFHT, the MOSAICII camera on the CTIO Blanco telescope and Suprime-Cam on Subaru. In general, each of the searches aimed at discovering SNe Ia at different redshifts and, hence, the search areas and the search depths vary from one search to the next. For example, the 2002 CTIO search exclusively targeted SNe Ia at $z\sim0.5$, and thus searched a relatively large area of

---

[1] Members of the SCP are listed at the end of this article
[2] In the context of this article, we use distant to refer to supernovae that have redshifts z > 0.1 and nearby to refer to supernovae that have redshifts z ≤ 0.1
[3] The equation is written in natural units, in which the speed of light is 1 and unitless
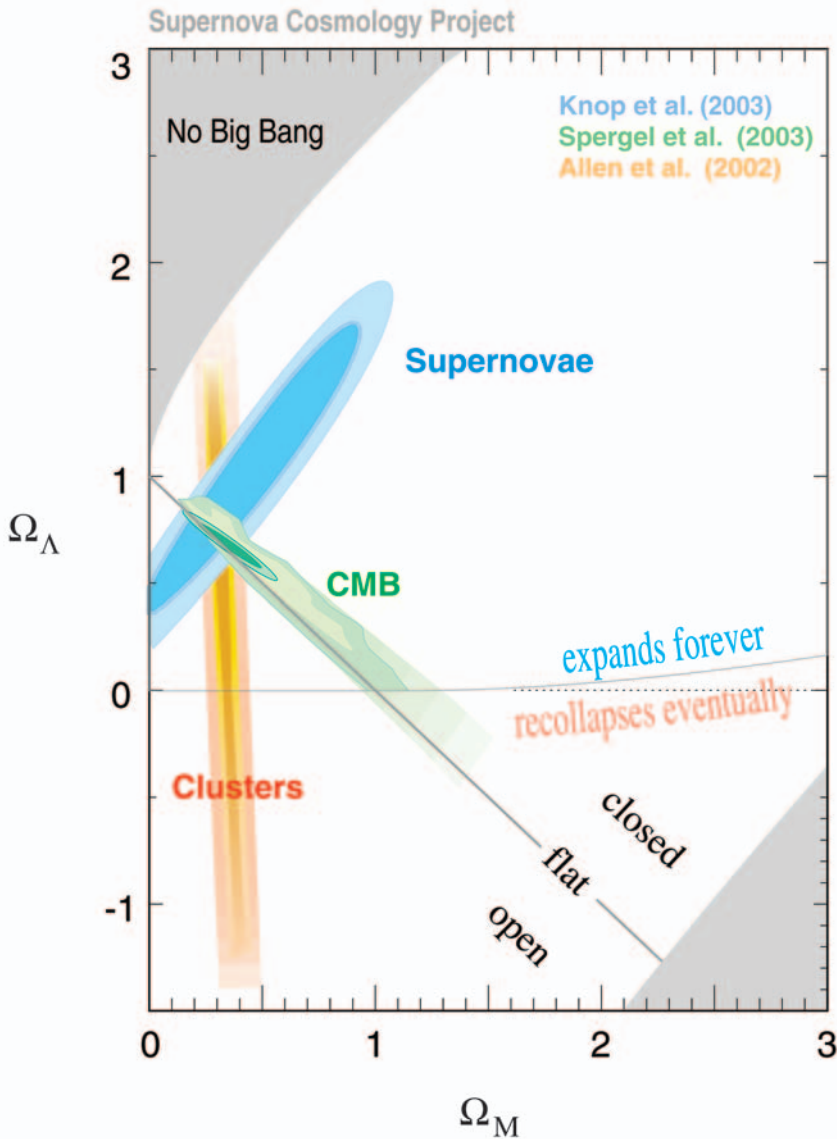[4] For a Hubble constant of H_o = 72 km/s/Mpc, the current age of the Universe is about 14 billion years.

Figure 1: An example of how studies of SNe Ia (cyan), CMB anisotropies (green) and the massive galaxy clusters (orange) restrict regions in the Ω_M and Ω_Λ plane, which are respectively, the energy densities in matter and dark energy as a fraction of the critical energy density. The three sets of studies overlap at $(\Omega_M, \Omega_\Lambda) \approx (0.25, 0.75)$, which is commonly referred to as the concordance ΛCDM model.

SPECTROSCOPIC CONFIRMATION

Candidate SNe Ia are distributed to teams working at the Gemini, Keck, Paranal, and Subaru Observatories for spectroscopic confirmation. The distribution is handled centrally and is done according to the priority of the candidates, the results from the analysis of data that were taken during previous nights, the capability and availability of instruments and the weather conditions at the individual observatories.

The goal of the spectroscopic follow-up is to determine the SN type and to obtain the redshift. The spectroscopy is critical. Only spectrally confirmed SNe Ia are followed during subsequent months.

Between 2000 and 2002, the SCP used FORS1 and FORS2 on the VLT to observe 39 SN Ia candidates. In general, we used FORS1 with the 300V grism to observe candidates that were thought to be at $z{\sim}0.5$ and FORS2 with the 300I grism and its red sensitive CCD to observe candidates that were thought to be at $z{\sim}1$. Since some key SN Ia spectral features are redshifted to very red wavelengths, where night sky lines are bright and variable and where detector fringing can be problematic, we have developed specialised techniques to reduce systematic error to a negligible level and to reach the Poisson noise limit. To achieve this, we employ the IR technique of combining several spectra dithered along the slit (some taken over different nights) to form a sky spectrum which is then scaled and subtracted from the data on a wavelength by wavelength basis. This technique works best if there is little instrument flexure, which is the case in both FORS1 and FORS2. Details of the technique are given in Lidman et al. (2004).

At high redshifts ($z > 0.4$), the broad Si II feature at ~6150Å, which is one of the defining signatures of the SN Ia class, is outside the wavelength range covered by the spectra. Therefore, we use other features, such as the Si II feature at ~4000Å and the Sulfur "W" feature at ~5500Å to spectrally identify SN Ia. The spectra of candidates are also matched against a library of nearby supernova spectra of all types and ages. The spectra

the sky. Others, such as the Fall 2002 Subaru search, exclusively targeted SNe Ia with $z > 1$, and thus covered a relatively small area to a much greater depth.

The standard high-redshift supernova search (Perlmutter et al. 1995) generally consists of 2 to 3 nights of imaging to take reference images, followed 3 to 4 weeks later by an additional 2 to 3 nights of imaging to take search images. Timing is critical to the success of the search. If the time span between reference and search runs is too small, the SN will not have brightened sufficiently to be detected. Alternatively, if the time span is too great, many of the supernova will be past maximum and these are less useful for the purpose of doing cosmology.

In 2000 and 2001 the searches were standard ones; however, the searches in 2002 were a variation on the standard theme. For example, the 2002 search with the CFHT12k camera on CFHT was a "rolling" search, where images were taken once every few nights during a two week period. This

was followed one, two and three months later by similar observations on the same fields. In this way, the search images of one month become the reference images of a later month, and, since images of the search fields are taken several times in any one month, one automatically gets a photometric time series without having to schedule follow-up observations separately, as one must do in a standard search. This rolling search is now in use for the supernovae search in the CFHT Legacy Survey.

The search data are immediately processed to find objects that have brightened and the most promising SN Ia candidates are given an internal SCP name and a priority. The priority is based on a number of factors: the significance of the detection, the brightness of the candidate, the quality of the subtraction and the percentage increase in the brightness together with the distance from the center of the apparent host, In any one search, several dozen good candidates are usually found.
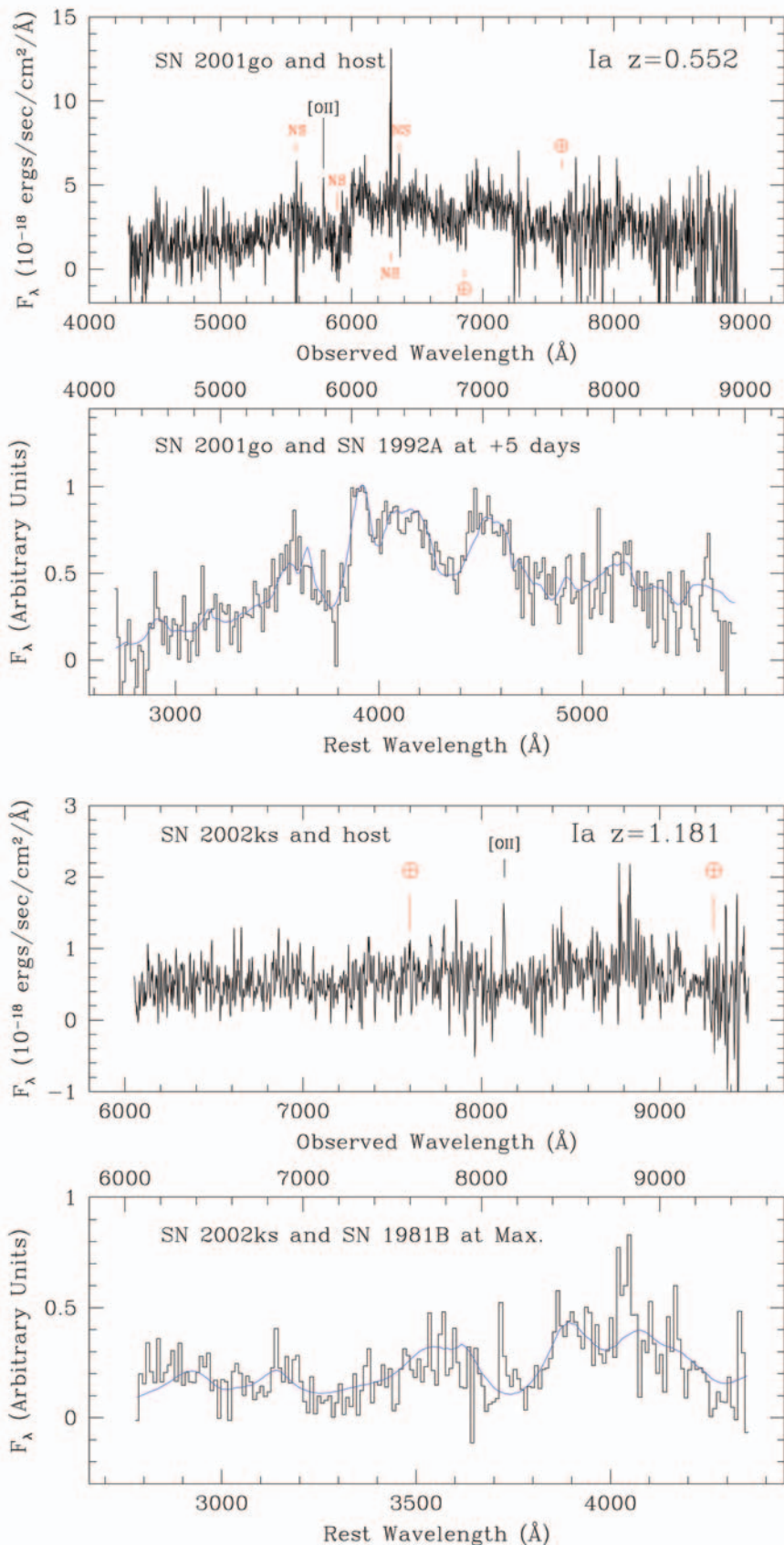
Figure 2: Spectra of SN 2001go and SN 2002ks - from Lidman et al. (2004). In the upper half of each figure, the unbinned spectrum of the candidate is plotted in the observer's frame and is uncorrected for host galaxy light. Night sky subtraction residuals are marked with the letters "NS" and telluric absorption features are marked with the symbol ⊕. Features from the host galaxy are also marked. In the lower half of each figure, contamination from the host is removed and the spectrum is rebinned, typically by 20 Å. This spectrum is plotted in black and it is plotted in both the rest frame (lower axis) and the observer's frame (upper axis). For comparison, the best fitting nearby SN Ia is plotted in blue. In both supernovae, the Si II feature at 4000 Å, which is visible only in SNe Ia, can be clearly seen.

of two spectrally confirmed SN Ia are shown in Figure 2. In both cases, the Si II feature at ~4000Å can be clearly identified.

In those searches that specifically targeted SNe Ia at z~0.5 for spectroscopic confirmation, the yield is very high – 13 out of 16 candidates were spectrally classified as SN Ia. In those searches that specifically targeted SNe Ia at $z > 1.0$ for spectroscopic confirmation, the yield is lower. In part, this is due to experimental design. Each candidate was first observed for one hour. Candidates that were found to have $z < 1$ were no longer observed. In some of these cases, a supernova might have been identified if we had chosen to integrate longer. Alternatively, if the candidate showed evidence for broad supernova features or if the redshift from host galaxy lines (in particular [O II]) placed the host at $z > 1$, the candidates were re-observed during later nights. This strategy enabled us to confirm several $z > 1$ SNe Ia, obtain their redshifts and schedule them for successful follow-up observations with ISAAC and HST.

For SNe Ia at $z > 1$, a secure classification relies on identifying the Si II feature at ~4000Å. However, this feature is not always present in SN Ia. At early phases or in slightly over-luminous SN Ia, such as SN 1991T, this feature is either weak or absent. Other, redder features, such as Fe II at ~4900Å are shifted to the near-IR. Although SN Ia spectra show Fe II features short-ward of the broad Ca II feature at ~3900Å that can be used to aid the classification, the lack of good quality UV spectra for nearby supernovae of all types means that these features cannot be reliably used alone. At these high redshifts, an additional source of difficulty often appears. Given the typical signal-to-noise ratio that one can achieve in a couple of hours with FORS2, one can sometimes match the spectra equally well with SNe Ia at two different redshifts. Fortunately, host galaxy lines, such as [O II] or the H and K of Ca II, or sometimes all three, are usually present, as is the case for SN 2002ks (Fig. 2).

COMPARING THE SPECTRA OF NEARBY AND DISTANT SNe Ia

Despite the widespread use of SNe Ia as a distance indicator, our understanding of these objects is still rather poor. It is thought that the progenitor is a carbon-oxygen white dwarf that undergoes a nuclear explosion. Given the vast span in time and distance over which SNe Ia can be observed, the Universe has undergone significant change. Could distant SNe Ia be different from their nearer cousins? The spectra of SNe Ia are probably the best place to look for signs of evolution.

Nearby SNe Ia are broadly divided into three sub-types: normal SNe Ia; sub-luminous SNe Ia, such as SN 1991bg or SN

1997cn, which, in the *B*-band, are approxi-
mately 2 magnitudes fainter than normal
SNe Ia; and SN 1991T-like SNe Ia, such as
SN 1999aa, which are slightly brighter than
normal SNe Ia and have broader *B*-band
light curves. The spectra of sub-luminous
SNe Ia and 91T-like SNe at maximum light
are very distinct from the spectra of normal
SNe Ia. In sub-luminous SNe Ia, absorption
features are deeper and expansion velocities
are lower, whereas, in 91T-like SNe Ia,
absorption features are shallower and expan-
sion velocities are higher.

We are currently comparing the integrat-
ed depths (similar to equivalent widths) of
some of the very broad features in SN Ia
spectra with the aim of searching for differ-
ences in the spectra of nearby and distant
SNe Ia, and we show an example of such a
comparison in Figure 3. On average, the dis-
tant SNe Ia lie within the band defined by
normal SNe Ia. Sub-luminous, 91bg-like
SNe Ia generally lie above the band, and
91T-like supernova lie below it. Distant SNe
Ia are neither clearly over-luminous nor sub-
luminous.

In Figure 4, we plot the velocity of the
minimum in the broad Ca II absorption fea-
ture at ~3900Å against light-curve phase for
a sample of nearby and distant SNe Ia. The
distant SNe Ia, which have a median redshift
of $z \sim 0.5$, and the nearby SNe Ia have simi-
lar expansion velocities. Distant SNe Ia are
clearly not sub-luminous.

THE HUBBLE DIAGRAM –
OPTICAL AND IR FOLLOW-UP

The magnitude-redshift relation (Hubble
diagram) is a relation between magnitude
(distance) and redshift (expansion), so the
position of a single SN Ia on the Hubble dia-
gram measures the integrated history of
expansion from the redshift at which the SN
Ia was observed to the present day. By
observing SNe Ia over a range of redshifts,
one is measuring the history of acceleration,
which depends directly on the relative
amounts of matter and dark energy. Hence,
universes with different amounts of matter
and dark energy trace different curves in the
Hubble diagram. Examples are shown in
Figures 6 and 8.

The accuracy at which cosmological
parameters can be derived depends on a
number of factors, such as the redshift inter-
val over which SNe Ia are observed, the
accuracy of the derived peak magnitudes,
systematic errors in the analysis and, obvi-
ously, the number of observed SNe Ia. It also
depends on how many cosmological param-
eters one is trying to fit, and if one includes
constraints from other experiments.

SNe Ia are not perfect standard candles,
but they are very good ones. The dispersion
in the peak absolute *B*-band magnitude is
~0.4 magnitudes. However, the absolute
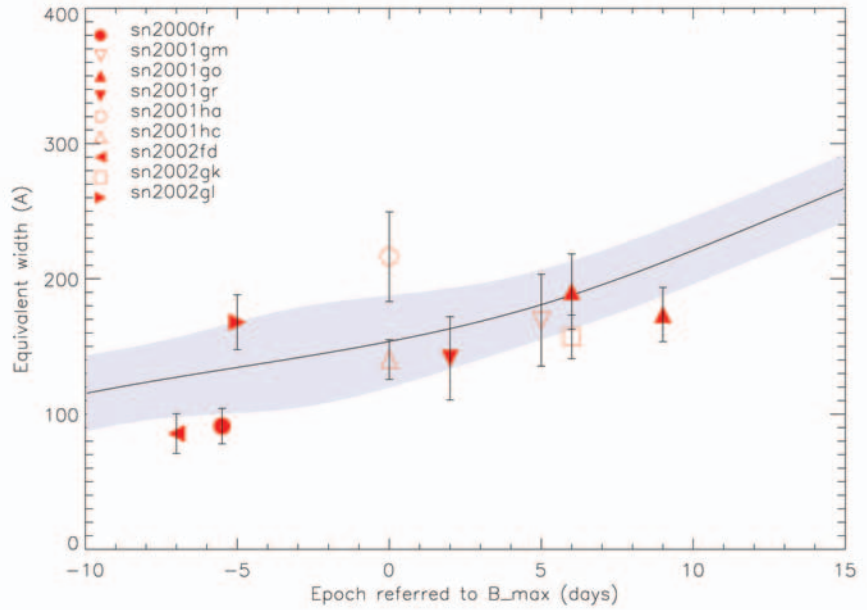luminosity is correlated with the shape of the

Figure 3: The equivalent width of the the broad absorption feature at 4800 Å,
which, at maximum light, is due to Fe II, plotted against SN epoch (plotted as
the day since maximum *B*-band light) – from Garavini et al. (in preparation).
Distant SNe Ia, with an average redshift of $z \sim 0.4$, are individually plotted as
large red symbols and nearby normal SNe Ia are plotted as a band. The black
line in the middle of the band represents the mean trend and the shaded band
represents the dispersion (one standard deviation). Sub-luminous, 91bg-like
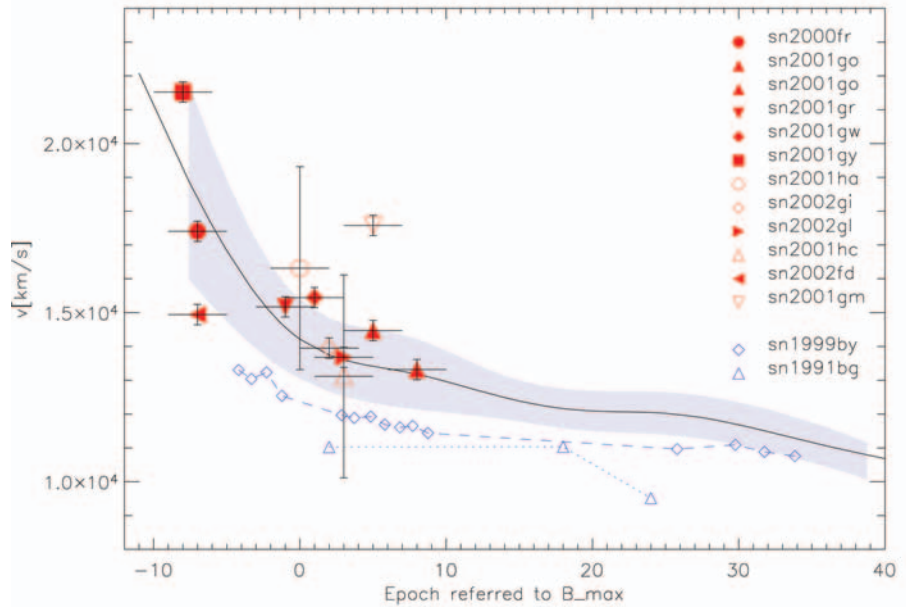SNe Ia generally lie above the band, and 91T-like supernova lie below it.

Figure 4: The velocity of the broad Ca II absorption feature at 3900 Å plotted
against SN epoch (plotted as the day since maximum B-band light) – from
Garavini et al. (in preparation). Distant SNe Ia, with redshifts ranging from
z=0.212 to z=0.912, are individually plotted as large red symbols and nearby
normal SNe Ia are plotted as a blue band. The black line in the middle of the
band represents the mean trend and the shaded area represents the dispersion
(one standard deviation). Sub-luminous, 91bg-like SNe Ia are plotted with small
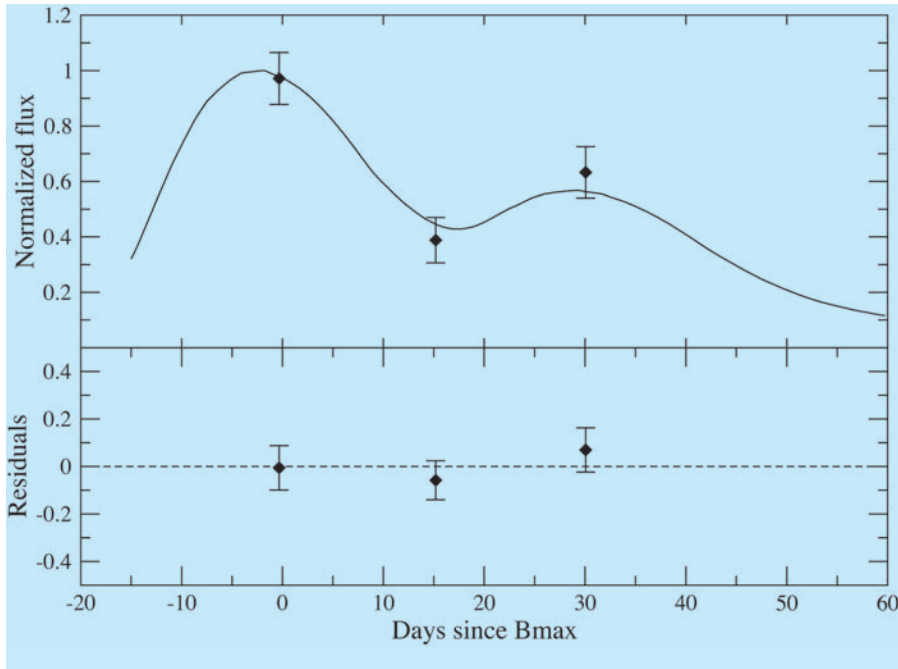blue symbols. Distant SNe Ia are clearly not sub-luminous.

Figure 5: The rest-frame *I*-band light curve (in units of normalised flux) of SN 2000fr (a SN Ia at *z*=0.543) – from Nobili et al. (in preparation). Given the redshift of the SN, the observations were done with ISAAC in the IR *J*-band. As in SN 1999Q (a SN Ia at *z*=0.46; Reiss et al. 2000), there is a second maximum about 30 rest-frame days after the first maximum. The timing and the relative amplitude of the two maxima in SN 2000fr can be used to show that SN 2000fr is not under-luminous. As a comparison, the *I*-band light curve of the best fitting nearby SNe (SN 1992bc) is plotted as the solid curve. The vertical scale is the only parameter in the fit. The time of *I*-band maximum is fixed by assuming that the delay between the rest-frame *B*- and *I*-band maxima are the same for SNe 1992bc and 2000fr. In nearby SNe, the difference between the two maxima is of the order of 1 day (the *I*-band mximum ocurrs first) with a dispersion of 2 days.

Figure 6: The rest-frame *I*-band Hubble diagram, with nearby SNe Ia plotted in blue and SN 2002fr (*z*=0.543) plotted in red – from Nobili et al. (in preparation). The inner error bars represent measurement errors and the outer error bars include 0.14 magnitudes of intrinsic dispersion, which is comparable to the dispersion in the *B*-band. Three models are plotted: a flat universe without dark energy (dashed line); the same universe with the addition of gray dust with R_V =9.5 (dotted line); and the concordance model (solid line).
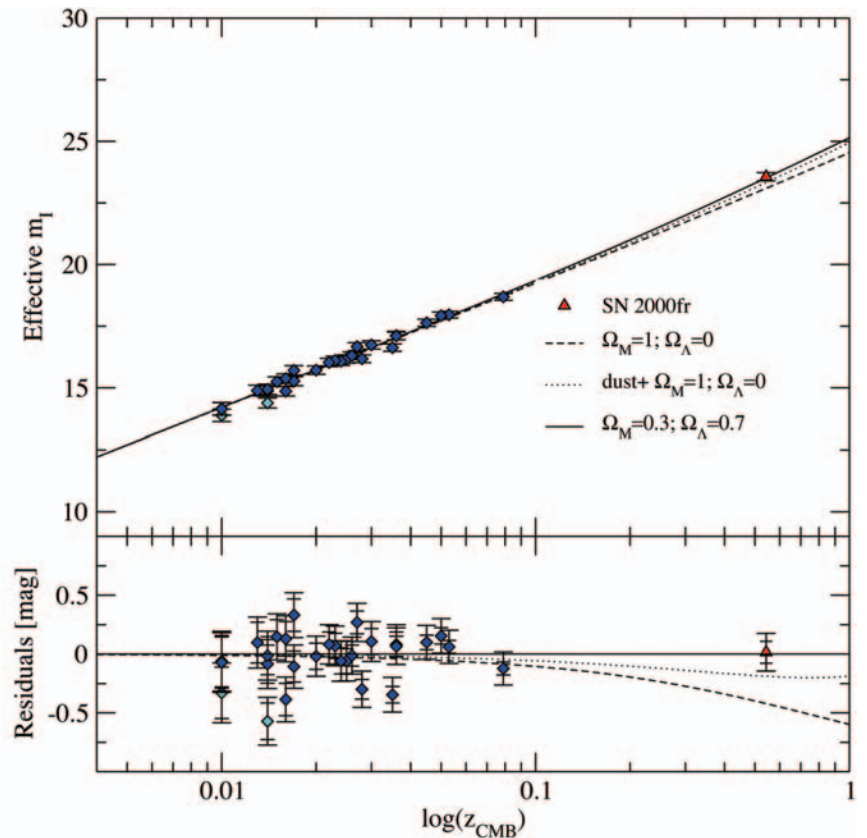
light curve. SNe Ia with broader light curves are also brighter. When the correlation is taken into account, the dispersion without extinction correction reduces to 0.17 magnitudes (Hamuy et al. 1996). This corresponds to a distance error of 9%.

The aim of the optical photometry is to sample the SN Ia light curve in the rest-frame *B*-band with at least five measurements, ideally starting before maximum, to determine the peak brightness and the light

curve shape. The light curve shape is then used to correct the peak brightness and this, together with the spectrally determined redshift, is plotted on the Hubble diagram.

If it were not for dust, then this would be all that one would need to do. Unfortunately, galaxies are full of it, and it can make SNe Ia fainter than they actually are. This would bias luminosity distances to higher values and one would derive a cosmology in which the acceleration was greater than it actually

was. However, dust also reddens, so one can use the colour as a check for reddening. See Knop et al. (2003) for a detailed study of the dust effects that can be measured in the optical bands with the HST.

For SNe Ia at *z* ~ 1.2, observations in IR *J*-band, which corresponds to the rest-frame *V*-band, are vital for testing for the presence of dust. Together with observations in the optical, one can compare the rest frame *B–V* colour of the distant SNe Ia with the colours

of nearby SNe Ia and hence test for extinction by dust, which would otherwise be difficult to constrain for such distant SNe Ia from optical observations alone.

At lower redshifts, $z \sim 0.5$, the IR J-band corresponds to the rest-frame I-band. By comparing rest-frame B–I colours of nearby and distant SNe Ia (Reiss et al. 2000; Nobili et al, in preparation) or by plotting SNe Ia on the rest-frame I-band Hubble diagram, it is also possible to assess the importance of extinction by dust.

We have used FORS1 and FORS2 to follow 23 SNe Ia at optical wavelengths (mostly R and I) and ISAAC to follow 8 SNe Ia (3 at $z \sim 0.5$ and 5 at $z > 1$) in the J-band. Although much of the data are still being analysed - we need to wait at least one year to take images after the SN has faded from view - we can present some preliminary results.

SECONDARY I-BAND MAXIMUM IN A DISTANT SN IA DETECTED

Normal SN Ia have a secondary I-band maximum that occurs about 25 days after the first maximum. In under-luminous SNe, the secondary maximum is fainter and appears earlier, and, in very sub-luminous SNe Ia, like SN 1991bg and SN 1997cn, it is completely absent (Reiss et al. 2000; Nobili et al. in preparation). The position and the relative amplitude of the second maximum are completely unaffected by dust, so they can be used as an independent indicator of the intrinsic luminosity of the supernova.

In Figure 5, we plot the rest frame I-band light-curve (observed with ISAAC in the J-band) of SN 2000fr, a spectrally confirmed SN Ia at $z = 0.543$. The second maximum is clearly detected about 30 rest frame days after the first maximum. The presence, location and relative amplitude of the second maximum in SN 2000fr suggest that it is a very normal SN Ia.

With only three data points, one cannot fit all the parameters that are needed to fit the light curve and to determine precisely the I-band maximum. For this, a minimum of five parameters are needed (Nobili et al. in preparation). However, with reasonable assumptions (see Figure 5), one can use the I-band light curves of nearby SNe Ia to get an estimate of the peak I-band magnitude of SN 2000fr. In Figure 5, we compare the light curve of SN 2000fr with SN 1992bc, a nearby SN Ia, and we use this to estimate the peak I-band magnitude of SN 2000fr. The only free parameter in the fit is the vertical scale. The time of I-band maximum is fixed by using B- and I-band data of both SNe.

In Figure 6, we plot the peak I-band magnitude of SN 2000fr on the I-band Hubble diagram together with a sample of 28 nearby SNe Ia. The location of SN 2000fr in the I-band Hubble diagram is fully consistent with the concordance model.
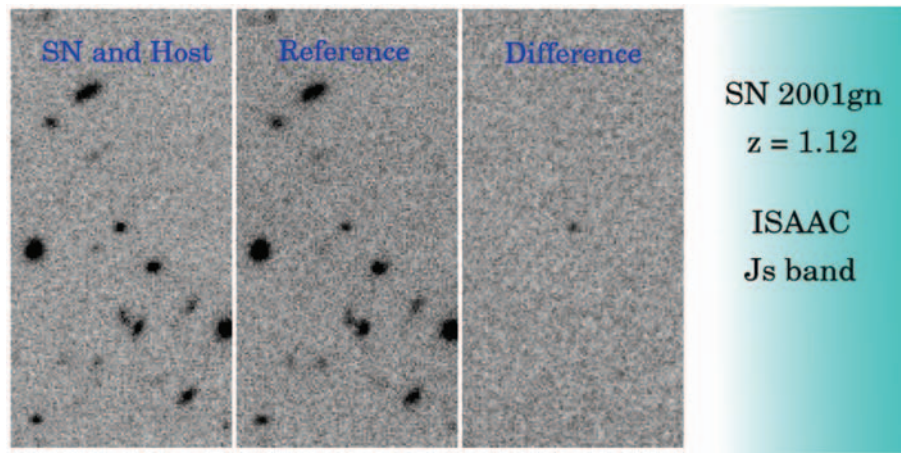

Figure 7: ISAAC observations of the distant SN Ia, SN 2001gn. On the left, we show an image with the supernova; in the middle, we show the reference image, which was taken 2 years later. The image on the right is the difference of the two and shows the supernova with a signal to noise ratio of ~12. Each image is the result of 10 hours of integration in good conditions. The image quality in the left hand image is 0.4″ and the magnitude of SN 2001gn at this epoch was around J=23.6.
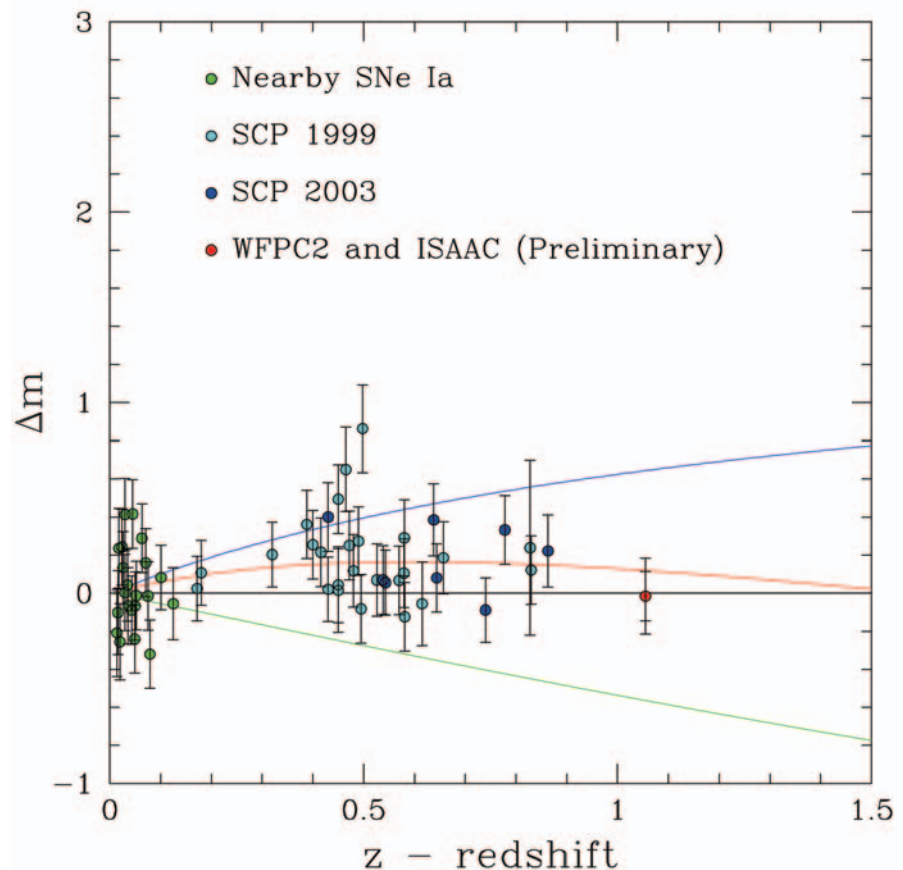

Figure 8: The differential B-band Hubble diagram with SNe Ia from Knop et al. (2003) and from a very preliminary and partial analysis of some of the data that were collected by the SCP in 2001. In this diagram, an empty universe is a horizontal line at zero. A flat universe consisting entirely of dark energy and a flat universe consisting entirely of matter are represented by the blue and green lines respectively. The red line represents the concordance model in which the universe was decelerating until z~0.5 and has accelerated ever since. The ISAAC observed SN Ia at z=1.06 favours the latter model, as do other recent observations (Tonry et al. 2003; Riess et al. 2004), which have extended the Hubble diagram to even higher redshifts

Lidman C., *Distant Type Ia SNe*

ISAAC OBSERVATIONS OF z>1 SNe IA

At $z \sim 1.2$, the rest frame U- and B-bands shift to optical I- and z- bands and the rest frame V-band shifts to the IR J-band. From the optical photometry, one derives the maximum B-band magnitude, the light curve shape, which is used to correct the peak magnitude, and, together with the IR data, the rest frame B–V colour. The corrected B-band maximum is plotted on the Hubble diagram and the B–V colour is used to verify that the supernova is unreddened and undimmed by dust.

IR observations of SNe Ia at $z \sim 1$ from the ground are challenging. Typically, these supernovae have $J \sim 23.5$ and, with ISAAC on the VLT, we integrate for 10 hours to reach a S/N ratio of about 20 when the IR seeing is 0.5″. In most cases, these observations have to be repeated one year later, so that a reference image without the supernova is available for doing photometry with image subtraction techniques. Good seeing is critical. The observations would not have been feasible if the seeing was much worse than 0.5″. In Fig. 7, we show ISAAC J-band images of SN 2001gn, a SN Ia at $z = 1.12$. The S/N ratio in the difference image is about 12.

In Fig. 8, we plot SNe Ia from Knop et al. (2003) on the differential Hubble diagram and we add one $z > 1$ SN Ia – SN 2001hb – as an example. SN 2001hb, which was also observed with ISAAC, has normal rest-frame B–V colours, so it is unlikely that it is significantly reddened. The host galaxy of SN 2001hb is very faint. Indeed, in very deep images with the ACS camera on HST, we do not detect the host galaxy.

The red line in Figure 8 is the concordance model (25% matter and 75% dark energy). In this model, SNe Ia initially become fainter with respect to the empty universe (the horizontal black line in Fig. 8). At $z \sim 0.5$, the relative difference reaches a maximum and, by $z \sim 1.5$, SNe Ia are relatively brighter – SNe Ia are still becoming fainter with increasing redshift, but relative to the empty universe, they become brighter. This is a characteristic signature of dark energy and it is the reason why well observed SNe Ia at $z > 1$ are so valuable. Although there is only one $z > 1$ SN Ia in this plot (see Riess et al. 2004 for additional SNe Ia at these redshifts), we expect to add seven additional $z > 1$ SNe Ia once all the final reference images have been taken and analysed.

PUSHING TO EVEN HIGHER REDSHIFTS

With current instrumentation, we have shown that it is possible to spectrally confirm and follow SNe Ia at $z \sim 1$ from the ground. Can we realistically use ground-based telescopes to observe even more distant SNe Ia and measure the expansion of the universe at even higher redshifts, or are we restricted to using telescopes that are in space?

For our ISAAC data, the most critical factor is the image quality. If the image quality in our ISAAC data would have been much worse than 0.5″, then observing $z \sim 1$ SNe with the required S/N ratio would not have been feasible, even in service mode. If the image quality could be improved to 0.2 to 0.3 arc seconds, then it becomes possible to observe SNe Ia at at $z \sim 1.5$ and possibly beyond with sufficiently good S/N ratios over several epochs.

In a few years now, *HAWK-I* – the planned wide-field near-IR imager with the possible provision of doing partial adaptive optics (AO) correction over the entire field of view – will become available. With its higher throughput, wider field-of-view and better image quality it will become possible to image several $z \sim 1.5$ SNe Ia simultaneously.

Indeed, instruments that provide partial or full AO correction will play a role in future distant SN Ia studies. With *NAOS-CONICA*, it is already feasible to image a SN Ia at $z \sim 1.5$ and to take a low S/N spectrum if one is fortunate enough to have a suitably bright natural guide star (NGS) that is a also nearby. Such a fortunate coincidence is unlikely, as such bright stars are usually avoided in supernova searches. With a laser guide star (LGS), one can use considerably fainter stars (a natural star is still needed to correct for tip and tilt) and hence increase the area over which very distant SNe Ia can be observed. However, the quality of the AO correction with a LGS is generally poorer, especially at shorter IR wave-lengths. Although imaging such SNe Ia should still be feasible with a LGS, low resolution IR spectroscopy will be very challenging.

In the meantime, the redshift limit for optical ground-based spectrographs can still be pushed higher by making a more judicious choice of which candidates to observe. One of the most promising ways to select high redshift candidates is to target areas that have already been observed at several wavelengths. The most promising high-redshift candidates can then be selected from the host redshifts that are derived from the broad-band photometric data. By using reduction techniques that are commonly used to process IR data, there is no fundamental reason why one cannot spectrally confirm a SNe Ia at $z \sim 1.5$ from the ground.

THE SUPERNOVA COSMOLOGY PROJECT (SCP)

The SCP is an international collaboration whose members include S. Perlmutter (P.I.), G. Aldering, R. Amanullah, P. Antilogus, P. Astier, G. Blanc, M. S. Burns, A. Conley, S. E. Deustua, M. Doi, R. Ellis, S. Fabbro, V. Fadeyev, G. Folatelli, G. Garavini, R. Gibbons, G. Goldhaber, A. Goobar, D. E. Groom, D. A. Howell, I. Hook, N. Kashikawa, A. G. Kim, R. A. Knop, B. C. Lee, J. Mendez, T. Morokuma, K. Motohara, S. Nobili, P. E. Nugent, R. Pain, V. Prasad, R. Quimby, J. Raux, N. Regnault, P. Ruiz-Lapuente, G. Sainton, B. E. Schaefer, K. Schahmaneche, E. Smith, A. L. Spadafora, V. Stanishev, R. C. Thomas, N. A. Walton, L. Wang, W. M. Wood-Vasey, N. Yasuda and the author of these lines.

REFERENCES

Aldering, G 1998 IAU 7046.
Allen, A. W. et al. 2002, MNRAS, 334, L11
Hamuy, M., et al. 1996, AJ, 112, 2398
Knop, R. A., et al. 2003, ApJ, 598, 102
Lidman, C., et al. 2004, A&A *in press*
Liebundgut, B. 2001, ARA&A, 39, 67
Perlmutter, S. et al. 1995, ApJ, 440, L41
Perlmutter, S. et al. 1999, ApJ, 517, 565
Perlmutter, S. & Schmidt, B. 2003, in *Supernovae and Gamma Ray Bursts*, ed. K. Weiler (Berlin: Springer)
Riess, A. G., et al. 1998, AJ, 116, 1009
Riess, A. G., et al. 2000, ApJ, 536, 62
Riess, A. G., et al. 2004, ApJ, 607, 665
Spergel, D. N., et al. 2003, ApJS, 148, 175
Tonry, J. L., et al. 2003, ApJ, 594, 1
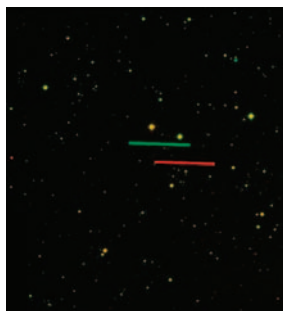
ESO Views of Earth-Approaching Asteroid Toutatis. Composite, false-colour image showing asteroid (4179) Toutatis moving in front of background stars, as seen from Paranal (red trail) and La Silla (green trail). The two photos used for this combination were obtained nearly simultaneously in the morning of September 29, at 02:30 hrs UT, when the asteroid was passing through the constellation of Triangulum Australe ("The Southern Triangle"). The offset between the two trails corresponds to the difference of the lines-of-sight from the two telescopes, 513 km apart, towards the object. Two 1-min images were taken almost simultaneously with the FORS-1 instrument on Kueyen, the second 8.2m VLT Unit Telescope on Paranal, and on the WFI camera installed on the ESO/MPI 2.2m telescope at La Silla. The WFI image was obtained though an R broad-band filter; on the VLT, a narrow band [O II] interference filter was used to attenuate the light of the bright asteroid. The images were then scaled and processed in order to compensate for the different characteristics of the two instruments (scale, orientation, distortion, sensitivity). The VLT image is displayed in red, the WFI image in green. As the stars are common to both images, they appear yellowish. (ESO PR Photo 28e/04)

Supernovae Shed Light on Gamma-Ray Bursts

We have believed for decades that supernovae were the most magnificent and energetic phenomena occurring in the Universe after the Big Bang. Today we know that this is only a part of the story. Astronomers have discovered that comparable amounts of energy (or even more) are released, in a few seconds, by gamma-ray bursts. Recently it was determined that these two classes of events have a deep connection. In this article we report the observations of supernovae associated with gamma-ray bursts carried out at ESO by our group. We also briefly review the status of the supernova/gamma-ray burst connection and highlight the open questions.

Massimo Della Valle[1], Daniele Malesani[2], Guido Chincarini[3,4], Luigi Stella[5], Gianpiero Tagliaferri[4], Lucio Angelo Antonelli[5], Sergio Campana[4], Stefano Covino[4], Fabrizio Fiore[5], Neil Gehrels[6], Kevin Hurley[7], Leonardo J. Pellizza[8], Filippo Maria Zerbi[4], Lorella Angelini[6], Luciano Burderi[5], Dave Burrows[9], Milvia Capalbi[10], Patrizia Caraveo[11], Enrico Costa[5], Giancarlo Cusumano[12], Philippe Filliatre[8], Dino Fugazza[4], Roberto Gilmozzi[13], Paolo Giommi[10], Paolo Goldoni[8], Gian Luca Israel[5], Elena Mason[13], Keith Mason[14], Andrea Melandri[5], Sandro Mereghetti[11], I. Felix Mirabel[8,13], Emilio Molinari[4], Alberto Moretti[4], John Nousek[9], Paul O'Brien[15], Julian Osborne[16], Rosalba Perna[17], Matteo Perri[10], Luigi Piro[5], Elizabeth Puchnarewicz[14], Mario Vietri[18] (*the MISTICI[1] collaboration*).

[1]INAF-Arcetri; [2]SISSA/ISAS; [3]Milano-Bicocca Univ.; [4]INAF-Brera; [5]INAF-Roma; [6]NASA-GSFC; [7]Berkeley Univ.; [8]CEA; [9]PSU; [10]ASDC; [11]IASF-Milano; [12]IASF-Palermo; [13]ESO; [14]MSSL; [15]Leicester Univ.; [16]UL; [17]CU; [18]SNS

ENTIRELY NEW AREAS of astronomical research sprouted out of the US political decisions arising from the Sputnik crisis. The race to space was primarily designed to reduce the "missile gap" evidenced by the crisis, but also to develop a space-based monitoring of the Soviet nuclear program, that had resumed extensive testing in the atmosphere. In addition, the need to counter the low-morale effects of the crisis and regain international prestige led to increased support for publicly exciting scientific investigations and explorations of space. The birth of extrasolar high-energy astrophysics (Giacconi et al. 1962) is certainly among the most important outcomes of this new political environment. Another exciting fruit of those times was the serendipitous discovery of gamma-ray bursts (GRBs). The first report about their cosmic origin came from the Vela satellites (Klebesadel, Strong & Olson 1973), launched to monitor compliance with the nuclear partial test ban treaty. We now know that GRBs are sudden and powerful flashes of gamma-ray radiation, which occur randomly in the sky at the rate of about one per day (as observed by the BATSE instrument). The distribution of the durations at MeV energies ranges from 10^{-3}s to about 10^3s and is clearly bimodal (Kouveliotou et al. 1993). The bimodality is also apparent from the spectral properties: long bursts ($T > 2$ s) tend to be softer than the short ones (Fig. 1). Klebesadel et al. (1973) pointed out the lack of evidence for a connection between GRBs with supernovae (SNe), as proposed by Colgate (1968), nevertheless they concluded that "*...the lack of correlation between gamma-ray bursts and reported supernovae does not conclusively argue against such an association...*". This was perhaps the very beginning of the galactic/extragalactic controversy on the origin of GRBs. Indeed
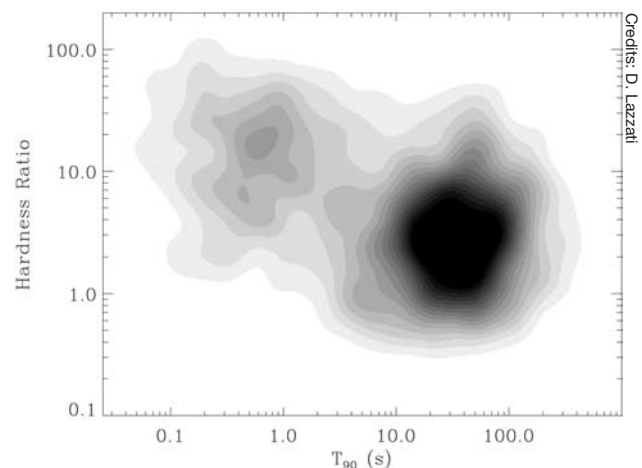

Credits: D. Lazzati

Figure 1: Distribution of GRBs in the plane spectral hardness vs duration (T_{90} is the time within which 90% of the counts are collected). Two classes of events emerge, called respectively "long" and "short" GRBs.

---

[1]Multiwavelength Italian Swift Team with International Co-Investigators.

the distance scale of GRBs remained a mystery for 25 years. By the mid-1980s the general belief was that GRBs originate from neutron stars harbored in the Milky Way. But this idea received a surprising blow in the middle of the 1990s, after the observations of the Compton Gamma-ray Observatory: "...*the positions of over 1000 gamma-ray bursts detected with the BATSE experiment onboard the Compton Gamma-ray Observatory are uniformly and randomly distributed in the sky with no significant concentration to the Galactic plane or to the Galactic center*" (Paczynski 1995). However the observed isotropic distribution of GRBs was not considered the ultimate evidence in favor of an extragalactic origin (Lamb 1995). A public debate of these issues took place in April 1995 in the main auditorium of the Smithsonian Natural History Museum in Washington: Bodhan Paczynski argued that GRB go off at cosmological distances, whereas Donald Lamb contended that GRBs originate from neutron stars in an extended halo around the Galaxy.

THE SN/GRB ASSOCIATION

Thanks to observations with *BeppoSAX*, the Italian-Dutch satellite for X-ray astronomy (e.g. Boella et al. 1997), the X-ray and optical afterglows of GRBs could be discovered (Costa et al. 1997; van Paradijs et al. 1997), leading to a revolution in the study of these enigmatic astrophysical phenomena. The optical counterparts, in particular, yielded the redshift of GRBs, thus establishing that most of them originate at cosmological distances. It took only a handful GRBs to find the first at a redshift $z > 4$: indeed, with an average $z \cong 1$, GRBs are amongst the most remote cosmological objects we know of.

The quarter-century dispute on the GRB distance and energetic scale was finally settled. GRBs were thus seen to involve the release of huge amounts of energy, comparable to the binding energy of a neutron star ($\leq 10^{53}$ ergs). Therefore, independent of any specific model, it appeared likely that GRBs (at least the long-duration ones, that is, those lasting more than 2 s), could be associated with the collapse of massive stars (Woosley 1993). Currently several lines of evidence support this scenario. **i)** SN 1998bw was the first SN discovered spatially and temporally coincident with a GRB (GRB 980425; Galama et al. 1998). Unexpectedly, SN 1998bw was discovered not at cosmological distances, but in the nearby galaxy ESO 184-G82 at $z = 0.0085$. This implied that GRB 980425 was underenegetic by 4 orders of magnitudes with respect to typical "cosmological GRBs". Moreover, the absence of a conspicuous GRB afterglow contrasted with the associated SN, which was extremely energetic, had expansion velocities a factor 3–4 larger than those of normal Ib/c SNe and was characterized by an exceptionally high luminosity. This association was thus
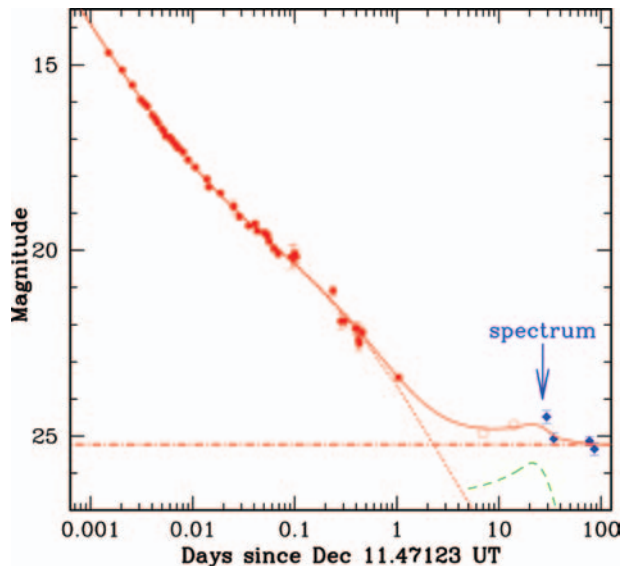

Figure 2: Light curve of the afterglow of GRB 021211; blue diamonds represent our data, while red circles are taken from the literature (see Della Valle et al. 2003 for a list of references). The dotted, dot-dashed and dashed lines represent the afterglow, host, and SN contribution respectively. The solid line is the sum of the three components.

Figure 3: Spectrum of the bump of GRB 021211 (red line) compared with the spectra of the type-Ia SN 1991bg and of the type Ic SN 1994I. The broad deep is due to the blend of the Ca H+K edges, a common feature among SNe. From Della Valle et al. (2003).
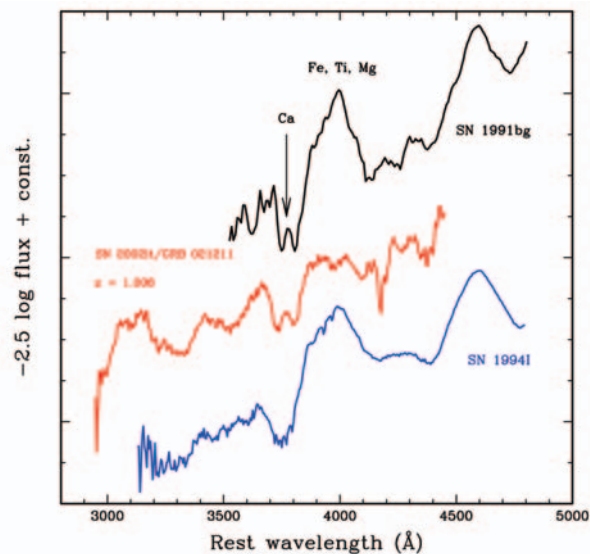
considered suggestive, rather than representative, of the existence of a general SN/GRB connection. **ii)** The light curves of many afterglows show rebrightenings which have been interpreted as emerging supernovae outshining the afterglow several days after the GRB event (e.g. Bloom et al. 1999). However, other explanations, such as dust echos, thermal re-emission of the afterglow, or thermal radiation from a preexisting SN remnant could not be ruled out. Only spectroscopic observations during the rebrightening phase could remove the ambiguity. Indeed spectroscopic features of SNe are unique, being characterized by FWHM ~100 Å.

SN 2002lt/GRB 021211

One of the first opportunities to carry out spectroscopic observations during a GRB afterglow rebrightening arrived in late 2002 (Della Valle et al. 2003). GRB 021211 was detected by the HETE–2 satellite, allowing the localization of its optical afterglow. We thus performed late-time follow-up photometric observations with the ESO VLT–UT4

(Yepun), during the period 2003 January–March. Figure 2 shows the results of our observations, together with those available in the literature. A rebrightening is apparent, starting ~15 days after the burst and reaching the maximum (R~24.5) during the first week of January. For comparison, the host galaxy has a magnitude $R = 25.22 \pm 0.10$, as measured in our late-time images. We obtained a spectrum of the afterglow + host with FORS 2 (grism 150I) on Jan 8 (27 days after the GRB), during the rebrightening phase. The resolution was about 20 Å, and the integration time was 4 h. Fig. 3 shows our spectrum in the rest frame of the GRB (red solid line), smoothed with a median filter and cleaned from the nebular emission line [O II] 3727 Å (observed at 7473 Å, thus implying a redshift $z = 1.006$). The spectrum of the bump is characterized by broad low-amplitude undulations blueward and redward of a broad absorption, the minimum of which is measured at ~3770 Å (in the rest frame of the GRB), whereas its blue wing extends up to ~3650 Å. The comparison with the spectra of SN 1994I, and to some
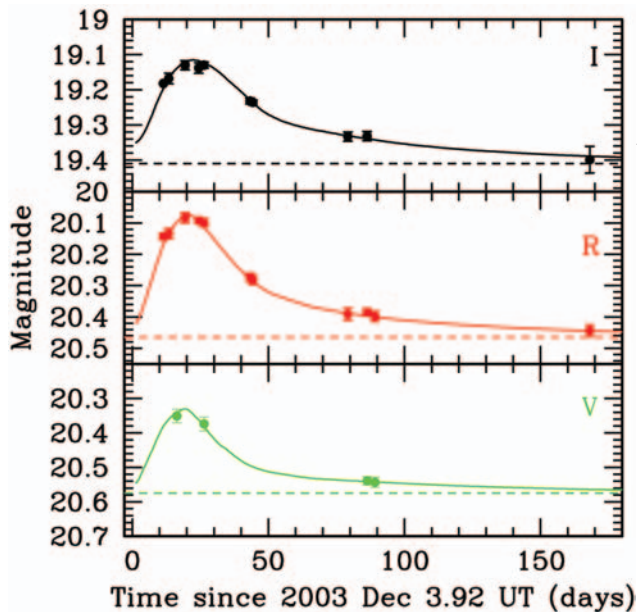
Figure 4: Light curves of GRB 031203. The solid line represents the contribution due to a 1998bw-like SN (Galama et al. 1998) at $z = 0.1055$, brightened by 0.5 mag and reddened with $E_{B-V} = 1.1$. The dashed lines represent the host galaxy contribution. From Malesani et al. (2004).

extent also of SN 1991bg and SN 1984L (the latter not plotted in Fig. 3) strongly supports the identification of the broad absorption with a blend of the Ca II H and K lines; the blueshifts corresponding to the minimum of the absorption and to the edge of the blue wing imply velocities $v \sim 14{,}400$ km/s and $v \sim 23{,}000$ km/s, respectively. The exact epoch when the SN exploded depends crucially on its rising time to maximum light. SN 1994I, SN 1998bw, and SN 1999ex (the best documented examples of type-Ic SNe) reached their B-band maximum ~ 12, 16, and 18 days after the explosion. In Fig. 2 we have added the light curve of SN 1994I (dereddened by $A_V = 2$ mag) to the afterglow and host contributions, after applying the appropriate K-correction (solid line). As can be seen, this model reproduces well the shape of the observed light curve. A null time delay between the GRB and the SN explosions is required by our photometric data, even if a delay of a few days is also acceptable given the uncertainties in the measurements.

It is interesting to note that SN 1994I, the spectrum of which provides the best match with the observations, is a typical type-Ic event rather than an exceptional 1998bw-like object, as the one proposed for association with GRB 980425 and other well-studied examples (GRB 030329: Stanek et al. 2003; Hjorth et al. 2003; GRB 031203: Malesani et al. 2004). The peak magnitude of SN 1994I was $M_V \sim -18$, a not unusual value among type-Ic SNe, to be compared with the extraordinary brightness $M_V \sim -19.2$ reached by SN 1998bw or $M_V \sim -19.7$ achieved by SN 2003lw (associated with GRB 980425 and GRB 031203, respectively). If the SN associated with GRB 021211 indeed shared the properties of SN 1994I, this would open the interesting possibility that GRBs may be associated with normally-energetic type-Ic SNe, and

not only with the more powerful events known as "hypernovae". We note however that the recently studied SN 2002ap (Mazzali et al. 2002) shared some of the properties of hypernovae (high expansion velocity, large kinetic energy), but was not significantly brighter than normal type-Ic SNe. Even if its pre-maximum spectra showed significantly broader lines than those measured in our case, this difference was vanishing at later stages, so that it may not be easy to distinguish between the two SN types.

We finally stress that even if GRBs are indeed mainly associated with normal type-Ic SNe, the discovery of overluminous type-Ic events (like SN 1998bw) associated with GRBs is favored by observations, since the SN can more easily dominate the afterglow component.

THE "SMOKING GUN": GRB 030329/SN 2003dh

The peculiarity of the SN 1998bw/GRB 980425 association (very faint gamma-ray emission, unusual afterglow properties, overluminous associated SN) and the objective difficulties to collect data for SN 2002lt at $z = 1$ (4 h to get one single spectrum) prevented us from generalizing on the existence of a SN/GRB connection (although both cases were clearly suggestive).

The breakthrough in the study of the GRB/SN association arrived with the bright GRB 030329. This burst, discovered by the HETE-2 satellite, was found at a redshift $z = 0.1685$, relatively close-by, therefore allowing detailed photometric and spectroscopic studies. SN features were singled out in great detail by several groups, among which the GRACE collaboration (Hjorth et al. 2003). The associated SN (SN 2003dh) looked strikingly similar to SN 1998bw. However, the gamma-ray and afterglow properties of this GRB were not unusual

among GRBs. Therefore, the link between GRBs and SNe was eventually established to be general, likely concerning all "classical", cosmological GRBs. In this respect GRB 980425 was considered a very peculiar event, unique among the ~40 GRBs with known redshift.

MORE CONNECTIONS: GRB 031203/SN 2003lw

GRB 031203 was a 30 s burst detected by the INTEGRAL burst alert system (Mereghetti et al. 2003) on 2003 Dec 3. Its precise (2.7′) localization was distributed within only 18 seconds from the beginning of the burst, the best combination between accuracy and speed ever reached for a GRB. At $z = 0.1055$, it was the second closest burst after GRB 980425. At this low redshift, the burst energy was extremely low, of the order of 10^{49} erg, well below the "standard" reservoir $\sim 2\ 10^{51}$ erg of normal GRBs (Frail et al. 2001). Only GRB 980425 and XRF 020903 were less energetic. In this case, a very faint NIR afterglow could be discovered, orders of magnitude dimmer than usual GRB afterglows (Malesani et al. 2004).

We observed this event with the VLT and NTT telescopes on a number of epochs, to seek the signatures of a SN (Tagliaferri et al. 2003). Our observations are plotted in Fig. 4. A few days after the GRB, a rebrightening is apparent in all optical bands. The rebrightening amounts to ~30% of the total flux (which is dominated by the host galaxy), and is coincident with the center of the host galaxy to within 0.1″ (~200 pc). For comparison, we plot in Fig. 4 the VRI light curves of SN 1998bw (solid lines; from Galama et al. 1998), placed at $z = 0.1055$ and dereddened with $E_{B-V} \sim 1.1$. Interpolation of the $UBVRI$ data was performed in order to estimate the fluxes of SN 1998bw at the frequencies corresponding to the observed bands. Even after correcting for cosmological time dilation, the light curve of SN 2003lw is broader than that of SN 1998bw, and requires an additional stretching factor of ≈ 0.9 to match the R and I bands. The R-band maximum is reached in ~18 (comoving) days after the GRB. Assuming a light curve shape similar to SN 1998bw, which had a rise time of 16 days in the V band, our data suggest an explosion time nearly simultaneous with the GRB. However, given that SN 2003lw was not strictly identical to SN 1998bw, and as we lack optical data in the days immediately following the GRB, a lag of a few days cannot be ruled out. Type-Ic SNe usually reach V-band maximum in ~12–20 days, the brightest events showing a slower evolution.

A precise determination of the absolute magnitude of the SN is made difficult by the uncertain extinction. Based on the Balmer ratios of the host galaxy we derive the average combined Galactic and host extinction to be $E_{B-V} \sim 1.1$. Given the good spatial coin-

cidence of the SN with the center of the host, such a value is a good estimate for the SN extinction. With the assumed reddening, SN 2003lw appears brighter than SN 1998bw by 0.5 mag in the *V, R,* and *I* bands. The absolute magnitudes of SN 2003lw are hence $M_V = -19.75 \pm 0.15$, $M_R = -19.90 \pm 0.08$, and $M_I = -19.80 \pm 0.12$.

Figure 5 shows the spectra of the rebrightening on 2003 Dec. 20 and Dec. 30 (14 and 23 rest-frame days after the GRB), after subtracting the spectrum taken on 2004 Mar. 1 (81 rest-frame days after the GRB). This assumes that the latter spectrum contains only a negligible contribution from the SN, which is confirmed by the photometry. The spectra of SN 2003lw are remarkably similar to those of SN 1998bw obtained at comparable epochs (shown as dotted lines in Fig. 8). Both SNe show very broad absorption features, indicating large expansion velocities, thus we classified SN 2003lw as a hypernova. The broad peaks near 5300 Å and 6600 Å are the emission components of P-Cyg profiles due to the blending of several lines. There is evolution between the two epochs: the bluer bump is observed at longer wavelengths in the second spectrum, and is slightly narrower. Moreover, the shape of the redder peak is different in the two epochs. Both peaks appear at redder wavelengths than in SN 1998bw. GRB 031203 was quite similar to GRB 980425, albeit more powerful. Both events consisted in a single, underenergetic pulse. Their afterglows were very faint or absent in the optical, and showed a very slow decline in the X-rays. Last, they were both accompanied by a powerful hypernova. Therefore, GRB 980425 can no longer be considered as a peculiar, atypical case. Both bursts were so faint, that they would have been easily missed at cosmological distances. Since the volume they sample is 10^5 to 10^6 times smaller than that probed by classical, distant GRBs with $\langle z \rangle \approx 1$, the rate of these events could be dramatically larger, perhaps they are the most common

GRBs in the Universe.

The parent galaxy of GRB 031203 has been studied in detail by Chincarini et al. (2004) and Prochaska et al. (2004). These authors found that the GRB host is a star forming galaxy with a fairly high (relative to the local Universe) star formation, of the order of 10 $M_\odot$/yr/L*. This independently corroborates the existence of a link with the death of massive stars.

…THERE IS AN EXPANDING FRONTIER OF IGNORANCE…[2]

All these facts provide robust empirical grounds to the idea that some types of core-collapse SNe are the progenitors of long-duration GRBs. On the other hand, the existence of a SN/GRB association poses intriguing questions which have not yet been answered: **1.** *What kind of SNe are connected with long-duration GRBs and XRFs?* Evidence based on the associations between SN 1998bw/GRB 980425, SN 2003dh/GRB 030329, and SN 2003lw/GRB 031203 would indicate that the parent SN population of GRBs is formed by the bright tail of hypernovae, that is peculiar type-Ib/c SNe which are characterized by high/intermediate luminosity peaks ($M_B \sim -19.5$ to -17) and high expansion velocity of the ejecta (~30,000 km/s). However, there is growing evidence that standard Ib/c SNe or dim hypernovae (like SN 2002ap) can also be connected with GRBs and possibly with X-Ray flashes (Fynbo et al. 2004). Even type IIn SNe cannot be excluded (Garnavich et al. 2003). The possibility that GRBs/XRFs are connected with standard-type Ib/c SNe, and perhaps with some other class of core-collapse SNe, would have dramatic implications for the rate of occurrence of GRBs and their energy budget; **2.** *Which is the relationship between the SN magnitudes at maximum light and the gamma-ray energy budget?* Taking at face values the associations SN 1998bw/GRB 980425, SN 2002lt/GRB 021211, SN 2003dh/GRB 030329, SN 2003lw/ GRB 031203, it looks like bright SNe might be associated to faint GRBs and viceversa; **3.** *Are the "red bumps" always representative of the signatures of incipient SNe?*
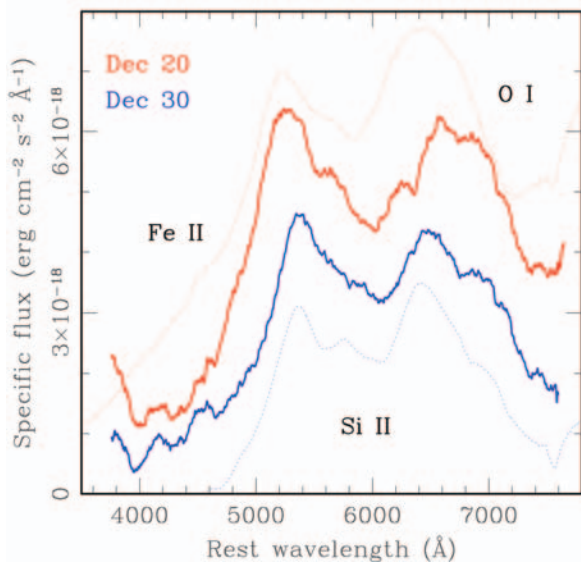
Or can some of them be produced by different phenomena (e.g. echos)? To date, only for GRB 021211/SN 2002lt (Della Valle et al. 2003) has a spectroscopic confirmation been obtained. On the other hand, it is puzzling that Garnavich et al. (2003) and Fynbo et al. (2004) did not find clear SN features in the bumps of GRB 011121 and XRF 030723 respectively; **4.** *Is the lack of an optical bump indicative of the lack of a supernova?* Or rather do GRBs have a heterogeneous class of progenitors including SNe of different magnitudes at maximum and merging between compact objects; **5.** *What causes some small fraction of SNe Ib/c to produce observable GRBs, while the majority do not?*

With an expected rate of discovery of about 1 event/week (observable from Paranal), the *Swift* satellite (Gehrels et al. 2004) will allow the GRB community to obtain in the next 2 to 3 years an accurate spectroscopic classification for dozens of SNe associated with GRBs and to provide conclusive answers to several of the above questions.

REFERENCES

Bloom, J.S., Kulkarni, S.R., Djorgovski, S.G., et al. 1999, Nature, 401, 453
Boella, G., Butler, R.C., Perola, G.C., et al. 1997, A&AS, 122, 299
Colgate, S. 1968, Can. J. Phys., 46, 476
Costa, E., Frontera, F., Heise, J., et al. 1997, Nature, 387, 783
Chincarini, G., Covino, S., Tagliaferri, G., et al. 2004, A&A, submitted
Della Valle, M., Malesani, D., Benetti, S., et al. 2003, A&A, 406, L33
Frail, D.A., Kulkarni S.R., Sari R., et al. 2001, ApJ, 562, L55
Fynbo, J.P.U., Sollerman, J., Hjorth, J., et al. 2004, ApJ, 609, 962
Galama, T.J., Vreeswijk, P.M., van Paradijs, J., et al. 1998, Nature, 395, 670
Garnavich, P.M., Stanek, K.Z., Wyrzykowski, L. et al. 2003, ApJ, 582, 924
Gehrels, N., Chincarini, G., Giommi, P., et al. 2004, ApJ, 611, 1005
Giacconi, R., Gursky, H., Paolini, F., & Rossi, B.B. 1962, PRL, 9, 439
Hjorth, J., Sollerman, J., Moller, P., et al. 2003, Nature, 423, 847
Klebesadel, R.W., Strong, I.B., & Olson, R.A. 1973, ApJ, 182, L85
Kouveliotou, C., Meegan, C.A., Fishman, G.J., et al. 1993, ApJ, 413, L101
Lamb, D.Q. 1995, PASP, 107, 1152
Malesani, D., Tagliaferri, G., Covino, S., et al. 2004, ApJ, 609, L5
Mazzali, P.A. et al. 2002, ApJ, 572, L61
Mereghetti, S., Götz, D., Tiengo, A., et al. 2003, A&A, 411, L29
Paczynski, B. 1995, PASP, 107, 1167
Prochaska, J.X., Bloom, J.S., Chen, H.-W., et al. 2004, ApJ, 611, 200
Stanek K.Z., Matheson T., Garnavich P.M., et al. 2003, ApJ, 591, L17
Tagliaferri, G., Covino, S., Fugazza, D., et al. 2004, IAUC 8308
van Paradijs, J., Groot, P.J., Galama, T., et al. 1997, Nature, 386, 686
Woosley, S. 1993, ApJ, 405, 273

Figure 5: Spectra of SN 2003lw, 3 days before (Dec 20) and 7 days after (Dec 30) its *V*-band maximum light. Dotted lines show the spectra of SN 1998bw taken at similar epochs. From Malesani et al. (2004).

---

[2]From R. Feynman, Six Easy Pieces, Chapter 1.

GRB Afterglows: Illuminating the Star-Forming Universe[1]

Gamma-Ray Burst (GRB) afterglows are distant powerhouses that can be extremely bright. Therefore, they can be used as a tool to study intervening matter along the line of sight, in exactly the same way that quasars have been used for decades, with two important differences: First, GRB afterglows fade away, thereby in time opening up their lines of sight for deep searches for the counterparts of the absorption systems. Secondly, a subclass of GRBs is related to the deaths of massive stars, and hence their afterglows provide sightlines directly into the very cores of star-forming regions, illuminating the line of sight all the way down to their immediate surroundings.

Paul Vreeswijk[1], Palle Møller[1], Cédric Ledoux[1], Sara Ellison[2], Nicola Masetti[3], Johan Fynbo[4], Páll Jakobsson[4] & Jens Hjorth[4]

[1]ESO; [2]U. Victoria, Canada; [3]IASFC Bologna, Italy; [4]U. Copenhagen, Denmark

SEVEN YEARS after the discovery of the first afterglow in 1997, several dozen have been discovered by an active and growing community. The distances, or redshifts, range from $z = 0.0085$ to $z = 4.5$, with a mean redshift of 1.4. The left panel of Fig. 1 shows the redshift distribution until August 2004. Afterglows can be spectacularly bright at early times: the afterglow of GRB 990123 (i.e. the burst that happened on 23rd of January 1999) was detected by the ROTSE robotic telescope at 50s after the burst at 9th magnitude (Akerlof et al. 1999). For a source whose distance was determined to be at $z = 1.6$, this is quite amazing. One comparison to visualise this brightness is the following: if this burst would have happened in the Andromeda galaxy, still some three million light years away, for a short moment it would have been as bright as the full moon. The right panel in Fig. 1 shows the light curve of GRB 990123 and those of all other afterglows whose redshifts have been determined.

Although the afterglow can be extremely bright, it fades away rapidly. Observations of GRBs therefore require fast response and quick decision making, and there is no chance to return to get the "missing observation". After it has faded, there is then plenty of time to explore the clear, undisturbed view of its place of birth. Deep observations performed several months after the GRB have shown that for almost every afterglow a host galaxy is detected at the afterglow position. The host-galaxy magnitudes range from roughly $V = 22$ to $V = 30$. GRB hosts show prominent emission lines, they are sub-luminous, under-massive and blue (e.g.

**Figure 1:** *Top:* Redshift histogram of all GRBs for which the distance could be determined up to August 2004; a total of 36. *Bottom:* The collection of available *R*-band light curves of the GRBs with redshifts. The colour coding of the different redshift bins matches that of the corresponding light curves, showing that the afterglow brightness does not depend very much on the redshift. Back-extrapolation of the late-time afterglows shows that all were probably brighter than 18th magnitude after 10 minutes. With the latest satellite missions such as *Swift* (launched in November 2004), it will become possible to catch a large sample of afterglows at early times, when they are still bright.
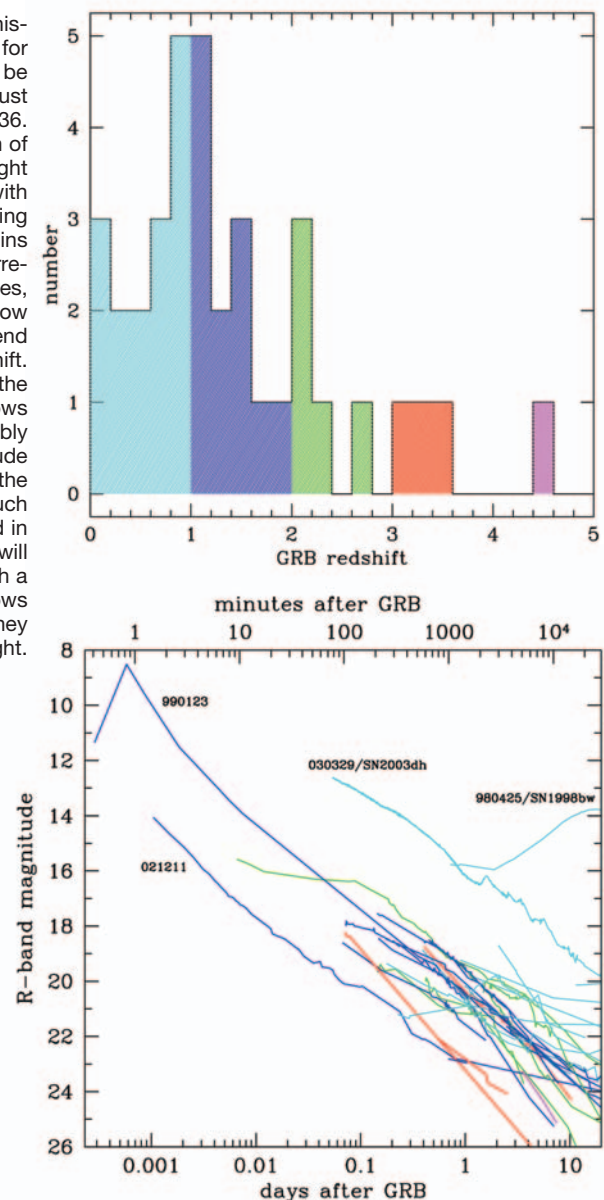
Figure 2: The afterglow (or optical transient - OT) of GRB 020405 and its environment, as imaged in the *R*-band by the VLT. The VLT/FORS1 afterglow spectrum (with the slit shown on the image) contains two absorption systems: one at *z* = 0.691, the redshift of the host galaxy, and a foreground system at *z* = 0.472. Objects "1" and "2" show emisssion lines that are measured to be at the same redshift as the foreground absorber: *z* = 0.472. Therefore, the likely counterpart of the absorption system is object "1", at an impact parameter of about 2″ (12kpc). From Masetti, Palazzi, Pian & GRACE (2003)
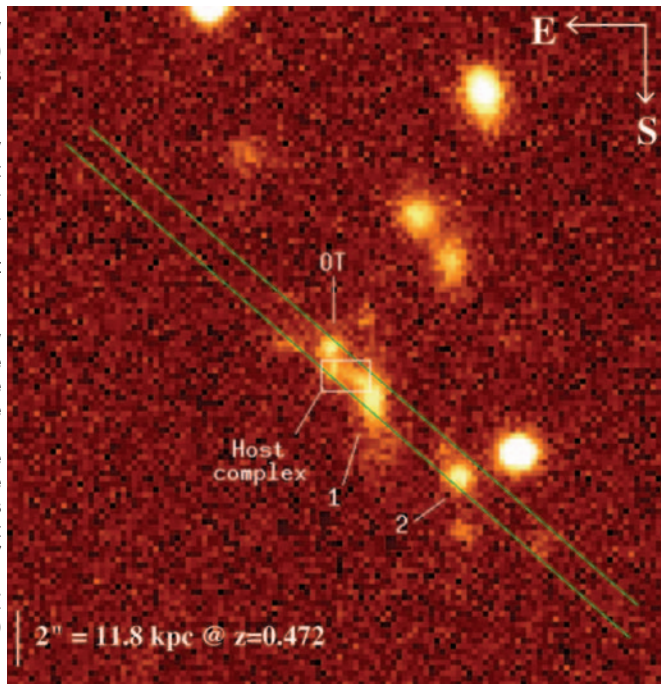
Le Floc'h et al. 2003), and their morphology is sometimes very disturbed. But in a few cases, a very large star-formation rate (hundreds of $M_\odot$ per year) has been inferred from radio and/or sub-mm observations (e.g. Frail et al. 2002). Overall, the emission properties of most GRB host galaxies seem to be very similar to those of a population of young starburst galaxies (Christensen et al. 2004).

Apart from their distance, the most important thing that we have learned from GRB afterglow studies so far, is the following clue to their origin. For at least two GRBs that were relatively nearby (GRB 980425 and GRB 030329 - see the labels in Fig. 1), the GRB afterglow lightcurve and spectrum are very similar to a supernova of type Ic (Galama et al. 1998, Hjorth et al. 2003), i.e. a core-collapse explosion of a massive star at the end of its lifetime, after having shed its hydrogen and helium layers. So apparently, at least some GRBs are produced in a special type of supernova event, and therefore their progenitors are massive stars.

As GRB afterglows are bright and distant, they can be used to perform detailed studies of any matter that is located along the line of sight, which will reveal itself through absorption lines in the spectrum of the afterglow. The systems that can be explored in this way range from the immediate environment of the GRB explosion (e.g. the stellar wind from the massive progenitor star) and the star-forming region in which it exploded, to more distant systems, either inside the host galaxy, or at lower redshift in the inter-galactic medium. Once the afterglow has faded, the absorption properties of

these systems can be complemented with studies in emission, to obtain a more complete picture of the processes governing star formation.

THE COUNTERPARTS OF FORE-GROUND ABSORPTION-LINE SYSTEMS

To use a bright background source to trace matter along the line of sight is a well-known technique in astronomy. The prime analog is that of the study of foreground absorption-line systems along QSO lines of sight (see the Messenger article by Max Pettini, 2003, which includes a very nice illustration of the technique of absorption-line spectroscopy). Through high-resolution spectroscopy of distant QSOs, one can probe inside the absorption systems, and determine detailed characteristics such as the metallicity, dust and H_2 content, and kinematics. Moreover, the physical conditions of the gas, such as density, temperature, and the local UV flux can be measured. Our knowledge of the chemical evolution of the universe has also greatly improved through such QSO absorption-line studies.

Several types of foreground absorbers are distinguished based on their neutral hydrogen (H I) column density. In order of increasing column density: the Ly-α forest, Lyman-limit systems (LLSs) and damped Ly-α absorbers (DLAs). The DLAs, with N(H I) > 2 10^{20} atoms cm^{-2}, have received considerable attention among the absorption-line systems, as they contain most of the neutral gas in the early universe, from which the stars that we see around us today must have formed. Therefore, DLAs play an important role in the study of the global star-formation evolution of the universe.

Detection of the counterparts of these absorption-line systems is extremely interesting, as it allows identification of the type of galaxy in which the absorption takes place, and determination of its internal characteristics. However, the counterpart identification is made very difficult by the glare of the bright QSO, which greatly complicates detection of faint systems close to the line-of-sight. After decades of QSO absorption-line studies, counterparts of only a handful of high-redshift DLAs have been identified. At lower redshifts, the searches have been more successful with the counterparts being brighter: about a dozen *z* < 1 DLA galaxy counterparts have been discovered, with one as close as 1.2″ from the line-of-sight. However, the inner 1″ is practically impossible to probe, so the possibility remains that some counterparts are hiding very close to the QSO sightline.

In order to use GRB afterglows for the same purpose, one has to be extremely quick to obtain a useful high-resolution spectrum (see Fig. 1). With a QSO of constant brightness one can integrate at leisure, obtaining a spectrum with the desired signal-to-noise. However, the transient nature of GRB afterglows harbours an advantage as well: as the afterglow fades away, its line of sight is opened up for deep searches for the counterparts of the absorption-line systems discovered in the spectrum. Although the background host galaxy may still present some contamination, its brightness is negligible compared to that of a QSO. And if needed, it may be separated from the counterparts of the foreground absorbers through the use of narrow-band filters, as outlined in Vreeswijk, Møller & Fynbo (2003), allowing detection of the absorber even when it is located exactly along the line of sight.

The accumulated redshift path covered by GRB afterglows is still fairly small, so it is not surprising that none of the rare foreground DLAs have been detected so far. However, several lower column density metal absorbers (or Lyman limit systems) have been detected, of which a couple of counterparts have been identified: the *z* = 0.47 system along the line of sight toward GRB 020405 (Masetti et al. 2003, see Fig. 2), and the foreground system at *z* = 0.84 toward GRB 030429 (Jakobsson et al. 2004). Both absorbers are located at a small impact parameter (i.e. the projected distance of the absorber to the line of sight at the absorber redshift): 12kpc for galaxy "1" of Fig. 2 in the 020405 sightline, and only 9 kpc (1.2″) for the 030429 foreground absorber. This is lower than the typical range of impact parameters measured for metal absorbers at similar redshifts along QSO lines of sight. For example, Guillemin & Bergeron (1997) find an impact parameter range of 2–23″ (12–127 kpc), for a few dozen Mg II counterparts at 0.15 < *z* < 1.3.

A possible explanation for this difference is exemplified in Fig. 2. If the absorbing galaxies are members of pairs or groups, then a companion to a QSO absorber further away from the line-of-sight is much easier to identify than the absorber itself. In the case of GRB 020405, the two objects "1" and "2" have the same redshift as that of the absorption system. Hence, object "1", at a impact parameter of about 2″ (12kpc) is the probable counterpart of the absorption system. Note that even if "1" would have been on top of the afterglow, its redshift would still have been obtained. Placing a bright quasar at the position of the GRB afterglow (marked "OT" in Fig. 2) would render "1" very difficult to detect, and could result in the obvious identification of "2" (at 6″, or 36 kpc) as the absorber, i.e. as a small galaxy with an extended halo of absorbing gas. The implication is that some of the counterparts of absorbers toward QSOs may have been misidentified. Rapid spectroscopic follow-up observations of GRBs and later studies of their host sightlines will uniquely resolve this question.

MASSIVE STAR-FORMING REGIONS INSIDE THE HOST GALAXY

As GRB afterglows are caused by the deaths of massive stars, they lead us directly to regions of massive-star formation. Star formation is an important ingredient in our understanding of galaxy evolution, and has therefore been extensively studied, mostly through emission properties of star forming regions in the ultra-violet, optical, infra-red, sub-mm and radio wavelengths. GRB afterglow spectroscopy will now in addition allow measurements of the internal proporties of star-forming regions, in the same way as for the foreground absorbers. The combination of both absorption and emission properties will provide additional insight in the understanding of the process of star formation.

Our study of the afterglow of GRB 030323 is a nice example of what can be done with GRB afterglows. VLT/FORS2 spectroscopy of the GRB 030323 afterglow (see Fig. 3), obtained by the GRACE collaboration, show several interesting properties of the host galaxy, even though the resolution of the spectrum is fairly low. First, a heavily damped Ly-α line (shown in green in the figure) is detected at the redshift of the GRB: z=3.37. The redshift of the GRB cannot be higher, as in that case Ly-α forest lines (shown in blue) would also be visible to the right of the Ly-α line, which is not the case. A fit to the DLA line (see the figure inset) implies a neutral hydrogen (HI) column density of log N(H I)=21.90±0.07. The H I column density of the z=3.37 DLA in GRB 030323 is larger than that of any intervening DLA observed along a QSO line of sight. In fact, several other GRB afterglows have shown evidence for a DLA at the GRB redshift (all of which have been discovered by the GRACE collaboration). All the GRBs for which the neutral hydrogen column could be measured (7 so far) are shown in Fig. 4. Most of the GRB absorbers have very high values for the H I column compared to the QSO distribution, but two are below the DLA definition. The sample is still too small to allow any firm conclusions, but it does show that there is a wide spread in the GRB
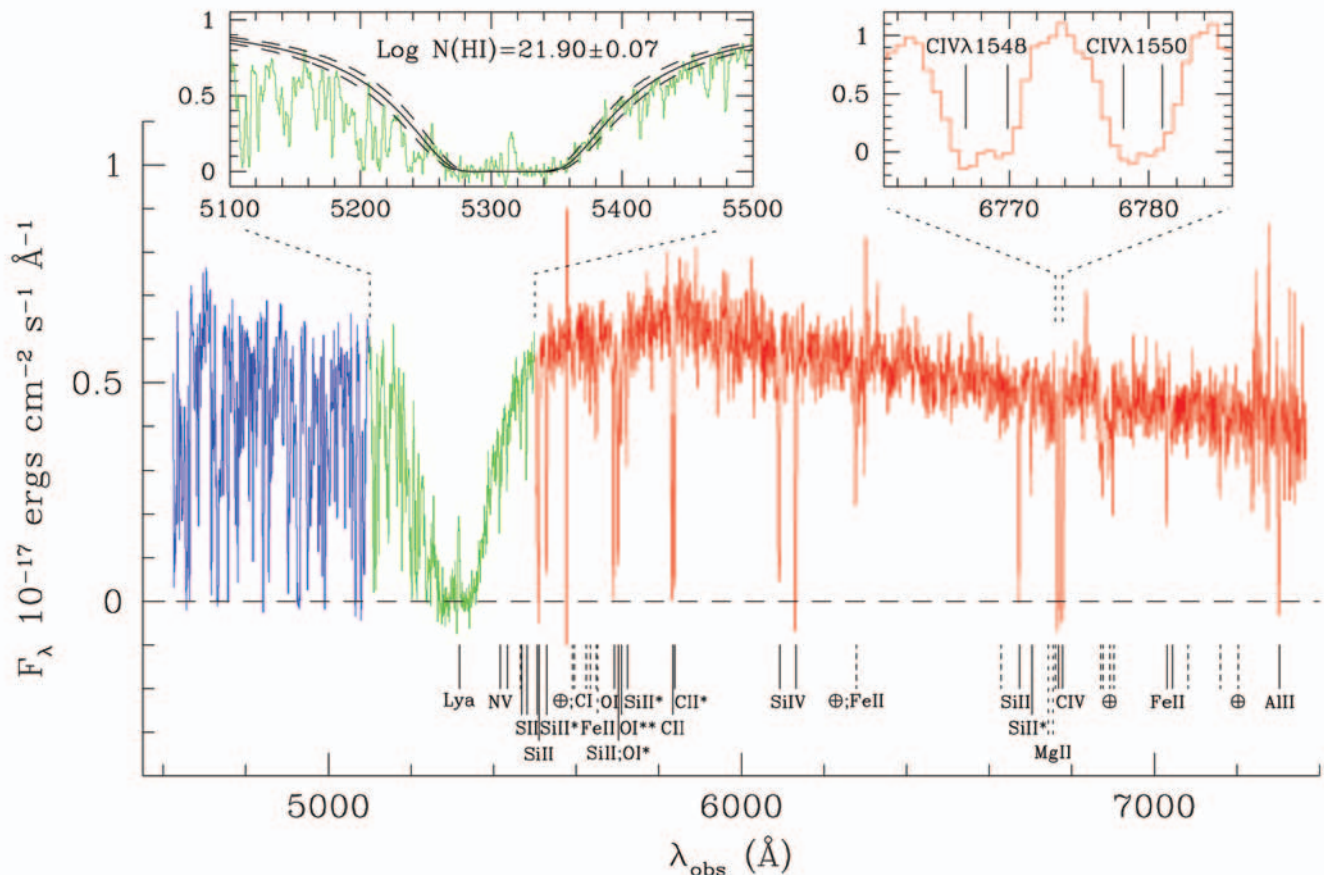

Figure 3: This VLT/FORS2 spectrum of the afterglow of GRB 030323 shows the imprint on the afterglow flux of numerous metal-absorption features in the red part, a strong damped Ly-α line (green), and the Ly-α forest (blue). The metal lines and the DLA are both caused by absorption in the interstellar medium of the GRB host galaxy, at z = 3.37. From a fit to the damping wings of Ly-α (see the inset) we measure a neutral hydrogen (H I) column density of log N(H I) = 21.9. As can be seen in Fig. 4, this column is larger than seen in any QSO-DLA. In the Ly-α trough, we also detect Ly-α in emission, which corresponds to a host-galaxy star-formation rate of about 1 M$_\odot$ per year. Interestingly, fine-structure lines of Si II (indicated with the ∗) are also detected, which have never been clearly seen in QSO-DLAs. This could imply that these lines are produced very close to the site of the GRB explosion. From Vreeswijk, Ellison, Ledoux & GRACE (2004)
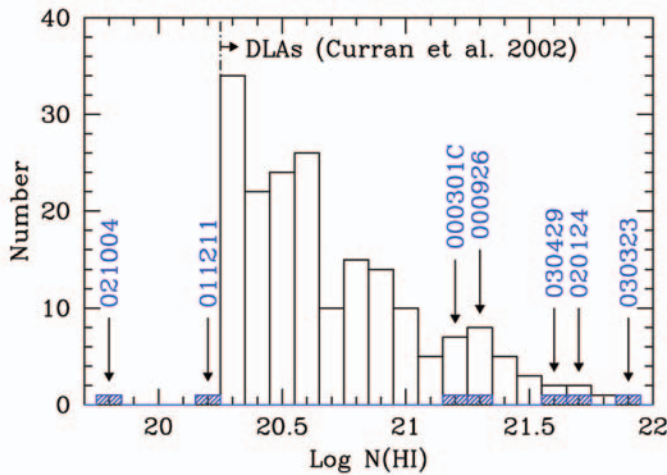
Figure 4: Histogram of the column densities of DLA systems measured through the damping wings of Ly-α discovered in the spectrum of a background QSO (compilation taken from Curran et al. 2002). The blue histogram shows measurements in GRBs for which the redshift was large enough to detect Ly-α. Out of 7 GRBs, 5 show neutral hydrogen column densities above the DLA definition of $2\ 10^{20}$ atoms cm^{-2} (log N(H I)=20.3). The host of GRB 030323 contains a column density larger than in any observed (GRB- or QSO-) DLA system. From Vreeswijk, Ellison, Ledoux & GRACE (2004)
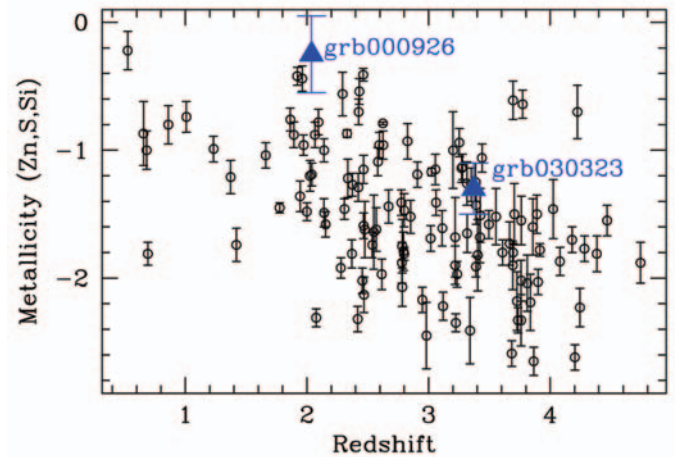
Figure 5: Comparison of the metallicities of a sample of QSO-DLAs (open circles) with the two GRBs for which a metallicity has been determined (solid triangles): GRBs 000926 and 030323 (this paper). The two GRB hosts are located at the metal-rich end of the QSO-DLA distribution. From Vreeswijk, Ellison, Ledoux & GRACE (2004)

H I column density distribution. It will be interesting to see how this plot will develop as the sample of GRB afterglow H I measurements increases, as it will tell us about the distribution of H I gas in high-redshift galaxies and their star-forming regions.

Several metal-absorption lines are detected redward of Ly-α (shown in red in Fig. 3). Even though most are saturated, we are able to obtain the abundance of iron and sulphur with respect to hydrogen: [Fe/H]=–1.5 and [S/H]=–1.3, where [X/H]=log (X/H)–log (X/H)$_\odot$, with X and H denoting the element and hydrogen abundance, respectively. So far metallicities have been determined this way for only two GRB afterglows: GRBs 030323 and 000926. Both are shown in Fig. 5, and are again compared to a sample of intervening QSO-DLAs. The GRB values seem to end up in the upper regime of the QSO-DLA metallicity distribution, but the sample is still very small. Higher values for GRB-DLAs is what one would expect, as GRBs probe star-forming regions, where the metallicity should be larger than along random sight lines through foreground galaxies, as probed by the QSOs.

Possibly the most surprising fact in the spectrum of 030323, is the discovery of fine-structure lines of singly-ionised Silicon: Si II*. These lines have never been clearly detected in QSO-DLAs, which suggests that either the lines have an origin related to the GRB, or it could be due to the very high column density observed. The population of fine-structure levels can be caused by collisions between several particles in the interstellar medium, direct photo-excitation by infra-red photons, or fluorescence, and thus depends either on the density of the absorb-

ing medium or the ambient photon-flux intensity. If we assume that the Si II* levels in the case of 030323 are caused by collisions (and neglecting direct excitation), we estimate that the volume density is 100-10,000 cm^{-3}, which is much higher than the density inferred for QSO-DLAs. Combined with the column density, we can then estimate the size of the Si II* absorption region to be 0.5–50pc. However, the population of these levels may well have been caused by the ionising radiation from the GRB afterglow. A larger sample of GRB spectra, taken at different epochs, will be able to discriminate between these two possibilities, and constrain either the volume density, or the strength of the ionising GRB flux in the surroundings of the GRB.

Only the lucky combination of a GRB occuring in this galaxy, and our ability to rapidly follow it up via the very efficient ESO ToO (Target-of-Opportunity) programme of GRACE, which is superbly supported by the Paranal and La Silla observatories, allowed us to study it in detail. Figure 6 shows a Hubble Space Telescope (HST) image of the field of the host, which is measured to be around $V = 28$. With conventional techniques one would have very little to say about this galaxy: basically its Ly-α star-formation rate and its color, nothing more. This shows the enormous power of GRB afterglows as a tool to study high-redshift star-forming galaxies.

Stellar wind from the GRB progenitor

Absorption systems along QSO lines of sight can roughly be divided into three different types according to their origin:

Intervening systems (unrelated to the QSO), local systems (in the environment surrounding the QSO host galaxy or galaxy cluster), and intrinsic systems (created close to the central engine of the QSO). The GRB analogy to QSOs would then suggest that maybe there could also be spectroscopic signatures of the third kind in GRB spectra. Such signatures of the progenitor itself could then provide detailed information on events prior to the actual burst of gamma rays. If, for example, the progenitor would have been in active wind phases at earlier times, then those winds could still be present as expanding shells at the time when the spectrum was obtained, and would tell us of the past history of the star leading up to its collapse.

In the low resolution spectrum of GRB 021004 obtained with the Nordic Optical Telescope (NOT) on La Palma (Møller et al. 2002), spectral signatures were seen which in a very curious way resembled intrinsic absorption systems seen in QSO spectra. One particular resemblance was the fact that some of the absorbers had relative velocities which exactly shifted one line of the strongly absorbing CIV-doublet into the other line of the same doublet. This is known as "line-locking" and had until then only been observed in quasar spectra. The line-locking phenomenon is thought to arise from radiative acceleration of a wind. This observation therefore strongly supports the suggestion that progenitor winds may indeed be part of the "family" of GRB absorption systems. The same GRB was observed with the VLT using the UVES spectrograph and at the much higher resolution of UVES the GRB 021004 spectrum is a veritable treasure-trove of information revealing a whole series
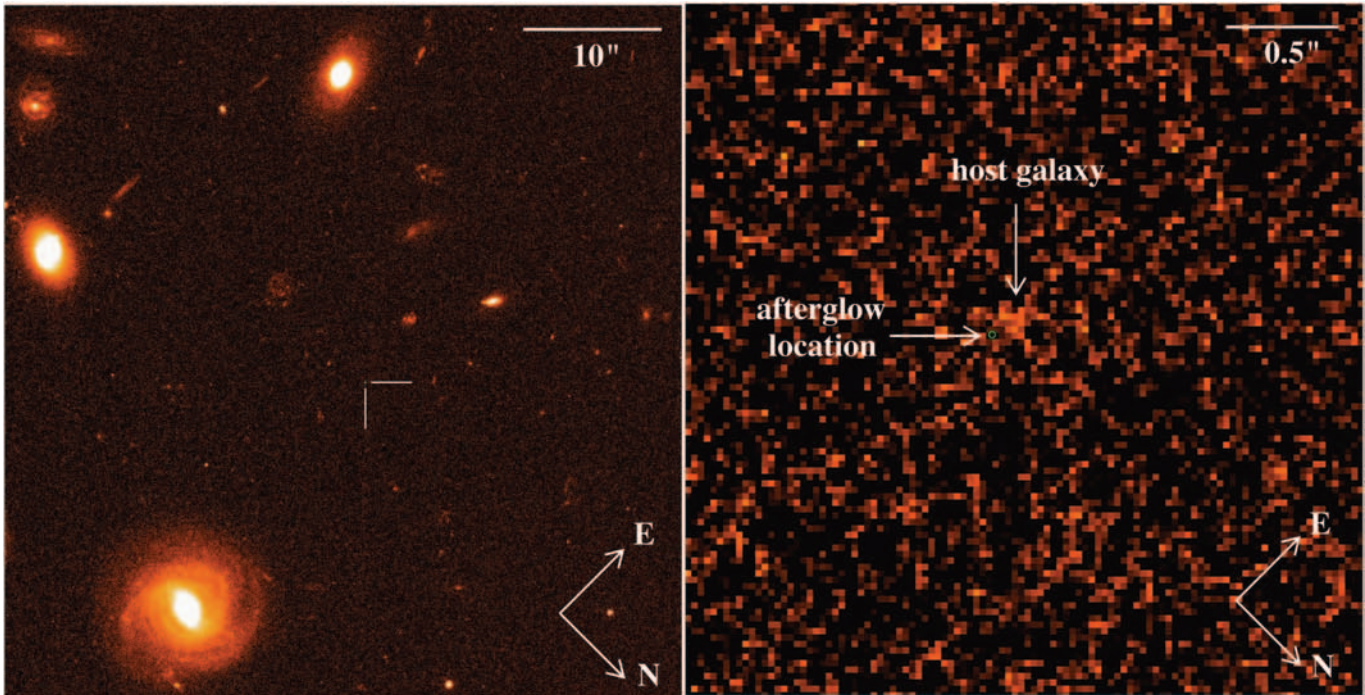
Figure 6: HST imaging in the F606W filter of the field of GRB 030323, obtained by the GOSH collaboration. On the left panel the 50″×50″ field surrounding the burst is shown, whose location is indicated by the cross hair. The right panel zooms in on the central region, where the green circle indicates the position of the early afterglow. The object next to it, with a magnitude of roughly $V = 28$, is the probable host galaxy of GRB 030323. From Vreeswijk, Ellison, Ledoux & GRACE (2004)

of absorption systems displaying ejection velocities from zero to more than 3,000 km/s (Castro-Tirado et al. 2004).

THE BRIGHT FUTURE OF GRB AFTERGLOWS

The future of GRB afterglows literally looks bright. Figure 1 shows that in time the afterglow brightness fades very rapidly, and that most afterglows to date have been discovered around 20th magnitude. This is because, so far, the discovering satellite missions such as *BeppoSAX*, had a delay of at least a couple of hours between detection of the burst, and determination of the GRB error box. So the afterglows are usually faint at discovery, and before a spectrum can be taken, another couple of magnitudes are lost. For example, the spectra of GRB 030323, discussed in the previous section, were taken when the afterglow had a visual magnitude of about 21.5. At that magnitude, high-resolution spectroscopy is impossible, but this will change in the near future.

The *Swift* satellite, successfully launched on November 20, 2004, is expected to cause yet another revolution in the field of GRB afterglows. It is designed to chase roughly 100 bursts per year. For each GRB it will determine a 4′ radius error circle from the gamma-ray emission with its *Burst Alert Telescope* (BAT) after 20s, a 5″ accuracy with its X-ray Telescope (XRT) after 70s, and an optical sub-arcsecond localisation with its UV/Optical Telescope (UVOT) will be distributed after 4 minutes.

This will allow extremely rapid follow-up observations from the ground, and telescopes of all sizes will play a role.

Many robotic telescope projects have popped up over the past several years, to chase GRB afterglows at very early times. Several clones of the successful ROTSE telescope, which detected the 9th magnitude flash of the afterglow of GRB 990123, have been spread around the world. At ESO's La Silla, both REM (Chincarini et al. 2003) and TAROT (Boer et al. 2003) are ready to chase Swift triggers in both the optical and near-infrared. The imaging data taken by this suite of robots will be unprecedented, and important to constrain the early light-curve evolution of GRB afterglows, of which very little is known at the moment.

However, for the science that we have been discussing in this article, what one would like is a world-class high-resolution spectrograph such as UVES at the VLT, to observe the afterglow only a few minutes after the GRB. For this to be possible, an ESO working group recommended implementation of the so-called Rapid-Response Mode (RRM) at the VLT, allowing semi-automatic observations. This mode has been installed for UVES at UT2 starting from Period 73, and will also be available for the FORSes and ISAAC from Period 74 onward. The typical delay time of the VLT with RRM will be around 5–10 minutes, and one can see from Fig. 1 that a large fraction of the afterglows will be brighter than 18th magnitude. Therefore, the powerful combination of VLT, UVES and RRM will allow

high-quality spectroscopy of GRB afterglows of a large sample of Swift bursts, which will provide unique clues to the nature of foreground absorption systems and the process of star formation in high-redshift galaxies.

REFERENCES

Akerlof, Balsano, Barthelmy et al. 1999, Nature, 398, 400

Boër, Klotz, Atteia et al. 2003, ESO Messenger, 113, 45

Castro-Tirado, Møller, García-Segura & GRACE 2004, Science, submitted

Chincarini, Zerbi, Antonelli et al. 2003, ESO Messenger, 113, 40

Christensen, Hjorth & Gorosabel 2004, A&A, 425, 913, astro-ph/0407066

Curran, Webb, Murphy et al. 2002, PASA, 19, 455

Frail, Bertoldi, Moriarty-Schieven et al. 2002, ApJ, 565, 829

Galama, Vreeswijk, van Paradijs et al. 1998, Nature, 395, 670

Guillemin & Bergeron 1997, A&A, 328, 499

Jakobsson, Hjorth, Fynbo et al. 2004, A&A, 427, 785, astro-ph/0407439

Hjorth, Sollerman, Møller & GRACE 2003, Nature, 423, 847

Kaper, Castro-Tirado, Fruchter & GRACE 2002, ESO Messenger 109

Le Floc'h, Duc, Mirabel et al. 2003, A&A, 400, 499

Masetti, Palazzi, Pian & GRACE 2003, A&A, 404, 465

Møller, Fynbo, Hjorth et al. 2002, A&A, 396, L21

Pettini 2003, ESO Messenger, 111, 13

Vreeswijk, Møller & Fynbo 2003, A&A, 409, L5

Vreeswijk, Ellison, Ledoux & GRACE, 2004, A&A, 419, 972

THE LARGE PROGRAMME "COSMIC EVOLUTION OF THE IGM"

Metal enrichment, clustering properties and main heating process of the intergalactic medium can be probed by analyzing the numerous Lyman "forest" lines in the spectra of distant quasars and their associated, absorption metal lines. Constraints can then be placed on the scenarii of structure formation, the origin of metals and how they have been expelled in the intergalactic medium, and the spectral shape of the metagalactic UV flux.

J. Bergeron[1], P. Petitjean[1,2],
B. Aracil[3], C. Pichon[1],
E. Scannapieco[4], R. Srianand[5],
P. Boissé[1], R. F. Carswell[6],
H. Chand[5], S. Cristiani[7],
A. Ferrara[8], M. Haehnelt[6],
A. Hughes[1], T.-S. Kim[6],
C. Ledoux[9], P. Richter[10],
M. Viel[6]

[1]Institut d'Astrophysique de Paris, France
[2]LERMA, Observatoire de Paris, France
[3]Department of Astronomy, University of Massachusetts, USA
[4]Kavli Institute for Theoretical Physics, UC Santa Barbara, USA
[5]IUCAA, Pune, India
[6]Institute of Astronomy, Cambridge, UK
[7]INAF-Osservatorio Astronomico di Trieste, Italy
[8]SISSA/International School for Advanced Studies, Trieste, Italy
[9]European Southern Observatory
[10]Institut für Astrophysik und Extraterrestrische Forschung, Universität Bonn, Germany

THE HISTORY OF THE UNIVERSE in its formative stages is recorded in the ubiquitous intergalactic medium (IGM), which contains almost all of the residual baryonic material from the Big Bang. During the epoch of structure formation, the IGM became highly inhomogeneous and acquired peculiar motions under the influence of gravity. It was the source of gas that accreted, and then cooled to form stars, and was also the sink for the metal-enriched gas and radiation produced by the population of primordial objects. Absorption lines in quasar spectra thus trace not only the chemical composition of the IGM, but also the density fluctuations in the early Universe and the background UV flux.

The IGM is revealed through numerous H I absorption lines in the spectra of remote quasars, the so-called Lyman-α forest. Numerical simulations and analytical modelling of a warm (~10^4 K) photoionised IGM within a cosmological context successfully reproduce many observational properties of the Lyman-α forest: the column density distribution, the Doppler parameter distribution, the flux decrement distribution and the redshift evolution of absorption lines above a certain column density threshold. Numerical hydro-simulations of CDM-based hierarchical structure formation have led to a new view of the IGM. In these models, structures arise from the action of gravity on density perturbations and the Lyman-α forest closely traces the density enhanced structures with geometrical shapes changing from sheets and filaments to more spherical halos as the column density increases.

The simulations have further demonstrated that the fluctuations of the neutral gas density responsible for the Lyman-α absorption trace the fluctuations in the underlying dark matter density field very well on scales larger than the Jeans length of the gas. In this paradigm, at $z \sim 2.5$ most of the baryons are located in somewhat overdense filaments and sheets, producing absorption in the column density range $10^{13.5} < N(H\ I) < 10^{15}$ cm^{-2}. However, most of the volume is occupied by underdense regions with typical column densities $N(H\ I) < 10^{13}$ cm^{-2}.

Concurrent with the progress in theoretical simulations, observations reveal that metal absorption features are associated with a considerable fraction of the high column density Lyman-α absorbers. The process responsible for the enrichment of the IGM is still only partially understood.

Considerable effort has been devoted to detect metal species associated with low column density Lyman-α systems, since the presence of metals in the underdense regions of the IGM is a distinguishing test between proposed pollution mechanisms.

THE DATA

The ESO Large Programme (LP) "Cosmological Evolution of the IGM" (PI J. Bergeron) has been devised to gather a homogeneous sample of echelle spectra of 21 QSOs, of which 19 are at $z_Q < 4.0$, with a uniform spectral coverage, resolution and signal-to-noise ratio suitable for studying the IGM in the redshift range 1.7–4.5. The data were obtained with the Ultra-violet and Visible Echelle Spectrograph (UVES) mounted on the ESO KUEYEN 8.2 m telescope at the Paranal observatory. Spectra were obtained in service mode observations spread over two years, for
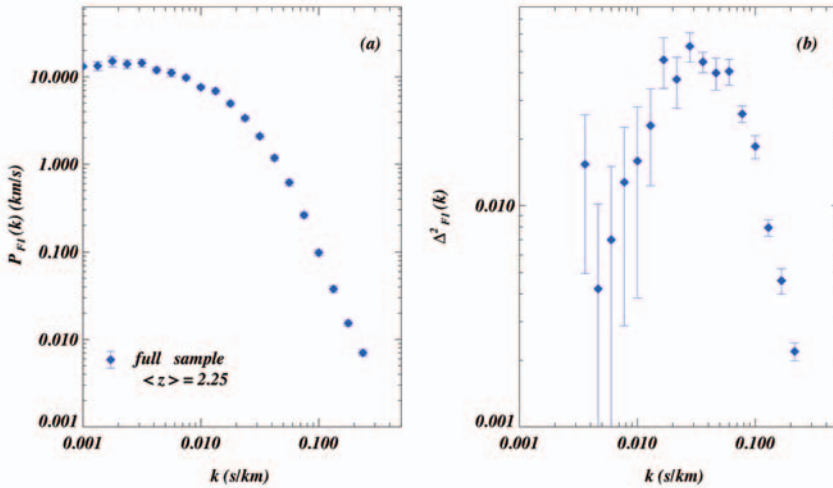
Figure 1: The 1D and 3D flux power spectrum in the Lyman-α forest.

a total of 334 h under good seeing conditions (≤ 0.8 arcsec).

The data were reduced using a version of the ESO-UVES pipeline upgraded by B. Aracil to solve problems specific to quasar spectra when the object continuum level is low (typically in the Lyman-α forest around strong absorption lines): 1) incorrect extraction of the object spectrum resulting in a lower signal-to-noise ratio than that measured on the 2D spectrum or even non-recognition of the position of the object in a given order, 2) error up to 5% on the intensity zero level, 3) non-recognition of some orders in the red, 4) strong residuals from weak sky emission lines/absorption bands in the UV after sky subtraction, 5) possibly, too large additional noise from the subtraction of the inter-order background when the object continuum is close to zero (e.g. damped Lyman lines).

With this upgraded version of the UVES data reduction pipeline, the final accuracy of the sky-background subtraction is better than 1%. Addition of individual exposures was performed using a sliding window and weighting the signal by the total errors in each pixel.

The wavelength calibration was carefully checked using the calibration lamp and it is better than $\delta\lambda/\lambda \sim 7\times10^{-7}$ rms over the full wavelength range of interest, 305–540 and 545–1000 nm. As an example of the quality of the wavelength calibration, we have found that we could obtain from the LP data better rest-wavelengths of the C IV doublet as compared to the laboratory wavelengths (Petitjean & Aracil, 2004). More details on the data redution can be found in Chand et al. (2004a) and Aracil et al. (in preparation). Signal-to-noise ratios of ~ 40 to 80 per pixel and spectral resolutions ≥ 45,000 are achieved over the wavelength range of interest.

The data analysis (identification of metal absorption lines and profile fitting) has been automated as far as possible to be able to perform the same procedures to the observed data as to simulated data constructed from *N*-body cosmological simulations.

PROBING THE MATTER DISTRIBUTION

The distribution of neutral hydrogen traces the underlying matter distribution sufficiently well that interesting constraints on the dark matter power spectrum can be obtained from the Lyman-α forest. Kim et al. (2004) have measured the power spectrum of the flux distribution in the Lyman-α forest of an augmented version of the UVES LP sample (Fig. 1).

Viel et al. (2004a) have used this flux power spectrum together with a large suite of hydrodynamical simulations to determine the dark matter power spectrum at scales of 2–20 (comoving) Mpc – a range of scales currently only probed by the Lyman-α forest. Together with constraints on large scales from CMB data important information on the power spectrum of initial density fluctu-

ations imprinted during the inflationary phase of the Early Universe can be obtained. The WMAP team has performed such an analysis and has found that the power spectrum of initial density fluctuations deviates from the canonical $n_s = 1$ power law and that a "running" of the spectral index is required. Based on the results of Kim et al. (2004), Viel et al. (2004a, 2004b) have refuted this claim and have shown that the joint analysis of the Lyman-α forest and CMB data gives results which are consistent with a Harrison-Zeldovich ($n_s = 1$) spectrum of initial density fluctuations with no evidence for a running of the spectral index as shown in Fig. 2.

METALS IN THE IGM

It is believed that the gas in the IGM traces the spatial structure of the dark matter, its overdense filaments as well as underdense voids. In the course of cosmic evolution, this gas was most likely enriched by winds flowing out from star-forming regions located preferentially in the center of massive halos. It is therefore not surprising that C IV absorption is observed to be associated with most of the strong H I lines with $N(H\ I) > 10^{14.5}$ cm^{-2}, as these lines likely trace filaments in which the massive halos are embedded. A crucial question is whether the gas filling the underdense space delineated by these filaments (the so-called voids) also contains metals. Indeed, it is improbable that winds from star-forming regions located in the filaments can pollute the voids. Therefore, if metals are found in this gas, they must have been produced by objects more or less uniformly spatially distributed, perhaps in the very early universe (z ~ 15–20).

The absorptions arising in the voids are mostly of low-column densities (typically of the order or less than $N(H\ I) = 10^{13}$ cm^{-2}). Given the low typical metallicities ([C/H] < –2.5, or 1/300 solar), direct detection of metals at such low neutral hydrogen optical depths is impossible and statistical methods must be used instead. Lu et al. (1998) used the stacking method to increase the signal-to-noise ratio and did not find any evidence
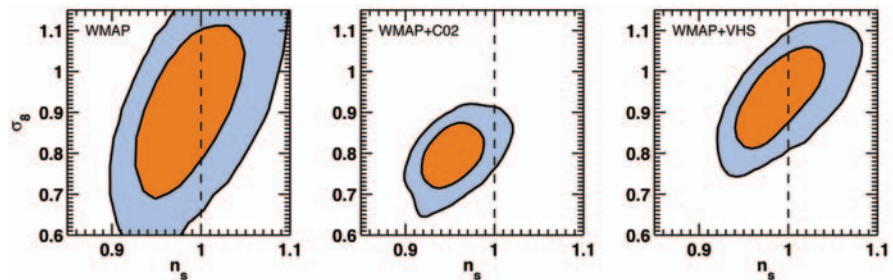

Figure 2: 1- and 2-σ likelihoods for the *rms* matter density fluctuation amplitude σ_8 and the spectral index of primordial density fluctuations n_s. The left panel shows the constraints from WMAP only. The middle panel is for a combined analysis of WMAP data and high resolution Lyman-α forest data with an effective optical depth as assumed by the WMAP team. The right panel is for a combined analysis of WMAP data and high resolution Lyman-α forest data with a Lyman-α effective optical depth suggested by high S/N, high-resolution data.

Figure 3: C IV (top panel) and O VI (bottom panel) optical depth versus H I optical depth for z < 2.4 (filled circles and solid line) and z > 2.4 (triangles and dashed line).
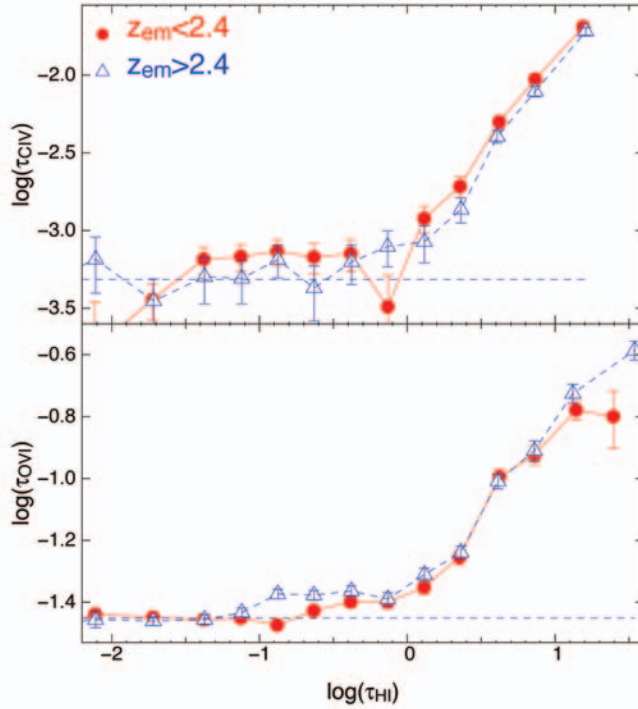
for metals in the range $10^{13} < N(\text{H I}) < 10^{14}$ cm^{-2}. Although uncertainties in the position of the lines can lead to underestimate the absorption, they concluded that metallicity is smaller than 10^{-3} solar in this gas. Cowie & Songaila (1998) calculated the C IV optical depth corresponding to each pixel of the Lyman-α forest (see Aguirre et al. 2002 for an extensive discussion of the method). They showed that the mean C IV optical depth correlates with τ_{HI} for $\tau_{\text{HI}} > 1$.

We have applied a slightly modified version of the method introduced by Cowie & Songaila (1998) to the very high quality data of the LP (Aracil et al., 2004). We find that the gas is enriched in carbon and oxygen for neutral hydrogen optical depths $\tau_{\text{HI}} > 1$ but, contrary to previous claims, there is no indication that C IV absorption is statistically associated with gas of $\tau_{\text{HI}} < 1$ (see Fig. 3). In addition, our observations strongly suggest that the C IV/H I ratio decreases with decreasing τ_{HI} with $\log \tau_{\text{CIV}} = 1.3 \log \tau_{\text{HI}} - 3.2$, which leads to $\log (\text{C IV/H I}) < -3.3$ for $\tau_{\text{HI}} < 1$. However, we observe that a small fraction of the low density gas is associated

with strong metal lines as a probable consequence of the IGM enrichment being highly inhomogeneous.

We detect the presence of O VI down to $\tau_{\text{HI}} \sim 0.2$, and the correlation between τ_{OVI} and τ_{HI} is consistent with a constant ratio $\log(\text{O VI/H I}) \sim -2.0$ (Aracil et al., 2004). We show that O VI absorption in the lowest density gas, $0.2 < \tau_{\text{HI}} < 1$, is located within ~ 300 km/s from strong H I lines (see Fig. 4). This suggests that this O VI phase may be part of winds flowing away from overdense regions. There is no O VI absorption, at $\tau_{\text{HI}} < 1$, associated with gas located at velocities larger than ~ 300 km/s away from strong absorption lines. Therefore, at the limit of present surveys, the presence of metals in the underdense regions of the IGM, is still to be demonstrated.

CLUSTERING OF INTERGALACTIC METALS

A second approach constraining the enrichment history of the IGM is to study the spatial clustering of metals. The main sample used comprises 643 C IV components with $N \geq 10^{12}$ cm^{-2} detected over 19 ($z_Q < 4.0$) LP sightlines. This sample was first used to derive the C IV column density distribution function $f(N)$ for two redshift bins, 1.5–2.3 and 2.3–3.1 (Pichon et al., 2003). This distribution does not evolve with redshift, as found by previous studies and is consistent with a power-law of the form $f(N) \propto N^{-1.8}$.

We then computed the C IV line-of-sight two-point correlation function in redshift space, using a sample based on 580 components with $N \geq 10^{12}$ cm^{-2} (Scannapieco et al., in preparation). This number differs slightly

Figure 4: Median O VI optical depth versus median H I optical depth for pixels located at less than 500 km/s (upper dashed curve) or less than 300 km/s (upper dotted curve) from strong absorptions ($\tau_{\text{HI}} > 4$) and for pixels located at more than 500 km/s (lower dashed curve) or more than 300 km/s (lower dotted curve) from strong absorptions.
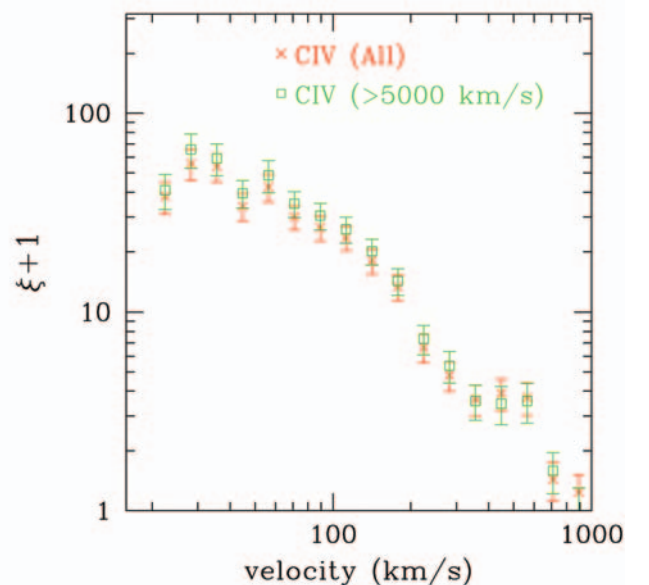

Figure 5: C IV correlation function for the whole sample (crosses) and excluding systems with velocity differences smaller than 5000 km/s compared to the QSO emission redshift (squares).
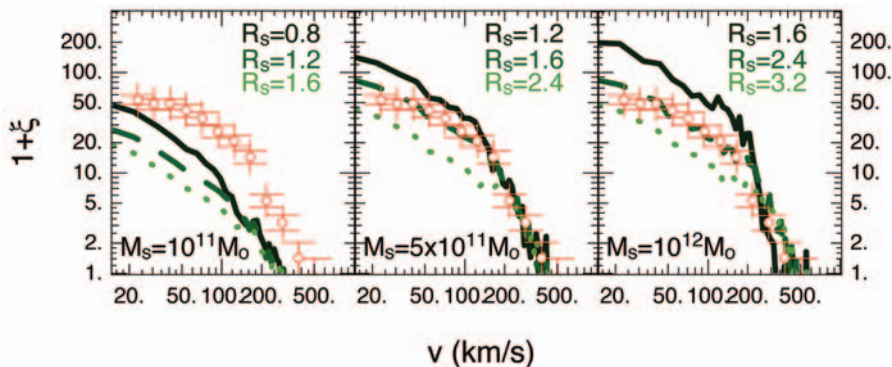
Figure 6: Comparison between detected C IV correlation functions (points) and simulated correlations (lines). In each panel the total mass M_s is fixed and the radius R_s (Mpc) is varied over three representative values.

from that mentioned above due to further refinements in the detection procedure. It should be noted that, as pixel methods are not suited to studying clustering, this analysis can only be carried out on the $\tau_{CIV} \geq 0.05$ components that can be well detected by Voit-profile fitting. The results are shown in Fig. 5: the features present in this correlation function are independent of optical depth and illustrate three important aspects of enrichment uncovered by our measurements.

At small velocity separations, $v \leq 100$ km/s, the correlation function is relatively flat, suggesting that metals are contained primarily within ~1 comoving Mpc h^{-1} from the sources, and within potential wells with velocity dispersions ~100 km/s.

At larger velocity separations, the C IV correlation function is steep and similar in shape and amplitude to that of the brightest Lyman-break galaxies. This is a clear indication of enrichment from overdense sources: either massive galaxies at late times, or dwarf galaxies at high redshifts. Finally, at the largest separations ($400 < v < 600$ km/s) there is a plateau in the correlation function possibly caused by the internal velocity dispersion between C IV systems in forming groups and clusters at z ~ 2.5.

The two-slope shape of the C IV correlation function is suggestive of a picture in which metal bubbles of a typical size (associated with the small scale clustering) are generated about objects of a typical mass (whose geometrical bias is associated with the large-scale clustering). In order to explore this connection further, we generated a simple model, based on a dark-matter-only simulation (Pichon et al., 2003).

We found that the measured correlation function is consistent with a picture where, at z = 3, metals are confined within bubbles of R_s ~ 2 Mpc about halos of total mass M_s ~5 10^{11} $M_\odot$ (see Fig. 6). This implies that the filling factor of the metals is only ~10% at the detection limit of the survey.

INTERGALACTIC O VI

The recent searches for O VI individual absorbers aim at probing low-density regions of the IGM with gas overdensities of $\rho/\bar{\rho} < 10$, where $\bar{\rho}$ is the cosmic mean density. These tenuous regions of the IGM are photoionized by the metagalactic UV flux and their ionization level should be higher than those of the regions usually traced solely by C IV. The goals are to derive the ionization level, metallicity and gas density of the IGM O VI phase, constrain the spectral shape of the UV ionizing flux, and estimate the contribution of the high ionization phase to the baryon cosmic density Ω_b.

The O VI $\lambda\lambda1031.9,1037.6$ doublet is more difficult to detect than that of C IV due to severe contamination by the Lyman forest lines. This leads to a reduction of the usable redshift path by at least a factor of two already at z ~ 2.3. Unambiguous detections can be made for column densities $N(\text{O VI}) \geq 1.5 \ 10^{13}$ cm^{-2}, or $\tau_{OVI} \geq 0.3$ for a Doppler parameter $b = 10$ km/s.

The heating source of the O VI absorbers can be constrained by their O VI line widths. For Doppler parameters $b(\text{O VI}) < 10$ [14] km/s, the derived temperatures are $T < 1$ [2] 10^5 K. In the assumption of shock heating, this leads to very small O VI ionic ratios, O VI/O $< 6 \ 10^{-8}$ [2 10^{-2}] (Sutherland & Dopita, 1993), and consequently super-solar metallicities (Bergeron et al., 2002). Among the absorbers of

low $N(\text{H I})$ ($< 10^{15}$ cm^{-2}), there are many clear cases of O VI lines with $b < 10$ km/s, thus photoionized gas (Bergeron et al., 2002; Carswell et al., 2002). An example with $b(\text{O VI}) = 9.5$ km/s is shown in Fig. 7. The distribution of the O VI Doppler parameter is presented in Fig. 8 for the currently analyzed O VI sub-sample. About half of the systems have $b < 14$ km/s which implies that radiative ionization is then the dominant process. Among the remaining systems, most are weak, thus possibly blends of narrower lines, but there are also systems with large $N(\text{H I})$. For the latter, the possibility of shock heating was suggested by Simcoe et al. (2002) and this remains an open issue.

For a given ionizing background flux, the O VI/N V/C IV ionic ratios (including limits) can be used to estimate the ionization parameter, thus the gas density and pathlength of the absorbers, and the metal abundances, thus constraining the [O/C] abundance ratio. We find that the observed ionic ratios are best reproduced by a hard ionizing
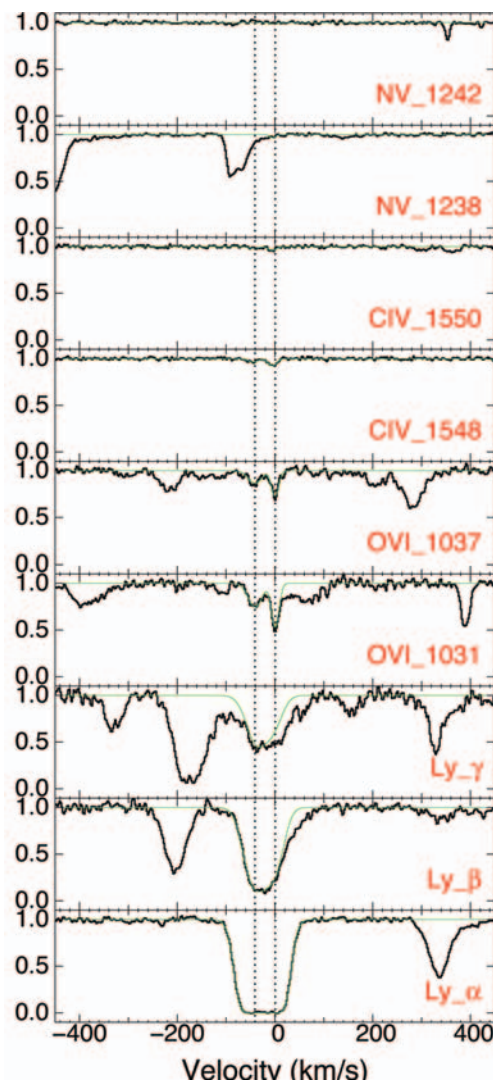

Figure 7: Normalized flux versus velocity of Lyman and metal lines for the system at z = 2.36385 in Q 0329–385 (thick lines) together with the best fit model (thin lines).
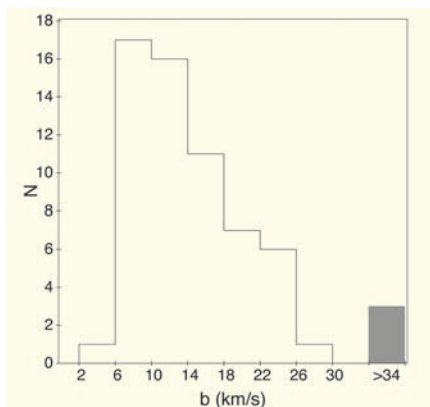
Figure 8: Histogram of the O VI doublet *b* values.

spectrum and the derived [O/C] abundance ratio depends on the spectral energy distribution of the UV flux. Even for a hard spectrum (break at 4 Ryd of about 3), a super-solar [O/C] relative abundance is needed in some cases which suggests that massive stars are a dominant source of metal enrichment of the IGM. The range in metallicity is large, ~ 10^{-3} to 10^{-1} solar, which implies very inhomogeneous metal enrichment.

The observed ionic ratios can also be analyzed using a relation between H I column density and gas density, n_H, which assumes hydrostatic equilibrium and photoionization. In this alternative approach, the observed ionic ratios constrain the spectral dependence of the ionizing flux for a given [O/C] abundance ratio. For absorbers with $N(H\ I) \geq 10^{13.5}$–10^{-15} cm^{-2}, the values derived for the gas density by the two methods are within a factor of 2–3, but for smaller $N(H\ I)$ this is not the case: the values derived from photoionization models are much larger than those using the n_H–$N(H\ I)$ relation. The latter include cases with or without detection of N v and may comprise absorbers of a different nature.

We are currently analyzing a O VI sample with $N(O\ VI) >> N(C\ IV)$, no associated N v and covering a wide range of $N(H\ I)$ (an example is the z = 2.24835 system in Q 0329–385 presented by Bergeron et al., 2002). These absorbers have a high ionization level and we will investigate whether any probe the more tenuous regions of the IGM.

ABUNDANCE PATTERNS IN SUB-DLAS

Next to the diffuse, photoionised IGM that gives rise to the Lyman-α forest, H I-rich absorbers represent important objects to study the metal enrichment history of the Universe. At $z > 1$, the Damped Lyman-α systems (DLAs), N(H I) $\geq 2\ 10^{20}$ cm^{-2}, con-

tain most of the neutral gas mass in the Universe and it is believed that they represent the progenitors of present-day galaxies. The excellent signal-to-noise ratio and high spectral resolution of the LP sample allows us to study sub-DLAs, $10^{19} < N(H\ I) < 2\ 10^{20}$ cm^{-2}, in great detail, a population not yet fully investigated. We have recently analysed two sub-DLAs at z = 2.2 and z = 3.1 toward HE 0001-2340 and Q 0420+388, respectively (Richter et al., 2004). A large number of ions are detected, including O I and N I. Both systems show a large number (>12) of velocity subcomponents spread over several hundred km/s, implying a complex structure of the absorbing gas.

Most interesting are the derived abundance trends for the CNO elements. For the sub-DLA toward HE 0001-2340, we find [O/H]=–1.81± 0.07, [N/H]≤ –3.3, and [N/O] ≤ –1.5 and this absorber is among the systems with the lowest ever measured [N/α] ratios. This result is consistent with the idea that primary nitrogen production by the very first stars have enriched the intergalactic gas to a level of [N/O] ≈ –1.5. Peculiar overabundances of a number of species such as Si, Al, and P are found in the outermost blue velocity components. Possibly, the line of sight toward HE 0001-2340 may pass through the gaseous environment of stellar clusters that locally enriched their interstellar neighbourhood by supernova ejecta.

The preliminary analyis of the z=3.1 sub-DLA toward Q 0420+388 shows that this system consists of two individual groups of absorbers, separated by ~100 km/s, that appear to have different oxygen abundances ([O/H] ≈–0.7 and –1.2). The relatively high overall abundance has led to the detection of a number of interesting ions such as Si I, Ni II, and Zn II. A detailed analysis of this sub-DLA is in progress.

The abundance variations and large velocity spread of individual subcomponents in these two sub-DLAs suggest that either recent star formation activity and/or merging of several individual galaxies/protogalactic structures with different chemical enrichment histories has led to an inhomogeneous distribution of heavy elements in the gas.

CONSTRAINING THE VARIATIONS OF THE FINE-STRUCTURE CONSTANT

Constraints on the possible time variation of the fine-structure constant, α, have been recently reported in a previous issue of the *Messenger* (Srianand et al., 2004a). This has important implications for some new theories of fundamental physics which require the existence of extra spatial dimensions and allow for a cosmic evolution of their scale size.

As the energy of the atomic transitions depend on α, the time evolution of α can be probed by measuring possible small shifts in the absorption line spectra seen toward high redshift QSOs and comparing them to its value on Earth.

This method, applied to a large heterogeneous sample of QSO absorption lines, has resulted in the claim for a smaller value of α in the past, Δα/α =(–0.574± 0.102) 10^{-5} for 0.2 ≤ z ≤ 3.7 (Murphy et al., 2003 and references therein). Using the LP data, Srianand et al. (2004b) and Chand et al. (2004a) have however derived the more stringent constraint Δα/α = (–0.06±0.06) 10^{-5} over the redshift range 0.4 ≤ z ≤ 2.3. The corresponding 3σ upper limit on the time variation of α is –2.5 10^{-16} yr^{-1} ≤ (Δα/αΔt) ≤ +1.2 10^{-16} yr^{-1}, in the most favored cosmological model today. This does not support the previous claims of a statistically significant change in Δα/α with cosmic time at $z > 0.5$.

Recently, we conducted a similar analysis on a sample of 15 Si IV doublets selected from the LP data, extending the probed redshift range up to z ~ 3. We obtained a value Δα/α= (+0.15±0.43) 10^{-5} over the redshift range 1.59 ≤ z ≤ 2.92 which, as at lower redshift, is consistent with no variation of α (Chand et al., 2004b).

REFERENCES

Aguirre, A., Schaye, J., & Theuns, T., 2002, ApJ, 576, 1

Aracil, B., Petitjean, P., Pichon, C., & Bergeron, J., 2004, A&A, 419, 811

Bergeron, J., Aracil, B., Petitjean, P., & Pichon, C., 2002, A&A, 396, L11

Carswell, B., Schaye, J., & Kim, T.-S., 2002, ApJ, 587, 43

Chand, H., Srianand, R., Petitjean, P., & Aracil, B., 2004a, A&A, 417, 853

Chand, H., Petitjean, P., Srianand, R., & Aracil, B., 2004b, A&A, in press, astro-ph/0408200

Cowie, L. L., & Songaila, A., 1998, Nature, 394, 44

Kim, T.-S., Viel, M., Haehnelt, M. G., Carswell, R. F., & Cristiani, S., 2004, MNRAS, 347, 355

Lu, L., Sargent, W. L. W., Barlow, T. A., & Rauch, M., 1998, astro-ph/9802189

Murphy, M. T., Webb, J. K., & Flambaum, V. V., 2003, MNRAS, 345, 609

Petitjean, P., & Aracil, B., 2004, A&A, 422, 523

Pichon, C., Scannapieco, E., Aracil, B., Petitjean, P., Aubert, D., Bergeron, J., & Colombi, S., 2003, ApJ 597, L97

Richter, P., Ledoux, C., Petitjean, P., & Bergeron, J., 2004, A&A, submitted

Simcoe, R. A., Sargent, W. L. W., & Rauch, M., 2002, ApJ, 578, 737

Srianand, R., Petitjean, P., Chand, H., & Aracil, B., 2004a, Messenger, 116 , 25

Srianand, R., Chand, H., Petitjean, P., & Aracil, B., 2004b, PhRvL, 92, 12130

Sutherland, R. S., & Dopita, M. A., 1993, ApJS, 88, 253

Viel, M., Haehnelt, M. G., & Springel, V., 2004a, MNRAS, 354, 684

Viel, M., Weller, J., & Haehnelt, M. G., 2004b, MNRAS, in press, astro-ph/0407294

VLT/FORS2 Spectroscopy in the GOODS-South Field

The FORS2 instrument at the ESO VLT has been used to obtain spectra of a large sample of faint galaxies in the Chandra Deep Field South in the framework of the Great Observatories Origins Deep Survey (GOODS). A total of 303 objects with magnitude $z_{850} \leq 25.5$ has been observed, providing 234 redshift determinations. The reduced spectra and the derived redshifts are released to the community (http://www.eso.org/science/goods/). They constitute an essential contribution to reach the scientific goals of GOODS, providing the time coordinate needed to delineate the evolution of galaxy masses, morphologies, and star formation, calibrating the photometric redshifts that can be derived from the imaging data at 0.36–8 µm and enabling detailed studies of the physical diagnostics for galaxies in the GOODS field.

E. Vanzella[1],
S. Cristiani[1],
M. Dickinson[2],
H. Kuntschner[3],
L. A. Moustakas[4],
M. Nonino[1], P. Rosati[5],
D. Stern[7],
C. Cesarsky[5],
S. Ettori[5],
H. C. Ferguson[4],
R.A.E. Fosbury[3],
M. Giavalisco[4],
J. Haase[3], A. Renzini[5],
A. Rettura[5,6],
P. Serra[3],
and the GOODS Team

[1]INAF - Osservatorio Astronomico di Trieste, Italy
[2]National Optical Astronomy Obs., Tucson, Arizona
[3]ST-ECF, Garching, Germany
[4]Space Telescope Science Institute, Baltimore, USA
[5]European Southern Observatory,
[6]Université Paris-Sud 11, Orsay, France
[7]Jet Propulsion Laboratory, California Institute of Technology, Pasadena, USA

THE Great Observatories Origins Deep Survey (GOODS) is a public, multi-facility project that aims to answer some of the most profound questions in cosmology: how did galaxies form and assemble their stellar mass? When was the morphological differentiation of galaxies established and how did the Hubble Sequence form? How did AGN form and evolve, and what role do they play in galaxy evolution? How much do galaxies and AGN contribute to the extragalactic background light? Is the expansion of the universe dominated by a cosmological constant? A project of this scope requires large and coordinated efforts from many facilities, pushed to their limits, to collect a database of sufficient quality and size for the task at hand. It also requires that the data be readily available to the worldwide community for independent analysis, verification, and follow-up.

The program targets two carefully selected fields, the Hubble Deep Field North (HDF-N) and the Chandra Deep Field South (CDF-S), with three NASA Great Observatories (HST, Spitzer and Chandra), ESA's XMM-Newton, and a wide variety of ground-based facilities. The area common to all the observing programs is 320 arcmin², equally divided between the North and South fields. For an overview of GOODS, see Dickinson et al. (2003), Renzini et al. (2002) and Giavalisco et al. (2004a). Spectroscopy is essential to reach the scientific goals of GOODS. Reliable redshifts provide the time coordinate needed to delineate the evolution of galaxy masses, morphologies, clustering, and star formation. They calibrate the photometric redshifts that can be derived from the imaging data at 0.36–8 µm. Spectroscopy will measure physical diagnostics for galaxies in the GOODS field (e.g., emission line strengths and ratios to trace star formation, AGN activity, ionization, and chemical abundance; absorption lines and break amplitudes that are related to the stellar population ages). Precise redshifts are also indispensable to properly plan for future follow-up at higher dispersion, e.g., to study galaxy kinematics or detailed spectral-line properties.

The ESO/GOODS spectroscopic program is designed to observe all galaxies for which VLT optical spectroscopy is likely to yield useful data. The program makes full use of the VLT instrument capabilities (FORS2 and VIMOS), matching targets to instrument and disperser combinations in order to maximize the effectiveness of the observations. The magnitude limits and selection bandpasses depend to some degree on the instrumental setup being used. The aim is to reach mag ~24–25 with adequate S/N, with this limiting magnitude being in the B-band for objects observed with the VIMOS LR-Blue grism, in the V-band for those observed in the VIMOS LR-Red grism, and in the z-band for the objects observed with FORS2. This is not only a practical limit, however, but is also well matched to the scientific aims of the GOODS program. The ACS i_{775} imaging samples rest-frame optical (B-band) light out to $z = 1$, where $i_{775} = 25$ reaches 1.5 to 2 magnitudes past L^{*}_{B} This is also the practical limit for high-quality, quantitative morphological measurements from the ACS images (cf. Abraham et al. 1996). Similarly, $i_{775} = 25$ is ~1 mag fainter than the measured L^{*} UV for $z = 3$ Lyman Break Galaxies (LBGs), and 0.5 mag fainter than that at $z = 4$ (Steidel et al. 1999). These are the limits to which GOODS/SIRTF IRAC data will robustly measure rest-frame near-IR light, and hence constrain the stellar mass.

The Selection of the Targets for the FORS2 Spectroscopy

Objects were selected as candidates for FORS2 observations primarily based on the expectation that the detection and measure-

ment of their spectral features would benefit from the high throughput and spectral resolution of FORS2, and its reduced fringing at red wavelengths, relative to other instrumental options such as VIMOS. In particular, we expect that the main spectral emission and absorption features for galaxies at $0.8 < z < 1.6$ would appear at very red optical wavelengths, out to ~1 μm. Similarly, very faint Lyman break galaxies at $z \geq 4$, selected as B_{435}, V_{606}, and i_{775}–dropouts from the GOODS ACS photometry, also benefit greatly from the red throughput and higher spectral resolution of FORS2.

In practice, several categories of object selection criteria were used to ensure a sufficiently high density of target candidates on the sky to efficiently fill out multi-slit masks. Using ACS photometry in the AB magnitude system, these criteria were:

1. Primary catalog: $(i_{775}–z_{850}) > 0.6$ and $z_{850} < 24.5$. This should ensure redshifts $z \geq 0.7$ for ordinary early-type galaxies (whose strongest features are expected to be absorption lines), and higher redshifts for intrinsically bluer galaxies likely to have emission lines.

2. Secondary catalog: $0.45 < (i_{775}–z_{850}) < 0.6$ and $z_{850} < 24.5$.

3. Photometric-redshift sample: $1 < z_{phot} < 2$ and $z_{850} < 24.5$, using an early version of GOODS photometric redshifts like those described by Mobasher et al. (2004).

4. i_{775}-dropout and V_{606}–dropout Lyman break galaxy candidates, selected from the criteria of Dickinson et al. (2004a) and Giavalisco et al. (2004b), respectively.

5. A few miscellaneous objects, including host galaxies of supernovae detected in the GOODS ACS observing campaign.

When designing the masks, we generally tried to avoid observing targets that had already been observed in other redshift surveys of this field, namely the K20 survey of Cimatti et al. (2002) and the survey of X-ray sources by Szokoly et al. (2004).

In the present spectroscopic catalog there are 303 targets, 114 meeting the primary selection criterion and 56 meeting the secondary selection criteria. The other targets belong to the remaining classes.

OBSERVATIONS AND DATA REDUCTION

The VLT/FORS2 spectroscopic observations were carried out in service mode during several nights in 2002 and 2003. In all cases the 300I grism was used as dispersing element without order-separating filter. This grism provides a scale of roughly 3.2Å/pixel. The nominal resolution of the configuration was $\Re = \lambda/\Delta\lambda = 860$, which corresponds to about 9Å at 8000Å. The spatial scale of FORS2 was 0.126″/pixel, the slit width was always 1″. Dithering of the targets
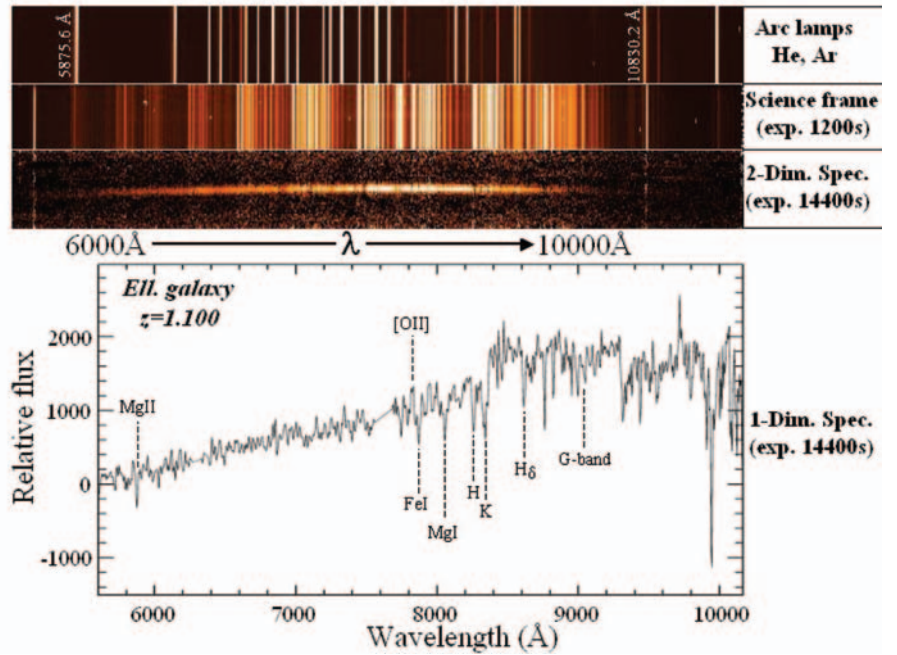

Figure 1: Typical FORS2 data products for an individual slit of the multi-object mask. From the top of the figure: the 2-D spectrum of the arc lines used for the wavelength calibration, a 2-D science exposure (1200 seconds), the final flat-fielded and sky-subtracted 2-D spectrum (co-addition of 12 exposures for a total of 4 h), and at the bottom the 1-D spectrum with the identification of the main absorption and emission lines (in this example an elliptical galaxy at $z = 1.100$, GDS J033217.46-275234.8).
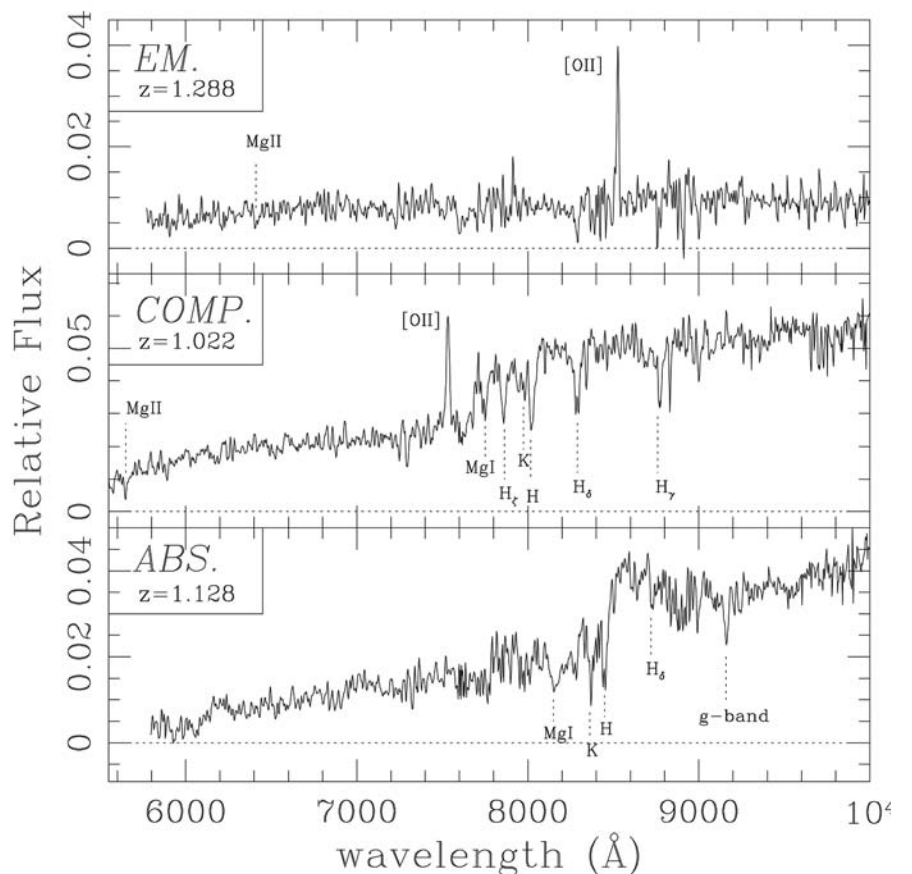

Figure 2: Three examples of objects classified as "em." (emission-lines detected), "abs." (absorption lines) and "comp." (both emission and absorption lines detected).
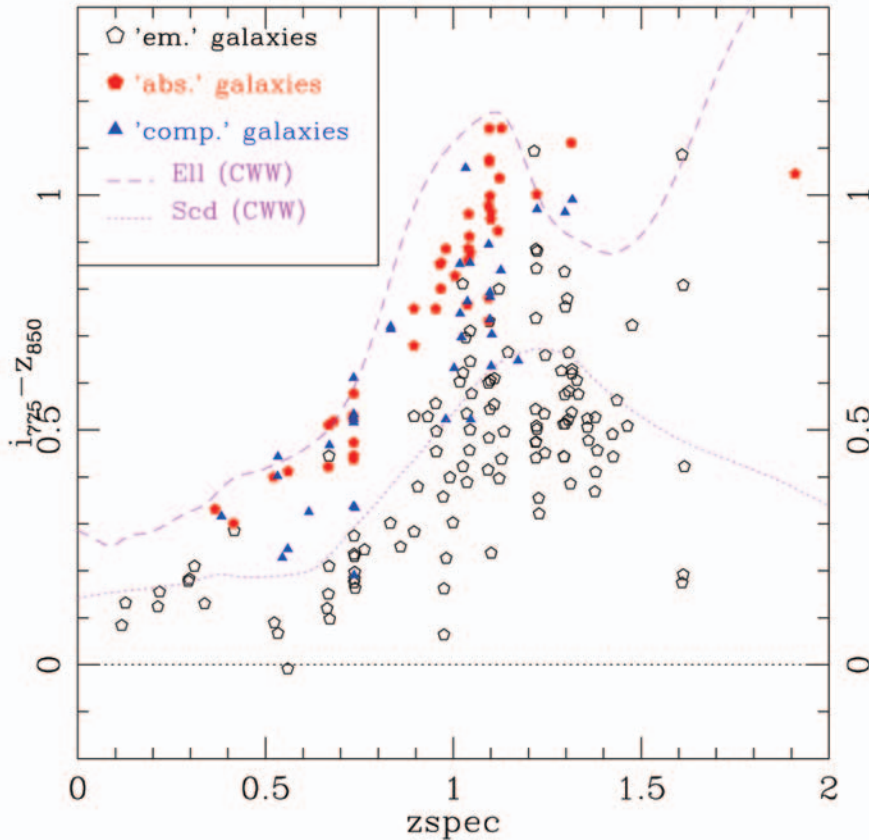
Figure 3: Color-redshift diagram of the spectroscopic sample. Only redshifts with quality flag "*A*" and "*B*" have been selected. Filled pentagons symbols are objects identified with absorption features only ("abs." sources), while open pentagons are objects showing only emission lines ("em." sources). The intermediate cases are shown by filled triangles ("comp." sources). The long-dashed line and the short dashed line show the colors of a non-evolving L^* elliptical galaxy and an Scd galaxy, respectively, estimated integrating the spectral templates of Coleman, Wu & Weedman (1980) through the ACS bandpasses.
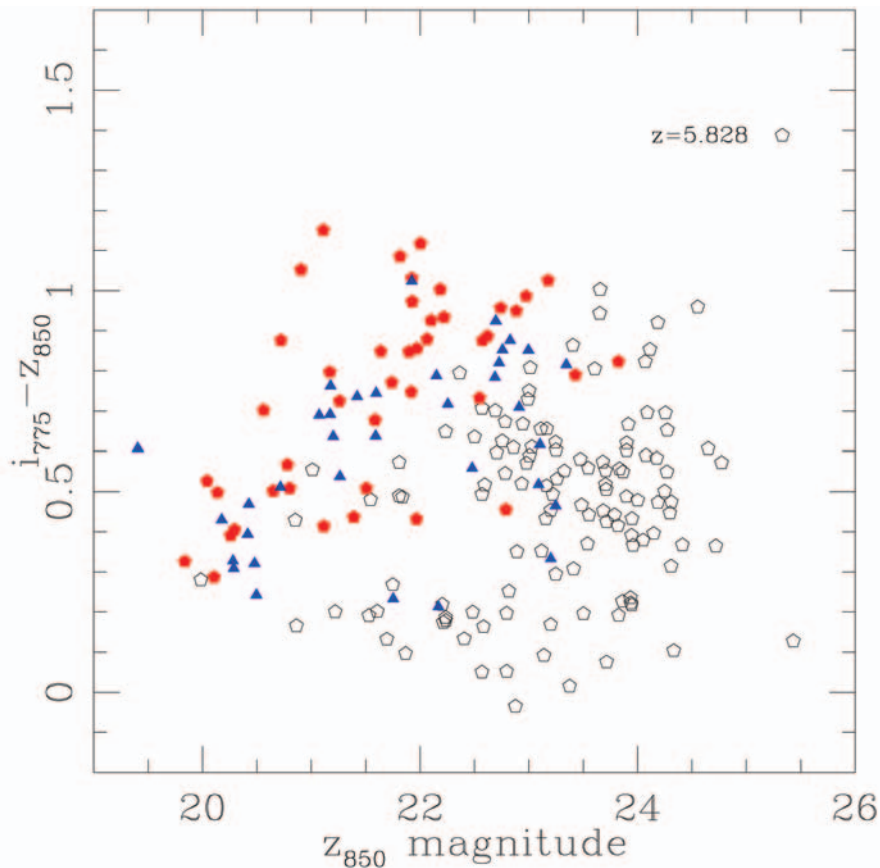
Figure 4: Color-magnitude diagram for the spectroscopic sample. Only redshifts with quality flag "*A*" and "*B*" have been selected. The symbols are the same as in Figure 3.

along the slits was applied in order to effectively improve the sky subtraction and the removal of CCD cosmetic defects.

399 spectra of 303 individual targets have been extracted and calibrated with a semi-automatic reduction tool that we have developed in the MIDAS environment using commands of the LONG and MOS contexts (Fig. 1). From the spectra we have been able to determine 234 redshifts. In the large majority of cases the redshift has been determined through the identification of prominent features of galaxy spectra: the 4000Å break, Ca H and K, g-band, Mg II 2798, Al II3584 in absorption and Ly-α, [O II]3727, [O III]5007, H$_\beta$, H$_\alpha$ in emission. The redshift estimation has been performed by cross-correlating the observed spectrum with templates of different spectral types (S0, Sa, Sb, Sc, Ell., Lyman Break, etc.), using the *rvsao* package in the IRAF environment. The redshift identifications are available at http://www.eso.org/science/goods/ and in Vanzella et al. (2004).

The objects have been classified in three categories (see Fig. 2) depending on the presence in the observed spectrum of emission line(s) (class *em.*), absorption-line(s) (*abs.*) or both (*comp.*). Eleven objects have been classified as stars. A quality flag has also been assigned to indicate "secure" redshift (flag *A*), "likely" (*B*) or "tentative" (*C*). In 38% of the cases the redshift is based only on one emission line, usually identified with [O II]3727 or Ly-α. In general these solo-emission line redshifts are classified as flag *C* or *B*. The presence of breaks, the absence of other spectral features in the observed spectral range and the broad band photometry are particularly important in the evaluation. The typical redshift uncertainty on the basis of internal and external comparisons, is estimated to be $\sigma_z \cong 0.001$ with a rate of "catastrophic" misidentifications at most few percent.

DIAGNOSTIC DIAGRAMS

Figures 3 and 4 show the color-redshift and the color-magnitude distributions for the spectroscopic sample. In Figure 3 the two populations of "emission-line" and "absorption-line" (typically elliptical) galaxies are clearly separated. The mean color of the "absorption-line" objects increases from i_{775}–z_{850} = 0.46 ± 0.079 at $<z>$ = 0.6 to i_{775}–z_{850} = 0.86 ± 0.18 at $<z>$ = 1.0, consistent with but increasingly bluer than the colors of a non-evolving L^* elliptical galaxy (estimated integrating the spectral templates of Coleman, Wu & Weedman (1980) through the ACS bandpasses).

The "emission-line" objects show in general a bluer i_{775}–z_{850} color and a broader distribution than the "absorption-line" sources: i_{775}–z_{850} = 0.16 ± 0.13 at $<z>$ = 0.6 and i_{775}–z_{850} = 0.52 ± 0.21 at $<z>$ = 1.1. The broader distribution, with some of the

"emission-line" objects entering the color regime of the ellipticals, is possibly explained by dust obscuration, high metallicity or strong line emission in the z_{850} band.

REDSHIFT DISTRIBUTION AND LARGE SCALE STRUCTURE

Figure 5 shows the redshift distribution of the objects observed in the present survey. The majority of the sources are at redshift of about one (the median of the redshift distribution is at 1.04), in agreement with the main criterion for the target selection (see Sect. 2). Table 1 shows the fraction of determined redshifts as a function of the spectral features identified, i.e. emission lines, absorption lines, emission & absorption lines, and no reliable spectral features (unclassified). There are 49 galaxies identified with absorption lines only (mainly Ca H and K) in the range of redshift between 0.4–1.3; an example is shown in Fig. 1. In 46% of the total sample we have measured emission lines (mainly [O II]3727), many of them entering the so-called "spectroscopic desert" up to z=1.61.

The main peaks in the redshift distribution are at $z\sim0.73$ (21 galaxies) and 1.1 (25 galaxies). Two concentrations at $z\sim1.6$ (with 5 galaxies at the mean redshift $<z> = 1.612 \pm 0.003$, see the two dimensional spectra in Fig. 6) and $z\sim0.67$ (9 galaxies) are also apparent. The presence in the CDF-S of large scale structure, (LSS) at $z\sim0.73$ and $z\sim0.67$ is already known (Cimatti et al. 2002, Gilli et al. 2003, Le Fevre et al. 2004). The peak at $z\sim1.1$ seems to be a new indication of large scale structure, of the 25 galaxies in the range $1.09< z <1.11$, 10 show emission lines, 9 are ellipticals and 6 are intermediate-type galaxies.

The significance of the LSS at z=1.61, which extends across a transverse size of ~ 5 Mpc in a wall-like pattern rather than a group structure, is confirmed by:

1. the observations of Gilli et al. (2003) who found a peak in the redshift distribution of X-ray sources at z=1.618 (5 galaxies) and measured a Poisson probability of $3.8 \ 10^{-3}$ for a chance distribution;

2. three more galaxies at z=1.605,1.610,1.615 in the K20 survey (Cimatti et al. 2002).

HIGH REDSHIFT GALAXIES

Three galaxies have been identified at redshifts larger than four: GDS J033240.01-274815.0 at z=5.828, the only i_{775}-dropout (see Sect. 2) actually targeted in the present observations, and two serendipitously-observed high redshift sources, GDS J033228.84-274132.7 and GDS J033228.94-274128.1, measured at z=4.800 and z=4.882, respectively. In the spectrum of GDS J033240.01-274815.0 the Ly-α line is clearly detected at z=5.828 and shows the blue cut–off characteristic of high–redshift Ly-α emitters and the Ly-α forest continuum break.

Figure 7 shows a peculiar system of three sources: two emission-line sources above (~1.5 arcsecond) and below (~3 arcsecond) the main galaxy GDS J033228.88-274129.3, clearly visible in the ACS color image and in the two dimensional spectrum. The same target has been observed in two different masks adopting the same orientation of the slits. The total exposure time is $\cong$43 ks. The extracted one dimensional spectra are shown in the right side of Fig. 7.

The main galaxy GDS J033228.88-274129.3 has a redshift z=0.733 with both emission and absorption lines measured (quality flag "A"): [O II]3727, MgI, Ca H and K, g-band, etc. The bottom object (GDS J033228.84-274132.7) shows a solo-emission line at 7052Å (see the 1D spectrum), and is not detected in the ACS B-band, we interpret this line as Ly-α at z=4.800 with quality "C".

The source above GDS J033228.88-274129.3 is most probably a Ly-α emitter at redshift
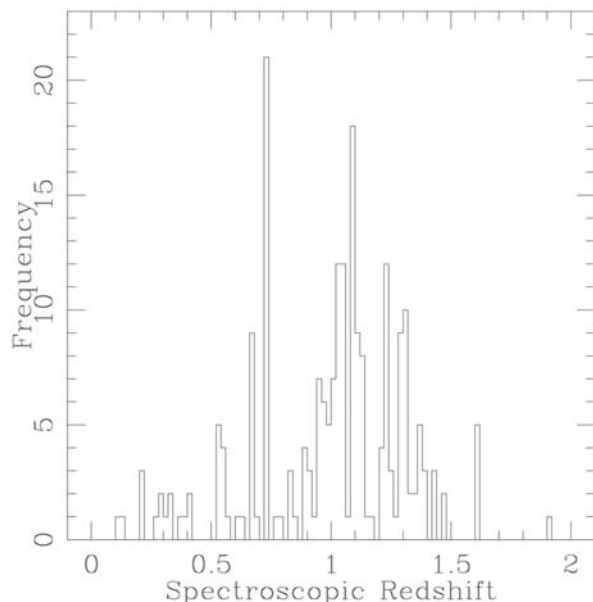

Figure 5: Redshift distribution for the spectroscopic sample with quality A, B and C (23 redshift determinations out of 224 have quality C). Three objects at z>4 are not shown in the histogram.

Table 1: Fractions of sources with different spectral features.

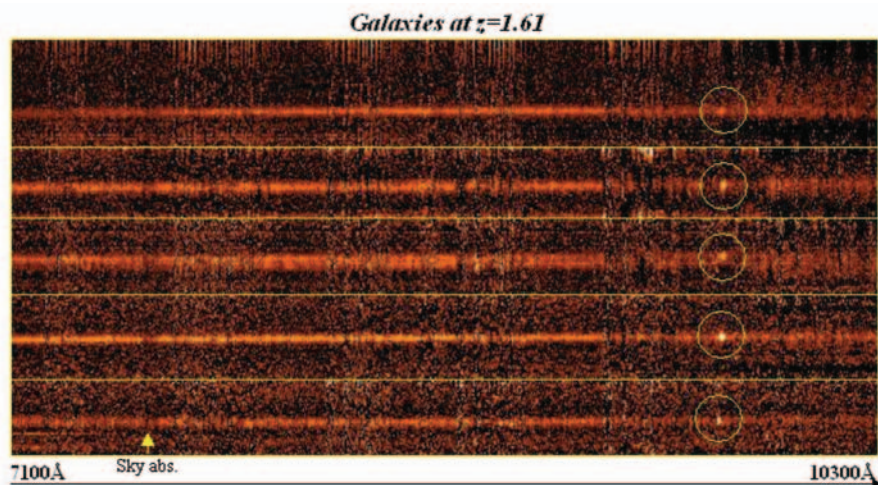| Spectral class	z_{mean}	z_{min}	z_{max}	Fraction
emission	1.131	0.117	5.828	46%
absorption	0.950	0.366	1.910	16%
em. & abs.	0.897	0.382	1.317	12%
stars	0.000	0.000	0.000	4%
unclassified	–	–	–	22%

Figure 6: Two dimensional spectra of 5 galaxies at z=1.61. The [O II]3727 emission line is marked with a circle at 9727.5Å. The absorption sky feature (~7600Å, A band) is indicated with an arrow. It is worth noting the optimal red sensitivity of FORS2.

Figure 7: Simultaneous spectrum of three sources in the slit. On the right of the figure, the 1D spectra of the z=0.733 main galaxy GDS J033228.88-274129.3, the single emission line ~3 arcsecond below (GDS J033228.84-274132.7) and the object ~1.5 arcsecond above are shown. The left-hand panel shows the ACS color image, 5 arcsec on a side. North is up, east is to the left. The bottom panel shows the 2D spectrum, with the spatial profile obtained by collapsing 80 columns (256 Å), centered at 7150 Å, shown to the right. Candidate serendipitous Ly-α emission lines are clearly marked. The object above the target source shows faint continuum redward of the emission line.
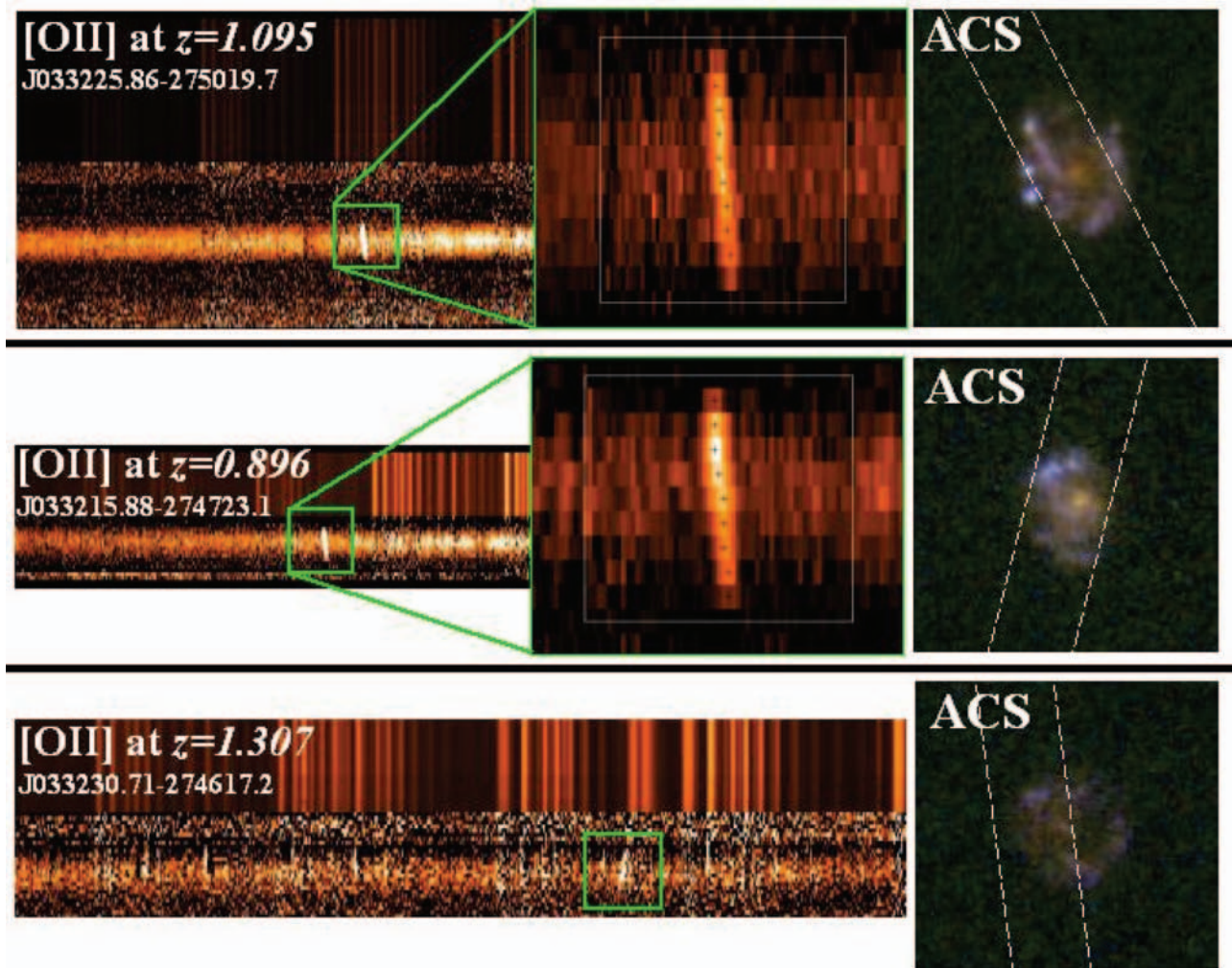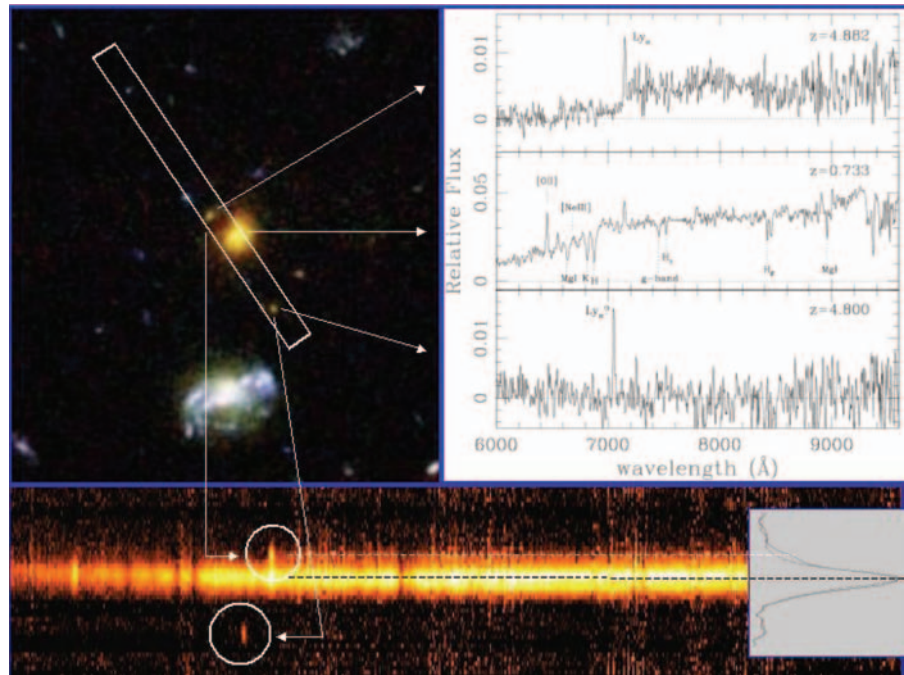
Figure 8: Three examples of tilted [O II]3727 emission line at redshift around 1. The two dimensional FORS2 spectra are shown (object and sky lines). In the first two spectra (top and middle) a zoom of the [O II]3727 emission line is shown (the white rectangle underlines the region where the Gaussian fit has been performed to derive the line peak, small black crosses), in the bottom spectrum the line is too faint to calculate a reliable peak (this object has been serendipitously-identified). In the right side of the spectra the ACS images of the galaxies and the slit orientations are shown.
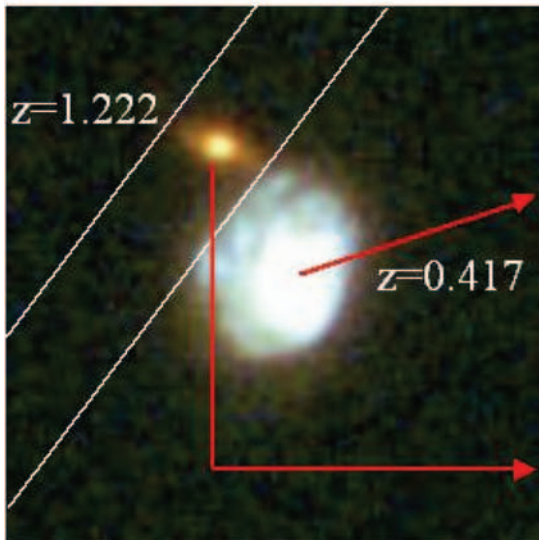
Figure 9: The light merged case, two objects at different redshift superimposed in the slit (marked with white lines in the left panel). In the right panel the same extracted spectrum with different identifications. An elliptical galaxy (the target, GDS J033210.93-274721.5) at z=1.222 clearly identified with the Ca H and K, Hδ, Mg I (quality flag "*A*"). The bright bluer object (GDS J033210.92-274722.8) shows absorption and emission lines: Ca H, [O III]5007, Na, Hα at z=0.417 (quality flag "*B*"). The Ca K is contaminated by the sky line ~5577Å.

z=4.882 (quality "B"). The spectrum has been extracted subtracting the contamination of the tail of the main galaxy. After the subtraction the shape of the spectrum shows the blue cut–off and the Ly-α forest continuum break, typical of the LBGs.

DYNAMICAL MASSES OF GALAXIES AT $z \sim 1$

Three galaxies, GDS J033215.88-274723.1, GDS J033225.86-275019.7 and GDS J033230.71-274617.2, at redshift z=0.896, 1.095 and z=1.307, respectively, show a spatially resolved [O II]3727 line (Fig. 8) with a characteristic "tilt", indicative of a high rotation velocity. The measured velocity increases with increasing distance from the center of the objects reaching a value of the order of and greater than 400 km/s at the extremes. Assuming that the observed velocity structure is due to dynamically-relaxed rotation, then it is possible to estimate the dynamical mass for the three galaxies, which turns out to be in the range 1.5–3.1 $10^{11}/sin^2$ (*i*) M$_\odot$. The estimates should be considered a lower limit to the total dynamical mass because more external parts of the rotating structure might have a lower surface brightness and remain undetected.

GDS J033210.93-274721.5: A SPECTRUM CONTAMINATED BY A NEARBY GALAXY

The spectrum of the galaxy GDS J033210.93-274721.5 simultaneously shows features corresponding to the redshifts z=1.222 and z=0.417 (Fig. 9). The origin of the overlap is the presence of a nearby galaxy (z_{850}=19.98, GDS J033210.92-274722.8) offset by 1.3 arcsecond with a redshift z=0.417. Light from the brighter z=0.417 galaxy contaminates the spectrum of the fainter (z_{850}=22.19), higher redshift galaxy GDS J033210.93-274721.5 (see Fig. 9). Such cases may represent a problem and a source of error in large spectroscopic surveys, which require highly automated data processing. A possible solution is to evaluate *a priori* on the basis of imaging what are the cases of light contamination requiring a "special" reduction. Alternatively, color-redshift diagrams (such as Fig. 3), a comparison of spectroscopic and photometric redshifts or similar diagnostics are required to carry out the necessary data quality control and single out possible misidentifications.

REFERENCES

Abraham, R., G., van den Bergh, S., Glazebrook, K., Ellis, R., S., Santiago, B., X., Surma, P., Griffiths, R., E., 1996, ApJ, 107, 1

Cimatti, A., Mignoli, M., Daddi, E., et al. 2002, A&A, 392, 395

Coleman, G., D., Wu, C.-C., & Weedman, D., W., 1980, ApJS, 43, 393

Dickinson et al. 2003, in the proceedings of the ESO/USM Workshop "The Mass of Galaxies at Low and High Redshift" (Venice, Italy, October 2001), eds. R. Bender and A. Renzini, astro-ph/0204213

Dickinson, M., et al., 2004, ApJ, 99, 122

Giavalisco, M., et al. 2004, ApJ, 600, L93

Giavalisco, M., Dickinson, M., Ferguson, H. C., Ravindranath, S., Kretchmer, C., Moustakas, L. A., Madau, P., Fall, S. M., Gardner, Jonathan P., Livio, M., Papovich, C., Renzini, A., Spinrad, H., Stern, D., Riess, A., 2004, ApJ, 600, 103

Gilli, R., Cimatti, A., Daddi, E., Hasinger, G., Rosati, P., Szokoly, G., Tozzi, P., Bergeron, J., Borgani, S., Giacconi, R., Kewley, L., Mainieri, V., Mignoli, M., Nonino, M., Norman, C., Wang, J., Zamorani, G., Zheng, W., Zirm, A., 2003, ApJ, 592, 721

Le Fevre, O., Vettolani, G., Paltani, S., Tresse, L., Zamorani, G., Le Brun, V., Moreau, C., and the VIMOS VLT Deep Survey team, submitted to A&A, (astro-ph/0403628)

Mobasher, B., Idzi, R., Benítez, N., Cimatti, A., Cristiani, S., Daddi, E., Dahlen, T., Dickinson, M., et al., 2004, ApJ, 600, 167

Renzini et al. 2002, in the proceedings of the ESO/USM Workshop "The Mass of Galaxies at Low and High Redshift" (Venice, Italy, October 2001), eds. R. Bender and A. Renzini

Riess, A.G.,2 Strolger, L.-G., Tonry, J., Casertano, S., Ferguson, H.C., et al., 2004, ApJ, 607, 665

Steidel, C.C., Adelberger, K.L., Giavalisco, M., Dickinson, M., Pettini, M., 1999, ApJ, 519, 1

Szokoly, G., P., Bergeron, J., Hasinger, G., Lehmann, I., Kewley, L., Mainieri, V., Nonino, M., Rosati, P., Giacconi, R., Gilli, R., Gilmozzi, R., Norman, C., Romaniello, M., Schreier, E., Tozzi, P., Wang, J., X., Zheng, W., Zirm, A., 2004, (astro-ph/0312324)

Vanzella, E., Cristiani, S., Dickinson, M., et al. astro-ph/0406591

Unveiling Old Massive Spheroidal Galaxies in the Young Universe

Very deep VLT spectroscopy has unveiled the existence of old and massive spheroidal galaxies when the Universe was still young, thus showing that massive galaxies formed earlier and faster than has been expected from current theories of galaxy formation.

A. Cimatti[1],
E. Daddi[2],
A. Renzini[2],
P. Cassata[3],
E. Vanzella[3],
L. Pozzetti[4],
S. Cristiani[5],
A. Fontana[6],
G. Rodighiero[3],
M. Mignoli[4],
G. Zamorani[4]

[1]INAF - Osservatorio Astrofisico di Arcetri, Italy
[2]European Southern Observatory, Garching, Germany
[3]Dipartimento di Astronomia, Università di Padova, Italy
[4]INAF - Osservatorio Astronomico di Bologna, Italy
[5]INAF - Osservatorio Astronomico di Trieste, Italy
[6]INAF - Osservatorio Astronomico di Roma, Italy

Understanding the physics and tracing the cosmic history of galaxy mass assembly is one of the main open questions of galaxy formation and evolution. Despite the tremendous progress in observational cosmology, the accuracy in the estimate of cosmological parameters and the successful convergence on the ΛCDM cosmological model, the mechanisms leading to the birth and the evolution of galaxies are still poorly known.

The generally accepted framework of galaxy formation is known as hierarchical merging. In the early Universe, small mass density fluctuations (such those observed with WMAP) trigger gravitational instability and dark matter halos begin to collapse from the ambient background. Each dark matter halo contains a fraction of baryonic matter. This pristine baryonic gas starts to condense and, through its cooling, the first disks form at the center of dark matter halos. Star formation converts cold gas into luminous stars and chemical enrichment and feedback effects also start to play a relevant role (e.g. through supernova explosions). Galaxies assemble and increase their mass gradually through the merging of dark matter halos, and a collision between two or more disk galaxies is thought to produce a spheroidal galaxy. In this scenario, the young Universe is expected to be populated by small mass objects which are the first to form, whereas the most massive galaxies are the last product of the "merging tree" evolution.

The empirical approach adopted by astronomers to investigate galaxy formation and evolution is to search for and to study the populations of distant galaxies. Samples selected in the optical bands allow us to cull star-forming galaxies where the redshifted ultraviolet (UV) radiation is dominated by hot, massive and short-lived stars. However, optical samples are affected by severe biases due to the strong influence of dust extinction in the UV and to the wide range of shapes that spectral energy distributions (SEDs) have in the UV depending on the level of star formation activity and the age of the galaxy.

At longer wavelengths, the above problems are alleviated, as the rest-frame optical and, even better, the near-infrared radiation is dominated by low mass, long-lived stars (with a lifetime comparable to the age of the Universe). Also, the shapes of the SEDs in the optical/near-IR are very similar for all galaxy types, and the effects of dust extinction become less severe. In addition, the rest-frame optical/near-IR luminosity is known to correlate with the galaxy mass. The above advantages make galaxy samples selected in the near- (e.g. *K*-band at 2.2 μm) or, even better, in the mid-IR (e.g. ~4–8 μm, now possible with the Spitzer Space Telescope) more suitable than optical samples to investigate galaxy evolution and, particularly, the history of galaxy mass assembly, because they allow us to observe the rest-frame optical and near-IR for high redshift galaxies.

Recent results based on *K*-selected samples consistently show that from $z\sim0$ to $z\sim1$ there is a mild evolution of the global stellar mass density in the Universe (e.g. Fontana et al. 2004 and references therein; Glazebrook et al. 2004). This suggests that most stellar mass was already in place and most galaxies completed their mass assembly by $z\sim1$, i.e. when the Universe was about 5.9 Gyr old (H_o=70 km/s/Mpc, with h_{70}=H_o/70, Ω_M=0.3 and Ω_Λ=0.7 are adopted throughout the article). However, the evolution is poorly known at higher redshifts ($z > 1$). In this context, the formation and evolution of E/S0 galaxies play a particularly relevant role because in the present-day Universe (13.7 Gyr old), up to 75% of the stellar mass is locked up in these galaxies with spheroidal morphology. While it is now generally accepted that the number density of field massive E/S0 systems remains rather constant out to $z \sim 1$, it is still unknown whether the paucity of spheroidal galaxies at $z > 1$ is a real effect of galaxy evolution or an observational bias.

Addressing this problem is difficult because for $z > 1.3$ these galaxies become very faint in the optical and lack strong spectral features observable in optical spectra. This makes such objects among the most difficult targets to identify even with the
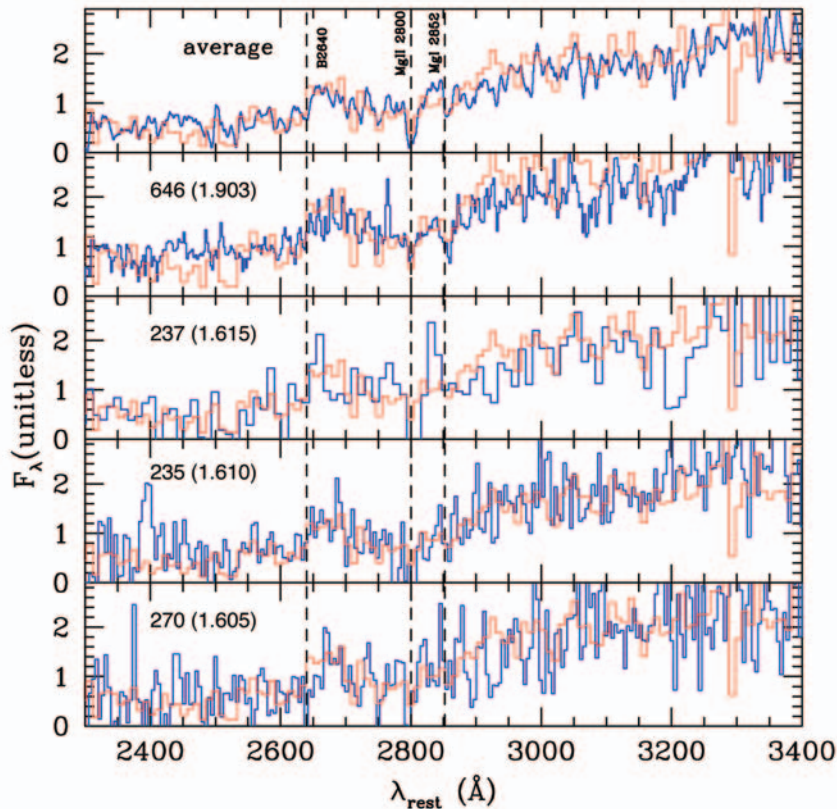
Figure 1: From top to bottom: the average spectrum of the four old galaxies ($z_{average}$=1.68) and the individual spectra. The red line is the spectrum of the old galaxy LBDS 53w091 (Dunlop et al. 1996; z=1.55) used to search for spectra with a similar continuum shape. Weak features in individual spectra (e.g. Mg II λ2800 and the 2640 Å continuum break, B2640) become clearly visible in the average spectrum.
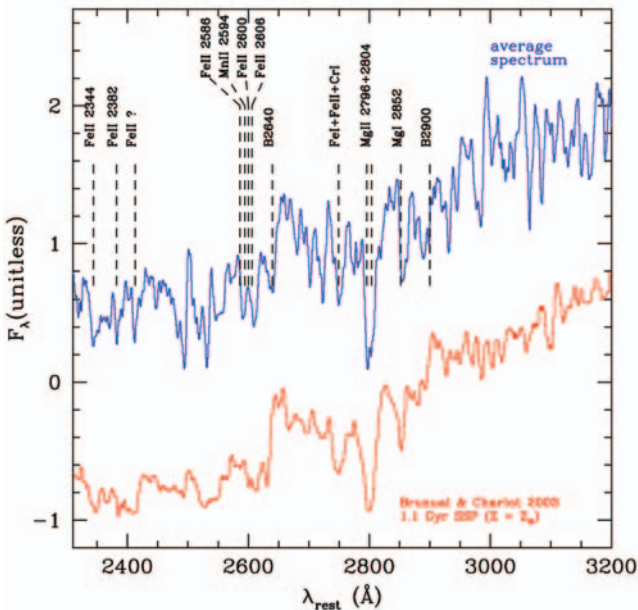
largest optical telescopes. Indeed, while star-forming galaxies and quasars are now routinely found up to $z \sim 6.5$, the most distant spectroscopically confirmed old spheroid is still a radio–selected object at $z = 1.55$ discovered almost a decade ago (Dunlop et al. 1996).

SEARCHING FOR THE OLDEST GALAXIES AT HIGH REDSHIFT

One way of addressing the question of massive and spheroidal galaxy formation is to search for the farthest and oldest galaxies with masses comparable to the most massive galaxies in the present-day Universe (10^{11-12} $M_\odot$), and to use them as the "fossil" tracers of the most remote events of galaxy formation.

Following this approach, we recently made use of the database resulting from the completed ESO VLT Large Programme called "K20 survey" (Cimatti et al. 2003). This dataset consists of deep optical spectra obtained with FORS1 and FORS2 for a sample of 546 K-selected objects with $K_S < 20$ (Johnson photometric scale) and extracted from an area of 52 arcmin^2. Part of the K20 sample (348 objects) is located in 32 arcmin^2 within the GOODS field (Giavalisco et al. 2004) (hereafter the GOODS/K20 field). The overall spectroscopic redshift (z_{spec}) completeness of the K20 survey is 92%, and multi-band photometry ($BVRIzJHK_S$) is also available for all galaxies to derive and characterize their SEDs and to estimate the photometric redshifts (z_{phot}) for galaxies without

Figure 2: A zoom on the average spectrum (blue), corresponding to 34.4 hours integration time, compared with the synthetic spectrum of a 1.1 Gyr old simple stellar population (SSP) with solar metallicity (Z=Z$_\odot$) and Salpeter IMF (red) (Bruzual & Charlot 2003 models).
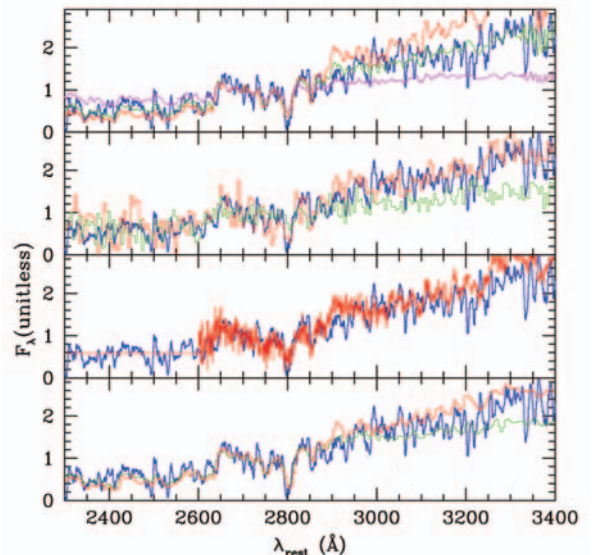
Figure 3: The average spectrum (blue) compared to a set of template spectra. From bottom: F2 V (green) and F5 V (red) stellar spectra with Z=Z$_\odot$, the composite spectrum (red) of 726 luminous red galaxies at 0.47< z <0.55 selected from the SDSS (available only for λ>2600 Å), the average spectra of z~1 old (red) and dusty star-forming (green) EROs, Bruzual & Charlot (2003) SSP synthetic spectra (Z=Z$_\odot$, Salpeter IMF) with ages of 0.5 Gyr (magenta), 1.1 Gyr (green) and 3.0 Gyr (red).
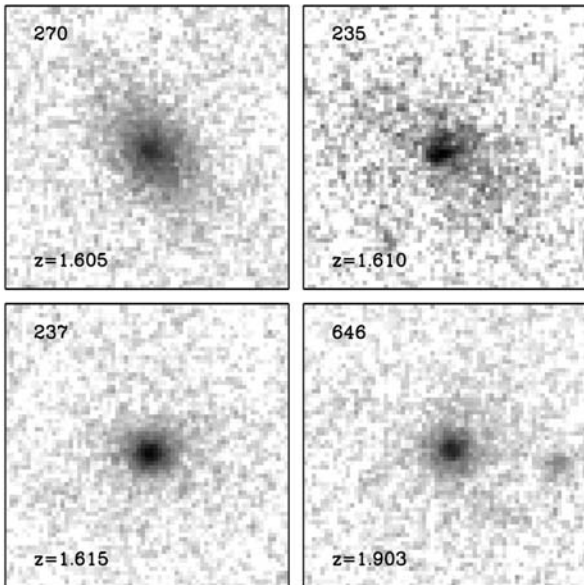
Figure 4: Images of the four galaxies taken with the *Hubble Space Telescope* + ACS through the F850LP filter (from GOODS data) which samples the rest-frame ~3000-3500 Å for $1.6 < z < 1.9$. The images are in logarithmic grey–scale and their size is 2″×2″, corresponding to ~17×17 kpc for the average redshift z=1.7 and the adopted cosmology.

spectroscopic redshifts. We complemented the K20 survey database with the ESO/GOODS public spectroscopy to increase the z_{spec} completeness to 94% (Vanzella et al. 2004). For the GOODS/K20 field it was also possible to complement VLT spectroscopy with deep imaging obtained using the *Hubble Space Telescope* equipped with the Advanced Camera for Surveys (ACS) (*BViz* bands) and publicly released by the GOODS HST *Treasury Program* (Giavalisco et al. 2004).

In order to investigate the evolution of distant massive galaxies, the available spectra within the GOODS/K20 field were then used to search for galaxies at $z > 1.5$ with the continuum UV spectra expected in case of old stellar populations. We spectroscopically identified four galaxies with $18 \leq K_S \leq 19$ and $1.6 \leq z_{spec} \leq 1.9$ which have rest-frame mid-UV spectra with shapes and continuum breaks compatible with being dominated by old stars and $R–K_S \geq 6$ (Cimatti et al. 2004) (i.e. the colour expected at $z > 1.5$ for old passively evolving galaxies due to the combination of old stellar populations and k-correction effects).

The spectra were obtained with FORS2 (MXU mode), grisms 200I (R(1″) ~ 400) (ID 237) and 300I (R(1″) ~ 600) (IDs 235, 270, 646), 1.0″ wide slit and ≤ 1″ seeing conditions (see Cimatti et al. 2003 for details on the observation techniques and data reduction). The integrations times were 3 hours for ID 237, 7.8 hours for IDs 235 and 270. For ID 646, the ESO/GOODS public spectrum (8 hours) was co-added to our K20 spectrum (7.8 hours), thus providing a very deep spectrum with 15.8 hours integration time. Figure 1 shows the spectra of the individual objects. A fairly precise determination of the redshift was possible based on

absorption features and the overall continuum spectral shape.

AGES AND FORMATION EPOCHS

In order to increase the signal-to-noise ratio and to perform a detailed spectral analysis, we co-added the spectra of the four galaxies and obtained an average spectrum corresponding to 34.4 hours of integration time. The co-added spectrum (Figs. 1–3) shows a mid-UV continuum shape, breaks and absorption lines that are intermediate between those of a F2 V and a F5 V star. It is also very similar to the average spectrum of z~1 old Extremely Red Objects (EROs) (Cimatti et al. 2003), and slightly bluer than that of the z~0.5 Sloan Digital Sky Survey (SDSS) red luminous galaxies and of the z=1.55 old galaxy LBDS 53w091 (Dunlop et al. 1996). However, it is different in shape and slope from the average spectrum of z~1 dusty star-forming EROs (Cimatti et al. 2003).

The observed average spectrum was compared through a χ^2 fitting to a library of synthetic template spectra of "simple stellar populations" (SSPs) with a range of ages of 0.1–3.0 Gyr with assumed metallicities $Z=0.4×, 1.0×,$ and $2.5×Z_{\odot}$. In the case of solar metallicity, the ranges of ages acceptable at 95% confidence level are $1.0^{+0.5}_{-0.1}$ Gyr and $1.4^{+0.5}_{-0.4}$ Gyr for SSP models of Bruzual & Charlot (2003) and Jimenez et al. (2004) respectively (see also Fig. 3, top panel). Ages ~50% younger or older are also acceptable for $Z=2.5 Z_{\odot}$ or $Z=0.4 Z_{\odot}$ respectively. The 2640 Å and 2900 Å continuum break amplitudes measured on the average spectrum are B2640=1.8±0.1 and B2900= 1.2±0.1. These values are consistent with the ones expected in SSP models for ages

around 1–1.5 Gyr and solar metallicity. For instance, the SSP model spectrum shown in Fig. 2 has B2640=1.84 and B2900=1.27.

An average age of about 1–2 Gyr $(Z=Z_{\odot})$ at $<z>~1.7$ implies that the onset of the star formation occurred not later than at $z~2.5–3.4$ ($z~2–2.5$ for $Z=2.5 Z_{\odot}$). These are strict lower limits because they follow from assuming "instantaneous bursts", whereas a more realistic, prolonged star formation activity would push the bulk of their star formation to an earlier cosmic epoch. As an illustrative example, the photometric SED of ID 646 ($z=1.903$) can be reproduced (without dust) with either a ~1 Gyr old instantaneous burst occurred at $z~2.7$, or with a ~2 Gyr old stellar population with a star formation rate declining with $exp(–t/\tau)$ ($\tau = 0.3$ Gyr). In the latter case, the star formation onset would be pushed to $z~4$ and half of the stars would be formed by $z~3.6$.

THE MORPHOLOGY OF THE OLD GALAXIES

In addition to spectroscopy, the nature of these galaxies was investigated with the *Hubble Space Telescope*+ACS (*Advanced Camera for Surveys*) imaging from the GOODS public *Treasury Program* (Giavalisco et al. 2004). On visual inspection, the galaxies have rather compact morphologies with most of the flux coming from the central regions. A quantitative analysis of their surface brightness profiles show that objects ID 237 and ID 646 have the steep profiles typical of elliptical galaxies, object ID 270 is better reproduced by a somewhat flatter profile, whereas ID 235 has a profile between a disk and spheroid. These two latter galaxies may be bulge-dominated spirals but no bulge/disk decomposition was attempted due to the faintness and small angular size of these galaxies. Ground-based near-infrared images taken under 0.5″ seeing conditions with the ESO VLT+ISAAC through the K_S filter (rest-frame ~6000–8000 Å) show very compact morphologies for all four galaxies, but no surface brightness fitting was done. The bottom line is that the surface brightness distribution of these galaxies is typical of elliptical/ early-type galaxies.

STELLAR MASSES AND MAIN IMPLICATIONS

Besides pushing the identification of the highest redshift elliptical galaxy to z~1.9, these objects provide new and enlightening clues on massive galaxy formation and on the evolution of the mass assembly.

In order to estimate the stellar masses of the identified galaxies, their multi-band photometric SEDs were successfully fitted without the need for dust extinction, and using a library of simple stellar population (SSP) models with a wide range of ages, $Z=Z_{\odot}$ and Salpeter IMF. This procedure yielded best-
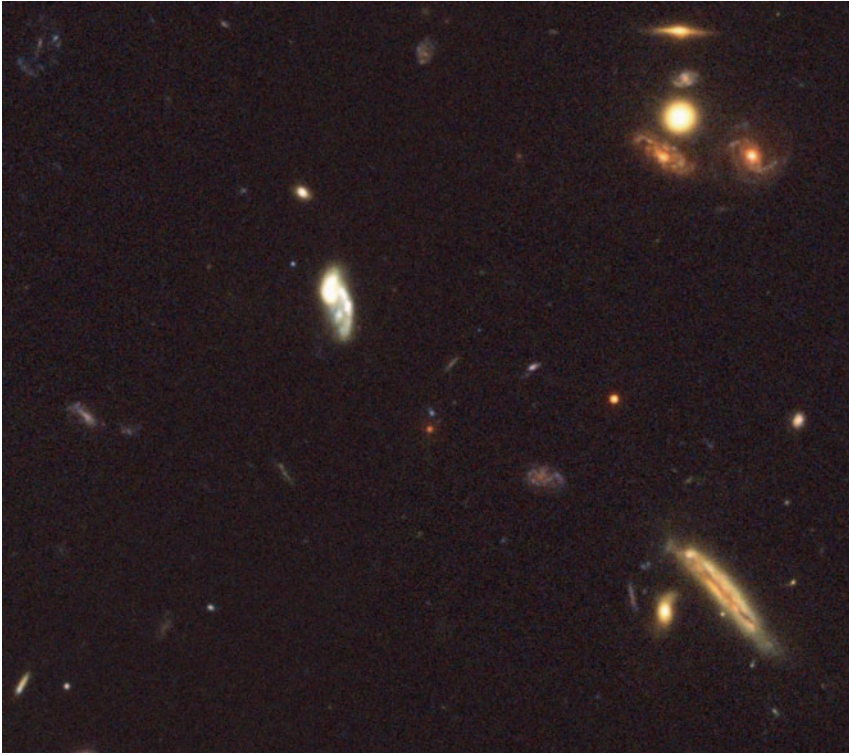
Figure 5: Zoomed image of the GOODS/K20 field (40×40 arcsec) centered on the highest redshift galaxy in the sample (ID 646; z=1.903). The colors are representative of the real galaxy colors, and it is evident that ID 646 is the reddest object in the field compared to the other faint galaxies. The red colors are due to the old stars contained in this evolved galaxy. This image was obtained with the public GOODS HST + ACS data in *bviz* bands (courtesy of R. Fosbury, ESO/ST-ECF, and P. Rosati, ESO).

fitting ages of 1.0–1.7 Gyr (consistent with the spectral analysis), the mass-to-light ratios and hence the stellar mass of each galaxy, which results in the range of 1–$3 \ 10^{11} \ h_{70}^{-2} \ M_\odot$. With stellar masses $M_* > 10^{11} \ h_{70}^{-2} \ M_\odot$, these systems would rank among the most massive galaxies in the present-day universe, suggesting that they were fully assembled already at this early epoch.

The number density of such systems turns out to be quite high. Within the comoving volume corresponding to 32 arcmin^2 and $1.5 < z < 1.9$ ($40{,}000 \ h_{70}^{-3} \ \text{Mpc}^{-3}$), their comoving density is about $10^{-4} \ h_{70}^{-3} \ \text{Mpc}^{-3}$, corresponding to a stellar mass density of about $2 \ 10^7 \ h_{70} \ M_\odot \text{Mpc}^{-3}$. This is about 10% of the local (z=0) value for masses greater than $10^{11} \ M_\odot$, ~20–30% of the total density at $1.5 < z < 2.0$, and a substantial fraction (up to ~50–60%) of the stellar mass density for galaxies with $M^* > 10^{11} \ M_\odot$ at $1.5 < z < 2.0$ (Fontana et al. 2004; Glazebrook et al. 2004). This mass density is comparable to that of star-forming $M_* > 10^{11} \ M_\odot$ galaxies at z~2, suggesting that while the most massive galaxies in the local universe are now old objects with no or weak star formation, by z~2 passive and active star-forming massive galaxies co-existed in nearly equal number.

Although more successful than previous models, the most recent realizations of semi-analytic hierarchical merging simulations still severely underpredict the density of such old galaxies: just one old galaxy with $K_S < 20$, R–$K_S < 6$, and $z > 1.5$ is present in the mock catalog for the whole GOODS/CDFS area five times wider (see also Fontana et al. 2004 and Glazebrook et al. 2004). As expected for early-type galaxies, the three galaxies at z~1.61 may trace the underlying large scale structure. In this case, our estimated number density may be somewhat biased toward a high value. On the other hand, the number of such galaxies (and their relative stellar mass density) in our sample is likely to be a lower limit due to the spectroscopic redshift incompleteness. There are indeed up to three more candidate old galaxies in the GOODS/K20 sample with $18.5 \le K_S \le 19.5$, $1.5 \le z_{phot} \le 2.0$, $5.6 \le R$–$K_S \le 6.8$ and compact HST morphology. Thus, in the GOODS/K20 sample the fraction of old galaxies among the whole $z > 1.5$ galaxy population is $15 \pm 8\%$ (spectroscopic redshifts only), or up to $25 \pm 11\%$ if also all the 3 additional candidates are counted.

The existence of such old, massive, fully assembled spheroidal galaxies when the Universe was only about one-quarter of its present age and supposed to be dominated by young galaxies with smaller masses, shows that the build-up of massive early-type galaxies occurred earlier and much faster than has been expected from theoretical simulations of galaxy formation. This raises crucial questions on the actual understanding of the processes regulating the birth and evolutionary history of baryonic structures in the Universe. Remaining within the framework of ΛCDM hierarchical merging, one possibility is to find a physical process capable of accelerating and boosting star formation in the most massive dark matter halos, and to rapidly suppress it. This is equivalent to make hierarchical merging mimic the old–fashioned "monolithic" collapse. From the observational point of view, searching for and studying the high-z progenitors of these old galaxies will allow us to understand what mechanisms make it possible to assemble such large masses in a relatively short time.

POPULATING THE "REDSHIFT DESERT"

The redshift range around $1.4 < z < 2.5$ has been traditionally known as the "redshift desert" because of the difficulty of spectroscopically identifying galaxies due to the lack of strong spectral features redshifted in the optical spectra. However, this redshift range is also considered critical because it may represent the cosmic epoch when most star formation activity and galaxy mass assembly took place. Recent work has started to unveil the nature of the galaxies living in the desert. Our results show that, in addition to actively star forming galaxies (Daddi et al. 2004; Steidel et al. 2004), a substantial number of "fossil" systems also already populate this redshift range, and hence remain undetected in surveys biased towards star-forming systems. The luminous/massive star-forming galaxies found at $z > 2$ in the sub-mm (Genzel et al. 2004) and near-infrared (Franx et al. 2003; Daddi et al. 2004) surveys may represent the progenitors of these old and massive systems.

A new VLT Large Programme (*GMASS: the galaxy mass assembly ultra-deep spectroscopic survey;* PI A. Cimatti) has been started in Period 73 with the main aim of tracing the history of galaxy mass assembly at $1 < z < 3$ by means of ultra–deep FORS2 multi-object spectroscopy.

REFERENCES

Cimatti A., Mignoli M., Daddi E. et al. 2003, The Messenger, 111, 29
Cimatti A., Daddi E., Renzini A. et al. 2004, Nature, 430, 184
Daddi E. et al. 2004, ApJ, 600, L127
Dunlop J.S. et al. 1996, Nature, 381, 581
Fontana A. et al. 2004, A&A, 424, 23
Franx M. et al. 2003, ApJ, 587, L79
Genzel R. et al. 2004, ApJ, 584, 633
Giavalisco M. et al. 2004, ApJ, 600, L93
Glazebrook K. et al. 2004, Nature, 430, 181
Somerville, R.S. et al. 2004, ApJ, 600, L135
Steidel C.C. et al. 2004, ApJ, 604, 534
Vanzella E. et al. 2004, A&A, in press (astro-ph/0406591)

THE FIRST STARS:
WHAT WE KNOW AND DO NOT KNOW

THE H&K SURVEY OF BEERS, PRESTON & SHECTMAN HAS BEEN THE MINE OF EXTREMELY METAL-POOR STARS DURING THE LAST DECADE OF THE XXTH CENTURY. THE VLT-UVES COMBINATION HAS ALLOWED US TO STUDY THE CHEMICAL COMPOSITION OF THE BRIGHTEST MEMBERS OF THIS POPULATION, FOSSIL COMPONENT OF EVENTS WHICH HAVE OCCURED EITHER DURING THE FORMATION OF THE GALAXY, OR EARLIER IN SMALLER SYSTEMS HAVING EVENTUALLY MERGED INTO OUR BEAUTIFUL MILKY WAY. WE REPORT HERE WHAT HAS BEEN DERIVED FROM A VLT LARGE PROGRAMME DEVOTED TO THESE OBJECTS, AS WELL AS ON OTHER QUESTIONS RELEVANT TO THE FIRST STARS.

R. CAYREL[1] AND M. SPITE[2]

[1]GEPI, OBSERVATOIRE DE PARIS-MEUDON, PARIS, FRANCE
[2]GEPI, OBSERVATOIRE DE PARIS-MEUDON, MEUDON, FRANCE

THERE IS AN INFALLIBLE WAY for recognizing a first star: it is born with the primordial composition left a few minutes after the big bang. The primordial big bang nucleosynthesis (BBN) is one of the safest part of nuclear astrophysics. The medium is very uniform, temperatures and densities are in a range where the reaction rates are known or inferred from experimental nuclear physics. There is a single free parameter, the density at a given temperature, or, in other words, the baryon-to-photon ratio η. The expansion, at its relativistic rate, sets the future of the medium, once the baryon-to-photon ratio is known. Figure 1 gives the result of such computations (Coc et al. 2004), adapted by the authors for the exact values of the observational results, and their uncertainties.

Qualitatively, the chemical composition is mostly hydrogen and ^{4}He, with traces of rare elements such as deuterium, ^{3}He and ^{7}Li. Quantitatively, it is necessary to know the value of η. Thanks to the results of the Wilkinson Microwave Anisotropy Probe (Spergel et al. 2003) this value is now firmly braketted $(6.2 \pm 0.2) \cdot 10^{-10}$, as shown in Fig. 1. It is remarkable that the predictions of the BBN are so close to the observations. Note that ^{7}Li is the only stellar abundance among the three. ^{4}He is observed in metal-poor blue-compact galaxies, and D in Lyman-α damped systems at high redshifts, because it has been destroyed in stars. What do we see in extremely metal poor (XMP in short) stars? We see hydrogen, the main constituent. We do not see ^{4}He, because of its lack of lines in the observed spectral range, but indirect inference from the position of the main sequence indicates an abundance of helium in agreement with BBN. We also see the primordial element ^{7}Li, with about the expected BBN abun-

dance (actually a little below), but we see also carbon, oxygen, magnesium, silicium, iron, etc..., admittedly in tiny proportions with respect to what we see in the sun (10^{-3} to 10^{-4} less), but still not zero, as it should be in a true first star. Sorry for that. We cannot offer a first star to you.

What does this mean? It means that the low mass stars still around, have been polluted by the ejecta of supernovae explosions, which have occured before their birth, or during their birth. The consolation is that analysing the abundances of these elements imprinted in an originally primordial matter gives an idea of the composition of the ejecta of primordial supernovae, which is interesting too.

THE ESO LARGE PROGRAMME 165.N-0276

In April 2000 an ESO Large Programme began: "*Galaxy Formation, Early Nucleosynthesis, and the First Stars*". Thirty eight nights were granted to this programme which spanned four ESO periods, 65 to 68. The aim of this programme was to observe, with VLT-UVES, all known stars of extremely low metallicity, bright enough to be observed with spectral resolution of 40,000, and S/N ratio of 200 per resolved spectral element.

The members of this LP were J. Andersen (DK), B. Barbuy (Brazil), T.C. Beers (US), P. Bonifacio (I), R. Cayrel (PI, F), E. Depagne (F), P. François (F), V. Hill (F), P. Molaro (I), B. Plez (F), F. Primas (ESO), B. Nordström (DK), F. and M. Spite (F). The programme has observed about 70 objects, 35 giants, 23 Turn-off (TO) stars and several other stars, practically all coming from the H&K survey of Beers, Preston and Shectman (1985). A significant part of them were classified as XMP, after medium resolution observations led at ESO, with slit
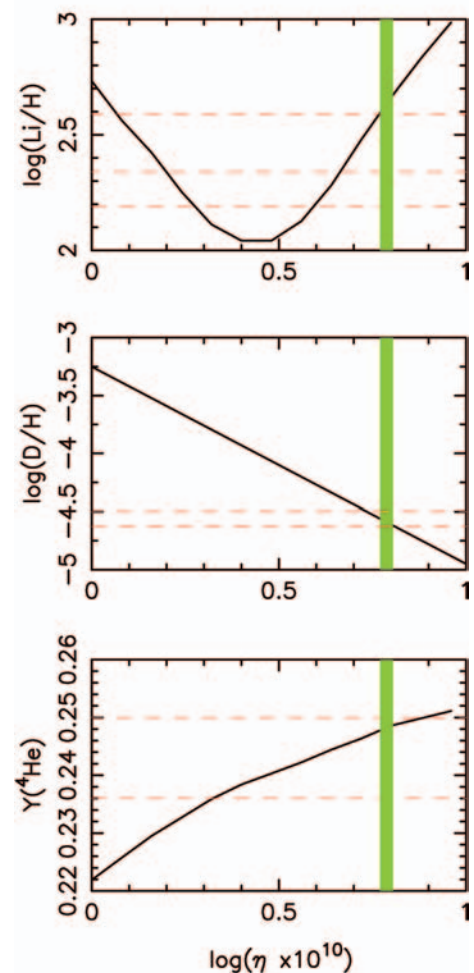

Figure 1: The primordial nucleosynthesis. η is the baryon/photon ratio. The ordinate are the logarithmic abundances per 10^{12} hydrogen atoms, except for helium, where the usual mass fraction Y is given. The curves are the theoretical predictions. The green lane is the WMAP determination of η. The horizontal red lines are the observed values, with their error bars. The error bar of Li is asymetrical because it includes the possibility that Li be depleted by gravitational settling or nuclear burning.
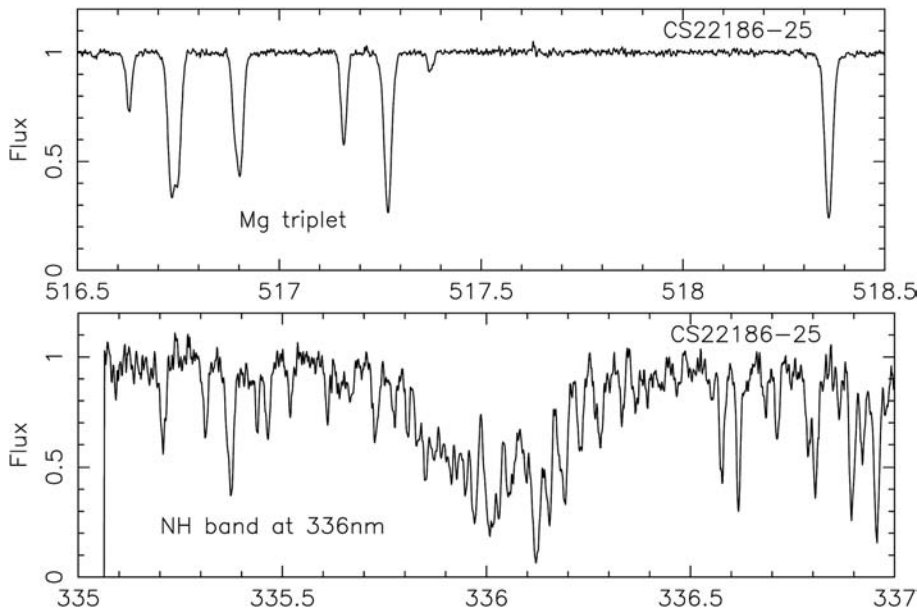
Figure 2: Sample spectrum of the Large Programme. The upper panel is the region of the Mg I *b* lines. The S/N ratio is about 200 per pixel. The lower panel shows the NH band at 336 nm. The S/N ratio has dropped to 30.

spectroscopy at 0.1 nm resolution, with the 1.5-m spectroscopic telescope. Figure 2 gives a sample spectrum of the observations with the spectrograph UVES. Note the weakness of the magnesium *b*-lines near 510 nm, very strong lines in pop. I, and the band of NH in the UV, but with an important loss in S/N ratio, due to the low flux in the UV of cool giants.

We summarize in the following sections a few findings of this programme, mostly in the 35 giants of the sample. The next section is devoted to three outstanding objects which have brought new insights into physical processes occuring in the early Galaxy. The following section summarizes what we have learned on the yields of the first supernovae, for the elements from C to Zn. A paper is near completion on the neutron-capture elements in the same sample of stars. Let us just say that the scatter is much larger for these elements than for those up to Zn. The last section comes back to the question of the absence of true population III objects in the observations.

CS 31082-001:
THE URANIUM STAR

When we started our programme, only upper limits had been obtained on the amount of uranium in halo stars. One of them, CS 22892-052 (Sneden 2003), though, was highly enriched in all *r*-process elements (by 1.5 dex), including thorium, but was also C and N rich, with the best line of U II at 385.97 nm obliterated by a CN line. One of our program stars CS 31082-001, a giant of metallicity [Fe/H]= −2.9 (Hill et al. 2002), is also enriched in *r*-process elements by a similar factor, but with two favorable features: CN lines are much weaker and U and

Th are even more enriched than the other *r*-process elements, by a factor of about two. This has allowed a good measurement of both U (see Fig. 3) and Th in the star, making available for the first time the cosmochronometer U/Th. The difficulty is of course to know the production ratio of U and Th, but the availability of this uranium abundance has immediately triggered work in this field. From available pubished data in 2001, we derived an age of 14.0±2.4 Gyr for the formation of the *r*-process elements present in the atmosphere of CS 31082-001, completely independent of the cosmological estimate of the first star formation age by

WMAP (13.5±0.4 Gyr). We do not hope to reduce our uncertainty to 0.4 Gyr, but only to reduce it to 1.5 Gyr in the near future. This value is also to be compared with the age of 13.2±1.5 Gyr obtained by Chaboyer for the galactic globular clusters, by a method independent of the other two. This convergence is very impressive.

Curiously, what has caused the greatest impact in the astronomical community was not the new availability of the U/Th chronometer, but the fact that the use of the older Th/Eu cosmochronometer was giving a negative age for CS 31082-001, under the assumption that the production ratio of Th/Eu was universal. If instead the age derived from U/Th is believed, one must conclude that U and Th have been overproduced with respect to the "universal ratio" by more than a factor of two, clearly not good for the universality hypothesis. More stars have now been found with Th/Eu values incompatible with the "universal" production ratio , such as CS 30306-132 and HD 221170.

CS 31082-001 has a gorgeous spectrum of the neutron capture elements. For example, thorium has ten measurable lines, when only two or three are such in the other XMP stars. Our abundances of U and Th would have been very uncertain without the crucial work of physicists in Lund (Sweden), who redetermined the absolute oscillator strengths of the lines of uranium and thorium. Unfortunately a large number of atomic data are still missing for heavy nuclei, hampering a non-LTE analysis of their stellar spectra.

The abundance of lead was also recently obtained in CS 31082-001 (Fig. 4). As lead is produced in the radioactive decay of Th
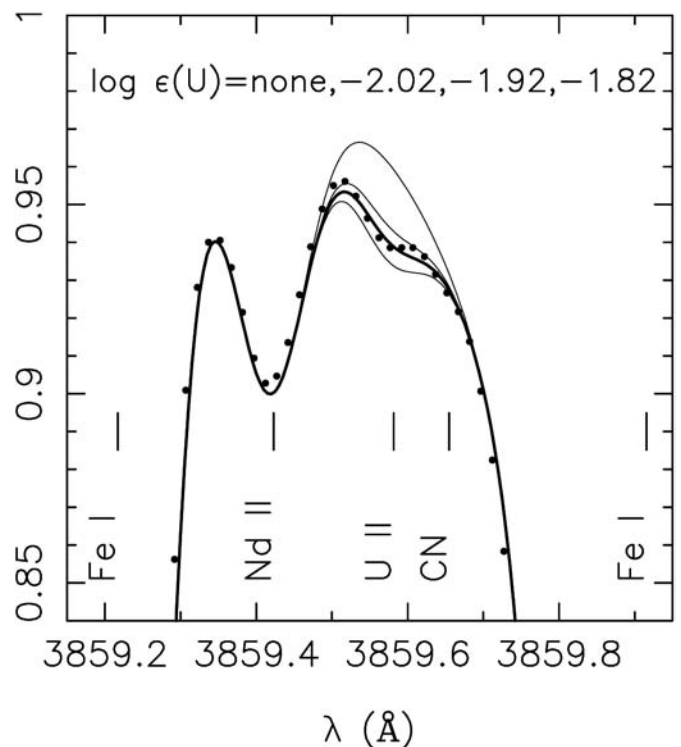

Figure 3: The spectrum of CS 31082-001 near the 3859.7 U II line.

Figure 4: The Pb I 4057.81 line in CS31082-001. It has been necessary to expose 17 hours to get this tiny feature out of the noise (S/N=600 for the cumulated exposures). The feature missing on the left is an unidentified molecular line containing carbon, because it becomes stronger in carbon-rich objects.
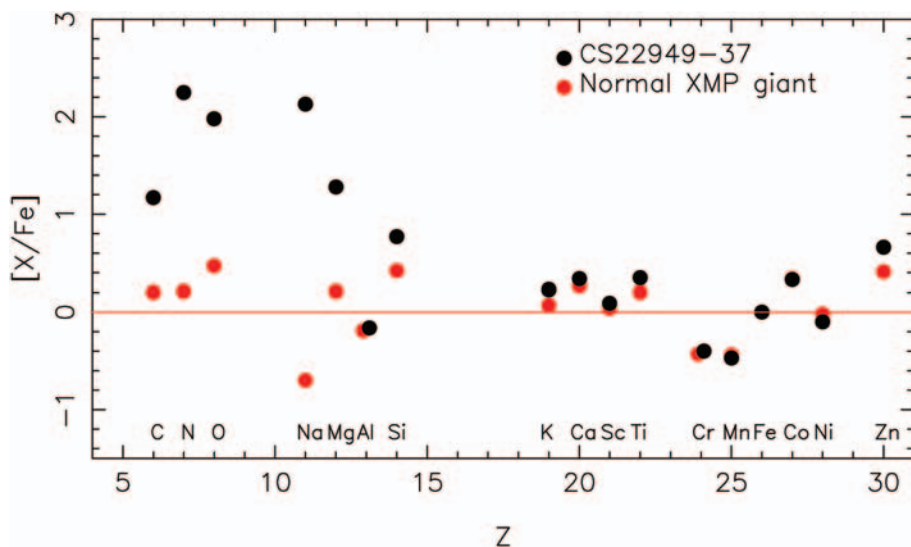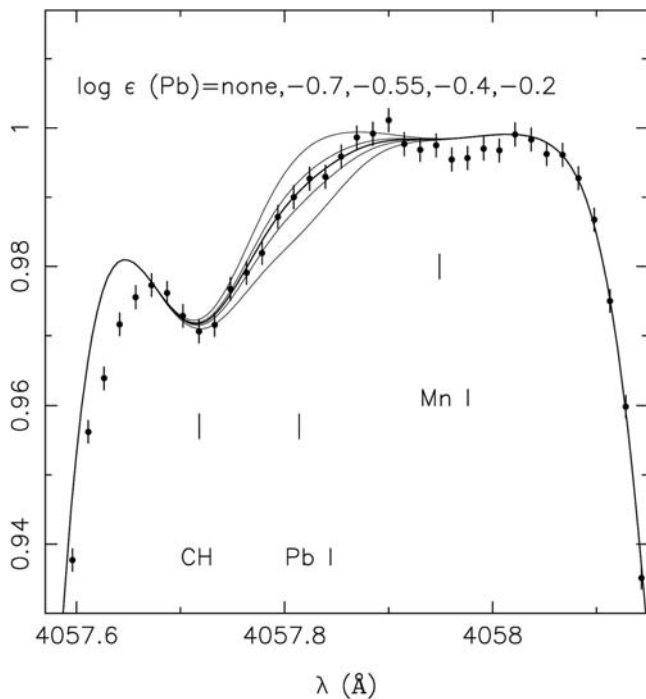

Figure 5: Abundance ratios in CS 22949-037 ([Fe/H]=–4), and in a normal mean XMP giant with [Fe/H] < –3. The abundance ratios are similar in both stars for elements heavier than Si. For the lighter elements there is a trend of decrease with increasing atomic number at variance with the normal XMP giants. This is very like what was predicted by Woosley and Weaver in 1995 as fall back in a supernova explosion.

(producing the isotope ^{238}Pb) and U (producing the isotopes ^{206}Pb and ^{207}Pb), it is interesting to know what fraction of lead is produced by this channel. The result of our LTE analysis is that 90 to 100 % of lead is produced by the decay of U and Th. A non-LTE analysis may lead to a smaller fraction, but it is unlikely that it can drop below 50 %. A non-LTE analysis is presently hampered by the lack of knowledge of the photoionization cross-sections of the ion Pb I.

Over 40 orbits of the HST have been obtained to extend our analysis of the neutron-capture elements to the spectral range 270 to 300 nm. The analysis is underway.

CS 22949-037: THE EVIDENCE FOR FALL-BACK IN SN II EXPLOSIONS

We have not discovered CS 22949-037, which is a XMP giant with [Fe/H] = –4.0, and which was already studied by Norris, Ryan, Beers et al. (2002). But we have found, against expectation for such low metallicity, that the forbidden line of [O I] at 630 nm was measurable, and determined the abundance of oxygen in the star. It was found that [O/Fe] = 2.0 ± 0.15, i.e. that oxygen is less deficient than iron by a factor of 100. This value is similar to what is found for nitrogen, [N/Fe]=2.2, and carbon, [C/Fe] = 1.2. Morover, we found evidence in

this star, as well as in all XMP giants which have lost their lithium, that dredge up bringing to the surface carbon processed into nitrogen has occured , suggesting that most of the N in CS 22949-037 was initially carbon, with [(C+N)/Fe] =1.7. If we plot the abundances as a function of [Fe/H] (Fig. 5), it is clear that the deficiency levels off at Si to a constant level.

In 1995 Woosley and Weaver had found, in a milestone theoretical paper, that if a supernova of 40 solar masses explodes with an energy of $1.9 \cdot 10^{51}$ erg, it expels only the upper shells containing C, O, and Ne (N if it has produced it), but that the lower layers fall back onto the core, feeding the remnant and not the interstellar medium. At an energy of $3 \cdot 10^{51}$ erg, on the contrary, the synthesized elements are all expelled.

The abundances in CS 22949-037 (Depagne et al. 2002) strongly suggest that we are witnessing a fallback event, as the deficiency gradient exactly follows the onionskin structure of the hydrostatic formation of the elements, those formed near the surface being much less depleted than those formed deeper. Usually, the computations with fallback expells a completely negligible amount of the most internal shells. The fact that CS 22949-037 shows a plateau for the elements produced in the most internal shells (K, Ca, Ti, Cr,Fe, Ni, ...) suggests that the fallback event occurred in a SN II born from a medium already slightly enriched, at the level [Fe/H] ≈ –4. Alternatively, some mixing may have occurred between the onion skins before or during the explosion.

CS 29497-030: A LEAD-STAR AT VERY LOW METALLICITY

Another remarkable object emerged from our programme. A theoretical prediction by Goriely and Siess in 2001 led to the expectation that s-process elements could be synthesized not by neutron-capture by Fe nuclei, but by neutron-capture of abundant species as C or Ne in zero-metal (primordial) AGB stars. Quickly after, Van Eck et al. discovered 3 stars, HD 187861, HD 196944, HD 224959, showing the predicted pattern of this theoretical work. The signature is a very high abundance of Pb, with a Pb/Ba ratio much greater than one. Because the mass of AGB stars is less than the mass of SN II, the yields of AGBs are expected to pollute a matter already enriched in iron by SN II, *even if these AGBs are initially of primordial chemical composition.* Indeed the three quoted stars have metallicities [Fe/H] in the range –1.7 to –2.5. This last metallicity was considered by former studies a little bit like the onset of the appearance of the s-process, only the r-process ocurring at lower metallicities. We were then very surprised (Sivarani et al. 2004) to find in our programme, devoted to stars of metallicity below –2.7, a lead-star, and not only a lead-
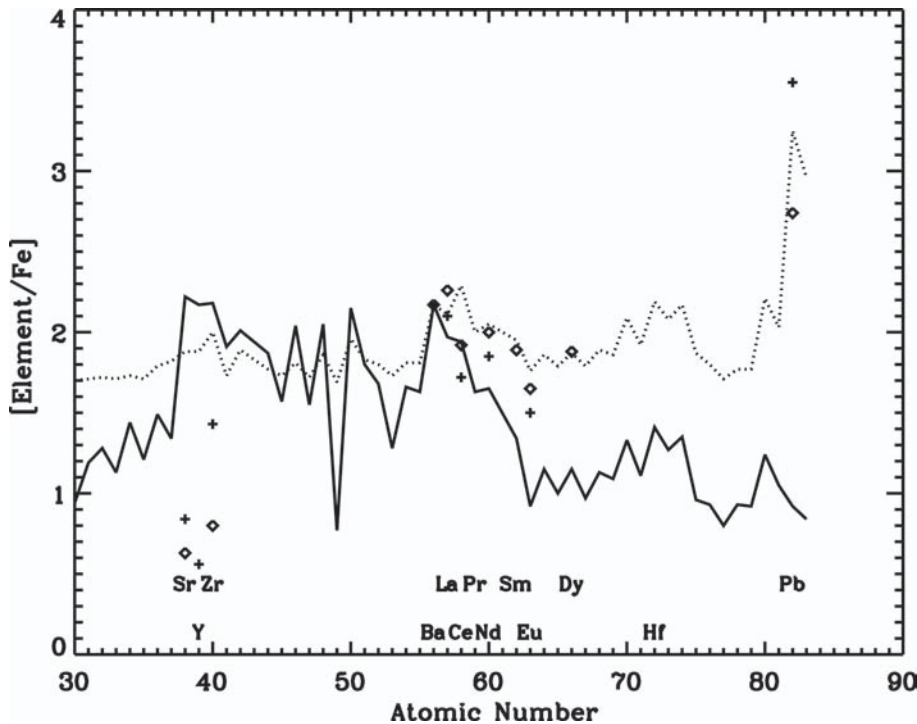
Figure 6: This figure represents the abundances of the neutron-capture elements in the star CS 29497-030 (+signs). The full line represents the s-fraction of the rescaled solar abundances. The dotted line shows results of computations by Goriely and Mowlavi (2000) for a metal-poor AGB stars after 50 thermal pulses. The lozenges are for a prototype lead-star CS31062-050. It is clear that CS 29497-030 is an extreme lead-star.

star, but the most extreme case of a lead-star, with [Pb/Fe] = 3.55 and [Pb/Ba] = 1.38 (Fig. 6).

THE YIELDS OF SNE IN THE PRIMEVAL GALAXY

The first elements in the Universe, aside from those synthesized in the primordial nucleosynthesis, were produced by massive supernovae of type II. This is simply a question of time scale. There are, though, two difficult questions with no certain answers. Did these first SNe pollute only the mini-halo (mostly composed of dark matter) in

which they originated, or the whole inter-galactic medium (IGM)? What delay has occured between the pollution of the surrouding matter by the ejecta of a SN and the moment in which this polluted matter has formed the small mass stars that we have observed with the VLT? These questions are part of the what we "do not (yet) know" of the title.

The first new element synthesized by massive SNe is carbon, formed by triple α-particle encounters. Our statistics on carbon are strongly biased by the fact that we have purposely avoided carbon-enriched stars in

our observing programme, because of the nuisance caused by CH and CN lines in the study of the rare elements, whose lines are frequently blended by the lines of these molecules, of course enhanced in C-rich objects. Even so, our diagramme [C/Fe] versus [Fe/H], Fig. 7, clearly shows an intrinsic dispersion of the abundance of carbon in our sample.

This is a first feature of the yields of the primeval SNe. A fraction of 15 to 25% of XMP stars are carbon rich, for their metallicity in iron-peak elements. The most extreme case is the star HE0107-5240, which has [Fe/H] = –5.3, the record for low metallicity, but [C/H]=–1.3. Note that, like CS 22949-037, the deficiency in O and N is also much less than for iron, with [O/H]=–3.3 and [N/H]=–3.0 (Christlieb et al. 2003, Bessell et al. 2004).

The intrinsic scatter, conspicious for carbon, is also significant for sodium, but the great surprise in our LP was that the scatter is surprisingly small from the majority of the other elements. The case of the diagram [Cr/Fe] versus [Fe/H] (Fig. 8) is especially puzzling. The scatter is entirely explained by observational errors! So, there is no room for intrinsic scatter. If there was no slope, we would concude that Cr and Fe are produced in a constant ratio by the SNe, and that we observe objects born from a primordial matter polluted by the ejectas, at various levels. No problem. But if the slope is interpreted as a variable production ratio of Cr and Fe in SNe as a function of the metallicity, we then have the problem, with no intrinsic dispersion, that a SN II has to mix its ejecta with a prescribed amount of interstellar matter. We do not accept this interpretation for two reasons. The first is that we believe that the mixing process is unavoidably of stochastic nature, and that the scatter in this process cannot be below 0.05 dex. The second reason is that, as we shall see later, there is a high probability
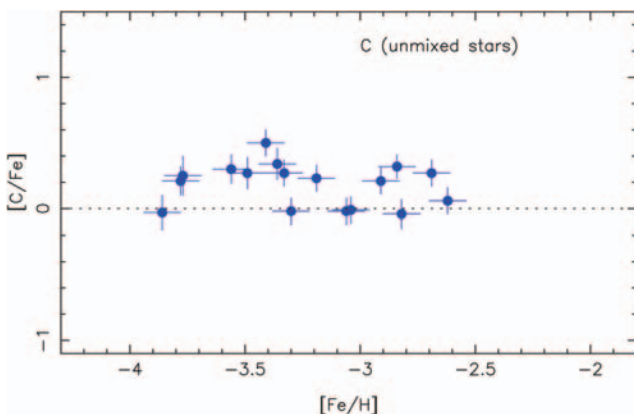

Figure 7: The abundance of carbon is affected by internal mixing in the giants brighter than the « bump ». This figure show the scatter in the original carbon abundance, after elimination from the sample of the giants affected by internal mixing, recognizable by the fact that they have lost their lithium and that they are nitrogen rich.
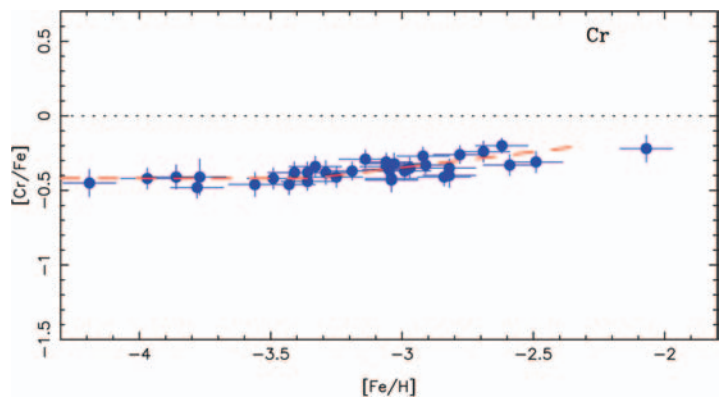

Figure 8: This plot was the one which puzzled us the most, from our Large Programme. The scatter is so small that it is entirely explained by the observational errors, about 0.05 dex. See the text for a discussion of this diagram. The slope disappears below [Fe/H] =-3.3.

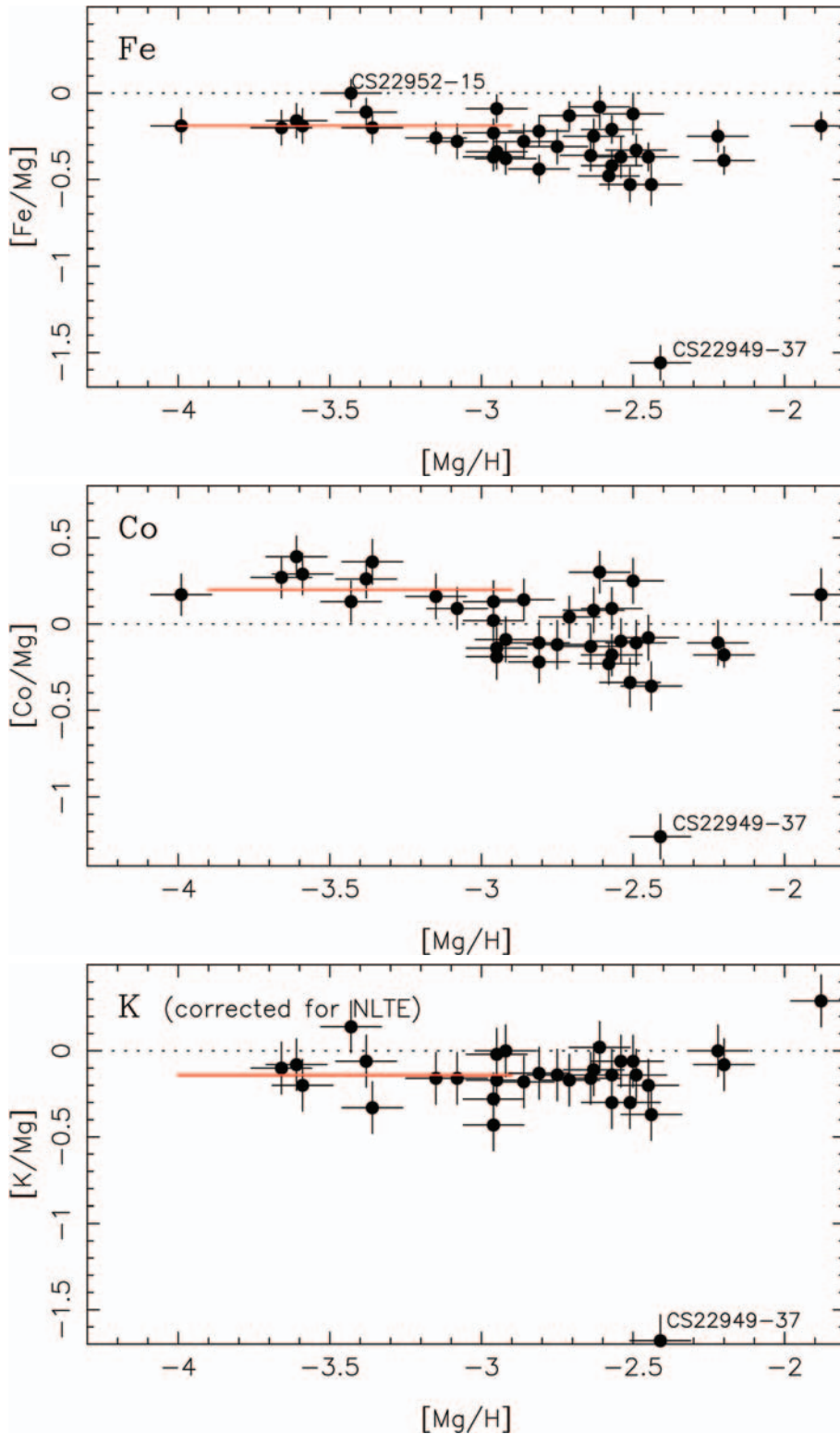**Figure 9:** Three plots representing, from bottom to top, [Fe/Mg], [Co/Mg] and [K/Mg] versus [Mg/H]. Note that the production ratios are not solar, but that no slope is apparent for [Mg/H] less than −3.0.

All of that leaves the impression that the slope may be spurious, generated by over-simplifications in the abundance determinations, and have nothing to do with nuclear physics.

The choice of iron as tracing the so-called metallicity in the sample is made for practical reasons, essentially the very large number of available lines. But iron may be a poor choice from a nucleosynthesis point of view. It is formed very close to the frontier between the ejected layers and the remnant core. The famous cut. It is safer to take an α-element as oxygen, magnesium or silicon. Oxygen is very difficult from a practical point of view. So we have tried magnesium, which has the advantage of being more easily ejected than silicon. A sample of plots of ejecta production ratios with [Mg/H] are given in Fig. 9a,b,c. Indeed there is very little metallicity effect visible in these diagrams. Table 1 summarizes the values of the abundances found in such diagrams, i.e. the flat abundance ratios when [Mg/H] is below −3.0. The last column is the number of stars in the mean. For the elements C, N, Na and Al, only the stars with no dredge up have been included.

We then conclude that we have reached the primordial yields of the early Galaxy, and we compare them to several theoretical yields in Fig. 10a,b,c. Obviously the yields to be rejected are the yields of the pair-instability SNe (Heger & Woosley 2002). The yields of the 15 to 50 solar mass SNe by Woosley and Weaver (1995), or Chieffi and Limongi (2003) are clearly closer to our observational results.

RETURN TO POPULATION III STARS

The details of the formation of massive stars are poorly known even in population I. Actually, the September 2004 issue (No. 117) of the *Messenger* contains the most up to date information on this subject (*The Birth of a Massive Star*, R. Chini et al.) for the stars in formation in our Galaxy. In a zero-metal environment, things are different, and what we know relies almost exclusively on theoretical work. The major physical change from star formation in the today Galaxy is that the cold gas from which stars form cools only by the unefficient H_2 quadrupole radiation, and has great difficulty to radiate. This may prevent fragmentation of the collapsing cloud below a certain limit, which may be higher than a few solar masses.

The exact value of this limit is one more thing we do not really know. But if this limit is 0.9 solar mass or larger, even the less massive primordial stars are now fully evolved as white dwarfs or neutron stars, not visible in our observing programmes. This is probably the simplest explanation for the lack of observed population III stars. Let us note,

that, at the level of metallicity of our sample, we oberve ejectas of primordial SNe, in which there is no dependence of production ratios with metallicity, as the metallicity is zero. Then, how do we explain the slope? Theoretical computations of departure to LTE for iron in dwarfs and sub-giants, have found a metallicity dependance, with corrections to LTE, about zero at solar metallicity; increasing to 0.3 dex at metalliciy −2.5. Virtually nothing is known for what is occurring between −2.5 and −3.5, still less in giants of log(g)=1.5, and still less for chromium. Note also that no significant slope is visible between [Fe/H] ≈ −3.5 and −4.2.

Table 1: This table gives the production ratios of the elements for [Mg/H] less than −3.0, believed to represent the yields of primordial supernovae, imprinted in the chemical composition of the most metal-poor stars

Elem	dex	rms	N
[C/Mg]	−0.01	0.10	9
[N/Mg]	0.00	0.11	9
[O/Mg]	+0.32	0.21	13
[Na/Mg]	−0.91	0.16	9
[Al/Mg]	−0.39	0.05	9
[Si/Mg]	+0.21	0.14	14
[K/Mg]	−0.14	0.14	13
[Ca/Mg]	+0.06	0.09	14
[Sc/Mg]	−0.17	0.14	14
[Ti/Mg]	−0.01	0.09	14
[Cr/Mg]	−0.63	0.09	14
[Mn/Mg]	−0.65	0.20	14
[Fe/Mg]	−0.21	0.10	14
[Co/Mg]	+0.13	0.17	14
[Ni/Mg]	−0.23	0.13	14
[Zn/Mg]	+0.21	0.19	14

Figure 10: Three plots comparing our yields with theoretical yields (bottom to top) of pair-instability hypernovae, with masses from 140 to 260 solar masses (Heger & Woosley 2002), SN II of masses between 15 and 35 solar masses (Woosley & Weaver 1995) and SN II of masse 15 to 50 solar masses (Chieffi & Limongi 2003). The pair-instability hypernovae have the larger misfit with our observations, in particular for odd elements and zinc.

however, that even if protostellar cores of small mass have developped in the vicinity of young massive stars, they have not had enough time to complete their formation before strong winds and supernovae explosions of the most massive stars have polluted their infalling matter, or brought their formation to abortion.

An excellent review paper on the theoretical work on the formation of population III has just been published (Bromm & Larson, 2004). It contains a wealth of information.

One of the most fascinating hopes for the future is the direct observation of the SNe having produced the yields that we have described here. In 1997, Miralda-Escudé & Rees established that these supernovae should be the brightest objects of the Universe at the epoch $z = 5$ to 10. They should be bright enough to be observed with the James Web Space Telescope in the K-band (2.2 μm). An interesting firework.

REFERENCES

Beers, T.C., Preston, G.W., Shectman, S.A. 1985 AJ 90, 2089
Bessell, M.S., Christlieb, N., Gustafson, B. 2004, ApJ, 612L, 61
Bromm, V., Larson, R.B., 2004, Ann. Rev. Astron. Astrophys. 42, 79
Chieffi A., Limongi, M. 2003 in ESO Astrophysics Symp. *From Twilight to Highlight: The physics of supernovae* (Hillebrandt & Leibundgut eds), p. 367
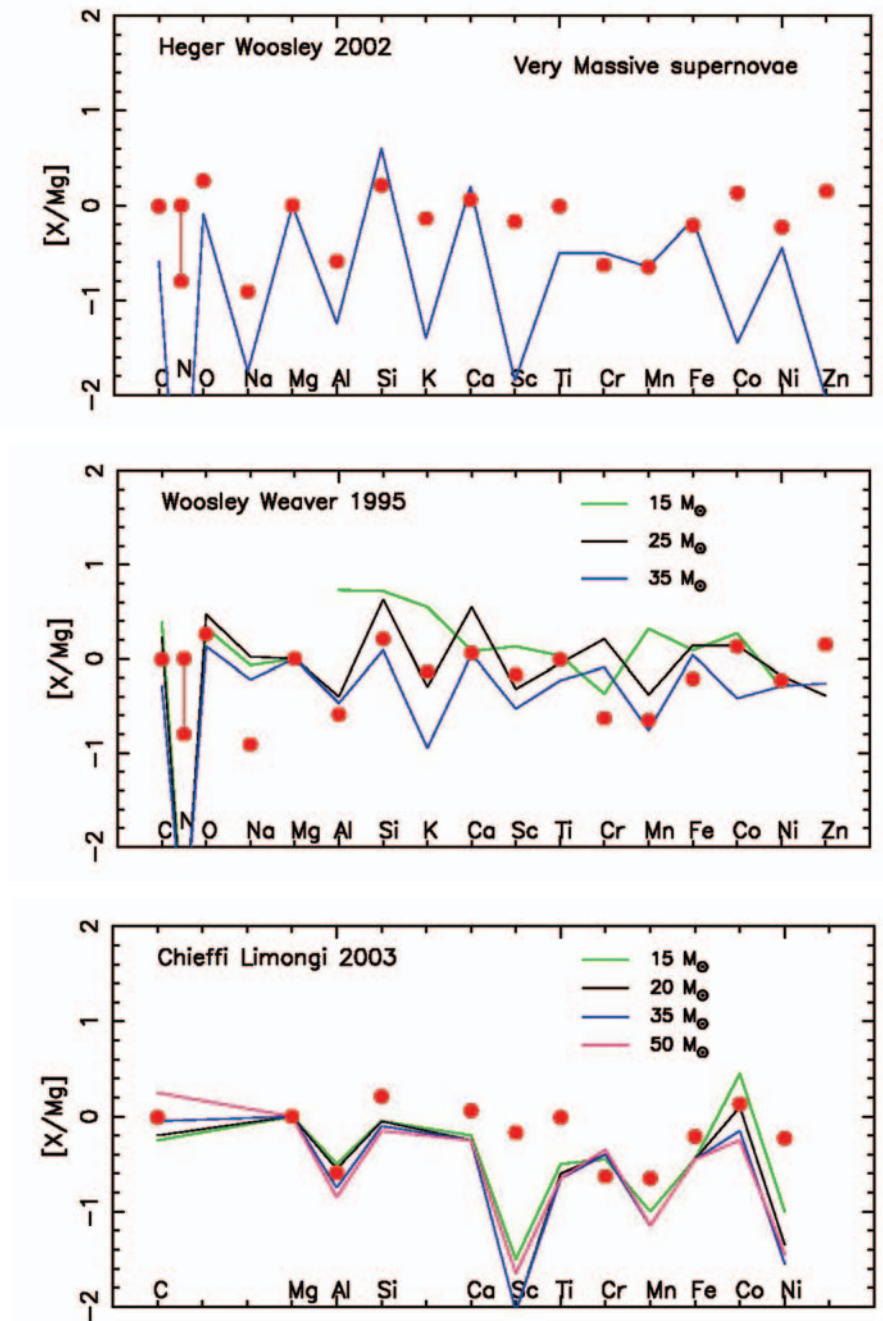Chini R. Hoffmeister, V., Kimeswenger S. et al. 2004, The Messenger, 117, 36
Christleb, N., Gustafsson, B., Korn, A.J. 2004, ApJ, 603, 708
Coc, A., Vangioni-Flam, E., Descouvemont, P. et al. 2004, ApJ, 600, 544
Depagne, E., Hill, V., Spite, M. et al. 2002, A&A, 390, 187
Goriely, S. & Siess, L. 2001, A&A, 378, L25
Goriely, S. & Mowlavi, N. 2000 A&A 362, 599
Heger, A. & Woosley, S.E. 2002, ApJ, 567, 532
Hill, V., Plez, B., Cayrel, R. 2002, A&A, 387, 560

Miralda-Escudé, J. & Rees, M.J. 1997, ApJ, 478L, 57
Norris, J.E., Ryan, S.G., & Beers, T.C. et al. 2002, ApJ, 569L, 107
Sivarani, T., Bonifacio, P., & Molaro, P. 2004 A&A, 413, 1073
Spergel, D.N., Verde, L., Peiris, H.V. et al. 2003, ApJ SS, 148,175
Sneden,C. , Cowan, J.J., Lawler, J.E. et al. 2003, ApJ, 591, 936
Van Eck, S., Goriely, S., Jorissen, A. et al. 2003 A&A, 404, 291
Woosley, S.E., Weaver, T.A. 1995, ApJS, 101, 181

A Livelier Picture
of the Solar Neighbourhood

The formation and evolution of galaxies is one of the great outstanding problems of modern astrophysics. A new radial-velocity survey of over 14,000 nearby, long-lived stars now documents the history of the Solar neighbourhood in unprecedented detail – and severely challenges models for the evolution of galactic disks.

Birgitta Nordström[1,2],
Michel Mayor[3],
Johannes Andersen[1,4],
Johan Holmberg[1,4],
Bjarne R. Jørgensen[2],
Frédéric Pont[3],
Erik H. Olsen[1],
Stephane Udry[3], and
Nami Mowlavi[3]

[1]Niels Bohr Institute for Astronomy, Physics, and Geophysics, Copenhagen University, Denmark
[2]Lund Observatory, Sweden
[3]Observatoire de Genève, Switzerland
[4]Nordic Optical Telescope Scientific Association, Spain

Spiral galaxies are an important part of the visible Universe, and the prototype is our own Milky Way. Our central vantage point is ideal for observing the most important component of Milky Way and any other spiral galaxy – the disk. And the numbers, ages, detailed chemical compositions, and galactic orbits of nearby, long-lived disk stars carry vital information on its evolution (Freeman & Bland-Hawthorn 2002).

In the Solar neighbourhood we can determine these parameters for stars from the entire history of the disk with a completeness and accuracy not available anywhere else in the Universe. The stars in the Solar neighbourhood therefore provide a fundamental benchmark for all theoretical models of the chemical and dynamical evolution of galaxy disks.

For truly incisive tests of the models we need space velocities and galactic orbits, metal abundances, ages, and binary star identification for a large, complete sample of long-lived stars. Until now, stellar samples were either complete but key data were missing, or the data were complete but the sample suffered from serious selection biases. Both cases may lead to wrong results.

The Geneva-Copenhagen Survey

The Geneva-Copenhagen Survey of the Solar Neighbourhood (Nordström et al. 2004) was designed to provide a new, superior basis for our understanding of the evolution of the Milky Way disk. For the first time, we have obtained accurate, multiple radial velocity observations for a large, complete, and unbiased sample of over 14,000 long-lived stars near the sun. These have been combined with other data and new calibrations to compute complete space motions, Galactic orbits, metallicities, and ages for all the stars. Binary stars (34% of the sample) are identified as well.
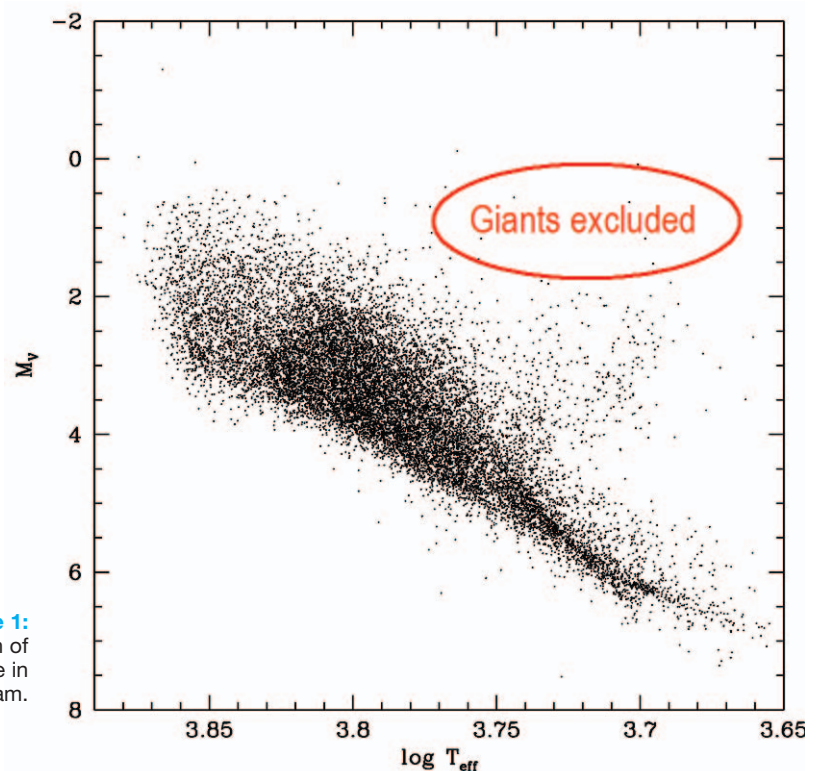

Figure 1:
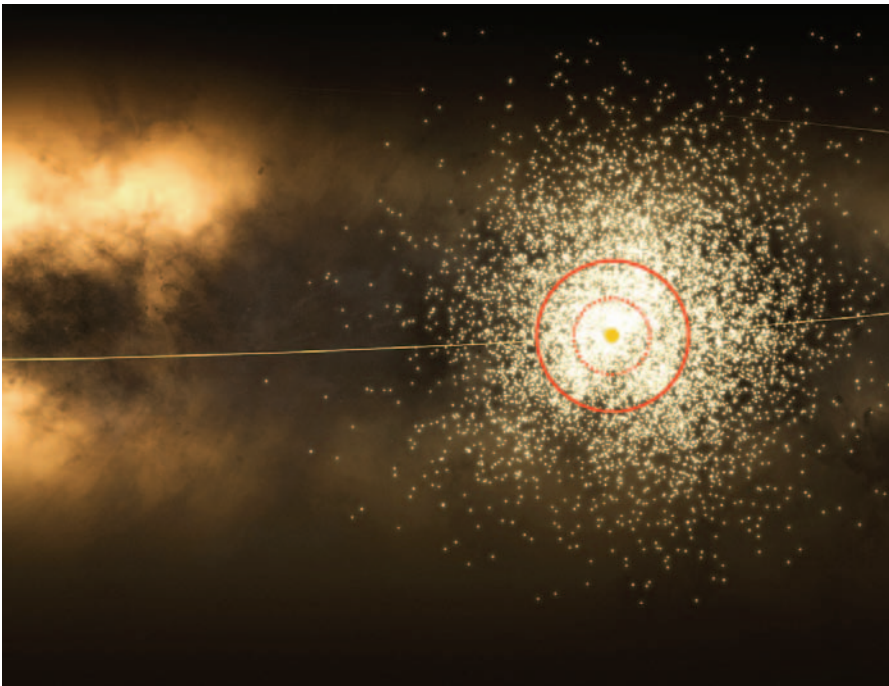Distribution of the sample in the HR diagram.

Figure 2: Artist's impression of the 3D distribution of the sample around the sun (cutaway view for clarity). The completeness distance of 40 pc is indicated by the dotted circle (courtesy Lars Christensen, ST/EcF).

The foundation for the survey was laid in the 1970s and 1980s by Bengt Strömgren and Erik Heyn Olsen. All stars of HD spectral type A5 to late G in the entire sky and brighter than visual magnitude ~8.5 were measured in the Strömgren $uvby\beta$ colour system, largely with the Danish 50cm telescope at La Silla - some 30,000 stars in total (Olsen 1994 and earlier papers).

From this photometry a complete sample of 16,682 F and G-type dwarf stars could be defined without any bias with regard to metal abundance or kinematics (see Fig. 1). The sample is defined by limiting apparent magnitude, but in such a way as to be essentially volume complete to a distance of 40 pc, while the brighter stars reach distances of 2-300 pc (Fig. 2).

Distances, metal abundances, and ages can be determined from the photometry, as outlined below. Proper motions – hence the velocity components in the plane of the sky – were available from the Hipparcos and TYCHO-2 astrometric catalogues. The "missing link" was the space motion component along the line of sight – the radial velocity.

A precise radial velocity completes the full 3D space motion vector of the star. Any variation of the radial velocity signals a binary star, for which the photometric values of distance, age, and metal abundance will be wrong.

However, multiple radial velocity measurements of many thousands of stars from conventional photographic spectra required such large amounts of telescope time that the task had long been considered impossible. Therefore, existing radial-velocity samples were biased towards 'interesting' kinds of stars, potentially introducing artificial correlations between age, metallicity, and kinematics.

However, the Geneva-Marseille radial-velocity spectrometer CORAVEL (Baranne et al. 1979) brought together cross-correlation spectroscopy, a low-noise photoelectric detector, and a computerised system for instrument control and data collection. This was the efficient tool needed to do the job right. The first CORAVEL was commissioned at the Swiss 1m telescope at Observatoire de Haute-Provence (OHP), France, in 1977, and it was agreed to place the second one at the Danish 1.5m telescope on La Silla. In 1981 our all-sky survey was initiated at both telescopes (see Fig. 3).

A THOUSAND AND ONE NIGHTS

Obtaining over 60,000 CORAVEL observations of more than 14,000 programme stars was still a huge task, requiring over 1,000 clear observing nights between the two telescopes. But the rapid scanning rate of CORAVEL made the instrument almost insensitive to sky conditions, so every night a star could be seen anywhere in the sky was usable. Veterans of La Silla may still remember gazing in amazement at the open dome of the Danish 1.5m on many a night when all other observers were fast asleep…
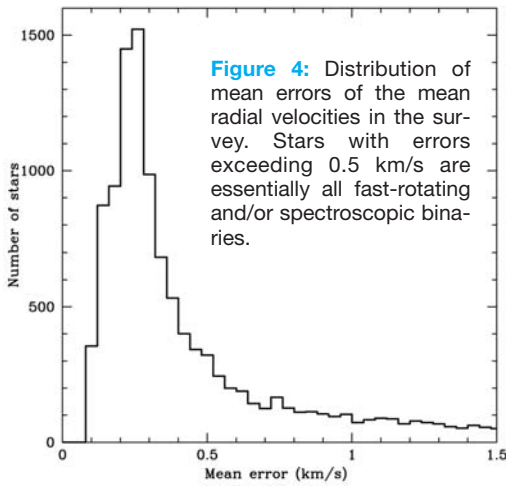
In view of later developments for the VLT, it is interesting to note that the CORAVEL team introduced flexible scheduling and service observing on La Silla long before those terms had even been coined. Several joint programmes were conducted in parallel, ranging from Cepheids and supergiants in the Magellanic Clouds over the detailed kinematics of 47 Tuc and ω Cen to all-sky programmes of bright field stars, such as ours.

When the seeing was good and the faint objects were up, or when observations at particular phases were needed, the observationally demanding programmes had priority; otherwise our bright stars got done. We
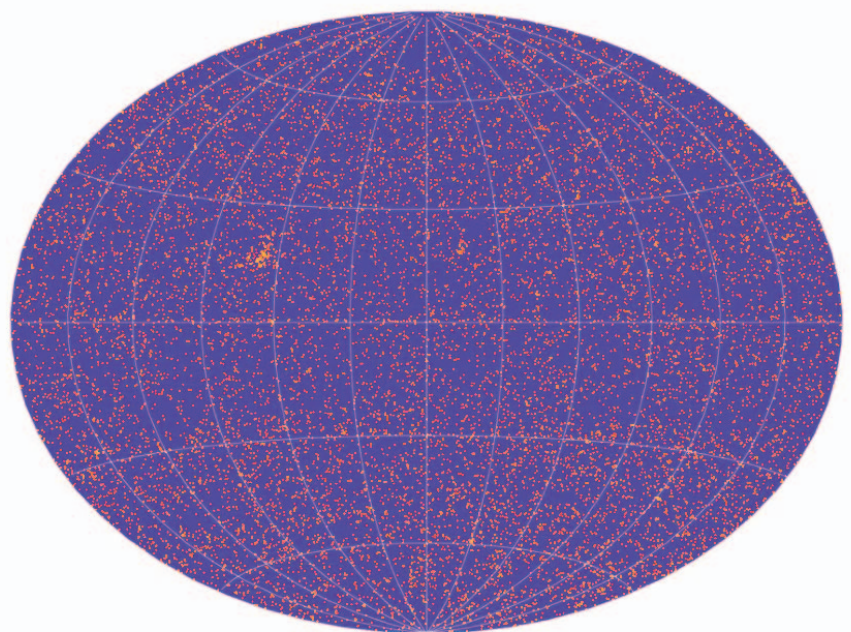
Sky Distribution of ~14.000 Observed Stars

Figure 3: The Geneva-Copenhagen survey stars projected on the sky (note the Hyades cluster at upper left).

Figure 4: Distribution of mean errors of the mean radial velocities in the survey. Stars with errors exceeding 0.5 km/s are essentially all fast-rotating and/or spectroscopic binaries.

owe a great debt of gratitude to the many colleagues who thus contributed to our programme at both telescopes.

The hardware correlation mask in CORAVEL is optimised for sharp-lined late-type stars. For the fast-rotating early F stars on our programme ($v \sin i \geq 30$ km/s), it gave results of poor accuracy – if any at all. Most of these stars were therefore reobserved at the Harvard-Smithsonian Center for Astrophysics (CfA), USA, where digitally recorded spectra correlated with synthetic templates yield good radial velocities for rotations up to 140 kms-1 (Nordström et al. 1997). The resulting radial velocities are of superb accuracy, with a typical mean error of 0.25 km/s (Fig. 4) – some 20 times better than those to be obtained from the GAIA mission. In order to identify spectroscopic binaries, the average star has 4 observations obtained over 1–3 years, but some have data extending over 10–15 years. Overall, we find 3,223 (19%) spectroscopic and 3,537 (21%) visual binaries of all kinds in the sample, for a total binary count of 5,622 (34%; some stars are in both categories).

DISTANCES, SPACE VELOCITIES, AND GALACTIC ORBITS

Photometric distances from the *uvby* photometry were compared with the Hipparcos results for stars with parallaxes better than 3%. We found that the photometric distances had an accuracy of 13% and no significant systematic errors. Thus, photometric distances were used if the Hipparcos parallax was worse than 13% or not measured at all, so all distances should be accurate to about this value.

Proper motions were taken from the TYCHO-2 catalogue. Together with the distances and radial velocities, they yield full 3D space motions U, V, W with an accuracy of about 1.5 km/s in each component. These, in turn, were used to compute the orbit of each star in its motion around the Galactic centre, assuming a smooth gravitational potential satisfying the observational con-

straints provided by the Galactic rotation curve and the local matter density. Within these assumptions, the motion of a star can be followed for two Galactic rotations backward and forward in time – still much shorter than the average lifetime of the stars.

METALLICITIES AND EFFECTIVE TEMPERATURES

The metal content of F and G dwarfs can also be derived from the Strömgren photometry, using a suitable calibration. We have checked the existing metallicity calibrations and consolidated and extended them to the highest and lowest temperatures seen in our sample, using reliable spectroscopic analyses for comparison. The resulting metallicities have an accuracy of 0.1 dex over the whole temperature range.

Effective temperatures are needed in order to compute ages for the stars. They were derived from the reddening-corrected Strömgren photometry through the calibration of Alonso et al. (1996).

COMPUTING AGES

Computing ages for our sample, which extends back to the formation of the disk 10 Gyr ago or more, is a far more complex task. The only reliable method is to fit stellar evolution models (isochrones, from Girardi et al. 2000) to the observed stellar parameters – simple in principle, but not so in practice.

If a star has not evolved perceptibly in the HR diagram its age is basically indeterminate; and most evolutionary changes remain fairly small relative to typical observational errors. Moreover, the strong variation in speed of evolution over the HR diagram combines with the prior distributions

in mass, absolute magnitude, and metal abundance in subtle ways. This can lead to large systematic errors in the ages and completely misleading estimates of their true reliability and accuracy.

Our stellar ages were determined by considering the three-dimensional HR 'cube' (T_{eff}, M_V, [Fe/H]). For each point in the cube, we computed the probability that the observed star could be located there and have the age of the isochrone passing through that point, given the observational errors. These probabilities were integrated in a Bayesian manner over the whole cube, taking the *a priori* distributions of masses, etc. into account.

The result is an *a posteriori* probability density distribution for the possible ages of the star. This so-called 'G function' is normalised to 1 at the maximum, which denotes the most likely value of the actual age (Fig. 5). The method is described in more detail by Jørgensen & Lindegren (2004); it is similar in many respects to that of Pont & Eyer (2004), but differs in some numerical respects and in the calibrations and corrections applied to the data and the models.

The points where the G function drops to the value 0.6 define the ±1σ error limits for the ages. If both are inside the age range of the models (0–17.8 Gyr) we call the age 'well-defined', and both are given in the catalogue (the error can still be large, but at least its value is reliably known!). If one of the limits is outside the range of the isochrones, only an upper or lower age limit is given, and none at all if the G function is too flat to go below 0.6 anywhere in the range.

In this manner, ages of any quality are determined for 13,636 of our total of 16,682 stars, 11,445 of which are 'well-defined'. If we limit the sample to the 11,060 single stars, 7,566 have well-determined ages, out
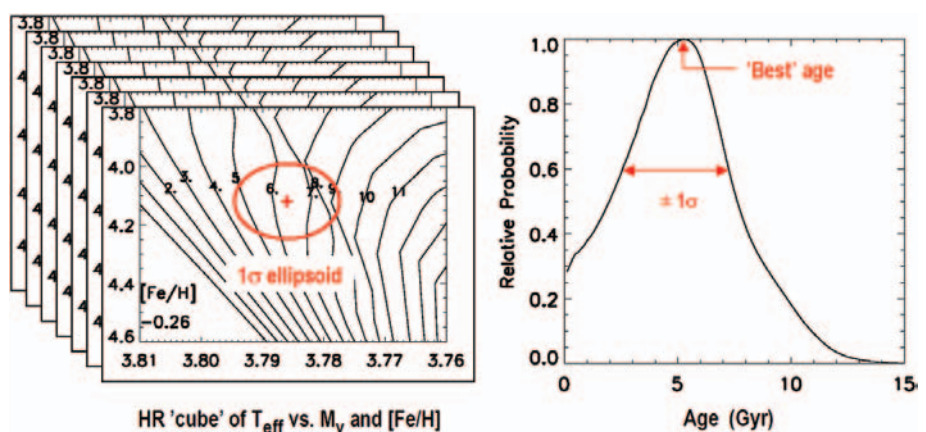

HR 'cube' of T_{eff} vs. M_V and [Fe/H]

Figure 5: For every point inside and outside the error ellipsoid in the HR 'cube' (left), the probability that the observed point could fall there is computed. Taking statistical biases into account, this is integrated to form the G function (right), i.e. the probability that the star has any given age in the interval covered by the isochrones.
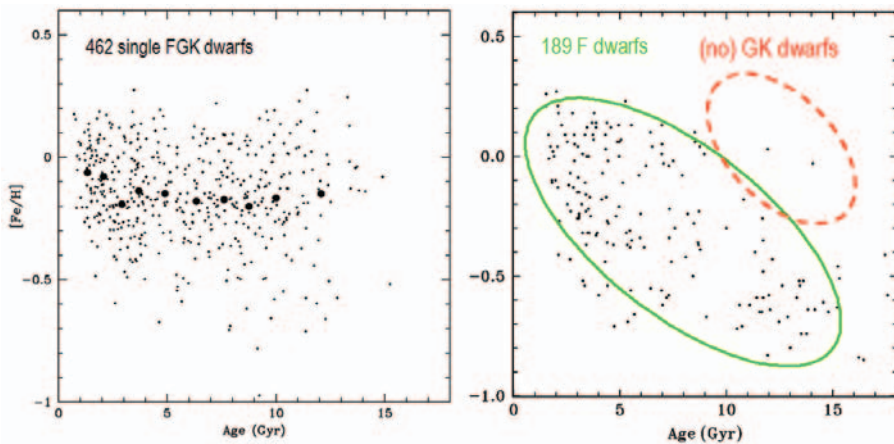
Figure 6: Age-metallicity diagrams for all single stars within 40 pc and with well-defined ages (left), and for the stars of Edvardsson et al. (1993, right).

of which 6,144 have ages better than 50% and 3,528 better than 25%.

We emphasise that because the conditions for accurate determinations vary dramatically across the HR diagram, the stars with (good) ages are not a representative sample of the Solar neighbourhood as a whole.

CLASSICAL TESTS OF CLASSICAL MODELS

The classical type of Galactic evolution models consider the disk to be a rotationally symmetric, well-mixed system, adequately described by the variation of mean chemical composition and kinematics with age and distance from the Galactic centre. Stars are assumed to be born with a constant Initial Mass Function and at specified rates over time, evolve, die, and gradually enrich succeeding generations of stars in heavy elements. The delay after which the two supernova types explode may be included, and infall of intergalactic gas may be added as another parameter.

Meanwhile, massive objects in the disk – perhaps spiral arms or giant molecular clouds – perturb the circular motions of the newborn stars and cause their random velocities to increase with time ('dynamical heating').

Such models yield specific, single-valued predictions for the variation of metallicity and kinematics as functions of age and radius in the disk. Thus, their degree of realism can be tested by comparison with samples of local stars with accurate data. But the samples must be large and cover the age of the disk, the data must be complete and accurate, and correlations between the parameters we want to study must not be built in.

As summarised above, this is exactly what we have strived to achieve. But before we describe the actual tests, it is worth pointing out that the importance of the radial

velocities extends far beyond the computation of velocity dispersions:

First, they allow us to identify – and if need be, eliminate – the spectroscopic binaries for which neither metallicity, age, nor space motion is reliable. Second, the velocities distinguish the 'transit passengers' from far away from the stars that have spent their life in our neighbourhood and contributed to its evolution. And third, they allow us to correct the frequencies of different stellar groups for the speed with which they cross the little volume around the sun that we have observed.

THE 'G DWARF PROBLEM'

The first classical test of the models is the metallicity distribution of long-lived stars that can survive from the formation of the disk. The long-standing 'G dwarf problem' (van den Bergh 1962) refers to the observed lack of old, metal-poor dwarf stars that

should have formed in large numbers together with the massive stars that produced the heavy elements we observe in the younger generations.

The problem was re-examined by Jørgensen (2000), who found that the deficit of metal-poor dwarfs was even more marked in our complete, unbiased sample: Our part of the disk certainly did not evolve as a closed system!

THE AGE-METALLICITY RELATION

The second classical test of the models is the gradual rise of metallicity with time, as new heavy elements are synthesised in stars and built into the following generations – the so-called Age-Metallicity Relation (AMR). The key features here are the shape of the average relation and the amount of scatter around it. Key questions are whether variation of the mean is consistent with the gradual enrichment picture, and whether a mean relation describes the distribution of the observed values adequately when the observational uncertainty is accounted for.

Figure 6 shows the AMR for our volume-complete subsample of stars within 40 pc and with 'well-defined' ages. Larger samples have been studied, but the conclusion is the same: There is no significant change in mean metallicity in the Solar neighbourhood over the past ~10 Gyr, and the scatter in [Fe/H] at all ages greatly exceeds the observational error of ~0.1 dex. Scatter is the key message here, not any 'mean trend', and classical models cannot explain it.

Figure 6 contrasts our result with the much-quoted spectroscopic study of 189 of our F dwarfs by Edvardsson et al. (1993). The two studies were planned to be complementary - exquisite detail vs. completeness and freedom from bias - and together they
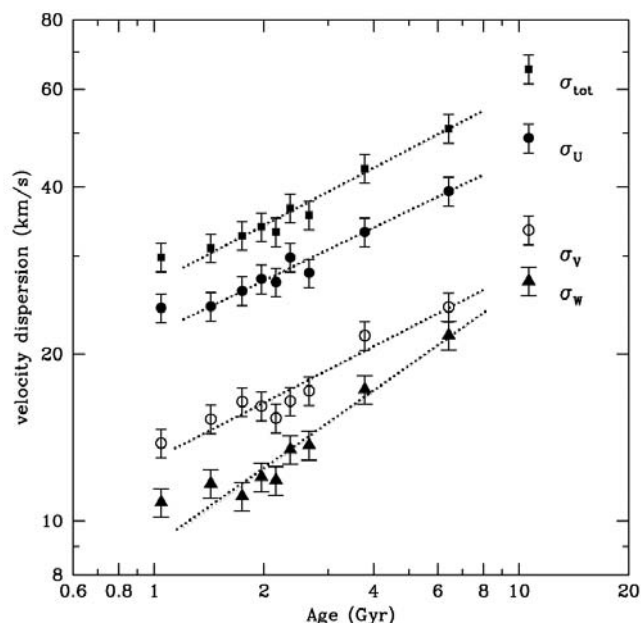

Figure 7: Velocity dispersions as a function of age for 2,852 single stars with ages better than 25%.
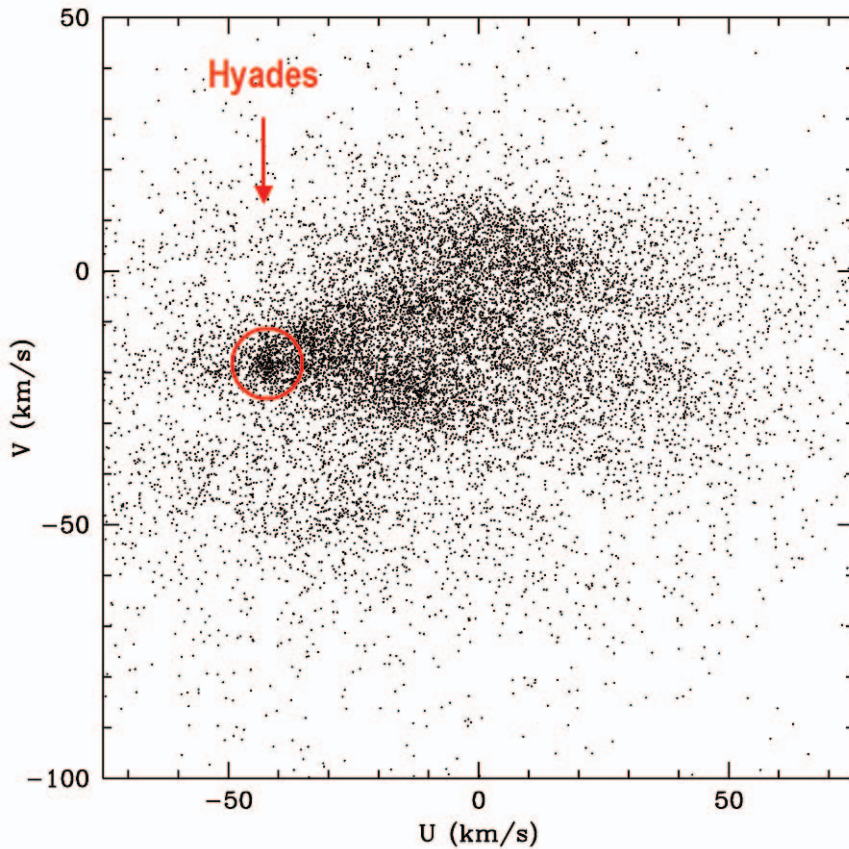
Figure 8: U-V diagram for all the stars in the sample.

provide very strong constraints on models of the evolution of our Galaxy.

It is obvious that the scatter in [Fe/H] is at least as large for their data as for ours, but their sample of F stars automatically excluded any old, metal-rich stars from consideration – a limitation recognised by Edvardsson et al. (1993) themselves. Accounting for this, the two diagrams are in fact consistent, although both ages and metallicities were obtained by quite different techniques.

THE LOCAL DYNAMICAL EVOLUTION

Figure 7 shows the velocity dispersions as functions of age for the stars with the best-determined ages in the sample. The slope of the relations is intermediate between earlier results and shows that (i) radial mixing of stellar orbits cannot explain the scatter in the AMR; (ii) the classical disk heating mechanisms cannot explain the observed results; but (iii) all kinematic traces of any dwarf galaxies that might have merged with the Milky Way in its early stages should be erased by now.

Finally, as Fig. 8 shows, the velocity distribution of the stars in our neighbourhood is far from smooth, but shows marked, discrete features. The stars in these have a broad range of both metallicities and ages. Thus, they were not simply formed together but are the result of dynamical focusing, probably from passing through a spiral arm.

This implies that, e.g. identifying local stars of the thick disk by Gaussian decomposition of the velocity distribution is risky at best. Further, a smooth, symmetric gravitational potential seems inadequate for computing stellar orbits for more than a short time span into the past or the future.

CONCLUSIONS AND OUTLOOK

As we have seen, classical disk evolution models spectacularly fail every classical test when confronted with our data: Neat sharp lines simply do not describe even the main features of the story correctly.

An entirely new generation of 3D models is needed, including real physical descriptions of the (hydro)dynamics of star formation, supernova explosions, and galaxy mergers. But it will be a long time before their numerical resolution is sufficient to match the full detail of our new picture of the Solar neighbourhood.

As a test sample for such models, the Geneva-Copenhagen survey will remain unique for many years: No similarly large set of accurate radial-velocity data for an astrophysically selected sample of stars exists, and none is planned. While the ESA cornerstone mission GAIA will provide many more radial velocities around 2015, their precision will be 20 times lower than ours, making binary star detection notably less complete than in our survey.

REFERENCES
Alonso, A., Arribas, S. Martínez-Roger, C. 1996, A&A 313, 873
Baranne, A., Mayor, M., Poncet, J.-L. 1979, Vistas in Astron. 23, 279
Edvardsson, B., Andersen, J., Gustafsson, B. et al. 1993, A&A 275, 101
Freeman, K.C., Bland-Hawthorn, J. 2002, ARA&A 40, 487
Girardi, L., Bressan, A., Bertelli, G., Chiosi, C. 2000, A&AS 141, 371
Jørgensen, B.R. 2000, A&A 363, 947
Jørgensen, B.R., Lindegren, L. 2004, A&A, in press
Nordström, B., Stefanik, R.P., Latham, D.W., Andersen, J. 1997, A&AS 126, 21
Nordström B., Mayor M., Andersen, J. et al. 2004, A&A 418, 989
Olsen, E.H. 1994, A&AS 106, 257
Pont, F., Eyer, L. 2004, MNRAS 351, 487
van den Bergh, S. 1962, AJ 67, 486

Report on the ESO-Arcetri Workshop on

Chemical Abundances and Mixing in Stars in the Milky Way and its Satellites

S. Randich (INAF-Osservatorio Astrofisico di Arcetri)

and L. Pasquini (ESO)

Between 13 and 17 September 2004, an ESO-Arcetri workshop took place in Castiglione della Pescaia, a middle age village in the south of Toscana, on the beautiful coast of Maremma.

Thanks to the advent of 8 m class telescopes and efficient high resolution spectrographs, detailed chemical composition can now be obtained for stars of different masses and evolutionary stages, both in our Galaxy and in its neighborhood satellites, and the VLT with FLAMES and UVES is providing a wealth of high quality data. Chemical abundance ratios and patterns represent key fossil records that can reveal the complex chemical history of the stellar aggregate out of which stars formed; if correctly interpreted, measured abundances will allow us to derive the star formation history and evolution of the host galaxies. As a crucial step, however, we must first ensure that the abundances presently observed in the stellar atmospheres are the pristine ones. We must therefore first understand stellar mixing, a phenomenon present in most stars which may affect not only the surface abundances of the fragile elements, such as lithium and beryllium, but also the most commonly studied heavier elements.

In this context, the workshop aimed to bring together theoreticians and observers to discuss the advancements of the last years both in observations and in the models. An impressive amount of new abundance data sets were indeed presented and the lively discussions which took place throughout the week testify that the interaction between observers and theoreticians was very successful. About 150 scientists were present; attendance by scientists from the ESO community was very high, complemented by a significant overseas participation. 70 talks were scheduled in the 6 sessions, complemented by more than 60 posters.

The first part of the programme of the 5 day long workshop addressed the chemical composition of the main components of the Galaxy: the Galactic disk, and the spheroidal components, the Halo and Bulge, respectively. The fragile light elements, Li and Be were discussed separately and the focus moved afterwards to chemical abundance measurements in Local Group neighborhoods. One day was then dedicated to the theory of mixing and to the analysis of the theoretical results, while the last session was devoted to chemical evolution models and to the implications for Big Bang Nucleosynthesis. We present here a selection from among the topics. The Proceedings will be published by Springer Verlag as part of the ESO *Astrophysics Symposia*.

The importance of Open Clusters as key probes of chemical evolution of the Galactic disk was emphasized, together with the fact that homogeneous, large, accurate data sets are required to achieve the goal. Available data on [Fe/H] and α elements suggest that the overall metallicity of a cluster depends more on the position in the disk than on its age. Indications have been found that the outermost clusters may deviate from the general abundance gradient and show enhanced α elements. New observations of several clusters are being obtained which will allow us to investigate these issues in greater detail. New, convincing arguments were presented, showing that the classical distance of the Pleiades cluster is favored with respect to the Hipparcos distance, eliminating the possible discrepancy with stellar evolution theory.

Detailed abundance studies of field disk stars now clearly indicate that stars belonging to different kinematical components (e.g. thin and thick disks) separate well when their elemental ratios are considered. For example, the thick disk appears more α enhanced than the thin disk. Based on currently available abundances and age determinations, the formation of the disk through a fast monolithic-like collapse appears problematic. On the other hand, a comparison of elemental ratios with similar ratios obtained for stars in nearby galaxies has so far revealed no chemical evidence that the thick disk was formed by the accretion of nearby dwarf galaxies. The production of α elements in all our neighborhood companions is much lower than what can be observed in the disk, suggesting that the rate of star formation in these galaxies is fairly slow.

There are, however, exceptions, the most noticeable being the Sagittarius dwarf, which is currently being swallowed by our own Galaxy and shows an interestingly high metal content and a relatively young population. It is also worth mentioning that the presence of multiple stellar populations, most likely spatially segregated and with extended halos, seems well established in nearby dwarf spheroidals.

A wealth of new results concerning the spheroidal component of the Galaxy were presented: Globular Clusters chemical anomalies and element-to-element anticorrelations (the most famous ones being the CN-CH and the O-Na anticorrelations) occur regularly, and it is now evident that internal mixing is not the main factor responsible for these. They are ubiquitous even on the main sequence and lower subgiant branch, where deep mixing can be ruled out; several observational examples instead favor the scenario of primordial pollution from a previous generation of stars. Whatever the polluters are, it is not trivial to quantitatively explain the observed abundance trends.

Field stars in the halo reveal instead extremely tight abundance and abundance-ratio patterns, down to the lowest levels of metallicity. It is also worth noting that bright giants in the halo show clear signatures of stellar CNO mixing even at the lowest metallicity which is now observed.

Finally, the difficulty of deriving accurate abundances for stars in the Galactic bulge was discussed in detail; available results show that chemical enrichment in the bulge of our Galaxy is not as extreme as in the most massive extragalactic spheroids.

A few talks were devoted to the light elements Li and Be. As far as Li is concerned, outstanding issues in the analysis and interpretation of the ^{7}Li plateau (commonly thought to be representative of the primordial Li abundance) have been examined. The virtually zero spread in the plateau has been confirmed, implying at most a small depletion in Li (<0.1 dex) in the Pop II hot dwarfs. In addition, recent UVES results suggest that we might soon be witness to the birth of a ^{6}Li plateau (a detection of ^{6}Li at [Fe/H]=–2.7 has also been reported) and of a Be plateau at the lowest metallicities. These are definitely topics to monitor in the coming months, especially if the disagreement between primordial Li abundances inferred from the Li plateau and values predicted by

BBN and WMAP values of the baryon density is not solved. The use of Be as a cosmochronometer for the early Galaxy has been successfully tested, and it has been shown that the observation of fragile elements is crucial to understanding globular cluster formation. New Li and Be observations have also been carried out in a variety of open clusters; models of pre-main sequence Li depletion still do not match observed patterns for solar-type stars, while a very good consistency is obtained for very low mass stars. The use of the lithium depletion boundary as an alternative and secure age indicator for young clusters has been stressed. The low level of Li in the Sun, one of the strongest factors of evidence for the existence of a non-standard mixing process on the main sequence (MS), remains unexplained and the depletion mechanism is still elusive. Whereas a few stars in old clusters share the low Li content of the Sun, the majority of solar-type stars intriguingly level out their Li content at an abundance of about a factor of 10 higher than solar. Finally, it has also been shown that planet-host stars, which are statistically more metal-rich than stars without planets, do not differ from the latter as far as the light elements are concerned. These results argue against pollution from planetary material as the key process leading to an overall metallicity excess, since in case of pollution an enhancement in

Li and Be should also be observed.

A general word of caution is appropriate: whilst the 1D treatment of stellar atmospheres is fairly primitive, most recent solar abundances retrieved with the 3D treatment show a large discrepancy between several chemical element abundances in the Sun, oxygen in particular, and the independent constraints from helioseismology.

In summary, from the observational point of view, we now have clear observational evidence of internal extra-mixing processes (i.e., mixing mechanisms not predicted by standard stellar theories) both during the MS and even more for stars evolved off the MS. Differences of abundances in key elements are observed in massive stars in the Galaxy and in the Magellanic Clouds at different evolutionary stages, and CNO cycled material and isotope ratios show the presence of deep mixing among bright RGB stars. The mixing mechanisms are most likely related to stellar rotation, which is relevant for both hot, rapidly rotating stars and for lower-mass, more slowly rotating stars. It is worth noting that, whilst extra-mixing does not seem to affect red giant evolution, it has very important implications for different issues (e.g., Galactic evolution of ^{3}He). As far as massive stars are concerned, rotating models and mixing have important consequences for chemical yields and thus Galactic enrichment. We would like to stress

that, perhaps for the first time, in addition to a large body of observations that provide abundances for several elements, for stars in a variety of evolutionary stages and environments, appropriate models are now available. By using fairly general treatments it is possible to reproduce quantitatively the behavior of observed chemical patterns for stars in a large range of masses.

Finally, models of Galactic evolution of Li and Be still have problems in reproducing the observed patterns, in particular the plateau at low metallicities. Galactic evolution models for heavier elements in our Galaxy and in its dwarf satellites have been presented. Whereas [α/Fe] ratios in dwarf spheroidals seem rather well reproduced, the evolution of elements such as N and C is less well constrained and appears critically dependant upon stellar evolutionary models and stellar yields. Nitrogen, for example, is overproduced in dwarf irregular galaxies.

Several of these aspects, including the bright future of these investigations, in particular with the advent of Gaia, were emphasized in the two summary talks.

A successful workshop benefits from the work of many. In addition to all the participants, special thanks go to the SOC and the whole LOC (C. Travaglio, E. Masini, D. Galli, P. Sestito, P. Bristow, G. Pace, C. Stoffer). Their excellent work made our stay not only interesting, but also pleasant.

ALMA Community Day

T. L. Wilson (ESO) and E. F. van Dishoeck (Leiden Observatory)

A major event has been the ALMA Community Day, held at ESO Garching 2004 September 24. This event was sponsored by ESO and RADIONET. There were more than 130 participants. Most of the members of the European Science Advisory Committee (ESAC) of ALMA actively participated in the organization of the Workshop and most were able to attend. The morning session opened with a greeting by the Director General. Then there was a review of the project by the Joint ALMA Office Director Massimo Tarenghi. This was followed by a series of 5 longer science samplers and 6 shorter presentations on topics relevant to ALMA. There was emphasis on how ALMA could further progress in these areas. After the lunch break there were 4 longer talks about plans for ALMA computing (from the users point of view), early science observing, and two talks on the ESO plans for the ALMA Regional Center (ARC) in terms of user support and science support. The meeting ended with a one hour discussion involving all of the participants. The Community Day agenda and presentations have been collected and are to be found on the website: http://www.eso.org/projects/alma/meetings/gar-sep04/. It was felt that there should be another, perhaps longer, Community Day meeting in about one year's time.

Within ESAC (for the current membership see http://www.eso.org/projects/alma/newsletter/almanews2/), there are plans for future meetings. Among the topics proposed are the SZ effect, for a meeting in

Paris, spectral line searches with an emphasis on molecules of biological interest, for a meeting in Denmark, and modeling of sources at a workshop in Sweden. In conjunction with North America, there are plans for the next global ALMA Science meeting, to be held in Madrid in 2006.

The NEON School Enters a New Era

Michel Dennefeld (IAP, France),
for the NEON consortium

THE NEON SCHOOL, a school on astronomical observations organised by a collaboration of observatories (Asiago, Calar Alto, ESO, La Palma and OHP) is well known by PhD students in astronomy all over Europe. It runs tutorial observations directly at the telescope for students in small groups, under the supervision of an experienced astronomer. This way, the participants can execute a real scientific program with all the steps needed in professional life: preparation of the program with selection of targets and feasibility estimates; set-up of the instrument and calibrations; running of the observations, in general both imaging/photometry and spectroscopy; data reductions; and, finally, the presentation of the results at the end of the school.

The first series, financed by a contract from the European Union under the Marie Curie program in FP5, held schools in Calar Alto Observatory, Spain (2000), in Haute-Provence Observatory, France (2001), and Asiago Observatory, Italy (2002). These observatories, while still at the forefront of research, are more easily accessible than the latest, largest telescopes like the VLT, where the pressure factor is higher, and they have a big advantage: one can still enter the telescope, open the camera if needed, or adjust the grating angle directly at the spectrograph. This hands-on experience gives good training: only those with good knowledge of an instrument are able to exploit its ultimate performance. Such experience is difficult to acquire on telescopes like the VLT where observations are conducted by the local staff (even in "visitor" mode) with the help of advanced software, and of course, not at all in service mode or with space observatories like Hubble or Spitzer. This first series finished with the end of the EU FP5 financing.

In the meantime it was also realised that many interesting projects can now be done with the wealth of archival data becoming available all over the world. Doing science with those archives is in fact not so different from the approach at the telescope: one still needs good preparation to define objectives and the instruments needed, and good analysis once the data are in hand. The first *Neon Archive Observing school* was therefore held last summer, following those lines, at ESO/ST-EcF in Garching, with generous support from both organizations. The *Opticon* network also sponsored some of the experts. Twenty students, coming from 11 different European countries, attended this school at ESO-Garching from July 14 to 24, to conduct small scientific projects in an exciting environment, using both ground and space data: such a multi-wavelength, multi-instrument approach is the modern way to do astrophysics! Introductory lectures were given in various topics by experts in the field: optical quality analysis of astronomical images (R. Hook from ST/Baltimore), photometric techniques (G. Piotto from Padova), tools for multi-wavelength archival data and virtual observatories (P. Padovani, ESO), etc. Other lectures presented the observatories accessible to young astronomers in Europe (those of the NEON consortium, and wider) and some of the future large projects (ALMA, OWL). The full program can be seen on ESO's web site: http://www.eso.org/gen-fac/meetings/neon-2004/.

The science projects dealt with evaluating star formation in merging galaxies (tutor: A. Pasquali, ETH Zurich); finding the galaxies responsible for the Lyman alpha absorption lines in the spectra of quasars (tutor: J. Liske, ESO); measuring the properties of globular clusters in M87 (tutor: S. Larsen, ESO); constructing the H-R diagram and derive metallicities of stars in the nearby Cetus Dwarf galaxy (tutor: M. Rejkuba, ESO); and measuring line strength indices and derive age and metallicities of globular clusters in NGC 3585 (Tutor: N. Cardiel, Calar Alto). Very interesting results were presented, demonstrating (if needed...) the value of modern archives: you can also find the full scientific presentations on ESO's Web page. Thanks to a very efficient organisation (particular thanks are due to co-organiser Harald Kuntschner and to Britt Sjoeberg!), this school was again a great success. When asked whether they would have preferred a school at the telescope, most of the students said they preferred the archive school! Reasons for that preference are to be attributed to the lively scientific environment of an institution like ESO, but probably also to the proximity of the town, compared with an isolated observatory!

So, what comes next? Schools on archival data are clearly needed, as AVO tools certainly have to be mastered by future astronomers. But that does not mean that schools with real observations should be discontinued: it is difficult to replace direct experience at the telescope, and it may well be that two different paths are now emerging in an astronomer's career. Those experienced astronomers needed to execute service observations probably need different skills than those sitting in their office making quality checks: but if the latter do not know how the observations have to be conducted, interaction will be difficult! So both type of schools should be conducted in the future. Fortunately, an FP6 proposal submitted by the NEON consortium to finance such schools has received a favourable evaluation, and negotiations are under way at the time of writing. The NEON schools will continue with EU support for another four years. It may well be that in some years, two schools will be scheduled in the same summer, one at the telescope, and one with archives, to satisfy the growing demand. Full information will, as usual, be available on the web pages of the European Astronomical Society (http://www.iap.fr/eas/) and on those of the participating observatories (Asiago, Calar Alto, ESO, La Palma and OHP). In the meantime further ideas to develop the interests and skills of students in astronomy are being considered also within the Opticon network (www.astro-opticon.org). We hope that we can count on many of you to act as lecturers or tutors during the coming NEON schools. Do not hesitate to contact us; it is a truly enriching experience, not only for the students.

THE COOL UNIVERSE: EXPLORING COSMIC DAWN

DANIELLE ALLOIN AND CHRIS LIDMAN (ESO)

In preparation for ALMA, the International Astronomical Observatories in Chile (IAOC) organised a conference on the topic of the cool universe. The conference was hosted by the Universidad Tecnica Federico Santa Maria (UTFSM) in the beautiful Chilean port city of Valparaiso from 4 to 8 October 2004 and was jointly supported by ESO, CTIO, LCO, Gemini, NRAO and NAOJ.

There were about 70 participants, of which 10 were students from countries in Latin America and 10 were students from the host university. We were extremely happy to be hosted by the UTFSM, where many of the technicians and engineers working at the astronomical observatories in Chile have been trained. This is a beautiful campus, from where one has clear views of the Pacific Ocean and Valparaiso. By chance, during this same week, the UTFSM opened its doors to young scholars from colleges in the area to visit and tour the campus. Therefore, we set up exhibitions about ESO and ALMA, and one of our SOC members, Dr. G. Garay from U. Chile, gave a public talk at the end of the Workshop.

In order to prepare the astronomical community in Chile for ALMA, we chose to organize the conference on the topic of the cool universe, which as everyone knows will provide key targets for ALMA! A broad range of astronomical topics were covered, from star-forming, primordial galaxies to star formation and the formation of disks and planets.

After a kind welcome given by Dr. O. Espinosa, Head of Physics Department at UTFSM, we started with a tutorial by Dr. M. Guelin, about observing in the millimeter domain and deriving physical information about the observed targets. The early universe was reviewed in two talks, by Dr. D. Spergel (CMB) and Dr. C. Carilli (epoch of re-ionization, galaxy formation, ...). Emission processes in the interstellar matter were discussed and colorfully presented by Dr. P. Ho, while the fate of dust particles was discussed by Dr. E. Dartois. All the activities related to the path from molecular clouds to stars and chemical enrichment were discussed by Dr. L. F. Rodriguez, Dr. J. Cernicharo and Dr. D. Mardones. Back to some cosmological relevance, Dr. A. Wolfe discussed the properties of the ISM as a function of redshift. Finally, protoplanetary and related discs were discussed by Dr. F. Menard. After each review, oral contributions on the topic were made. The last day was devoted to more technical aspects, starting with a review by Dr. M. Rubio, of all astronomical facilities on the Chajnantor plateau (the site of ALMA), either existing, in construction or in planning. Then, a detailed presentation was made of each of the facilities. Posters on different subjects discussed at the Workshop were presented as well. The concluding remarks of the Workshop were kindly given by Dr. T. Geballe.

During the conference, there were interviews with local newspapers and radio stations, a delicious cocktail (in spite of the rather cold and grey weather), "mariscos", a Chilean delicacy, and walks in the amazing city of Valparaiso with its "escaleras", "ascensores", flowers, cats and colorful houses. The foreshore of Valparaiso was the site of the workshop dinner where we also enjoyed South American music, dancing and a wonderful display of pictures taken during the Workshop.

We hope that more young astronomers will join the millimeter fan club and start considering ALMA as a near reality and not as a distant project! Many thanks to our host, the UTFSM, to the IAOC sponsoring organisations and to all the SOC/LOC members and staff who helped with the preparation of the Workshop.

THE "VENUS TRANSIT EXPERIENCE"

HENRI BOFFIN AND RICHARD WEST (ESO EPR DEPT.)

On November 5-7, 2004, an unusual conference took place at the French Ministry of Research in Paris. Entitled the "*Venus Transit Experience*", this meeting was organised by the VT-2004 International Steering Committee (ISC) and the local arrangements were ably taken care of by the staff of the IMCCE and the Observatoire de Paris, with Jean-Eudes Arlot and William Thuillot at the helm. It brought together more than 150 persons connected to the VT-2004 programme. The aim was to sum up the vast experience gained through this unique public education programme and, in particular, to perform an evaluation of its many components. On the first day, more than 50 students from the Paris areas who participated actively in this programme were also present.

The meeting was opened by the Directrice de la Recherche, Mme Elisabeth Giacobino, on behalf of the French Minister of Research, as well as Mr. Bernard Leroy, from the CNRS, on behalf of the Director General of the National Institute of the Sciences of the Universe (INSU, CNRS). Following an overview of the VT-2004 programme by ISC members with the presentation of some of the highlights, a lecture by famous astrophysicist and populariser

Hännes Heyer (ESO)

The lecture by famous astrophysicist and populariser Hubert Reeves was followed with great attention.

Hubert Reeves on "Humanity and Astronomy" placed the associated themes into a larger perspective.

They were succeeded by the showing of ten Laureate Videos selected by the jury for the VT-2004 Video Contest. The participants accorded a "*Prix du Public*" to the Video "... 121 ans après" produced by a team of Belgian students led by Audrey Coeckelberghs and Aurore Genicq. The three top prizes went to the following teams:

1st Prize: "The Venus Transit in the Golden Valley" by Matthews Biggs, James Hendry, and Louisa Llewellyn, (Herefordshire, UK).

2nd Prize: "Venus in Sole Visa" by Martin Lhotak and Robert Smolik (Prague, Czech Republic)

3rd Prize: "Millenium Transit" by Piotr Majewski and Jerzy Rafalski (Torun, Poland).

The Jury, in agreement with ESO, and in recognition of the excellent quality of all three winners decided to award all three teams a trip to Paranal, a gesture that was received with much emotion by all.

On the second day of the conference, reports were given by experts in various areas e.g. primary and secondary schools, media and amateur astronomers, which demonstrated the success of the entire effort but also served to identify some areas in which experience was gained that will become useful for future projects of this kind. National Committees from about 25 countries, either orally or by posters, documented in a comprehensive way the individual approaches taken in different regions and cultural environments and reported many useful "lessons learned" within the unique VT-2004 pilot project.

This was also the opportunity to announce the interesting outcome of the vast "VT-2004 Observing Campaign" that was organized to re-enact the historical determination of the distance to the Sun (1 AU) by means of timings of the four contacts made by observers in and outside Europe. A large number of groups of observers registered; at the end, there were 2763 all over the world and among these almost 1000 school classes. As expected, not all groups delivered timing observations of the transit. In some places, the weather did not co-operate, some observers may have had instrumental problems, e.g., with the time signals, and others may not have felt confident to send in their measurements. Still, the resulting database is impressive: by the stipulated deadline on July 10, 2004, no less than 4550 contact timings had been received from 1510 registered observing teams.

Following extensive analysis of this large material at IMCCE, the final result was: **1 AU = 149 608 708 ± 11 835 km**, or just 0.007% larger than the currently accepted value, as determined by radar measurements – a splendid outcome of a truly unique international collaboration! More details are available at the VT-2004 website (http://www.vt-2004.org).

On the last day of the meeting, representatives of the National Nodes met with the International Steering Committee members to discuss how to build on the enormous momentum gained throughout the VT-2004 project. By unanimous vote, it was decided to work towards the creation of a continent-wide "*European Astronomy Day*" (an attractive name still to be found!) in autumn 2006, aimed at the broad public in general, and the schools in particular. The intention would be to manage it in a wide collaboration between European astronomy-oriented organizations and institutes, science communication institutions (planetaria, science centres) and amateur organizations, all bound together by a network with national/regional nodes, based on the current VT-2004 National Nodes, but suitably modified and amended to reflect the change of emphasis.

Everybody agreed that the "Venus Transit Experience" meeting proved very successful and was a nice conclusion to a unique public education project. Most of the presentations given at this conference are available on the web at http://www.vt-2004.org/FinalEvent/.

The winners of the VT-2004 Video Contest show their joy when they learn they are good for a trip to Paranal.

Hännes Heyer (ESO)

Personnel Movements

(1 September 2004 - 31 November 2004)

ARRIVALS

EUROPE

BEDIN, Luigi (I)	Fellow
BIK, Adrianus (NL)	Fellow
BORTOLUSSI, Alessandro (I)	Paid Associate
CASALI, Mark (I)	Astronomer
DI CESARE, Stephane (F)	Software Engineer
FEYRIN, Sylvie (F)	Software Engineer
GERKEN, Bettina (D)	Student
JORDAN, Andres (CL)	Fellow
JÖRVINEN, Arto (FI)	Student
KELLERER, Aglae (F)	Student
KIRCHBAUER, Jean Paul (D)	Mechanics Technician
KJAER, Karina (DK)	Student
KNIAZEV, Alexei (RU)	Paid Associate
MESSINEO, Maria (I)	Fellow
MORA, Marcelo (CL)	Student
RZEPECKI, Jaroslaw P. (PL)	Student
SEDGHI, Babak (IR)	Paid Associate OWL
SEICHTER, Nicole (D)	Paid Associate
SEIFAHRT, Andreas (D)	Student
THEBAUD, Nathalie (F)	Paid Associate
UTTENTHALER, Stefan (AT)	Student
VANDAME, Benoit (F)	Fellow
WEHNER, Stefan (D)	Software Engineer

ESO Presentation in Copenhagen

C. Madsen and S. D'Odorico (ESO)

On November 8, ESO continued its series of presentations in member-states with an event in Copenhagen. So far events have been organised in Belgium, Finland, Portugal, Sweden, Switzerland and the United Kingdom. The purpose of these presentations is to raise the awareness of ESO amongst decision-makers, academia and the media. Over time, the scope and specific focus of the national events have varied, considering the particular circumstances and the wishes of the national hosts, and accordingly, the presentation in Denmark was primarily oriented towards industry. The meeting was initiated by the Royal Danish Consulate General in Munich in conjunction with the Confederation of Danish Industries and the Ministry for Science, Technology and Innovation. Leading up to the meeting, several articles about ESO had appeared in the Danish press and the 2nd TV Channel featured a report on the ESO projects also in connection with the event.

A total of 12 companies and 7 research institutes, covering a wide spectrum of activities including systems engineering, antenna technologies, mechanical engineering, construction, software development, optical systems and composite materials participated in the meeting, together with a number of representatives of the relevant authorities, including the Danish members of the ESO Council, and the Confederation itself.

In the morning, the participants were welcomed by the deputy Director General of the Confederation of Danish Industries Mr Ole Krog and by Mr Leo Bjørnskov, Permanent Secretary of State for Science, Technology and Innovation. During the morning session, the ESO Director General and several ESO staff members gave talks about ESO and its projects, especially the VLT 2nd generation instrumentation, ALMA and the 100-m OWL project. These talks were complemented by presentations by Danish astronomers and high-tech industries that had been involved with ESO projects.

In the afternoon, the meeting continued with dedicated workshops about the ALMA and OWL projects as well as a presentation about ESO procurement policies and practices. The workshops discussed a host of technical and procurement issues and gave the participating companies ample opportunity to familiarize themselves with the technical and commercial requirements by ESO.

As far as the industry presentation was concerned, the companies expressed great satisfaction with the information provided by ESO and many participants showed strong interest in a follow-up visit to the ESO Headquarters in Garching. It is the intention, with the help of the Consulate General, to organise such a visit in late January 2005.

In a separate ceremony in the afternoon, the ESO Director General and the Vice-Chancellor of the Copenhagen University, Mr Jørgen Olsen, signed the agreement for the construction of the *X-shooter*, a second generation VLT instrument scheduled to go into operation at one of the VLT Unit telescopes at Paranal in 2008 (see Page 7). The *X-shooter* will have the unique capability to

The ESO Director General addressing the participants to the industry presentation in Copenhagen.

obtain in a single exposure a high quality spectrum of a faint celestial target from the atmospheric cut-off in the UV to the near infrared. It will be particularly suited for the follow up of rapidly varying objects with an unknown spectrum like the powerful Gamma-Ray Bursts. *X-shooter* is a joint project of ESO with institutes in France, Denmark, Italy and the Netherlands. The Niels Bohr Institute (NBI) of the University of Copenhagen will provide several subsystems of the instrument including one of the spectrographs. For this project, the NBI will invest 19 man-years and has benefited from a grant by the Carlsberg Foundation and funding by the Descartes Prize.

Rounding up the visit, ESO's Director General gave a well-attended colloquium entitled 'ESO after 5 years of VLT', reviewing the most significant scientific results and the status of the ESO's projects, at the University of Copenhagen's Rockefeller complex.

CHILE

ANDERSSON LUNDGREN, Andreas (SE)	Fellow
BAES, Maarten (B)	Fellow
BORISSOVA, Jordanka (BG)	Astronomer
CARUSO, Fabio (I)	Instr. Engineer
HERMANT, Charlotte (B)	Logistics Officer
LYNAM, Paul (UK)	Fellow
MIRABEL, Igor-Felix (F)	Repres. of ESO Chile
SUC, Vincent (F)	Student
STEFL, Stanislav (CZ)	Op.staff Astronomer
TELLO, Cristobal (CL)	Officer Chilean Affairs

DEPARTURES

EUROPE

BERRINGTON, Sylvia (PL)	Legal Advisor
BIANCHINI, Andrea (I)	Student
CRETTON, Nicolas (CH)	Fellow

DADDI, Emanuele (I)	Fellow
ETTORI, Stefano (I)	Fellow
GUZMAN, Ronald (BO)	Student
HEMPEL, Maren (D)	Student
KHRISTOFOROVA, Maria (RU)	Student
MASSERON, Thomas (F)	Student
MULLIS, Christopher (US)	Fellow
PIRENNE, Benoit (B)	Head, Ots Group
RICCIARDI, Francesco (I)	Software Engineer
PACE, Giancarlo (I)	Student

CHILE

BLANCO LOPEZ, Leonardo (F)	Student
EHRENFELD, German (CL)	Mechanical Engineer
GUEGUEN, Alain (F)	Student
GUZMAN, Juan Carlos (CL)	Application Programmer
HUNTER, Ian (UK)	Student
MATHIEU, Michele (CL)	Logistics Supervisor
RAHOUI, Farid (F)	Student

CONTENTS

TELESCOPES AND INSTRUMENTATION

REPORTS FROM OBSERVERS

OTHER ASTRONOMICAL NEWS

Front Cover Picture: *Majestic Spiral*

The beautiful multi-armed barred spiral galaxy NGC 7424 is seen almost face on. Located in the constellation Grus (the Crane), it was observed by ESO Paranal Science Operation Astronomers with VIMOS on the VLT in three filters (*B*, *V* and *R*). It was further processed in this colour composite by Henri Boffin (ESO).